Université de Montréal

Modélisation de la rétrodiffusion des ultrasons par le sang. Application à la mesure de l'agrégation érythrocytaire.

par
David Savéry

Institut de génie biomédical
Faculté de médecine

Thèse présentée à la Faculté des études supérieures
en vue de l'obtention du grade de Philosophiae Doctor (Ph.D.)
en génie biomédical

Juillet 2003

Université de Montréal

Faculté des études supérieures

Cette thèse intitulée :

Modélisation de la rétrodiffusion des ultrasons par le sang.

Application à la mesure de l'agrégation érythrocytaire.

présentée par :

David Savéry

a été évaluée par un jury composé des personnes suivantes :

Louis-Gilles Durand
président-rapporteur

Guy Cloutier
directeur de recherche

Yves Goussard
membre du jury

Pascal Laugier
examinateur externe

Robert Guardo
représentant du doyen de la FES

Résumé

Le sang humain fait partie de ces liquides qualifiés de « fluides complexes » en physique de la matière molle. Lorsqu'il s'écoule à faible vitesse de cisaillement, sa viscosité s'accroît de plusieurs ordres de grandeur, tandis que les globules rouges forment une phase dense, plus ou moins organisée, d'amas enchevêtrés. Dans certaines situations pathologiques, incluant les maladies cardiovasculaires et vasculaires cérébrales, la rhéologie sanguine est altérée : le sang perd de sa fluidité.

Aucune méthode ne permet encore la mesure *in vivo* des propriétés mécaniques sanguines. Pourtant, les liens pathophysiologiques de corrélation existant entre les maladies vasculaires et les anomalies hémorhéologiques restent manifestement à élucider. Pour se doter d'un tel outil, l'imagerie ultrasonore paraît prometteuse, puisque l'échogénicité sanguine croît significativement avec le niveau d'agrégation érythrocytaire. Il reste cependant à exploiter ce phénomène acoustique d'une façon plus quantitative.

Dans cette thèse, nous nous proposons donc de modéliser la rétrodiffusion acoustique d'une onde ultrasonore par une suspension sanguine. Plus spécifiquement, l'effet de l'agrégation des hématies sur le coefficient de rétrodiffusion sanguin χ, la propriété acoustique pertinente à l'imagerie échographique, est étudié. Pour parvenir à une spectroscopie de rétrodiffusion, la dépendance fréquentielle de χ est formulée dans l'approximation de Born de faible diffusion. Nous montrons que trois facteurs contribuent à sa valeur :

- la densité en nombre des globules rouges m,
- la section de rétrodiffusion σ_b,

– le facteur de structure S.

La densité élevée des hématies — $m \sim 5 \times 10^6$ mm^{-3}, fraction volumique $H \sim 0.4$ — entraîne la sensibilité des propriétés acoustiques sanguines à la microstructure de la phase érythrocytaire et la forte non-linéarité de la relation $m \rightarrow \chi$.

La section de rétrodiffusion est une propriété acoustique du globule rouge isolé et plongé dans le plasma. Nous montrons semi-analytiquement que l'hématie est assimilable acoustiquement à un cylindre plat (de rayon 3.9 μm et de hauteur 2 μm).

Le facteur de structure traduit l'effet de l'organisation spatiale de la phase érythrocytaire sur la rétrodiffusion. On peut le modéliser soit géométriquement (a) par une description stochastique du processus de positionnement des globules rouges, soit physiquement, en utilisant la thermodynamique statistique de particules en interaction à l'équilibre (b), ou en écoulement cisaillé (c). L'approche (a) a permis de trouver analytiquement le facteur de structure d'une dilution d'amas érythrocytaires via un modèle ponctuel de Neyman-Scott. L'approche (b) bidimensionnelle met en évidence l'effet de l'énergie d'adhésion et de l'anisotropie sur les propriétés de rétrodiffusion. L'approche (c) est esquissée en mettant en perspective les résultats de la littérature.

Forts de ces descriptions originales, nous proposons de caractériser la spectroscopie de rétrodiffusion du sang par deux paramètres acoustiques effectifs : le facteur de *packing* W et le tenseur de gyration des agrégats Σ_2. Ils sont dérivés du développement de Taylor au second ordre du facteur de structure basses fréquences. Couplés à l'évaluation Doppler de la vitesse de cisaillement, ces indices acoustiques pourraient directement servir à l'imagerie paramétrique *in vivo* du niveau d'agrégation érythrocytaire.

MOTS CLEFS : ultrasons, échographie, diffusion, sang, rhéologie, agrégation, érythrocyte, facteur de structure, physique statistique, géométrie stochastique.

Summary

Condensed matter physicists would describe blood as a "complex fluid" because of its singular rheological behavior. When flowing at a low shear rate, suspended erythrocytes tend to form an intricate network of cell clusters: blood appears much more viscous (by several orders of magnitude) than at a high shear rate. Resulting blood shear-thinning has a pathophysiological significance: hemorheological impairment appears as a risk factor of cardiovascular or cerebrovascular accidents.

To clarify how the atherothrombogenesis and the hemorheological abnormalities are related, an imaging method for *in vivo* assessment of the red cell aggregation level is required. Medical ultrasound seems promising as blood echogenicity is known to vary with shear-dependent erythrocyte clustering.

In this context, this thesis intends to model the acoustical backscattering of an ultrasound wave by blood, to specifically quantify the effect of red cell clustering on the blood acoustic properties. Assuming weak scattering Born hypothesis, one shows that the blood backscatter χ is the product of three factors:

- the erythrocyte number density m,
- the red cell backscattering cross-section σ_b,
- the structure factor S.

High density of the scattering erythrocytes ($m \sim 5 \times 10^6$ mm^{-3}, volumic fraction $H \sim 0.4$) leads to the high sensitivity of the backscattering coefficient to red cell microstructure, and to the strong non-linearity of the relation $m \rightarrow \chi$.

The backscattering cross-section represents an intrinsic property of the isolated ery-

throcyte immersed in aqueous plasma. It is shown that modeling the red blood cell by a flat cylinder with radius 3.9 μm and height 2 μm represents a good acoustical approximation.

The structure factor reflects the influence of the red cell spatial correlations (and therefore clustering) on blood echogenicity. Different approaches enabled to predict how microstructure affects its value. Stochastic models of a geometric nature describe the aggregates pattern without considering the underlying physics. An analytical formulation of the structure factor was derived for diluted suspensions of red cell aggregates using the Neyman-Scott random point process. On the contrary, statistical thermodynamics can depict the process of aggregate formation for physiological hematocrits more physically. A 2D equilibrium Gibbs-Markov random model enabled to derive the effect of the adhesion energy and of the medium anisotropy on the frequency dependence of blood backscattering coefficient. The effect of the shear flow is further tackled by the results of the literature.

Pertinent acoustical indices for *in vivo* parametric imaging of red cell aggregation have been derived. Second-order parameters of the Taylor expansion of the frequency dependence $\chi(f)$, namely the packing factor W and the gyration aggregate tensor Σ_2, are proposed as quantitative markers of the clustering state of erythrocytes.

KEYWORDS: ultrasound, medical imaging, scattering, blood, rheology, aggregation, erythrocyte, structure factor, statistical physics, stochastic geometry.

Table des matières

Liste des tableaux

Liste des figures

Liste des symboles et abréviations

a	rayon d'une sphère de volume $\mathcal{V}$
a^*	paramètre d'interaction hydrodynamique
$\mathcal{A}, A_i$	fenêtre de comptage
$\mathcal{A}_h$	constante d'Hamaker
$a_i(H)$	fonctions auxiliaires
$a_{ii} = \sqrt{5\Sigma_{ii}}$	axes de l'ellipsoïde ayant le même tenseur d'inertie Σ qu'une particule donnée
a^{VdW}	paramètre énergétique de l'équation d'état de Van der Waals
A^T	transposée de la matrice A
α_0	paramètre de régression en puissance $\chi = \alpha_0 f^\beta$
(α_2, α_4)	paramètres géométriques du profil normalisé du globule rouge
$\alpha(\vec{k})$	coefficient d'atténuation acoustique
α_p	atténuation particulaire
α_{exc}	atténuation d'excès
α_{vis}	atténuation visqueuse
b^*	paramètre d'interaction hydrodynamique
$(B, C, D, \dots)$	coefficients du viriel
b^{VdW}	paramètre de volume de l'équation d'état de Van der Waals

β	pente spectrale définie par la régression en puissance $\chi = \alpha_0 f^\beta$
c	vitesse du son
c^*	paramètre d'interaction hydrodynamique
c_0	vitesse du son dans le plasma
$\vec{C}_h$	coefficient hydrodynamique d'interaction particulaire
C_i	classe d'un échantillon sanguin
$c(\vec{r})$	fonction de corrélation directe
γ	energie surfacique d'adhésion
$\dot{\gamma}$	taux de cisaillement
$\gamma_\kappa(\vec{r})$	contraste relatif de compressibilité adiabatique
$\gamma_\rho(\vec{r})$	contraste relatif de densité massique
$\gamma_z(\vec{r})$	contraste relatif d'impédance acoustique entre particule et plasma
$\chi(\vec{k})$	coefficient de rétrodiffusion acoustique
χ^0	coefficient de rétrodiffusion à 5 MHz, $H = 0.4$
χ_{ref}	coefficient de rétrodiffusion de référence à 5 MHz, $H = 0.4$, suspension désagrégée
d	dimension fractale ou de symétrie
D	diamètre vasculaire
$\mathcal{D}$	diamètre érythrocytaire
$d\Omega$	angle solide
$dP(\vec{e}_r, d\Omega)$	puissance diffusée dans la direction $\vec{e}_e$ dans l'angle solide $d\Omega$
d_S	paramètre de variabilité d'une distribution de taille

$\Delta = a/\left(\sqrt{2}\sigma\right)$	facteur de taille
ΔP	chute de pression à travers un vaisseau
$\delta(\vec{r})$	impulsion de Dirac
ΔU	différentiel d'énergie entre deux transitions de l'algorithme de Métropolis
e_+	charge élémentaire
$E[X]$	espérance mathématique d'une variable aléatoire X
$\vec{e}_i$	vecteur unitaire pointant dans la direction d'insonification
e_{ij}, e'_{ij}	matrices de résultats de classification
$\vec{e}_r$	vecteur unitaire pointant dans la direction d'observation
ϵ	énergie d'adhésion
$\bar{\epsilon}$	énergie d'adhésion normalisée
ϵ_{min}	énergie minimale d'un puits de potentiel
ϵ_P, ϵ_0	permittitivité du plasma et du vide
f	fréquence acoustique
f_e	force de dissociation dans le modèle de pontage d'agrégation
$\vec{F}_h$	force hydrodynamique perçue par une sphère
$\vec{F}_i$	force hydrodynamique subie par la particule i
$F(\vec{k})$	facteur de forme
Φ	fonction numérique
$\phi(u)$	profil normalisé du globule rouge
$\phi_0(u)$	profil normalisé du potentiel de paire
$\phi_1(u)$	surface d'intersection $/\pi$ de deux disques unités distants de $2u$

$g(\vec{h})$	fonction de corrélation de paire
$\vec{h}$	distance interparticulaire
H	hématocrite
h_0	hauteur
H_d	hématocrite de décharge
HDL	high density protein
η	viscosité (de cisaillement)
η_e	viscosité efficace
η_h	viscosité de la solution d'hémoglobine intracellulaire
η_{plasma}	viscosité du plasma
η_∞	viscosité limite à vitesse de cisaillement infinie
$\imath = \sqrt{-1}$	nombre imaginaire
I_0	intensité de l'onde acoustique incidente
$\mathbb{I}_{[X]}$	fonction indicatrice valant 1 si X est vraie, 0 sinon
j_0,j_1	fonctions de Bessel d'ordres 0 et 1
k, $\vec{k} = k_r\vec{e}_R + k_z\vec{e}_z$	nombre d'onde, vecteur d'onde, composantes cylindriques
k_0	nombre d'onde central d'une onde pulsée
k_B	constante de Boltzmann
k_f	constante de temps de formation d'un complexe ligand-récepteur
K_m	module d'expansion surfacique de la membrane
k_r	constante de temps de dissociation d'un complexe ligand-récepteur
κ	compressibilité adiabatique
κ_0	compressibilité adiabatique plasmatique

κ_D^{-1}	portée des interactions dans le modèle de Yukawa ou de double couche (longueur de Debye)
κ_s	compressibilité adiabatique du diffuseur
κ_T	compressibilité isotherme
L	longueur d'un vaisseau ou dimension du volume diffusant
(L)	ligand dans un complexe ligand-récepteur
l_{cor}	longueur de corrélation
LDL(ox)	low density protein (oxydée)
λ	longueur d'onde acoustique
λ_0	portée réduite des interactions adhésives
m	densité en nombre des particules
M	nombre de fenêtres de comptage
MC	Monte Carlo
μ_m	module surfacique de cisaillement de la membrane
n	pente spectrale entre 0 et 40 MHz
N	nombre de particules dans V
N_a	nombre d'Avogadro
$N_{\mathcal{A}}$	nombre de points de Ω tombant dans la boîte $\mathcal{A}$
$N_b(t)$	nombre de ponts formés entre deux globules rouges
$n_c = E[N_c]$	nombre moyen de globules rouges par agrégats
N_c	nombre aléatoire de globules rouges par agrégats
N_i	nombre de points tombant dans la boîte A_i
$N_\Omega(\vec{r})$	densité microscopique
n_P	concentration plasmatique (en nombre) des protéines
n_x	pente spectrale entre 0 et 40 MHz parallèlement à l'axe des agrégats

n_y	pente spectrale entre 0 et 40 MHz perpendiculairement à l'axe des agrégats
ν	indice d'anisotropie
ω, Ω	ensemble de N particules, son modèle aléatoire
$\otimes$	produit tensoriel
$\vec{\omega}_i$	vecteur-rotation de la particule i
$\vec{\nabla}$	gradient
p	pression
p	variable aléatoire uniforme entre 0 et 1
p_0	amplitude de l'onde de pression incidente
pdf	probability density function
$\mathcal{P}_e$	nombre de Péclet
PEG	polyéthylène glycol
p_i	amplitude complexe de l'onde incidente
p_Ω	fonction de densité de probabilité de Ω
p_s	amplitude de l'onde de pression diffusée
PY	Perkus-Yevick
Π	pression osmotique
$\psi_i(u)$	fonctions auxiliaires
$q = \exp(-\Delta U/k_B T)$	ratio de Métropolis
$\vec{q} = k(\vec{e}_r - \vec{e}_i)$	vecteur de diffusion
Q	débit sanguin
$r = R_g/2a$	rayon de gyration de macromolécules réduit
$\vec{r} = x\vec{e}_x + y\vec{e}_y + z\vec{e}_z =$ $r\vec{e}_R + z\vec{e}_z$	vecteur courant de l'espace, ses coordonnées cartésiennes ou cylindriques

R	résistance vasculaire
R	rayon
(R)	recepteur dans un complexe ligand-récepteur
RBC	red blood cell
r_e	ratio des axes hydrauliques d'une particule sphéroïde
R_g	rayon de gyration de macromolécules
$\mathcal{R}_p$	nombre de Reynolds particulaire
ρ	densité massique
ρ_0	densité massique plasmatique
ρ_{ij}	coefficient de corrélation entre V_i et V_j
ρ_{RBC}	densité massique du globule rouge
ρ_s	densité massique du diffuseur
$\mathcal{S}$	surface érythrocytaire
SEC	spontaneous echo contrast
$S(\vec{q})$	facteur de structure
s_{ij}	composantes du tenseur de gyration Σ_2
σ	rayon de gyration d'un agrégat
$\Sigma = \frac{1}{\mathcal{V}} \int_{\mathcal{V}} \vec{r} \otimes \vec{r}\, d^3r$	tenseur d'inertie d'une particule
σ_0	densité surfacique de charge du globule rouge
Σ_2	tenseur de gyration des agrégats défini par $S(\vec{q}) \approx W + \vec{q}.\Sigma_2\vec{q}$
$\sigma_b(\vec{k}) = \sigma(-\vec{k}/k, \vec{k})$	section de rétrodiffusion
$\sigma_c = \sqrt{\mathrm{Var}[N_c]}$	écart-type du nombre de globules rouges par agrégats
$\sigma(\vec{e}_r, \vec{k})$	section de diffusion observée dans la direction $\vec{e}_r$ lorsque le vecteur d'onde incident est $\vec{k}$

σ_i	écart-type de V_i
Σ_{ii}	valeurs propres du tenseur d'inertie
σ_{ij}	composantes du tenseur Σ
t	temps
T	température absolue
T_j	période de rotation du globule rouge
τ_s	contrainte de cisaillement
τ	indice de collage de Baxter
u	variable auxiliaire adimensionnée
$U_\Omega(\omega)$	energie totale de l'état ω
US	ultrasound
UTC	ultrasonic tissue characterization
V	volume d'un diffuseur macroscopique
$\mathcal{V}$	volume érythrocytaire
$\vec{V}$	vecteur acoustique de classification
$V_2(\vec{h})$	énergie potentielle de deux particules distantes de $\vec{h}$
$\mathcal{V}_{\text{exclusion}}$	volume d'exclusion des protéines liées à l'agrégation
$\vec{v}_i$	vitesse de translation de la particule i
$(V_i)_{i=1...4}$	composantes de $\vec{V}$
$\vec{V}(\vec{r})$	champ de vitesse plasmatique
$\mathcal{V}(\mathcal{A})$	volume d'un ensemble $\mathcal{A}$
Var[X]	variance d'une variable aléatoire X
VLDL	very low density protein
V_{rep}	potentiel de répulsion

$W = \lim_{\vec{q}\to 0} S(\vec{q})$	facteur de packing
$\hat{W}$	estimateur (par l'approche particulaire) du facteur de packing
$\langle X \rangle$	moyenne spatiale d'une quantité X
$\vec{x}_i$	position de la particule i
ξ	paramètre morphologique d'une particule convexe
$z_0(r)$	profil radial du globule rouge
Z	impedance acoustique
Z_c	valence des contre-ions plasmatiques
Z_Ω	fonction de partition

À mon père

Remerciements

J'aimerai en premier lieu remercier mon directeur de thèse Dr. Guy Cloutier. Non seulement pour m'avoir accordé beaucoup de lattitude et d'indépendance durant cinq années de recherche, pour m'avoir inspiré pour la rigueur, le souci de l'exactitude dans la démarche scientifique, pour son support financier, ou pour m'avoir permis de participer à de nombreuses conférences. Mais surtout pour savoir rester proche de ses étudiants en instaurant une ambiance « familiale » au sein du Laboratoire de Biorhéologie et d'Ultrasonographie Médicale, un environnement où « il fait bon » travailler. *Merci !*

J'ai ressenti ce même confort durant la première partie de la thèse qui s'est déroulée à l'Institut de Recherches Cliniques de Montréal, au Laboratoire de Génie Biomédical. Cela est indubitablement dû au Dr. Louis-Gilles Durand, directeur du LGB, qui me fait l'honneur d'être le président de mon jury. Qu'il soit remercié d'avoir accepté de rapporter ce travail.

Ma formation doctorale doit aussi beaucoup au Dr. Yves Goussard, membre du jury. En effet, j'ai d'abord fait mes premières armes en traitement du signal et de l'image grâce à lui, dès septembre 1998, en participant au fameux cours GBM6103 du programme de Génie Biomédical. Mes connaissances alors disparates en ce domaine ont pris une toute autre ampleur grâce à ses compétences pédagogiques et scientifiques. Je lui suis également extrêmement reconnaissant de m'avoir fait confiance en me donnant la chance d'exercer comme chargé de cours au département de génie électrique de l'École Polytechnique de Montréal ou comme chargé de laboratoire. Ces périodes

auront été très marquantes pendant mon cursus. Je lui exprime ici toute ma gratitude. Je tiens également à remercier les autres membres du comité qui accepteront de fournir l'effort de juger cette thèse.

Ces cinq dernières années ont été une décoction d'activités scientifiques dans beaucoup d'amitié et de francs bons moments. Isabelle Fontaine m'a ainsi beaucoup aiguillé dans mes débuts, et dans la fin aussi ! Je la remercie pour son adorable gentillesse et pour ces temps caféinés de réflexion sur le facteur de structure. Partenaire d'étude dans les premiers mois Montréalais, Constantin Tranulis m'a accordé une amitié indéfectible durant cinq ans, je lui dois beaucoup personnellement. Damien Garcia a été un frère de route formidable. Je lui suis redevable à vie pour tout le support scientifique et moral qu'il m'a accordé durant toutes ces années. J'aimerai également remercier Christine Bertolotti pour les beaux sourires zébrés qu'elle m'a donnés. Je suis reconnaissant envers Zhao Qin d'avoir méticuleusement mené les expériences de quelques projets parallèles qui m'ont aguerri à la recherche. Je souhaite également beaucoup de succès aux équipes de la « nouvelle génération » du LBUM et du LGB. Spéciale dédicace à Roch Maurice et Amar Amararene pour avoir été mes complices de bureau.

Un certain nombre de personnes de mon entourage n'ont jamais franchi les portes du laboratoire mais m'ont aidé au moins tout autant en formant ma deuxième famille sur le nouveau continent. Benjamin Thierry m'a énormément encouragé, nourri(!), et sorti(!) durant ces derniers mois, je lui souhaite beaucoup de réussite dans sa prometteuse carrière de recherche. Marc Allain et Sandrine Le Querrec sont mes colocs de toujours: ils m'ont soutenu et apporté beaucoup d'équilibre moral (et scientifique) durant ces belles années de Mile End. Sophie Debrus m'a aussi beaucoup aidé moralement et a souvent prononcé des paroles réconfortantes déterminantes. Anabelle Masclet m'a fait l'honneur de non seulement connaître par cœur l'intitulé de ma thèse, mais aussi de corriger le premier chapitre introductif. Je remercie Marianne Giguère pour sa profonde amitié et pour m'avoir communiqué sa passion pour Montréal.

Enfin, j'exprime toute ma reconnaissance à ma famille qui a accepté mon éloignement durant ces années.

Ce travail a été effectué grâce au soutien financier du groupe de recherche en modélisation biomédicale de l'Institut de Génie Biomédical de l'École Polytechnique et de l'Université de Montréal.

Chapitre 1

Introduction : hémorhéologie, intérêt, mesures et ultrasons

1.1 Résumé du chapitre

Ce premier chapitre expose le contexte du projet. Après un bref rappel d'hématologie, nous justifions la pertinence de la rhéologie sanguine pour la physiologie de la circulation, le diagnostic clinique et l'étude étiologique de l'athérosclérose. Pour mesurer *in vivo* les paramètres hémorhéologiques, une méthode ultrasonore quantifiant l'échogénicité ultrasonore du sang s'avère prometteuse. Nous énonçons alors les objectifs généraux et le plan de cette thèse de doctorat qui contribue à la théorisation acoustique de cette technique.

1.2 Bases d'hématologie

Comme le corps humain se subdivise en organes aux fonctions bien spécifiques et distribuées, un système de transport doit pouvoir véhiculer entre eux matière et signaux informatifs nécessaires à la physiologie systémique. Le sang qui circule dans le système bouclé cardio-vasculaire — tel qu'observé par William Harvey en 1628 — assure ce rôle de transporteur. Toutes les fonctions de l'organisme dépendent ainsi plus ou moins directement de la circulation sanguine, à savoir de l'efficacité de la

pompe cardiaque et de l'irrigation des tissus en nutriments, oxygène etc.

Le sang est un fluide hétérogène : les cellules sanguines — globules rouges, globules blancs et plaquettes — sont suspendues dans le plasma, solution aqueuse constituée d'électrolytes et de solutés organiques. La composition sanguine est résumée dans le tableau (1.2). Le volume sanguin circulant s'élève à 5 L en moyenne, le débit normal de sang chez l'adulte au repos est de 5 $L.min^{-1}$, le cœur battant à quelques 72 contractions par minute [215].

Les globules blancs ont une fonction immunitaire (phagocytage par les neutrophiles et macrophages, sécrétion d'anticorps par les lymphocytes...) et les plaquettes jouent un rôle hémostatique en s'agrégeant et en participant à la cascade de coagulation. Les globules rouges représentent 99% des cellules sanguines. Ces cellules énuclées (Fig. 1.1) transportent l'oxygène, qui se combine avec l'hémoglobine, et le dioxyde de carbone — déchet du métabolisme cellulaire. On peut aisément concevoir que par leur proportion élevée, les globules rouges conditionnent largement les caractéristiques physiques du sang observées à l'échelle macroscopique, tandis que les autres cellules sanguines n'y contribuent que minimalement.

1.3 Propriétés mécaniques du sang

1.3.1 Notion de résistance vasculaire

Le travail cardiaque est régulé de manière à ce que le débit sanguin satisfasse aux besoins conjugués de tous les organes. Schématiquement, la pression artérielle est contrôlée par différents mécanismes fondamentaux :

- la capacité de la pompe cardiaque à fournir un travail moteur donné,
- la morphologie régulée du réseau artériel et veineux,
- la rhéologie vasculaire,
- la rhéologie sanguine qui joue conjointement sur la résistance de chaque « or-

Composants	Concentrations normales
globules rouges (*érythrocytes*, *hématies*)	4 à 5×10^6 mm^{-3} $H \sim 40\%$ en volume
globules blancs (*leucocytes*)	5 à 10×10^3 mm^{-3}
plaquettes (*thrombocytes*)	1 à 2×10^6 mm^{-3}
plasma	$\sim 60\%$ en volume
ions	
sodium	3.4 $g.L^{-1}$
chlorure	3.6 $g.L^{-1}$
bicarbonate	1.5 $g.L^{-1}$
potassium	0.2 $g.L^{-1}$
...	
sucres	0.9 $g.L^{-1}$
lipides, lipoprotéines	7 $g.L^{-1}$
protéines	73 $g.L^{-1}$
albumine	45 $g.L^{-1}$
globulines	25 $g.L^{-1}$
fibrinogène	3 $g.L^{-1}$

TAB. 1.I – Composition du sang, d'après [94, 215].

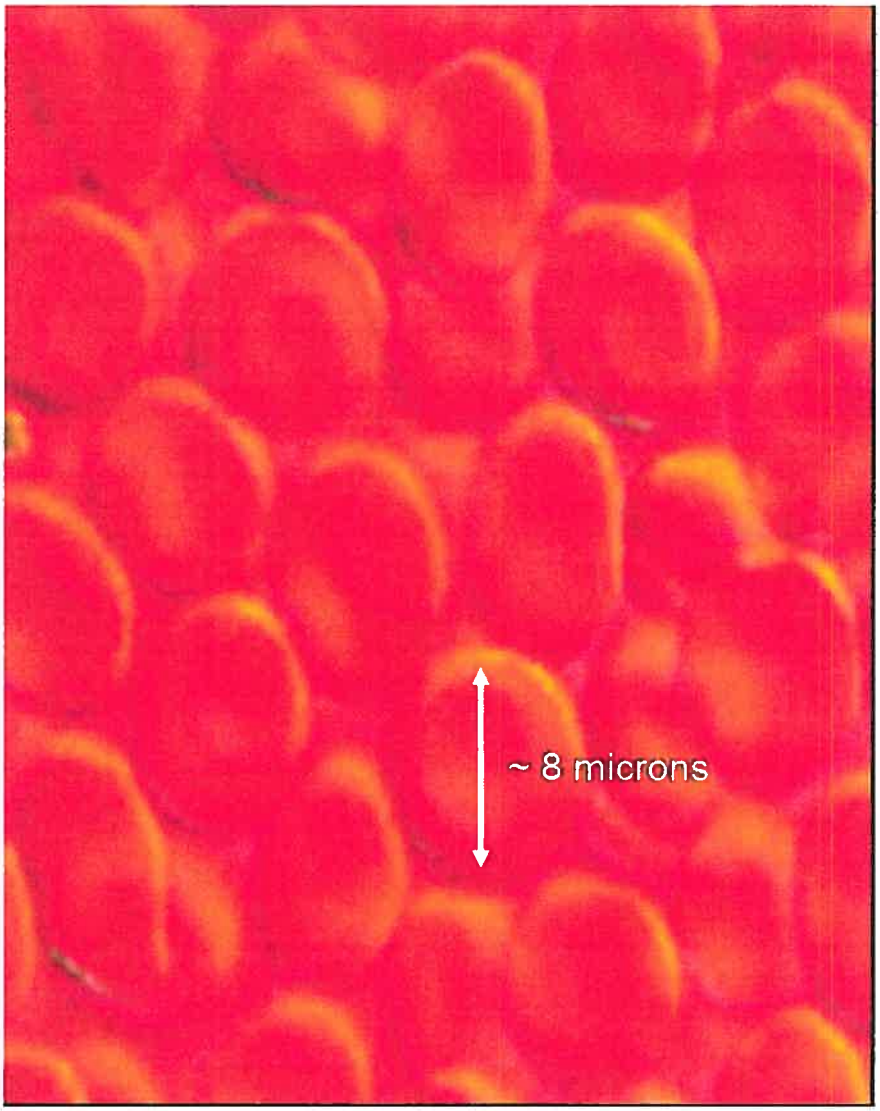

FIG. 1.1 – Morphologie des globules rouges

gane » sang-vaisseau.

L'approche classique pour aborder l'hémodynamique globale du réseau circulatoire est d'évaluer la résistance à l'écoulement de chaque vaisseau par le rapport :

$$R = \frac{\Delta P}{Q},$$

où ΔP est la chute moyenne de pression entre les deux extrémités du vaisseau, et Q

est le débit sanguin moyen à travers l'artère ou la veine. Moyennant des hypothèses très réductrices (diamètre D constant du vaisseau cylindrique de longueur L, rigidité du tube, écoulement stationnaire et laminaire, fluide Newtonien de viscosité η), le facteur de résistance peut s'exprimer en fonction de la viscosité sanguine et de la géométrie vasculaire par l'équation de Hagen-Poiseuille [161] :

$$R = \frac{128 L \eta}{\pi D^4}.$$

La dépendance en D^{-4} de cette résistance-modèle fait prendre conscience de l'impact de la section luminale vasculaire sur l'hémodynamique. Dans ce paradigme simple, une constriction de 50% du rayon vasculaire entraîne une multiplication par 16 de la résistance ! Cela explique simplement pourquoi la distribution du débit sanguin à travers l'arbre vasculaire est régulée en grande partie par l'action des muscles lisses des artérioles.

L'approche de type Poiseuille-Hagen a pourtant ses limites. La relation $\Delta P = f(Q)$ est loin d'être linéaire, et doit être abordée différemment : la complexité de la *biomécanique* circulatoire est difficilement réductible à la mise en série ou en parallèle de tubes cylindriques rigides traversés par un fluide homogène !

Parmi les spécificités de la circulation que les biomécaniciens doivent prendre en compte, notons l'importance de la géométrie tortueuse du vaisseau et de la compliance vasculaire naturelle — alliée au caractére pulsé de l'écoulement à la sortie du ventricule gauche — qui complexifie la description spatio-temporelle de l'écoulement. De surcroît, le degré de complexité de la biomécanique circulatoire ne provient pas exclusivement de la pompe cardiaque et du réseau : le sang dispose de propriétés rhéologiques singulières à cause de son hétérogénéité.

1.3.2 Introduction à l'hémorhéologie

Bref historique

Les spécificités des propriétés mécaniques du sang, considéré macroscopiquement comme un fluide, doivent être évoquées pour expliquer la relation entre les forces motrices et la dynamique de l'écoulement. Il faut souligner que l'*hémorhéologie*[1], la discipline étudiant les propriétés mécaniques sanguines, est un domaine relativement nouveau. La complexité de ce fluide hétérogène (de type colloïdal) explique sans doute pourquoi la rhéologie sanguine est si peu exploitée dans l'analyse de certains faits pathophysiologiques cardiovasculaires et notamment microcirculatoires. En 1702, Van Leeuwenhoek observe pour la première fois l'accroissement de viscosité sanguine dans la microcirculation des têtards [218]. Profitant des améliorations de l'époque en microscopie, il relate ainsi sa fascination pour l'observation de ces phénomènes (traduction tirée de [62]) :

> « Le mouvement du sang chez ces têtards dépasse celui de tous les autres petits animaux et des poissons que j'ai vus ; à vrai dire, ce plaisir a souvent été pour moi tellement réconfortant, que tous les plaisirs que peuvent donner les fontaines, ou les ouvrages aquatiques naturels ou artificiels, ne pourraient être plus grands pour ma vue que l'observation de ces créatures. »

En 1931, Fåhraeus et Lindqvist [78] mesurent la viscosité *efficace* du sang η_e, définie empiriquement par la formule de Poiseuille-Hagen, pour de petits capillaires *in vitro* :

$$\eta_e = \frac{\Delta P}{Q} \times \frac{D^4}{128L}.$$

Ils montrent que η_e décroît lorsque le diamètre du capillaire varie d'une taille ma-

[1] Le terme « hémorhéologie » a été utilisé pour la première fois par Copley en 1958.

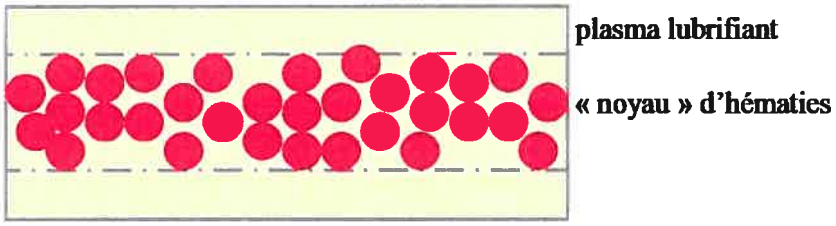

FIG. 1.2 – Couche plasmatique lubrifiante dans les microvaisseaux (diamètre de l'ordre de 30 à 40 μm).

croscopique $\sim$ 1 mm à une taille microscopique $\sim 7\mu$m, puis croît rapidement pour des diamètres inférieurs, le différentiel de pression et l'hématocrite global étant par ailleurs fixés. L'effet Fåhraeus-Lindqvist ne peut clairement pas être observé pour un fluide Newtonien (de viscosité efficace constante et égale à sa viscosité intrinsèque) et dénote tout à fait la nature hétérogène du sang — suspension de cellules micrométriques dans le fluide plasmatique Newtonien.

L'effet Fåhraeus [77] permet d'expliquer une partie de ce phénomène. En mesurant l'hématocrite de *décharge* H_d circulant effectivement dans les petits capillaires et en le comparant à l'hématocrite initial H du sang du réservoir, Fåhraeus prouve que le ratio H_d/H décroît de 1 à ~ 0.5 lorsque D passe de 1 mm à 15 μm. Le plasma, occupant une proportion croissante à la paroi du capillaire, crée une certaine lubrification (Fig. 1.2), et contribue ainsi à l'effet Fåhraeus-Linqvist en contraignant les hématies à circuler dans la partie centrale du capillaire.

Fonctions rhéologiques sanguines et déterminants

L'hétérogénéité de la suspension sanguine se manifeste également dans la macrocirculation, plus précisément dans sa loi de comportement rhéologique, mesurable en viscosimétrie « macroscopique » *in vitro*. En régime de cisaillement simple stationnaire, le sang se révèle être un fluide rhéofluidifiant, i.e. de viscosité décroissant avec la vitesse de cisaillement [117]. En mode instationnaire, son caractère non Newto-

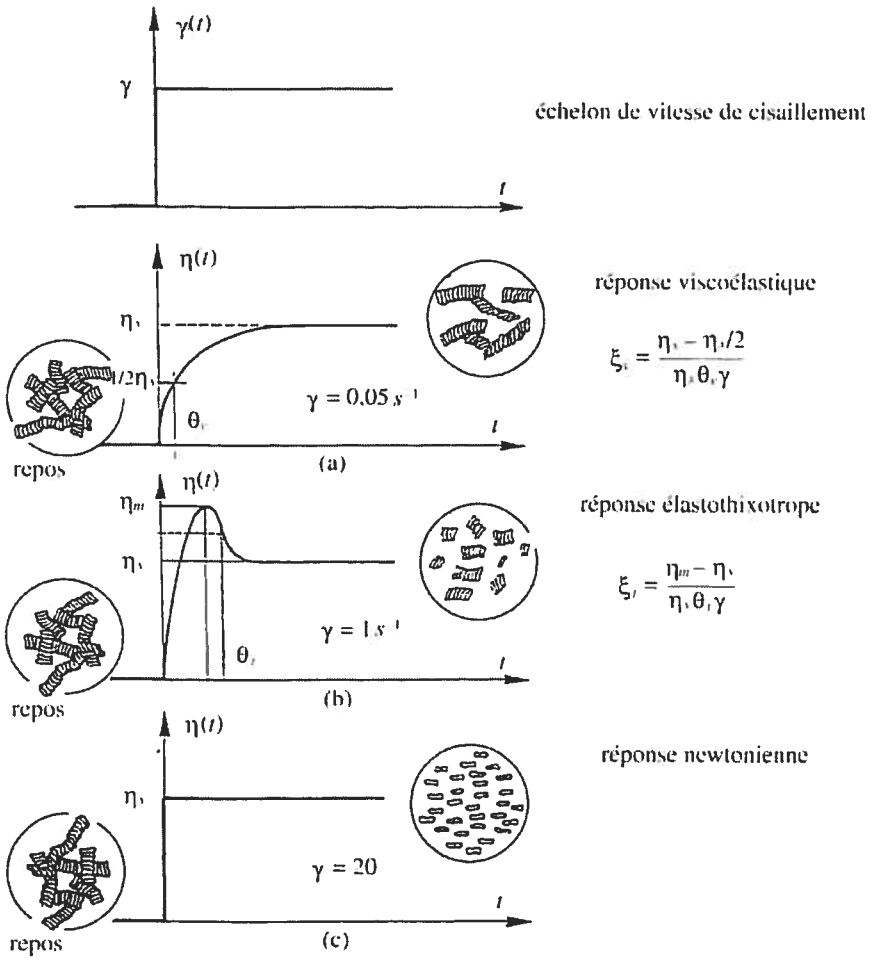

FIG. 1.3 – Expériences d'accroissement de contraintes pour du sang et les trois types de réponses rhéologiques pouvant être rencontrées suivant l'intensité de l'échelon de cisaillement. D'après [117].

nien est encore plus prononcé. Cela peut se quantifier, par exemple, par l'étude de la réponse en contrainte $\tau(t) = \eta(t)\dot{\gamma}(t)$ à un échelon de cisaillement $\dot{\gamma}(t) = \dot{\gamma}_0 \mathbb{I}_{[t>0]}$, où $\mathbb{I}_{[.]}$ est la fonction indicatrice et $\eta(t)$ est la viscosité sanguine (Fig. 1.3). Cette dernière est viscoélastique lorsque l'échelon est faible ($\dot{\gamma}_0 \lesssim 0.05$ s^{-1}), thixotrope lorsque l'échelon est intermédiaire et quasi-Newtonienne (de réponse instantanée $\tau(t) = \tau(\dot{\gamma}_0)\mathbb{I}_{[t>0]}$) lorsque le cisaillement imposé est fort ($\dot{\gamma}_0 \gtrsim 20$ s^{-1}).

Le plasma étant un fluide Newtonien, le comportement rhéologique particulier du sang s'explique assez logiquement par la conformation et le comportement

mécanique des globules rouges en suspension qui occupent une grande partie du volume total. La variabilité de la viscosité sanguine avec l'hématocrite démontre l'importance de la phase érythrocytaire dans la biomécanique circulatoire (Fig. 1.4). Chien et coll. [51] prouvent ainsi l'influence primordiale de l'agrégation et de la déformation érythrocytaire en comparant la rhéologie sanguine à celle de suspensions salines de globules rouges non-agrégeants, ou à celle de suspension de globules rouges durcis (Fig. 1.5). La concentration des protéines plasmatiques — de fonctions hémostatique ou inflammatoire telles que le fibrinogène, les immunoglobulines ou la protéine C-réactive, moins spécifiquement avec l'albumine — interagissant avec les hématies, accroît notablement la viscosité sanguine à faible cisaillement (Fig. 1.6). On retiendra que plus le niveau d'agrégation érythrocytaire est élevé, plus la viscosité sanguine *in vitro* est élevée. Plus la déformabilité des globules rouges est grande, plus la viscosité à forte vitesse de cisaillement est faible.

1.4 Implications pathophysiologiques de l'hémorhéologie

1.4.1 Déformation et agrégation érythrocytaires en situation physiologique

La déformabilité et l'agrégabilité des globules rouges jouent un rôle important dans la macrocirculation. Elles conditionnent la loi de comportement mécanique du sang et ce faisant, la résistance périphérique. Leur impact biomécanique se situe toutefois majoritairement au niveau microcirculatoire, lorsque les diamètres vasculaires se montrent inférieurs aux dimensions érythrocytaires (cf. fig 1.7 et 1.8). Le faible module de cisaillement de la membrane et la fluidité normale de la solution d'hémoglobine intracellulaire permet au globule rouge de se faufiler comme

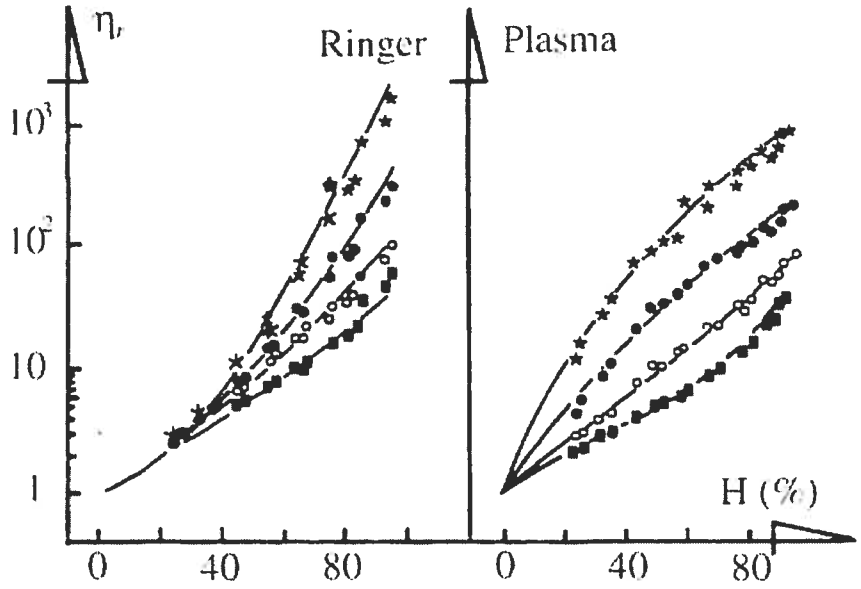

FIG. 1.4 – Effet de l'hématocrite sur la de la viscosité sanguine relative (par rapport à la viscosité du fluide suspendant) d'une suspension de globules rouges dans une solution de Ringer et dans du plasma. Les mesures sont effectuées à 37°C à différentes vitesses de cisaillement: (★) $\dot{\gamma} = 0.052\ s^{-1}$, (•) $\dot{\gamma} = 0.52\ s^{-1}$, (○) $\dot{\gamma} = 5.2\ s^{-1}$, (■) $\dot{\gamma} = 52\ s^{-1}$. D'après [51].

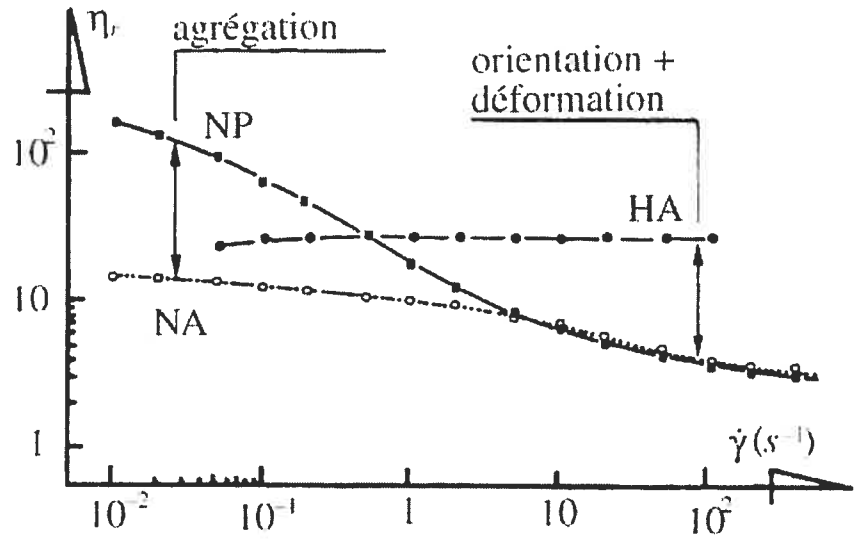

FIG. 1.5 – Viscosité relative du sang en fonction de la vitesse de cisaillement: (■) globules rouges + plasma, (○) globules rouges (non-agrégeants) dans Ringer-albumine, (•) globules rouges durcis dans Ringer-albumine. Fait à 25°C. D'après [51].

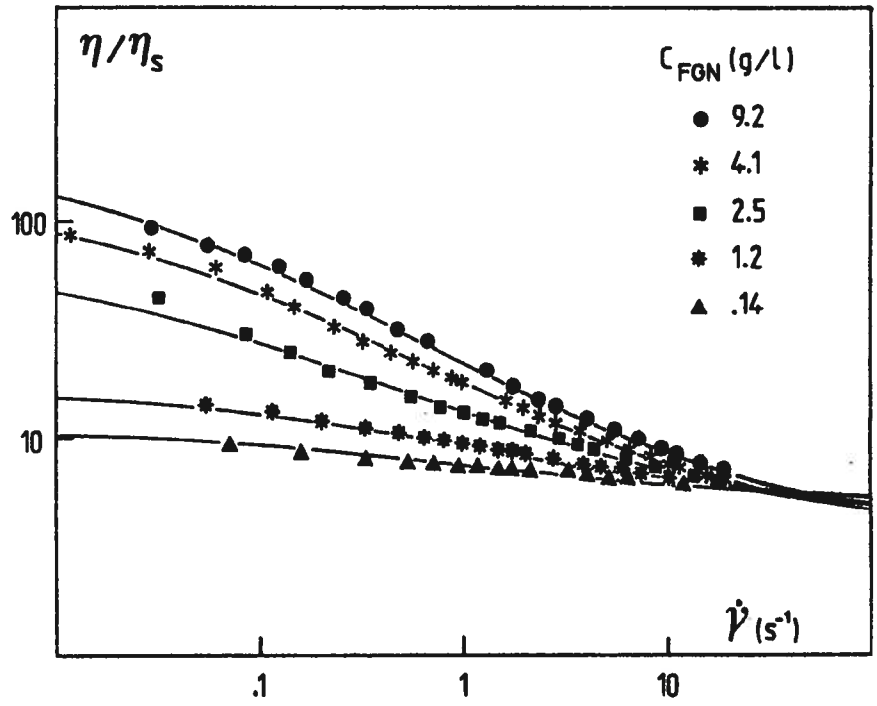

FIG. 1.6 – Influence de la concentration en fibrinogène (C_{FGN}) sur la rhéofluidification sanguine relative. La viscosité relative est notée ici η/η_s. D'après [46].

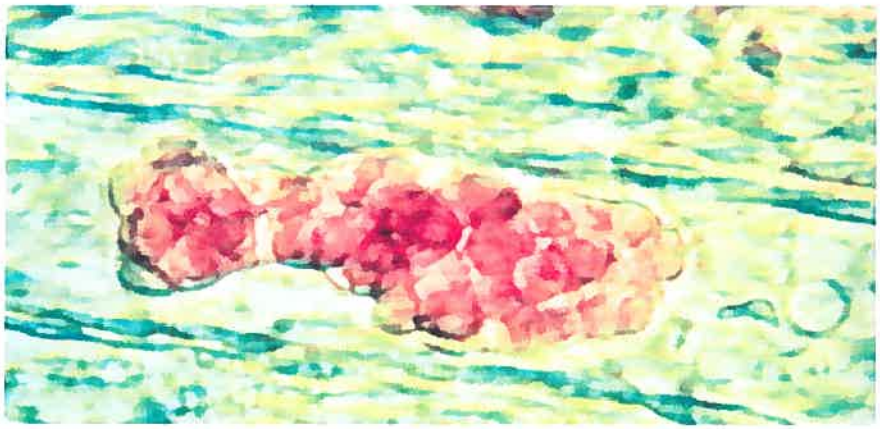

FIG. 1.7 – Un gros agrégat globulaire se formant dans une situation pathologique, d'après [72].

un « parachute » dans les capillaires, sans modification majeure de son volume et de son aire. De plus, cette déformation favorise la libération d'oxygène dans ces territoires d'échanges gazeux sang-tissu.

L'écoulement se déroulant à faible vitesse et le déplacement des cellules étant

FIG. 1.8 – Aux bifurcations, les agrégats de globules rouges se défont, tandis que les érythrocytes se déforment dans les microvaisseaux, d'après [72].

contraint par les dimensions vasculaires réduites, les globules rouges entrent en collision et s'agrègent en formant des « piles » d'hématies. Cette adhésion réversible qui conduit à la formation de *rouleaux* est permise par les protéines plasmatiques et est modulée par les forces de cisaillement hydrodynamiques. En situation physiologique, l'influence de l'agrégation des hématies sur la résistance microcirculatoire est toujours un sujet à controverse. La présence d'amas de globules rouges augmente-t-elle ou bien diminue-t-elle cette résistance ? On peut imaginer que deux phénomènes entrent en compétition suivant la taille, la compacité et la solidité des amas d'hématies formés. D'un côté, l'appariement des globules rouges entre eux devrait faciliter la migration centrale des cellules, l'apparition de la couche plasmatique périphérique lubrifiante, et ainsi l'effet Fåhraeus. La friction et la résistance pourraient s'en trouver alors diminuées. De l'autre, la solidité et la taille de ces structures érythrocytaires peuvent mener à des bloquages, plus ou moins intermittents, de leur écoulement. En effet, la morphologie microcirculatoire s'écarte souvent de la géométrie cylindrique et est le plus souvent courbe, tortueuse et parsemée de nombreuses bifurcations. Une telle altération de l'écoulement augmente manifestement la résistance capillaire.

1.4.2 Hémorhéologie et pathologie

Plusieurs études viscosimétriques posent les bases de l'*hémorhéologie clinique* en démontrant que le comportement mécanique du sang de patients atteints de certaines pathologies spécifiques se distingue du comportement normal. Le sang de ces malades est en effet moins « fluide » que le sang d'un sujet normal. L'hématocrite, la viscosité du plasma suspendant, l'agrégabilité érythrocytaire et la déformabilité du globule rouge (déterminée à la fois par la membrane et par la solution d'hémoglobine intracellulaire) sont les facteurs susceptibles de modifier la rhéologie du sang total. Certaines pathologies (hémopathies génétiques, maladies cardiovasculaires) touchent

ces déterminants et par conséquent la rhéologie sanguine.

Hémorhéologie et maladies génétiques

Plusieurs maladies génétiques, comme les hémoglobinopathies, induisent des modifications structurales des protéines intervenant dans la rhéologie sanguine. Les cas de l'anémie falciforme et de la β-thalassémie ont fait l'objet de nombreuses études : lorsque le globule rouge est désoxygéné, l'hémoglobine (de chaîne modifiée) se polymérise anormalement, rigidifie le globule rouge et modifie sa forme en faucille. Ceci génère des occlusions microcirculatoires, provoque des crises douloureuses [94] — qui s'autoentretiennent par une rétroaction positive lors de la raréfaction progressive d'oxygène — et une anémie[2] chronique chez le patient. La rhéologie de la solution intracellulaire [36], l'élasticité membranaire [202] et la propension accrue des érythrocytes falciformes à s'agréger modifient totalement l'hémorhéologie des sujets atteints [180]. Une autre anémie hémolytique génétique affectant les propriétés mécaniques sanguines est la sphérocitose héréditaire. Celle-ci touche les protéines sous-membranaires, entraînant une déficience de la spectrine [2]. La rigidité cellulaire s'altère et l'hématie, plus petite, adopte une forme sphérique [226].

Hémorhéologie et pathologies vasculaires

Un spectre large de maladies atteint la rhéologie sanguine du fait de la multiplicité des facteurs physico-chimiques susceptibles de l'influencer. Les études épidémiologiques massives de Edimbourg [129, 130], MONICA [112, 113], et Caerphilly [231] mettent en évidence des liens de corrélation (tab. 1.II) entre l'hyperviscosité sanguine (ou uniquement plasmatique) et les maladies vasculaires coronarienne, périphérique, ou cérébrale à incidence majeure[3]. Ces études cliniques démontrent

[2]L'anémie est un déficit de la concentration d'hémoglobine.

[3]D'après les données épidémiologiques de l'American Heart Association, de l'Organisation Mondiale de la Santé et de la Fondation des maladies du cœur du Canada, un tiers des morts en 2001 ont eu une cause cardiovasculaire dans le monde, 16.6 millions de personnes mourrant chaque année

que les déficiences hémorhéologiques sont des facteurs indépendants de risque de maladie vasculaire, au même titre que les risques « classiques » tels que l'hypercholestérolémie, la cigarette et l'hypertension. Ceci est une découverte de taille ! L'hyperviscosité s'avère de plus corrélée à l'augmentation de l'épaisseur intima-media au niveau carotidien, qui se déroule durant la phase asymptomatique du développement de l'athérosclérose [116].

Le diabète et l'hyperlipidémie ont également été associés à des anomalies de viscosité sanguine. Ces observations nous conduisent alors naturellement à nous interroger sur les mécanismes intimes liant les dérèglements hémorhéologiques à l'athérogenèse ou à la thrombogenèse. Ces désordres rhéologiques sont-ils concomitants à l'apparition des maladies vasculaires ou participent-ils à leur étiologie ? Sont-ils des facteurs primaires explicatifs ou secondaires aggravants ? Comment s'adjoignent-ils aux phénomènes inflammatoires, hémostatiques ou hémodynamiques intervenant dans les modèles modernes d'athérogenèse [119, 120, 121, 168] ?

Athérogenèse, dyslipidémie et hémorhéologie Depuis les années 70, la recherche clinique a démontré un lien fort entre l'athérosclérose et l'hypercholestérolémie, à preuve qu'une correction intensive de la dyslipidémie par les statines (considérées comme inhibiteurs de la synthèse du cholestérol) diminue la mortalité liée à la maladie coronarienne de 30 à 50% [178]. Une concentration trop élevée de LDL[4] plasmatique initie l'athérogenèse par un mécanisme expliqué aujourd'hui de manière assez consensuelle [119, 200]. Tant que leur concentration reste modérée, les LDL pénètrent et sortent librement de l'intima sans conséquence vasculaire. Cependant, l'hyperlipidémie peut entraîner une accumulation anormale des LDL dans la tunique interne. Les particules de LDL captées s'oxydent progressivement. Puis le

de ces maladies. Un Canadien sur quatre est atteint par une forme de maladie cardiovasculaire. Dix-huit milliards de dollars sont dépensés par an au Canada pour leur soin et prévention. Source : `www.americanheart.org, www.heartandstroke.ca`.

[4]Low Density Lipoprotein.

étude	durée	population	facteur de risque	résultat
Caerphilly, Speedwell study [231]	5.1 ans	4860 h, âge moyen	viscosité plasmatique	odd-ratio (quintile 5 vs. 1) d'ischémie myocardique : 4.5
Edinburgh Artery study [129, 130]	-	1581 h et f, 55-74 ans	viscosité plasmatique	odd-ratio de claudication : 3.4
	5 ans	1592 h et f, 55-74 ans	viscosité totale	> pour accident cardiovasculaire majeur
MONICA Augsburg [112, 113]	8 ans	964 h, 45-64 ans	viscosité plasmatique	odd-ratio de mortalité : 2
	8 ans	933 h, 45-64 ans	viscosité plasmatique	odd-ratio d'infarctus ou de mort cardiaque : 3.3

TAB. 1.II – Quelques données épidémiologiques sur les liens hémorhéologie - maladies vasculaires.

LDL oxydé résultant réveille l'activité immunitaire à la surface intima-lumière et déclenche le processus athérogène.

Il se trouve que la rhéologie sanguine est dépendante des concentrations plasmatiques en lipoprotéines. La viscosité sanguine s'accroît lorsque les concentrations plasmatiques en chylomicrons, VLDL[5] et LDL sont augmentées [167], tandis qu'elle varie en raison inverse du HDL[6] athéroprotecteur [197]. À l'opposé, une aphérèse des lipoprotéines diminuant les LDL plasmatiques réduit la viscosité sanguine, augmente la déformabilité érythrocytaire et diminue l'agrégation érythrocytaire [151]. Les facteurs de risques hémorhéologiques et lipoprotéiques varient donc tout à fait dans le même sens. Cette conjonction amène d'ailleurs Sloop à nier (de manière peut-être abusive) le rôle de l'inflammation dans l'athérogenèse, en ne retenant que l'effet hémorhéologique des lipoprotéines pour expliquer le lien entre dyslipidémie

[5]Very Low Density Lipoprotein.
[6]High Density Lipoprotein.

et athérosclérose [196, 198].

Athérogenèse, hémodynamique, fonction endothéliale et hémorhéologie

Les lésions athéromateuses sont souvent localisées en des foyers précis de l'arbre vasculaire : aorte abdominale, artères coronaires, artères des membres inférieurs, illiaques, fémorales, poplitées et tibiales, artères carotides, sous-clavières et vertébrales, le plus souvent près des courbures et des bifurcations. Ce caractère déterministe fait penser que l'hémodynamique joue un rôle essentiel dans l'athérogenèse [85]. Plus spécifiquement, il a été observé que les parois soumises à de faibles contraintes de cisaillement hydrodynamiques sont plus propices au développement athéromateux. On peut d'abord imaginer que la captation des LDL circulantes et des monocytes (en particulier dans les zones de recirculation) ainsi que l'activation plaquettaire sont favorisées dans ces zones, leur temps de résidence étant plus long. On peut également évoquer l'effet de la réduction de la friction hydrodynamique sur la fonction endothéliale, via la méchanotransduction cellulaire. La diminution du cisaillement pariétal perturbe en effet la morphologie des cellules endothéliales, l'activité enzymatique antioxidante, vasoactive, la synthèse de médiateurs inflammatoires et de molécules d'adhésion, la prolifération et l'apoptose cellulaire [61, 135].

L'hémodynamique locale est évidemment conditionnée par les propriétés rhéologiques sanguines, au niveau du débit ou des contraintes mécaniques ressenties par les cellules endothéliales. On comprend alors que l'hémorhéologie joue un rôle mécanique déterminant dans la pathogenèse vasculaire. De récentes études ont ainsi démontré son effet direct sur l'élasticité vasculaire (contrôlée par des agents relaxants endothéliaux et l'activation des cellules des muscles lisses) [80] et sur la vasodilatation (contrôlée par les agents vasoactifs endothéliaux) [87].

Athérogenèse, inflammation et hémorhéologie D'après les théories récentes [119, 168], l'invasion de LDL modifiées dans la tunique vasculaire interne entraîne une réaction inflammatoire initiant le développement athéromateux. On donne ici un aperçu du mécanisme. Après l'invasion de l'intima par les LDL oxydées, les monocytes et les lymphocytes T adhèrent à la paroi endothéliale (via les molécules dédiées VCAM-1) puis ces leucocytes migrent plus profondément dans l'intima. Ils s'y multiplient, se transforment en macrophages, se couvrent de récepteurs *scavenger*, puis internalisent les LDL modifiées. Saturés de molécules lipidiques, les macrophages ressemblent à de la mousse, ou à des cellules *spumeuses*. Après libération de certains facteurs, la matrice constituée de l'endothélium, des macrophages et des cellules musculaires de la media en pleine prolifération forment une chape fibreuse, riche en collagène. Les cellules spumeuses meurent, déversant des lipides qui forment le noyau lipidique de la plaque. La croissance du tissu fibreux s'effectue le plus souvent vers la media, mais peut engendrer la sténose du vaisseau lorsqu'elle s'effectue vers l'extérieur.

Une corrélation a été établie entre l'agrégation érythrocytaire la la présence des protéines de la phase inflammatoire aigüe par [227]. Des marqueurs inflammatoires hématologiques émergeants (car nouvellement cités comme facteurs de risque cardio-vasculaires [65, 209], mesurables précisément et à moindre coût) sont le fibrinogène et la protéine C-réactive : leur lien avec l'agrégabilité mesurée par microscopie a été prouvée par [172].

L'agrégation érythrocytaire joue également un rôle « mécanique » dans le processus inflammatoire. Pearson et coll. [155] démontrent que le recrutement des leucocytes se jouant à la paroi vasculaire augmente lorsque les agrégats érythrocytaires croissent — sous l'effet d'une diminution du taux de cisaillement ou d'un niveau d'agrégabilité augmenté. Ces études démontrent donc un lien évident entre les facteurs hémorhéologiques et l'inflammation.

Athérogenèse, thrombogenèse et hémorhéologie Il est bien connu que le risque le plus important d'accident vasculaire dû à l'athérosclérose (comme l'infarctus du myocarde par exemple) ne vient pas de l'occlusion du vaisseau par la plaque (15% des infarctus) mais plutôt de l'obstruction de celui-ci par un thrombus sanguin. Le caillot se forme lorsqu'une plaque d'athérome instable se fissure et lorsque le sang rencontre le noyau lipidique, provoquant la cascade de coagulation. Les plaques les plus dangereuses ne sont donc pas forcément les plus oblitérantes. Le fibrinogène, étant la première protéine plasmatique agissant physiologiquement sur l'agrégation érythrocytaire, se trouve être également le monomère de la fibrine, support de l'enchevêtrement complexe de cellules et de fibres qu'est le thrombus sanguin. Le lien de corrélation entre l'anomalie hémorhéologique et l'athérothrombose à risque est donc direct. De plus, l'hémodynamique, directement dépendante de la rhéologie sanguine, affecte le mouvement plaquettaire et par conséquent influence localement la thrombogenèse.

1.5 Mesures hémorhéologiques

1.5.1 Justification de l'hémorhéologie clinique

À la lumière des corrélations présentées ci-dessous entre les anomalies hémorhéologiques et certaines pathologies — incluant les maladies cardiovasculaires qui constituent la première cause de mortalité dans les pays occidentaux, il serait judicieux de clarifier pourquoi les propriétés mécaniques sanguines et leur déviation par rapport à leur niveau physiologique participent à leur étiologie.

1.5.2 Mesures *ex vivo*

La mesure de la loi de comportement rhéologique du sang, ou des déterminants de cette loi que sont la déformabilité et l'agrégabilité érythrocytaires, s'est ef-

fectuée jusqu'ici *ex vivo* à des fins de recherche. Ces études viscosimétriques directes (par des rhéomètres de différentes géométries et à différents régimes de sollicitation) nécessitent évidemment une prise de sang, ce qui peut entraîner différents inconvénients.

L'examen est d'abord invasif (minimalement cependant), mais surtout n'autorise pas l'investigation hémorhéologique locale. Il représente plutôt une mesure systémique globale, comme tout bilan hématologique.

D'autre part, d'autres types d'instruments hémorhéologiques ont été développés pour la mesure d'autres paramètres physico-chimiques pertinents sur des échantillons sanguins. On en cite ici quelques exemples.

Taux de sédimentation érythrocytaire

La mesure du taux de sédimentation apparaissant dans le bilan hématologique est la plus ancienne des méthodes liées à l'hémorhéologie. À cause de la densité différentielle des hématies, celles-ci sédimentent dans une colonne de sang, à une vitesse dépendant de multiples facteurs, dont la taille des agrégats érythrocytaires formés. Ce taux est souvent utilisé cliniquement comme un marqueur non-spécifique (et donc de faible valeur diagnostique) d'inflammation [240].

Optique

L'ektacytomètre de Bessis et Mohandas [29] et d'autres dispositifs plus récents (Myrenne, LORCA, Érythroagrégamètre) basés sur la diffusion ou la transmission [236] de la lumière dans le sang, en réponse à des régimes transitoires de cisaillement, permettent de construire des indices cinétiques ou stationnaires d'agrégation.

Microscopie

La conformation microscopique des agrégats érythrocytaires ne peut être visualisée qu'après dilution, sous lame ou dans un très fin entrefer, à cause de l'opacité naturelle du sang. L'utilisation d'un rhéoscope (rhéomètre cône-plan couplé à un microscope inversé) permet de mesurer la circularité des amas de globules rouges [179]. La dynamique de ce paramètre morphologique sous cisaillement imposé permet de quantifier géométriquement l'agrégabilité érythrocytaire.

Méthodes électriques

Caractéristiques diélectriques La permittivité complexe du sang à différentes fréquences (0.2 MHz et 14 MHz par exemple) semble pouvoir être utilisée pour quantifier l'agrégation. Cependant le lien entre l'agrégabilité et ces propriétés électriques demeure complexe. En effet, la mesure absolue des propriétés sanguines, indépendamment des effets d'électrode, s'effectue avec difficulté [162].

Électrophorèse Placés dans un champ électrique, les globules rouges migrent dans un solvant donné suivant leur mobilité, déterminée par la morphologie, la charge surfacique cellulaire, la force ionique (et le pH), la composition macromoléculaire, la viscosité du solvant, et les différents phénomènes membranaires conditionnant l'agrégabilité érythrocytaire [19]. Ce type de caractérisation n'a permis jusqu'ici que des études fondamentales sur les mécanismes du processus d'agrégation.

Microrhéologie de la cellule

Des études microrhéologiques ont permis de caractériser la rhéologie membranaire du globule rouge, et en particulier de déterminer les modules d'élasticité (cisaillement, dilatation, flexion) membranaires, et les composantes visqueuses cytoplas-

mique et surfacique (la bicouche lipidique étant passablement fluide). Différents régimes de solicitation microscopique existent : aspiration (dépression) par micropipettes [117], micromanipulation par pincettes optiques [118]...

À notre connaissance, aucune étude microrhéologique n'a par contre été menée pour analyser le contact adhésif hématie-hématie.

1.5.3 Nécessité de procéder à des études *in vivo*

Les techniques de caractérisation évoquées ci-dessus ont comme point commun la nécessité de prélever un échantillon de sang d'un patient afin de mesurer ses diverses propriétés physiques dans des dispositifs de laboratoire. Il semble pourtant qu'une étude locale *in vivo* soit nécessaire pour permettre d'élucider l'impact de l'hémorhéologie sur l'étiologie de pathologies aussi complexes que la maladie vasculaire. Les outils d'imagerie médicale pouvant capter, *in situ* et non-invasivement, divers phénomènes physico-chimiques, s'avèrent maintenant primordiaux pour progresser dans cette compréhension.

Plusieurs arguments peuvent être avancés pour justifier des mesures hémorhéologiques non globales (i.e. qui s'opposent à un bilan hématologique par exemple) pratiquée *in situ*.

- Alors que l'effet Fåhraeus a été découvert par des expériences *in vitro*, les premières études de microcopie intravitale ont montré que la résistance à l'écoulement des petits vaisseaux était au moins deux fois plus élevée que ce que la prise en compte du calibre du vaisseau et que l'effet Fåhraeus pouvaient prévoir, cela prouve que la glycocalyx endothéliale a une fonction importante [163], difficile à reproduire *in vitro*.
- La compliance vasculaire conditionne l'hémodynamique et par conséquent l'hémorhéologie : affectée par le développement athéromateux, sa prise en compte n'est possible effectivement que par des études *in vivo*.

- L'athérogenèse et la thrombogenèse sont des phénomènes locaux, qui dépendent de la libération d'agents endothéliaux inflammatoires ou hémostatiques, jouant sur l'agrégation ou la déformabilité érythrocytaires. Leurs effets ne se manifestent qu'en des *loci* particuliers de l'arbre vasculaire et leur étude demande de pouvoir les détecter.

1.5.4 Hémorhéologie *in situ*: approche ultrasonore

L'approche ultrasonore est une méthode de choix qui permet de mesurer localement les propriétés acoustiques des tissus, en profondeur, de manière non invasive. Or, depuis les premières études de Shung et coll. en 1976 [185], on sait que les caractéristiques sanguines d'échogénicité ultrasonore sont liées au niveau d'agrégation érythrocytaire. Depuis lors, divers groupes (dont le laboratoire de biorhéologie et d'ultrasonographie du centre hospitalier de l'université de Montréal) ont tenté de comprendre comment le niveau d'agrégation des hématies affectait les propriétés acoustiques sanguines pour ainsi poser les bases d'une mesure échographique d'indices hémorhéologiques.

1.6 Objectifs et descriptif de la thèse

Objectif

L'objectif de cette thèse est par conséquent de clarifier la relation entre les paramètres physiques affectant la microstructure sanguine, conditionnant l'hémorhéologie, et les propriétés ultrasonores du sang. On s'intéressera au premier chef au coefficient de rétrodiffusion, qui quantifie la capacité du sang à émettre des échos lorsqu'une onde ultrasonore le rencontre.

Les indices ultrasonores d'agrégation déjà proposés antérieurement se révélent empiriques, et sous-tendus par des modèles physiques peu satisfaisants. L'approche

proposée dans cette thèse s'inspire des principes de la physique statistique, repris par les physiciens des fluides colloïdaux complexes, pour améliorer les modèles décrivant la microstructure sanguine. Nous cherchons à modéliser physiquement les interactions entre les particules suspendues dans le liquide, pour forger une description stochastique du fluide multiphasique. Puis par un changement d'échelle microscopique-macroscopisque permis par le moyennage statistique, le coefficient de rétrodiffusion sanguin peut être estimé.

Cette thèse aborde assez largement le problème direct { paramètres microstructuraux } $\rightarrow$ { coefficient de rétrodiffusion }. Quelques pistes sont aussi proposées pour résoudre le problème inverse { coefficient de rétrodiffusion} $\rightarrow$ { paramètres microstructuraux }, problématique commune à toutes les expériences de diffusion et de diffraction des rayonnements en caractérisation des matériaux. Nous posons ainsi les bases théoriques de l'évaluation *in vivo*, rigoureuse et physique, du niveau local d'agrégation érythrocytaire.

Plan de la thèse

Premier article Le chapitre (2) consiste en une revue de la littérature sur le sujet. Les caractéristiques ultrasonores mesurables du sang sont définies, et leurs variations expérimentales en relation avec l'hématologie, l'hémodynamique ou l'hémorhéologie sont discutées. La logique de la factorisation du coefficient de rétrodiffusion sanguin en une composante cellulaire, liée aux propriétés acoustiques du seul globule rouge, et en une composante liée à l'organisation spatiale des globules rouges, le facteur de structure, est particulièrement détaillée.

Second article Le chapitre (3) présente une approche de géométrie stochastique pour décrire la microstructure. Conçue indépendamment du processus physique sous-jacent, la disposition aléatoire des globules rouges dans le plasma est décrite

par un processus ponctuel de Neyman-Scott. La morphologie tridimensionnelle des agrégats érythrocytaires est quantifiée par les moments statistiques du nombre de globules rouges par amas, et par leur dimension fractale (en masse). L'inférence de ces paramètres est testée sur des données expérimentales « spectroscopiques » de rétrodiffusion. Nous montrons que cette description est satisfaisante pour des suspensions diluées de globules rouges, mais qu'elle doit être améliorée pour prendre en compte la densité physiologique des hématies.

Troisième article La biophysique des interactions intercellulaires (du type *noyau dur* complétées par une adhésion à courte portée) est modélisée par une approche de physique statistique dans le chapitre (4). Cette approche permet en particulier d'inclure l'effet de l'hématocrite à un niveau physiologique. La conformation bidimensionnelle de globules rouges est décrite par un processus aléatoire de Gibbs-Markov. L'augmentation et l'anisotropie de l'échogénicité sanguine sous l'effet de ces interactions sont quantifiées. La détermination de l'état agrégé et anisotrope de la microstructure sanguine par l'observation de données acoustiques est évaluée par une approche de reconnaissance de forme.

Discussion - Conclusion Les résultats trouvés sont mis en perspective avec, notamment, la mesure *in vivo* des paramètres microstructuraux de tissus par échographie.

Chapitre 2

Revue de littérature

2.1 Avant-propos au chapitre

Dans ce chapitre, nous définissons les caractéristiques sanguines acoustiques qui sont mesurables par des techniques classiques d'échographie : la vitesse du son, le coefficient d'atténuation des ultrasons, et le coefficient de rétrodiffusion. Les variations de ces indices acoustiques avec certains paramètres hématologiques, les conditions d'écoulement et la microstructure érythrocytaire sont décrits d'après une revue des résultats expérimentaux publiés dans la littérature depuis 1953 (premiers articles sur l'atténuation des ultrasons par le sang par Carstensen et Schwann [43]), jusqu'à aujourd'hui, en passant par les premières études sur la diffusion acoustique par le sang par Shung et coll. [185] en 1976.

Nous exposons ensuite les différentes approches de modélisation du coefficient de rétrodiffusion du sang, en exhibant particulièrement le *facteur de structure* $S(\vec{q})$ du processus stochastique ponctuel Ω constitué par les centres des particules diffusantes. La valeur du facteur de structure constitue *le* facteur sensible à la microstructure — et donc à la microrhéologie — des érythrocytes circulants.

Pour quantitifier l'effet de l'agrégation des hématies sur $S(\vec{q})$, ou sa limite basse fréquence (le facteur de *packing* W), nous détaillons particulièrement les approches thermodynamique et géométrique. La physique de l'agrégation des globules rouges,

maintenant encore controversée, est examinée : les interactions cellule-cellule et hydrodynamiques cellule-plasma sont décrites puisqu'elles conditionnent à la fois hémorhéologie et microstructure.

Ce chapitre est constitué par le manuscrit de l'article « Microstructural determinants of ultrasound blood scattering properties: a statistical physics perspective » en voie d'être soumis.

2.2 Abstract

Blood physical properties observed at a macroscopic scale are inherited from the heterogeneous composition of this singular biofluid. Micrometric erythrocytes immersed in aqueous plasma occupy a volumic fraction (hematocrit) $H \sim 40$ % of the blood volume and form a gel-like colloidal phase that largely conditions blood rheological and acoustical properties. As the shear-thinning biorheological behavior of blood is of primary importance for the microcirculatory physiopathology, several groups have investigated the possibility of measuring red blood cell (RBC) aggregation non-invasively by ultrasonic scattering methods. Although the first acoustical scattering characterization of blood dates back from 1976, the definition of meaningful aggregation-related acoustic parameters is still missing. As exposed in this paper, statistical physics of condensed matter can however bring a useful unifying vision to relate microstructure and blood scattering acoustic properties. The frequency dependence of the blood backscattering coefficient is analyzed by means of a model of the erythrocyte acoustical cross-section and of the structure factor $S(\vec{q})$, classically introduced in crystallography and material characterization by X-ray, neutron and light scattering. The structure factor carries all informations extractible from scattering measurements related to the RBC spatial pattern. The subtle evolution of $S(\vec{q})$ with the intercellular colloidal energies, the hydrodynamic forces arising in shear flow

and the hematocrit is discussed with literature results. This lays the scaling basis of an ultrasonic scattering method for characterizing intercellular biophysics or for non invasive hemorheologic measurements.

2.3 Introduction

Ultrasound tissue characterization techniques [92, 190] are echographic methods that provide diagnostic informations complementary to the anatomic examination given by conventional B-scans. These techniques allow to quantitatively image a number of acoustic features of the tissues, as the speed of sound c, the attenuation coefficient α, the backscattering coefficient χ or the non-linearity parameter B/A. These values physically characterize the interaction of an ultrasonic wave with a sample of a biological tissue and can be used as acoustic markers of the microstructural state of a tissue. Changes in the microstructure of the investigated organs (as induced by bone loss in osteoporosis [148], ischemia of the myocardium [125, 149, 222], hardening of vessel wall [147] or presence of tumors [150]) can indeed affect these physical properties and any deviation from their normal values is the signature of a pathological event.

Several approaches have been proposed to understand how microscale properties (e.g. cellular organization and nuclear condensation in apoptosis [103] and molecular composition [183]...) modify tissue acoustic characteristics. They would help to deduce the morphological, biochemical or biophysical information contained in the microstructure from echographic radio-frequency signals. In particular, blood was shown to possess a varying echogenicity in B-mode [191] or in power Doppler imaging [6], and the flow-dependent microscopical clustering of red blood cells (RBCs) was proven responsible for these variations. This paper intends to review the various methods that aimed at understanding how ultrasonic characteristics of blood vary with erythrocyte

microstructural organization, focusing primarly on blood backscattering properties.

2.4 Definition of instrument-independent tissue acoustical properties

2.4.1 Interaction between ultrasound waves and biological tissues

Robust, repeatable (between sites [134]) and reliable measurements of tissue acoustic properties by echographic means require the definition of physical parameters that should minimally depend on the type and characteristics of the transducers (focusing, beam characteristics, excitation, acquisition or amplification parameters ...) and of the ultrasound (US) apparatus. A simple model of acoustic propagation within the tissue of interest consists of assuming that a monochromatic plane wave (generated by an ideal infinite aperture) excites the biological structures. The tissue-wave interaction results in the following energetic balance: a part of the acoustic energy is absorbed by the tissue, while a new scattered wave redistributes the remaining incident energy over all directions in space. The total pressure field, i.e. the sum of the incident and of the scattered waves, mathematically obeys a new wave equation with modified boundary conditions because of the insertion of the sample into the homogeneous propagation space. The global principle of tissue ultrasonic characterization is to measure certain characteristics of the scattered wave and to use them to infer the pathophysiological state of the insonified organ.

The complete prediction of the energy absorption and of the amplitude of the scattered wave in highly heterogeneous materials as biological tissues involves a considerable amount of information: the spatial distribution of thermomechanic properties as the adiabatic compressibility, density, heat capacity, thermal conductivity; the biorheo-

logical properties as viscosity or viscoelasticity of cells, interstitial fluids, conjonctive tissues or of other subcellular biological materials.

Observed at a nano-or micrometric scale, heterogeneous living tissues appear difficult to characterize, but as medical US wavelengths are typically ranging from 50 to 800 micrometers long for transmitted frequencies of 2 to 30 MHz, only ensemble-averaged quantities are necessary to describe ultrasonic tissue properties. In this section, one defines three tissue acoustic properties that are commonly measured and reported in literature: the speed of sound, the attenuation coefficient, and the backscattering coefficient of tissues. The physical determinants of the speed of sound and attenuation in blood are also examined in this section, while the following sections are devoted to the models of US backscattering by RBCs and blood.

2.4.2 Speed of sound

Basic definition

Ultrasonic waves are pressure waves that induce longitudinal tissue vibrations throughout their propagation inside the body. The sound velocity c of the US waves inside a given tissue reflects some of its thermomechanical properties. Theoretically, the speed of sound of a material is defined as follow. Consider a slight perturbation of pressure p created in a homogeneous non viscous fluid material. In the acoustic approximation, the perturbation p remains small compared to the equilibrium pressure and adiabatically travels inside the volume according to the wave equation:

$$\Delta p = \frac{1}{c^2}\frac{\partial^2 p}{\partial t^2}, \tag{2.1}$$

where the sound velocity c is related to the mass density ρ and to the *adiabatic* compressibility $\kappa = 1/\rho\,(\partial\rho/\partial p)_{\text{entropy}}$ by:

$$\kappa\rho c^2 = 1. \tag{2.2}$$

The planar monochromatic wave, of frequency f, wavevector $\vec{k}$ and amplitude p_0, is the particular solution of the wave equation that travels in the direction of the wavevector as defined by:

$$p(\vec{r},t) = \mathcal{R}\left[e^{2\imath\pi ft}p_0(\vec{r})\right] = \mathcal{R}\left[p_o e^{\imath(2\pi ft-\vec{k}.\vec{r})}\right], \tag{2.3}$$

where $\imath$ is the imaginary number, $\mathcal{R}$ the real part of a complex number, and $(\vec{r},t)$ are spatio-temporal coordinates.

Such a planar wave can propagate ($p_0 \neq 0$) provided that the frequency and the wavevector satisfy:

$$|\vec{k}| = \frac{2\pi f}{c} = \frac{2\pi}{\lambda}, \tag{2.4}$$

where λ is the acoustical wavelength.

Typical values in blood

For echographic imaging purpose, most of the US scanners assume that the speed of sound is constant $\sim$ 1540 m.s^{-1} inside biological tissues. This assumption produces sound speed errors on the order of $\pm 5\%$ as real velocities for mammalian tissues [7, 90] actually range from 1400 to 1650 m.s^{-1}. This crude assumption degrades morphometric measurements, the focusing efficiency, the image resolution and its contrast. For blood characterization however, Ahuja and Hendee [3, 4] developed an acoustic model of sound propagation through a dilute suspension of oblate particles having contrast in density, viscosity, and adiabatic compressibility, and showed that blood sound velocity is not dispersive and that it can be expressed as follow:

$$\bar{\rho}\bar{\kappa}c^2 = 1, \tag{2.5}$$

where $\bar{\rho}$ and $\bar{\kappa}$ are the volume averaged density and compressibility[1] in blood. Blood sound velocity sensitivity to $\bar{\rho}$ and $\bar{\kappa}$ was used for hematologic purpose to characterize the hematocrit or the variations of the hemoglobin/plasma protein concentrations [14, 33, 181].

2.4.3 Attenuation coefficient

Definition

Dissipative properties of tissues are quantified by the frequency-dependent attenuation coefficient $\alpha(k)$ [144]. It represents the decay rate in amplitude of a plane wave due to the loss of acoustic energy during the propagation. By definition, the amplitude of a pressure wave of wavevector $k\vec{e}_x$ exponentially decreases along the propagation axis according to:

$$|p_0(x\vec{e}_x)| = |p_0(0)|e^{-\alpha(k)x}. \tag{2.6}$$

Measurements of attenuation in blood

The effect of the hematocrit and of the acoustical frequency on blood US attenuation coefficient has been extensively studied by several groups. Figure (2.1) reports some data that show that $\alpha(k)$ increases with the hematocrit H and roughly linearly with the frequency at a rate $\sim 0.17 - 0.24$ dB.cm^{-1}.MHz^{-1} for normal whole blood.

Microscopic determinants of US attenuation

The attenuation of an incident plane wave in a medium is due to local conversion of acoustical energy into other energetic forms (heat, elastic, molecular conformation changes, ionization, ...), and to the scattering of the wave that spreads acoustical energy in all directions. Experimental studies [64] assign a marginal effect to the

[1] $\bar{\rho} = H\rho_{RBC} + (1-H)\rho_{\text{plasma}}$ and $\bar{\kappa} = H\kappa_{RBC} + (1-H)\kappa_{\text{plasma}}$.

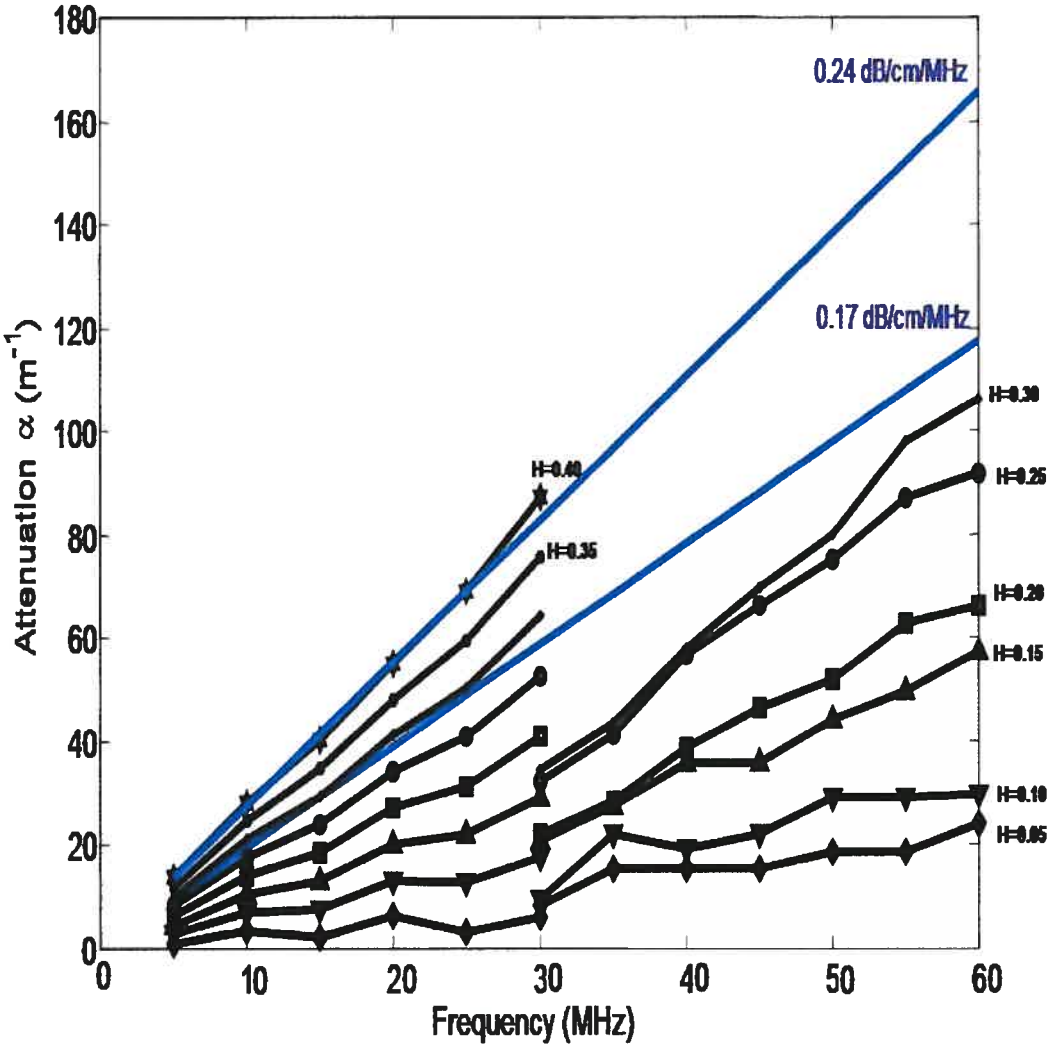

FIG. 2.1 – Frequency and hematocrit dependencies of the attenuation $\alpha(k)$ in suspensions of (non aggregating) porcine red blood cells in saline and in whole blood. Experimental values below 30 MHz are taken from [224], above 30 MHz from [136] and apply to porcine erythrocyte suspensions. Linear attenuation frequency dependence bounds for whole blood are taken from [92].

scattering on the total attenuation in biological tissues, compared to heat dissipation and other energy conversion. Heat dissipation originates from irreversible viscous friction and thermal conduction. Homogeneous viscous fluids have an attenuation coefficient that increases quadratically with the frequency, as given by [144]:

$$\alpha_{vis}(k) = \frac{2\eta_{tot}k^2}{3\rho c}\left(1 + (C_p/C_v - 1)\, P_r^{-1}\right), \tag{2.7}$$

where $\eta_{tot} = \frac{4}{3}\eta + \eta_v$ is a combination of the shear viscosity η and volume viscosity η_v, C_p is the heat capacity at a constant pressure, C_v is the heat capacity at constant volume, and $P_r = C_p\eta_{tot}/K$ is the Prandlt number that quantifies the intensity of thermal convection (K is the thermal conductivity).

However, experiments show that the physics of the attenuation for blood is somewhat different, as the frequency dependence $\alpha(k)$ appears rather linear. Blood or erythrocyte suspensions in particular exhibit this linear behavior as shown in figure (2.1) and in [136, 208].

The heterogeneity of the medium explains this deviation. At least two scales of heterogeneities can be taken into account: at a microscopic scale, the presence of vibrating and elastic particles like RBCs induces additional viscous and thermal dissipation $\alpha_p(k)$ [3, 4], while at the molecular scale, chemical energy absorption can occur. Energy transfers between the various molecular degrees of freedom of the biomolecules (translational energy to rotational, vibrational energies, isomeric rearrangements, ionization,...) imply several kinetic relaxation times $\{\tau_i\}$ that involve an excess of acoustic attenuation [104]. A frequency dependence of this excess of attenuation [110] has been proposed under the form:

$$\alpha_{exc}(k) = \sum_i \frac{ck^2\tau_i A_i}{1 + (ck\tau_i)^2}, \tag{2.8}$$

where A_i quantifies the absorption at the time scale τ_i. Plasmatic or erythrocyte

proteins, including albumin and hemoglobin [16], have specific signatures on the frequency dependence of α_{exc}, which was shown in the pioneering work of Carstensen [43], and in more recent studies in broadband ultrasonic spectroscopy [110]. Characteristic peaks of each energetic transition appear at distinct frequencies $\{\tau_i^{-1}\}$ when observing the spectrogram of the excess of attenuation per wavelength (the graph $f \rightarrow \alpha_{exc}(k)\lambda$), and are more or less pronounced depending on the values of A_i. The effect of these temporary protein structural transitions can affect the measured frequency dependence of the total attenuation $\alpha(k) = \alpha_{vis}(k) + \alpha_p(k) + \alpha_{exc}(k)$, that significantly deviates from the square law. So far, the effect of RBC aggregation on the particle attenuation $\alpha_p(k)$ has unfortunately never been studied.

However, the measurement of blood US attenuation seems useful to perform specific biochemical or hematological examination. As demonstrated in [187], hemoglobin oxygen saturation and pH modify US absorption, and this phenomenon could be used for monitoring pathological RBC sickling.

2.4.4 Backscattering properties

Scattering of an incident wave by tissues gives birth to wavelets that are further transduced by piezoelectric sensitive elements. Collected radiofrequency (RF) signals are then processed to synthesize the different echographic signals as the A- and B-scans. Scattering properties of tissues directly govern the amplitude of the RF signals, and are therefore the primary acoustic features that can be investigated by echographic means. The intrinsic material property that describes the ability of a tissue to generate US echoes is the backscattering coefficient. In this subsection, the acoustic cross-section of a particle is first defined, and the backscattering coefficient of a soft tissue is derived hereafter. This physical quantity objectively measures the echogenicity of a tissue or more precisely its "echoicity" (Yuan et al. [235] proposed to use this more appropriate term to denote the instrument-independent ability of a tissue

to backscatter sound).

Definition of the scattering cross-section of a particle

A particle sample of volume $\mathcal{V}$ (imagine a microscopic RBC or a millimetric blood sample) of the studied material is centered in O, and inserted in an infinite, non-attenuating, homogeneous propagation fluid, characterized by the mass density ρ_0 and sound speed $c_0 = (\rho_0\kappa_0)^{-1/2}$. An incident monochromatic plane wave with wave vector $\vec{k}$, complex amplitude $p_i(\vec{r}) = p_0 e^{\imath\vec{k}.\vec{r}}$ and intensity $I_0 = p_o^2/2\rho_0 c_0$ encounters the particle (Fig. 2.2). A part of the incident wave is deviated from its original course, as a result of the wave-material interaction, and a scattered wave $p_s(\vec{r})$ is radiated (at the same frequency for linear media) in all spatial directions. The scattered power, that can be measured in various directions by transduction, is expected to convey information on the material and geometrical properties of $\mathcal{V}$ [60, 106].

In the far field of the sample ($r \gg \mathcal{V}^{1/3}$), the amplitude of the scattered wave asymptotically reaches a spherical form [60]:

$$p_s(r\vec{e}_r) = p_0 \frac{e^{\imath kr}}{r} \sigma(\vec{e}_r, \vec{k})^{1/2} e^{\imath\phi(\vec{r})}. \tag{2.9}$$

The positive quantity $\sigma(\vec{e}_r, \vec{k})$, homogeneous to a surface, is the scattering cross-section of the particle $\mathcal{V}$ in direction $\vec{e}_r$ ($|\vec{e}_r| = 1$). The information carried by the phase term $\phi(\vec{r})$ will not be examined in this review article.

This definition of the cross-section can also be generalized to non-linear materials (for which the scattered wave contains harmonic and subharmonic components) using energetic considerations. If the scattered power measured in the small solid angle $d\Omega$ of direction $\vec{e}_r$ is noted $dP(\vec{e}_r, d\Omega)$, then the ratio $\frac{dP(\vec{e}_r, d\Omega)}{I_0 d\Omega}$ can be seen as a new equivalent definition of the scattering cross-section $\sigma(\vec{e}_r, \vec{k})$. The cross-section $\sigma(\vec{e}_r, \vec{k})$ can alternatively be seen as the geometric area of the plane perfect reflector that deviates the same power than the particle $\mathcal{V}$ in direction $\vec{e}_r$.

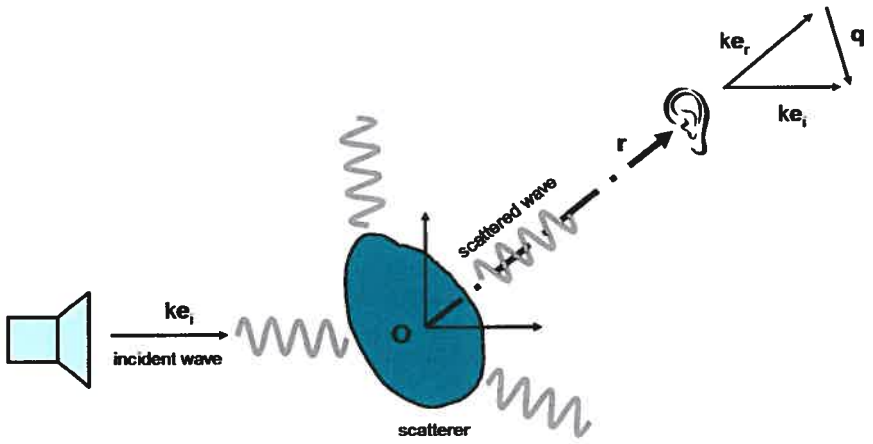

FIG. 2.2 – Schematics of the scattering of a monochromatic wave by a particle.

Backscattering cross-section

The backscattering cross-section $\sigma_b(\vec{k})$, the scattering cross-section measured at 180°, is particularly important for two reasons. First, as most of the echographic probes are emitting-receiving transducers, the observing point is in the reverse direction of the incident wave. The whole angle dependence $\vec{e_r} \rightarrow \sigma(\vec{e_r}, \vec{k})$ cannot be entirely measured: only the backscattering cross-section $\sigma_b(\vec{k}) = \sigma(-\vec{k}/k, \vec{k})$ contributes to the recorded RF echographic signal. The second reason is that the notion of backscattering cross-section enables to define an intrinsic material property, measurable by US scanners, that is independent on the shape of the sample tissue: the so-called backscattering coefficient.

Tissue backscattering coefficient

When a tissue sample is investigated, its volume V has macroscopic dimensions. Biological tissues are generally heterogeneous and composed of many submillimeter uncoherent scatterers randomly dispersed inside the bulk volume. However, when V is small and homogeneous enough, the acoustic impedance $Z(\vec{r}) = \rho_0 c_0 (1 + \gamma_z(\vec{r}))$ smoothly varies and deviates little from the bulk spatial impedance $\rho_0 c_0$ (i.e. the

relative impedance contrast $|\gamma_z(\vec{r})| \ll 1$). In those conditions (Born approximation), the mean backscattering cross-section $E[\sigma_b^V(\vec{k})]$ of the sample is shown to scale as the particle volume V ($E[]$ is the ensemble average). An intensive variable $\chi(\vec{k})$, the backscattering coefficient, is then defined by:

$$\chi(\vec{k}) = \frac{1}{V} E[\sigma_b^V(\vec{k})]. \tag{2.10}$$

Provided the volume V is sufficiently large compared to the correlation length of the embedded inhomogenities (typically a few millimeters versus a few micrometers), $\chi(\vec{k})$ does not depend on the shape or on the volume of the investigated sample. It can however be noted that the variance of the scattering cross-section depends on (and decreases with) the volume V. On the contrary, the mean value $\chi(\vec{k})$ represents an intrinsic property of the tissue, function of the frequency, of the acoustical properties of the embedded subscatterers, and of the spatial organisation of the scatterer positions. US tissue characterization methods should ideally tend to extract the absolute value of this material property for reliable and comparable measurements.

Measurements of blood ultrasound backscattering

The first study on blood intrinsic scattering properties was performed by Shung, Siegelman and Reid in 1976 [185]. Their interest was first to further investigate the fundamental scattering characteristics of biological tissues, and more specifically of blood for better interpreting US Doppler flowmetry in cardiovascular diagnosis. Hematological (hemolysis monitoring, hematocrit and RBC volume measurements, plasma concentration of RBC aggregation related proteins) or hemorheological (blood shear thinning viscosity) applications of blood characterization by US scattering were rapidly proposed by the same investigators [187], and their feasibility has been investigated by many groups since then. The intricacy of the adverse effects of RBC characteristics, hematocrit, flow hemodynamics and erythrocyte aggregability on the

relatively low echogenicity of blood probably explains the fact that no clinical protocol for US hematological routine characterization really exists.

In the next paragraphs, the basic experimental findings on the backscattering coefficient of blood, or more generally on its B-mode or Doppler power echogenicity, are reviewed, as "raw material" for a deeper understanding of blood scattering properties.

Hematocrit dependence The hematocrit H is the primary characteristic to consider when reviewing the physical determinants of blood backscatter, as RBCs are, in practice, the main scattering particles in blood. Since [185], the relation $H \rightarrow \chi(H)$ has been known to be non-linear. Mo et al. [142] obtained the hematocrit dependence (0 to 100%) of the backscattering coefficient at 7.5 MHz of saline suspensions of porcine red cells. At a low H, the backscattering coefficient linearly increases, peaks at $H \sim 0.15$ and then smoothly decays to zero.

Shear and red blood cell aggregation dependencies Under flow circulation, blood echogenicity varies because of motion related direct effects (turbulence scattering e.g.) and of shear dependent collective RBC reorganization at the microscopic scale. When the shear rate $\dot{\gamma}$ becomes low, χ tends to increase as firstly reported by Sigel et al. in 1982 [191]. The fact that the backscatter of non-aggregating porcine RBCs in saline suspension is invariant with the shear rate $\dot{\gamma}$ (in laminar flow) tends to prove that aggregation is the most significative factor explaining the flow dependence of human blood backscatter [232].

Cloutier and Qin [59] quantified the Doppler power variations with shear at 10 MHz by an exponential relation $P_\infty + (P_0 - P_\infty)e^{-\dot{\gamma}/\dot{\gamma}_c}$, where P_∞ and P_0 are the limit Doppler power at infinite and zero shear rates respectively, and $\dot{\gamma}_c$ quantifies the decay of the power with the shear rate. They found $\dot{\gamma}_c \sim 5 - 20$ s^{-1} and $P_0/P_\infty \sim 10 - 450$ for equine blood. The dependence of the backscattering coefficient on the concentrations of plasmatic proteins (as fibrinogen) or artificial polymers (dextran,

PEG in saline) mediating RBC aggregation has also been observed by a number of groups. Shung and Reid [187] firstly observed the echogenicity enhancement at 7.5 MHz with the fibrinogen bulk concentration. Haider et al. [95] showed that the backscattering coefficient at 8 MHz of human hardened RBCs in a dextran 70 saline suspension varies as $\chi^{8\text{MHz}}(\dot{\gamma})/\chi_\infty = 1 + \left(\frac{\tau_s}{\tau_c}\right)^{-3/2}$, where $\tau_s = \eta(\dot{\gamma})\dot{\gamma}$ is the bulk shear stress, η being the whole blood viscosity and (τ_c, χ_∞) are fitting parameters. The shear stress τ_c ($\sim$ 0.1 Pa), related to the dextran concentration, could be seen as a critical disaggregation shear stress. The dependence of the critical parameters $\dot{\gamma}_c$ or τ_c on the incident frequency is however unknown and would need to be elucidated. When studying the frequency dependence $k \rightarrow \chi(\vec{k})$, Shung et al. [185] showed that non-aggregating saline RBC suspensions exhibit the classical k^4 dependence that is characteristic of the Rayleigh scattering regime. Yuan and Shung [233] firstly demonstrated for porcine blood that at low shear rate the frequency dependence β, as defined by a power law[2] $\chi(k) = \alpha_0 f^\beta$, significantly decreases below 4: RBC aggregation therefore induces non-Rayleigh effects when RBC *rouleaux* form in plasma. The two mentioned acoustical indices (α_0, β) are therefore expected to convey information on the RBC aggregation level. Systematic rheoacoustical characterization of the dependence $\dot{\gamma} \rightarrow (\alpha_0, \beta)$ in stationary Couette shear flow, as studied by van der Heiden et al. [216], Foster et al. [84] or Haider et al. [95], still needs to be investigated to test the feasibility and reliability of ultrasonic scattering measurements of RBC aggregability, and to test the pertinence of the data reduction (α_0, β).

Cross-sectional distribution of blood echogenicity in stationary flow Shear rate distribution is non-homogeneous across the vessel lumen. Erythrocyte microscopic density is therefore not constant in flow, which leads to hematocrit and clustering spatial pattern that vary with the hemodynamic conditions and hemorheological variables. This is revealed by the inhomogeneous cross-sectional profiles of blood echo-

[2]Note that the wavevector and the frequency are related by $k = 2\pi f/c$.

genicity in stationary Poiseuille flow, as firstly reported by Yuan and Shung in 1989 [235]. While the power backscattered by bovine blood at 7.5 MHz remains homogenously low, an anechoic central zone (the "black hole") surrounded by an hyperechoic zone appears on B-scans of the porcine or human blood flowing in a rigid tube. Radial redistribution of aggregates and hematocrit, orientation of *rouleaux* [164] or modal shear rate variation of blood hypoechoicity [184] are potential explanations of this spatial heterogeneity.

Time dependence of blood echogenicity in non-stationary flow Natural pulsatility of blood flow in arteries raised the question of how blood scattering properties react to time-varying hemodynamics. Using high frequency intravascular ultrasound at 30 MHz, time variations of blood echogenicity of three patients were recorded *in vivo* by de Kroon et al. [66]. This initiated a number of studies (using Doppler power or RF backscattered power) that aimed to clarify how time and spatial variations of blood backscatter evolves as a function of the cardiac frequency [41, 56, 154], mean flow rate [56], hematocrit [41, 55, 126], vessel elasticity [138], or RBC aggregability [56, 164]. The time variation of the indices (α_0, β) has nevertheless never been studied in pulsatile flow.

Dynamic response of blood backscatter has also been studied in transient flow [165, 169, 187]. After flow stoppage or reduction (in Couette or Poiseuille flow), RBCs form clusters and blood echogenicity increases accordingly. Time variation $\chi(\vec{k}, t)$ can then be characterized by the backscatter plateau and by an aggregation time constant [169]. Disaggregation kinetics should symmetrically be exploited in applying a shear rate step to resting blood, but this still has to be studied.

Rationale for acoustic modeling of the backscattering coefficient There is undoubtedly a need to scrupulously define which physical properties define the meanings of the words "aggregation level" , or "aggregability" . Whereas these biophysical

phenomena originate at the cell scale, these terms refer to macroscopic observables. The aggregation level is commonly seen as a geometric quantification of the fact that RBCs are packed into clusters, while aggregability designates the increase in aggregation level when the shear forces decrease, more or less rapidly. In sections (2.7), (2.8) and (2.9), physical determinants of the aggregation level are defined and we attempt to relate them to the frequency dependence of the backscattering coefficient. We will especially distinguish the impact of the aggregation/aggregability factors from the effect of the single RBC property (section 2.5) and of the hematocrit by defining the so-called *structure factor* in section (2.6).

2.5 Ultrasound backscattering by a single red blood cell: analytical models of the erythrocyte cross-section

In this section, different models of the acoustic cross-section of a single RBC in plasma are proposed, as a first step towards the understanding of the global backscattering properties of blood. We first review the different analytical approaches to model the (back)scattering cross-section of a material particle, as a function of its morphology and thermomechanical properties. It is then applied to the erythrocyte case, and one derives a semi-analytical model for the RBC backscattering cross-section. Cross-sections of scatterers with primitive geometric shapes are also compared to the experimental results obtained with RBCs, and it is shown that the acoustical backscattering behavior of a single RBC can be described by a cylinder model with a good accuracy.

2.5.1 Properties and approximations of the scattering cross-section

The scattering cross-section of a particle $\mathcal{V}$ depends on the shape of the scatterer (observed at the precision of the wavelength) and on the acoustic properties of its subcomponents: viscosity, compressibility, density for a fluid particle, and the elastic tensor coefficients for a solid. Non-linear scatterers as ultrasound contrast agents often have acoustical cross-sections several orders of magnitude greater than biological samples of comparable dimensions and even greater than their own geometrical cross-section [152]. On the contrary, the RBC typical cross-section is of the order of one square nanometer while its typical surface is 130 μm^2.

The derivation of the scattering cross-section as a function of the particle rheological and acoustical properties, or inversely, the inference of geometric and physical characteristics of $\mathcal{V}$ from a collection of measurements $(\vec{e_r}, k) \rightarrow \sigma(\vec{e_r}, \vec{k})$ can be a difficult task, because of the subtle variations of cross-section as a function of the frequency, scattering angle, etc. Three principal methods enable the mathematical solving of the direct problem, i.e. the determination of the pressure amplitude in the far field, and of the cross-section as a function of the properties of $\mathcal{V}$.

Firstly, the decomposition of the scattered pressure field $p_s(\vec{r})$ in a convenient basis of spatial harmonic functions, can provide the solution of the homogeneous Helmholtz equation in the propagation medium, writing appropriate boundary conditions on the sample surface $\partial\mathcal{V}$ under the form of infinite series [144]. This method essentially holds for simple shapes and rigid scatterers.

Secondly, when the Born approximation $p_s \ll p_i$ is valid, a Fourier method [105, 144] can be used to derive the cross-section expression of weak fluid scatterers. This method provides close analytical approximations of the RBC cross-section or of the cross-section of macroscopic blood samples.

Finally, as a last mathematical resort, the solving of the inhomogeneous Helmholtz

equation in the whole space can be (numerically) done, exploiting the linearity of the relation between the spatial distribution of the scattering source and the pressure field through the Green propagation function [60]. This approach will not be detailed here as RBCs reasonably respect Born weak scattering conditions.

Acoustical cross-section of a rigid sphere

The case of the rigid sphere is firstly proposed as a reference. A single geometric parameter, the radius a, is sufficient to characterize this scatterer. A serial expansion of the scattered pressure field (first method) can be used as presented in [144]. The first-order approximation for a small rigid sphere ($ka \ll 1$) is:

$$\sigma(\vec{e_r}, k\vec{e_i})/4\pi a^2 = \frac{1}{36\pi}(ka)^4(1 - 3\vec{e_r}.\vec{e_i})^2. \tag{2.11}$$

It can be emphasized that the acoustic cross-section of a small rigid sphere increases rapidly with the frequency as it scales as k^4a^6. The backscattered power (that corresponds to the situation $\vec{e_r}.\vec{e_i} = -1$) is four times greater than the forward scattered power ($\vec{e_r}.\vec{e_i} = 1$).

On the contrary, a big rigid sphere has a nearly frequency- and angular-independent cross-section, as given by a first order approximation for $1/ka \ll 1$:

$$\sigma(\vec{e_r}, k\vec{e_i})/4\pi a^2 = \frac{1}{16\pi}\left(1 + \frac{1 + \vec{e_i}.\vec{e_r}}{1 - \vec{e_i}.\vec{e_r}} j_1^2\left(ka\left(1 - \vec{e_i}.\vec{e_r}\right)^{1/2}\right)\right) \approx \frac{1}{16\pi} \text{ (for } \vec{e_i} \neq \vec{e_r}), \tag{2.12}$$

where j_1 is the first order Bessel function.

Acoustical cross-section of a weak scattering fluid particle

Born approximation for fluid particles We now consider a non-attenuating fluid particle, characterized by two position-dependent distributions, namely the re-

lative density $\gamma_\rho(\vec{r}) = \frac{\rho_s(\vec{r})-\rho_0}{\rho_s(\vec{r})}$ and the relative (adiabatic) compressibility contrast $\gamma_\kappa(\vec{r}) = \frac{\kappa_s(\vec{r})-\kappa_0}{\kappa_0}$, where the subscripts $_s$ and $_0$ respectively refer to the sample and to the propagation medium. The Born approximation $p_s \ll p_i$, valid when the particle creates small inhomogeneities ($|\gamma_\rho|, |\gamma_\kappa| \ll 1$), gives the scattering cross-section of a weak fluid scatterer [144]:

$$\sigma(\vec{e}_r, k\vec{e}_i) = \frac{k^4}{16\pi^2} \left| \int_{\mathcal{V}} \gamma_\kappa(\vec{r}) e^{-\imath\vec{q}.\vec{r}}\, d^3r + \vec{e}_i.\vec{e}_r \int_{\mathcal{V}} \gamma_\rho(\vec{r}) e^{-\imath\vec{q}.\vec{r}}\, d^3r \right|^2, \tag{2.13}$$

where $\vec{q} = k(\vec{e}_r - \vec{e}_i)$ is the scattering vector. This formulation (second method) enables us to emphasize the role of the Fourier spatial transforms of γ_ρ and γ_κ on the value of the acoustical cross-section of a particle.

Rayleigh approximation for small and weak scatterers Rayleigh scatterers are tenuous scatterers ($|\gamma_\rho|, |\gamma_\kappa| \ll 1$) that have negligible dimensions compared to the wavelength ($k\mathcal{V}^{1/3} \ll 1$). In this case, the scattering cross-section has a simple expression:

$$\sigma(\vec{e}_r, k\vec{e}_i) = \frac{k^4\mathcal{V}^2}{16\pi^2} \left(\langle\gamma_\kappa\rangle + \vec{e}_i.\vec{e}_r \langle\gamma_\rho\rangle \right)^2, \tag{2.14}$$

where brackets represent spatial averaging over the scatterer volume $\mathcal{V}$. The isotropic part of the scattered pressure corresponds to the monopole radiation due to the compressibility inhomogeneity γ_κ, whereas the anisotropic part due to the density contrast γ_ρ can be seen as a dipole radiation. As for the small rigid sphere, the acoustical cross-section of a weak Rayleigh scatterer increases rapidly with the frequency and volume, as it scales as $k^4\mathcal{V}^2$, provided its size remains small compared to the wavelength. The exact shape and orientation of the particle does not influence the value of $\sigma(\vec{e}_r, k\vec{e}_i)$, being geometrical details that cannot be perceived at the wavelength scale. One can assess the effect of the Born approximation on the estimation of the real backscattering cross-section value as follow. Morse and Ingard [144] showed

that the scattering cross-section of a small homogeneous fluid sphere ($ka \ll 1$) has a scattering cross-section given by:

$$\sigma(\vec{e}_r, \vec{k}) = \frac{k^4 \mathcal{V}^2}{16\pi^2} \left(\langle \gamma_\kappa \rangle + \vec{e}_i . \vec{e}_r \langle \gamma_\rho \rangle \left(1 - \langle \gamma_\rho \rangle / 3\right)^{-1} \right)^2, \tag{2.15}$$

expression which is consistent, at the first order in $\langle \gamma_\rho \rangle$, with the Rayleigh approximation. With the typical contrasts encountered in blood, the values of the cross-section given by Eqs. (2.14) and (2.15) differ by less than 3%, which shows that the Born approximation is satisfactory.

Backscattering cross-section and form factor of a weak scattering fluid particle

In the Born approximation, the backscattering cross-section of a weak scatterer can be derived from Eq. (2.13):

$$\sigma_b(\vec{k}) = \frac{1}{4\pi^2} k^4 \left| \int_{\mathcal{V}} \gamma_z(\vec{r}) e^{2\imath \vec{k}.\vec{r}} \, d^3r \right|^2, \tag{2.16}$$

where $\gamma_z = \frac{1}{2}(\gamma_\rho - \gamma_\kappa) \ll 1$ is the relative contrast in acoustical impedance $Z = (\rho/\kappa)^{1/2}$ (using a first order expansion). In the Rayleigh scattering regime, this reduces to:

$$\sigma_b(\vec{k}) = \frac{1}{4\pi^2} k^4 \mathcal{V}^2 \langle \gamma_z \rangle^2. \tag{2.17}$$

For non-Rayleigh conditions, but still in Born approximation, one defines the correction quantity $F(\vec{k})$ [105]:

$$\sigma_b(\vec{k}) = \frac{1}{4\pi^2} k^4 \mathcal{V}^2 \langle \gamma_z \rangle^2 F(\vec{k}). \tag{2.18}$$

This factor $F(\vec{k})$ is called the form factor and takes into consideration the shape

Shape	Form factor $F(\vec{k})$	Rayleigh Limit ($F > 0.95$)
Sphere	$\phi_s(2ka) = \left(\frac{3\sin 2ka - 6ka\cos 2ka}{(2ka)^3}\right)^2$	$ka < 0.25$
Ellipsoid	$\phi_s\left(2\left(k_1^2a_1^2 + k_2^2a_2^2 + k_3^2a_3^2\right)^{1/2}\right)$	$\left(k_1^2a_1^2 + k_2^2a_2^2 + k_3^2a_3^2\right)^{1/2} < 0.25$
Cylinder	$\left(\frac{\sin k_z h_0}{k_z h_0}\frac{J_1(2k_r R)}{k_r R}\right)^2$	$\left(k_z^2h_0^2 + 3k_r^2R^2\right)^{1/2} < 0.38$

TAB. 2.I – Form factors of several primitive shapes. The wavevector $\vec{k}$ is decomposed in the ellipsoid system of axes $\vec{k} = k_1\vec{e}_1 + k_2\vec{e}_2 + k_2\vec{e}_3$ where $(1,2,3)$ refer to the ellipsoid principal directions of the axes (a_1, a_2, a_3), or in a cylindrical system of axes $\vec{k} = k_z\vec{e}_z + k_r\vec{e}_R$. The height of the cylinder is h_0 and its radius is R. The form factor of the sphere is $F(\vec{k}) = \phi_s(2ka)$.

of the scatterer in the expression of the non-Rayleigh backscattering cross-section. By definition, it has a limit of 1 in the Rayleigh conditions defined by $k\mathcal{V}^{1/3} \ll 1$. Several analytical expressions of form factors can be computed for simple shapes of homogeneous weak scatterers, as shown in table 2.I, by calculating Fourier transforms of given 3D forms. The size limits of the Rayleigh approximation can be subsequently given by indicating the range of wavevectors $\vec{k}$ that satisfy e.g. $F(\vec{k}) > 0.95$.

2.5.2 Red blood cell physical properties and US scattering cross-section

Physical erythrocyte properties

Erythrocytes are the main US scatterers in blood as they represent 99 % of the blood cells immersed into plasma. They are very deformable and their shapes can vary in response to the external stress conditions (hemodynamic shear forces e.g.) and to the osmolarity of the surrounding environment. In static equilibrium, the RBC is a biconcave disk [210] with volume $\mathcal{V} = 98 \pm 16\ \mu\text{m}^3$, an optimal exchange surface area $\mathcal{S} = 130 \pm 16\ \mu\text{m}^2$ and a diameter $\mathcal{D} = 7.65 \pm 0.7\ \mu\text{m}$. The red blood cell content is roughly a 32% hemoglobin solution [44] with physical properties reported in Table (2.II). Plasmatic properties are also given for comparison. The erythrocyte membrane

	ρ (kg.m^{-3})	κ (Pa^{-1})	η (Pa.s)	c (m.s^{-1})	Z (kg.m^{-2}.s^{-1})
human hemoglobin solution [185, 86]	1092	3.41×10^{-10}	6×10^{-3}	1639	1.79×10^{6}
porcine hemoglobin solution [232]	1078	3.50×10^{-10}	?	1628	1.755×10^{6}
bovine hemoglobin solution [232]	1084	3.52×10^{-10}	?	1619	1.75×10^{6}
human plasma [185]	1021	4.09×10^{-10}	1.2×10^{-3}	1547	1.58×10^{6}
saline suspension (0.9%) [185]	1005	4.49×10^{-10}	1×10^{-3}	1489	1.50×10^{6}
relative contrast (human)	0.065	-0.199	4	0.06	0.13

TAB. 2.II – Some physical properties of the plasma and of the RBC inner fluid. The density is noted ρ, the adiabatic compressibility κ, the (shear) viscosity η, the speed of sound c and the impedance Z.

behaves as a thin viscoelastic bag [86], having both solid and "fluid mosaic" rheological properties, confered by the lipid bilayer and by the subsurface spectrin network of the reinforcing skeleton [71, 101, 118, 143]. Until now, most of the authors have related the RBC scattering cross-section to the contrast in compressibility and density between plasma and red cell content. To our knowledge, the relevance and specific effect of the RBC membrane viscoelasticity on its US scattering cross-section has never been adressed.

Rayleigh scattering by a red blood cell

Neglecting the acoustic absorption and the RBC membrane deformation, and applying classical Rayleigh approximation to a RBC, the low frequency acoustical cross-section of an erythrocyte embedded in plasma can be computed by using equation (2.14) and

the values $\langle\gamma_\kappa\rangle = -0.199$ (a relatively elevated contrast) and $\langle\gamma_\rho\rangle = 0.065$ from Table (2.II). Defining the mean RBC radius a by $\frac{4}{3}\pi a^3 = \mathcal{V}$, one obtains the angular dependence of the cross-section of a RBC for $ka < 0.25 \leftrightarrow f < 21$ MHz:

$$\sigma(\vec{e}_r, k\vec{e}_i)/4\pi a^2 = \frac{1}{36\pi}(ka)^4(\langle\gamma_\kappa\rangle + \vec{e}_i.\vec{e}_r\langle\gamma_\rho\rangle)^2. \tag{2.19}$$

Scattering is more pronounced in the backward direction because of the dipole radiation term. The angle dependence of the RBC Rayleigh cross-section and of the small rigid equivalent sphere are compared in figure (2.3).

2.5.3 Backscattering cross-section of the red blood cell

A more complex description of the erythrocyte shape must be adopted to predict the backscattering properties of blood at non-Rayleigh high frequencies (typically $f \gtrsim 20$ MHz). The interest of using high US frequency is motivated by the improvement of the scanner resolution. Using an analytical model of the geometrical cross-section of a RBC and assuming the validity of the Born approximation, new semi-analytical expressions of the angular and frequency dependencies of the form factor are derived in this subsection. A numerical approach using the T-matrix method has already been proposed in [114], but is less tractable than the proposed expression because of its numerical formulation. Coussios [63] also proposed a weak scattering approach to derive the erythrocyte cross-section, assuming a cylindrical shape. The impact of the precise RBC morphology will be assessed in the next paragraph.

Form factor of a volume of revolution mimicking a red blood cell

Considering that the acoustical impedance distribution is homogeneous inside the RBC, that the RBC shape has a cylindrical symmetry around Oz (see Fig. 2.4) , and a mirror symmetry with respect to Oxy, the impedance contrast can be written:

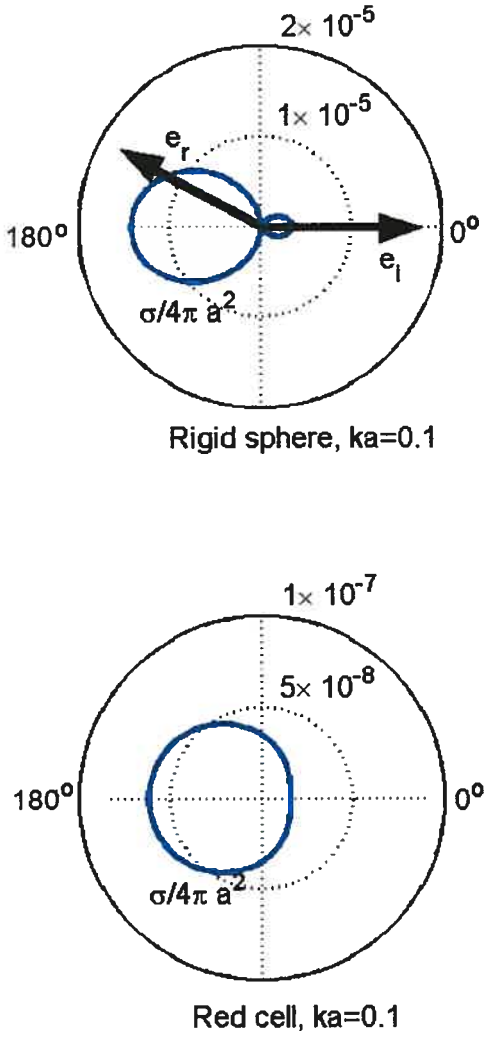

FIG. 2.3 – Polar diagram of the angle dependence of the scattering cross-section σ (blue line) of the rigid sphere and of the red blood cell in the Rayleigh approximation. The mean radius is a and k is the wavenumber. The incident direction is $\vec{e}_i$ (corresponds to zero degree) and the observation direction is $\vec{e}_r$. The frequency f is defined by the conditions $ka = 0.1 \leftrightarrow f = 8.7$ MHz.

Tonicity (mosmol)	h_0 (μm)	$\mathcal{D}$ (μm)	α_2	α_4	$\mathcal{V}$ (μm^3)	$\mathcal{S}$ (μm^2)
131 (hypotonicity)	6.78	6.78	0	0	164	145
217 (hypotonicity)	2.10	7.60	3.6	-2.7	116	135
300 (normal tonicity)	0.81	7.82	9.7	-5.4	94	135

TAB. 2.III – Geometrical descriptors of red blood cell shape under different medium tonicities, from [76]. The height of the red cell along Oz is h_0, the diameter in the plane Oxy is $\mathcal{D}$, $\mathcal{V}$ is the RBC volume, $\mathcal{S}$ is the RBC surface, and (α_2, α_4) are geometric parameters that define the discoidal shape of the RBC.

$\gamma_z(\vec{r}) = \gamma_z(r,\theta,z) = \langle\gamma_z\rangle \mathbb{I}_{[|z|<z_0(r)]}$, where $\mathbb{I}_{[]}$ is the indicator function. Applying Eq. (2.16) and after some algebra (cf. (2.12.1) for the detailed derivations) to derive the backscattering cross-section, the form factor $F(k_r, k_z)$ is shown to have the following expression:

$$F(k_r,k_z) = \left| \int \mathbb{I}_{[|z|<z_0(r)]} e^{2\imath(k_z z + k_r r\cos\theta)}\, r dr d\theta dz \right|^2 / \mathcal{V}^2, \tag{2.20}$$

$$= \left| \int r z_0(r) \mathrm{sinc}(2k_z z_0(r)) j_0(2k_r r)\, dr \Big/ \int r z_0(r)\, dr \right|^2, \tag{2.21}$$

where $\mathrm{sinc}(x) = \frac{\sin x}{x}$ is the sinus cardinal function, and j_0 is the bessel function of order 0. Evans and Fung [76] have formulated a convenient analytic form for the erythrocyte profile $z_0(r) = \frac{1}{2} h_0 \phi(2\frac{r}{\mathcal{D}})$, with some geometric coefficients (α_2, α_4) that can vary to consider variations of the RBC shape with the tonicity of the medium (Fig. 2.4 and table 2.III):

$$\phi(u) = \mathbb{I}_{[0<u<1]}(1-u^2)^{1/2}(1+\alpha_2 u^2 + \alpha_4 u^4). \tag{2.22}$$

Defining the function $\Phi(\omega_1, \omega_2, \alpha_2, \alpha_4)$ by:

$$\Phi(\omega_1,\omega_2,\alpha_2,\alpha_4) = \int_0^1 u\phi(u)\mathrm{sinc}(\omega_1\phi(u)) J_0(\omega_2 u)\, du, \tag{2.23}$$

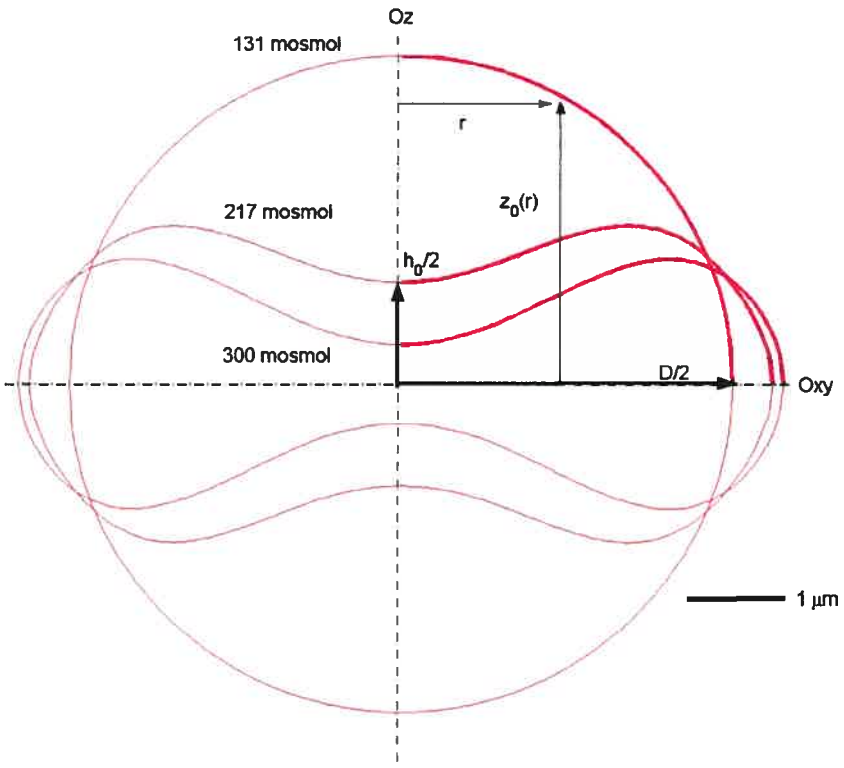

FIG. 2.4 – Geometrical cross-section of the red blood cell in varying medium tonicity.

the form factor can be computed by numerical integration:

$$F(k_r, k_z) = |\Phi(k_z h_0, k_r \mathcal{D}, \alpha_2, \alpha_4)/\Phi(0, 0, \alpha_2, \alpha_4)|^2 . \tag{2.24}$$

Resulting values of the backscattering cross-section as a function of the frequency, along Oz and Ox are shown in figure (2.5).

Comparison to simpler shapes of scatterer

A second order expansion in ka of the form factor is helpful to examine which geometrical features of a given shape significantly contribute to the frequency dependence of the backscattering cross-section. In the Born approximation and for a homogeneous scatterer, a second order Taylor expansion in $\vec{k}$ of equation (2.16) gives (cf. 2.12.2):

Shape	Volume (μm^3)	$a_{xx} = a_{yy}$ (μm)	a_{zz} (μm)	Other geometrical descriptors (μm)
Red cell (isotonic)	94	4.3	1.4	cf table (2.III)
Sphere	94	2.8	2.8	$a = 2.8$
Spheroid	94	4.3	1.2	$a_{zz} = \mathcal{V}/(\frac{4}{3}\pi a_{xx}^2)$
Cylinder	94	4.3	0.9	$R = \sqrt{0.8}a_{xx} = 3.9, h_0 = \mathcal{V}/\pi R^2 = 2$

TAB. 2.IV – Volume $\mathcal{V}$ and inertia characteristics of the red blood cell and other equivalent shapes. The equivalent axes a_{ii} are computed from the eigenvalues $a_{ii}^2/5$ of the inertia tensor Σ. The cylinder is described by its radius R and its height h_0. The mean RBC radius is a.

$$F(\vec{k}) = 1 - 4\vec{k}.\Sigma\vec{k} + \ldots, \tag{2.25}$$

where Σ is a definite positive shape-dependent tensor defined by:

$$\Sigma = \frac{1}{\mathcal{V}} \int_{\mathcal{V}} \vec{r} \otimes \vec{r}\, d^3r, \tag{2.26}$$

the dyadic product of two vectors being noted $\otimes$. The principal axes of the particle are the eigenvectors of Σ, and its eigenvalues $\Sigma_{11} \leq \Sigma_{22} \leq \Sigma_{33}$ are related to the axis of the equivalent inertia ellipsoid $a_{11} \leq a_{22} \leq a_{33}$ by the relations $5\Sigma_{ii} = a_{ii}^2$, for $i = 1, 2, 3$. The equation (2.25) shows that two material particles having the same mean impedance contrast $\langle \gamma_z \rangle$, volume $\mathcal{V}$ and inertia tensor Σ have close acoustical backscattering cross-sections, up to the second order in ka. We can now try to simplify the previous description of RBC scattering by finding simple shaped particles acoustically equivalent to the RBC.

Figure (2.5) shows the frequency dependence of the backscattering cross-section of the "equivalent" sphere, spheroid, and cylinder, using RBC characteristics of table (2.III) at normal osmolarity, the expressions of the form factor given in table (2.I) and experimental data from [234]. Table (2.IV) shows their geometric features. According

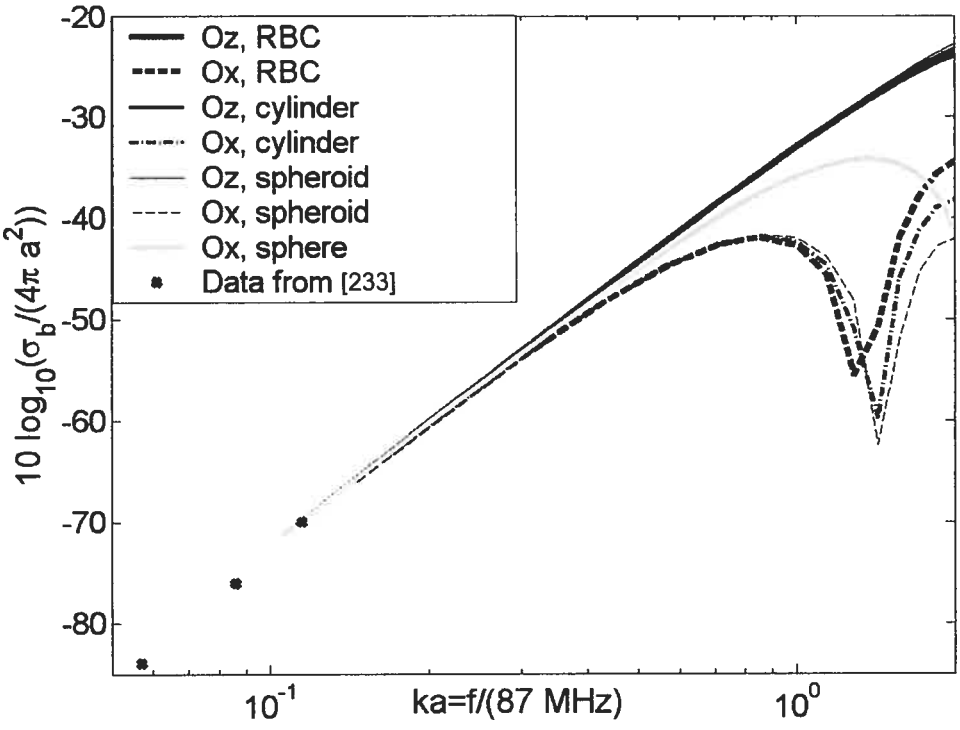

FIG. 2.5 – Frequency dependence of the backscattering cross-section of the modeled red blood cell and of equivalent particles as described in Table (2.IV), in comparison with experimental results obtained by Yuan [234]. The insonification direction is parallel with the revolution axis (Oz) or perpendicular (Ox) to it. Values are given in dB, in reference to the surface of a sphere having the same volume.

to figure (2.5), the cylinder with dimensions $R = 3.9$ μm and $h_0 = 2$ μm and the RBC have very similar cross-sections: their form factors differ by less than 6 % for $ka < 2 \leftrightarrow f < 170$ MHz. Computation of the form factor gives a Rayleigh limit $F > 0.95$ whatever the angle when $ka < 0.16 \leftrightarrow f < 14$ MHz. The figure (2.5) also shows that the insonification angle becomes an important parameter to consider when $ka > 0.3 \leftrightarrow f > 26$ MHz (for which the orthogonal and radial RBC cross-sections differ by 3 %), which is fairly in agreement with [63].

2.6 Ultrasound backscattering by blood: introduction to the structure factor

2.6.1 Empirical introduction to the structure factor

The previous section focused on the understanding of US scattering by a single RBC. This can be considered as a first small step towards the whole modeling of blood backscattering coefficient as each millimeter cube of blood approximately contains five millions of erythrocytes ! A naïve method to derive the blood backscattering coefficient $\chi(\vec{k})$ would be to consider that each RBC equally and individually contributes to the backscattered power. This simplistic reasoning leads to the following expression:

$$\chi(\vec{k}) = m\sigma_b(\vec{k}), \tag{2.27}$$

where $m = 4.2 - 4.7 \times 10^{15}$ m^{-3} is the number density of RBCs in blood, related to the hematocrit (erythrocyte volumic fraction) $H = m\mathcal{V} = 0.4 - 0.45$. However, experiments have shown that the backscattering coefficient does not linearly increase with the RBC concentration m, and that it varies with hemodynamics or with plasma protein concentrations, which do not modify nor the RBC number, neither their dimension. This proves that Eq. (2.27) must be corrected for the effect of the microstructural pattern induced by cell-cell and cell-plasma interactions. From the very first corrective attempts by Shung et al. [185], the first modeling study by Atkinson and Berry [12], to now, no model has been unanimously approved. Our purpose in the following sections is therefore to clarify how blood backscattering properties is influenced by RBC microstructure.

Inspired by the formalism of cristallography, X-ray or neutron scattering used by material physicists, several authors [95, 212, 81] introduced the *structure factor* S to correct the formula (2.27) for blood US backscattering:

$$\chi(\vec{k}) = mS\sigma_b(\vec{k}), \tag{2.28}$$

This non-dimensional parameter S should depend on the frequency and on all interaction parameters characterizing the erythrocyte microstructure, including the hematocrit H. This section intends to rigourously give its definition in the case of a random assembly of identical weak scatterers.

2.6.2 Structure factor of randomly dispersed weak scatterers

A volume sample V of blood is modeled here as a biphasic suspension composed of $N = mV$ identical erythrocytes embedded in plasma. The RBCs of volume $\mathcal{V}$ have their centroids located in the random positions $(\vec{X}_1, \ldots, \vec{X}_N)$ that jointly define a random configuration Ω of the phase space V^N. Erythrocytes, considered as weak scatterers, are characterized by a common backscattering cross-section $\sigma_b(\vec{k})$. This paragraph derives the relation between the statistical properties of the random point process Ω and the structure factor previously introduced by phenomenological arguments.

For this purpose, the random microscopic density $N_\Omega(\vec{r}) = \sum_{i=1}^{N} \delta(\vec{r} - \vec{X}_i)$ is introduced. The number N_A of RBCs falling into any volume A is simply the integral $N_A = \int_A N_\Omega(\vec{r})\, d^3r$. As RBCs are supposed to be identical and to have a constant orientation, one writes the impedance contrast distribution inside V:

$$\gamma_z(\vec{r}) = \sum_{i=1}^{N} \gamma_{RBC}(\vec{r} - \vec{X}_i), \tag{2.29}$$

$$= N_\Omega(\vec{r}) * \gamma_{RBC}(\vec{r}), \tag{2.30}$$

where $\gamma_{RBC}(\vec{r})$ is the spatial inhomogeneity of impedance created by a single RBC centered in O. Using the convolution theorem and applying Born approximation (Eq.

2.16), one obtains the mean backscattering cross-section of the blood sample V:

$$E[\sigma_b^V(\vec{k})] = \frac{1}{4\pi^2}k^4 E\left[\left|\int_V \gamma_z(\vec{r})e^{2i\vec{k}.\vec{r}}\,d^3r\right|^2\right] \tag{2.31}$$

$$= \frac{mV}{4\pi^2}k^4\left|\int_{\mathcal{V}} \gamma_{RBC}(\vec{r})e^{2i\vec{k}.\vec{r}}\,d^3r\right|^2 E\left[\frac{1}{N}\left|\int_V N_\Omega(\vec{r})e^{2i\vec{k}.\vec{r}}\,d^3r\right|^2\right]. \tag{2.32}$$

This gives the final formula for the backscattering coefficient, previously defined as the mean backscattering cross-section per unit scattering volume:

$$\chi(\vec{k}) = E[\sigma_b^V(\vec{k})]/V = m\sigma_b(\vec{k})E\left[\frac{1}{N}\left|\int_V N_\Omega(\vec{r})e^{2i\vec{k}.\vec{r}}\,d^3r\right|^2\right]. \tag{2.33}$$

Comparison of Eqs. (2.28) and (2.33) gives the expression of the backscattering coefficient:

$$\chi(\vec{k}) = mS(-2\vec{k})\sigma_b(\vec{k}), \tag{2.34}$$

where the scattering vector dependent function $S(\vec{q})$, the structure factor, is defined by:

$$S(\vec{q}) = E\left[\frac{1}{N}\left|\int_V N_\Omega(\vec{r})e^{-i\vec{q}.\vec{r}}\,d^3r\right|^2\right]. \tag{2.35}$$

2.6.3 Structure factor and pair-correlation function

According to equation (2.35), the non-dimensional structure factor $S(\vec{q})$ is directly derived from the power spectrum of the microscopic density $N_\Omega(\vec{r})$. When Ω is a Poisson point process (non structured point pattern), the structure factor is constant, equals to 1, which agrees with Eq. (2.27). The structure factor therefore quantifies the specific effect of the scatterer organization on the backscattering strength of the material, in comparison with a Poisson-distributed medium with the same global

hematocrit. In order to characterize the second order correlation properties of the microscopic density, it can be alternatively written:

$$S(\vec{q}) = E\left[\frac{1}{N}\left|\int_V N_\Omega(\vec{r})e^{-\imath\vec{q}.\vec{r}}\,d^3r\right|^2\right], \tag{2.36}$$

$$= E\left[\frac{1}{N}\left|\sum_{i=1}^{N} e^{-\imath\vec{q}.\vec{X}_i}\right|^2\right], \tag{2.37}$$

$$= 1 + m\int\left(g(\vec{h})-1\right)e^{-\imath\vec{q}.\vec{h}}\,d^3h. \tag{2.38}$$

There is a one-to-one correspondence (through the Fourier transform) between the structure factor $S(\vec{q})$ and the so-called pair-correlation function $g(\vec{h})$, used by condensed matter physicists to describe microstructure [15] of gas and liquids. The pair correlation-function is defined by the autocorrelation equation:

$$E\left[N_\Omega(\vec{r}_0)N_\Omega(\vec{r}_1)\right] = m^2 g(\vec{r}_0-\vec{r}_1) + m\delta(\vec{r}_0-\vec{r}_1). \tag{2.39}$$

The value $g(\vec{h})$ can be seen as a conditional probability. Given that $\vec{x}$ belongs to the point process Ω, then $mg(\vec{h})d^3h$ is the probability that the small neighborhood of center $\vec{x}+\vec{h}$ and volume d^3h contains any other point of Ω. Repulsion between particles at distance $\vec{h}$ results in values $g(\vec{h}) < 1$ whereas attraction gives values $g(\vec{h}) > 1$. The correlation length l_{cor} is defined as the minimal distance such that $|\vec{h}| > l_{cor} \Rightarrow g(\vec{h}) = 1$. This distance reflects the typical lengthscale of the induced microstructure. For a homogeneous Poisson point process, the absence of organized structure in the spatial pattern results in $l_{cor} = 0$.

2.7 Low frequency US backscattering: the packing factor approximation

The measurement of the non-linear increase of blood or saline RBC suspensions echogenicity with the hematocrit led several authors [12, 139, 140, 141, 185] to propose corrections to the formula (2.27) that is only valid for suspensions of uncorrelated weak scatterers. The corrected formula had the following common form:

$$\chi(\vec{k}) = mW\sigma_b(\vec{k}), \tag{2.40}$$

where W represents the so-called *packing factor*, that differs from the structure factor $S(\vec{q})$ by its frequency independence, as found when scattering experiments are carried out at low US frequencies. In this section, the relation between the microstructure and the packing factor is investigated. Two different approaches for modeling the packing factor of particles in interaction are presented. The first uses methods from condensed matter statistical physics (compressibility equation), and the second uses statistical geometry for characterizing the point process Ω (particle approach). The relevance of these models to assess the blood packing factor and the limitations of the packing factor approximation in the context of medical ultrasound are discussed hereafter.

2.7.1 Definition of the packing factor

At a low frequency $2kl_{cor} \ll 1$, the structure factor $S(-2\vec{k})$ tends towards a constant value W, that is independent on the insonification angle and frequency.

$$S(\vec{q}) \rightarrow S(0) = W \tag{2.41}$$

This can be taken as the definition of the packing factor, that was extensively in-

vestigated by Twersky [211, 212] when studying optical and acoustical scattering by correlated polydisperse particle systems, and applying this notion to RBC US scattering afterwards [27, 132]. The packing factor can be related to the pair-correlation function:

$$W = 1 + m \int_{|\vec{h}|<l_{cor}} \left(g(\vec{h}) - 1 \right) d^3h. \tag{2.42}$$

The packing factor approximation $ka \ll a/2l_{cor} \Rightarrow S(-2\vec{k}) = W$ is often valid for low conventional frequencies used in medical US and non aggregating media. Number of investigators have therefore experimentally and theoretically studied the packing factor of saline suspensions of RBCs. In particular, the non-linear effect of the hematocrit H on the backscattering coefficient has been accurately elucidated in this approximation range.

Two points of view can be adopted to relate W to the characteristics of the random point process Ω. The first approach relies on thermodynamic and statistical physics concepts as introduced by the compressibility equation, whereas the particle approach is based on the statistical moments of the number density $N_\Omega(\vec{r})$. They are described in subsections (2.7.2) and (2.7.3).

2.7.2 Thermodynamic approach for modeling the packing factor

The compressibility equation

A physical hypothesis on the stochastic nature of RBC positioning in plasma is to consider that Ω is a Gibbs-Markov point process [217]. This comes from statistical physics postulates that are equivalent to Boltzmann equation for thermostated systems of interacting particles in equilibrium.

Suppose that the particle interactions derive from energetic potentials. This hypo-

thesis enables us to assign a total energy function $U_\Omega(\omega)$ to each configuration (or microstate) $\omega = (\vec{x}_1, \ldots, \vec{x}_N) \in V^N$ of N particles located in the volume V. The Boltzmann law states that, for a given temperature T and fixed mean energy, a certain microstate ω appears with a probability $p_\Omega(\omega)$ that is less likely when its total energy $U_\Omega(\omega)$ is elevated[3] (the Boltzmann constant is noted k_B):

$$p_\Omega(\omega) \propto \exp\left(-U_\Omega(\omega)/k_B T\right). \tag{2.43}$$

When particles interact by pairs, and if the partial energy of two particles separated by $\vec{h}$ is noted $V_2(\vec{h})$, the total energy function can be written:

$$U_\Omega(\omega) = \sum_{i<j} V_2(\vec{x}_i - \vec{x}_j). \tag{2.44}$$

The random Gibbs-Markov point process Ω is then completely defined by the temperature T, the number of particles N and the pair energy profile $V_2(\vec{h})$. All the statistical properties of Ω can theoretically be expressed as a function of these characteristics, using Boltzmann law. A large branch of the statistical physics, and of condensed matter physics consists of estimating macroscopical physical properties, as the structure factor and the packing factor, from the description of the microscopic particle interactions [15, 97]. We will examine in this paragraph how these techniques could help to tackle our acoustical issue.

The thermodynamic equation of state of a particle system Ω is the relation between the thermodynamic pressure $p = -\left(\frac{\partial E[U_\Omega(\Omega)]}{\partial V}\right)_{\text{entropy},N}$ and (N, V, T) [97]. The well-known equation of state of a perfect gas, $pV = Nk_BT$, corresponds to a Poisson point process which describes positions of non-interacting molecules ($V_2(\vec{h}) = 0$).

Using Boltzmann law, it can be shown [15] that the packing factor W is directly

[3]The probability density function (pdf) defined by Boltzmann law is the pdf that maximizes the entropy of the system, under the constraints of positivity, unit sum over V^N, and mean energy $E[U_\Omega(\Omega)]$.

related to the equation of state of Ω by the compressibility equation[4] :

$$1/W = \frac{V}{k_B T} \left(\frac{\partial p}{\partial N} \right)_{V,T} . \tag{2.45}$$

Applied to a perfect gas, the compressibility equation confirms $W = 1$. Knowing the equation of state of a random assembly Ω of interacting particles therefore enables us to predict their packing factor.

As condensed matter physicists obtained a number of equations of state for many liquid and gas models, using either experimental means, or simulations, one can benefit from their results obtained during the last 50 years. Analytical methods (that elucidate the relation between $g(\vec{h})$ and $V_2(\vec{h})$ using closure relations), molecular dynamics, Monte Carlo or hybrid simulations are the main methods to derive the equation of state of interacting particles. In the next two subsections, the compressibility equation is used to clarify the effect of particle high density (as in blood) and of attractive interactions on the packing factor.

Hard particle systems

The first success of the packing factor approximation for modeling blood US scattering has been the explanation of the counter-intuitive variations of χ with the hematocrit H. As a non-linear modal relation was experimentally found, although the naïve prediction (Eq. 2.27) of the relation expected a linear dependence, the corrective factor W should be hematocrit dependent and decrease with H for RBC saline suspensions. The experiments being conducted with non aggregating RBCs, the steric repulsion between the non-punctual scatterers was expected to be the main determinant of the packing factor value. This subsection intends to precise the random models of steric hardcore repulsions, and their corresponding packing factors, using pertinent

[4]The packing factor is directly related to the *isothermal* compressibility $\kappa_T = 1/N \, (\partial N/\partial p)_{V,T}$ by $W = m \kappa_T k_B T$.

Virial Coefficient	$B/4N_a\mathcal{V}$	C/B^2	D/B^3	E/B^4	F/B^5	G/B^6
Value	1	0.625	0.2869	0.1103	0.0386	0.0138

TAB. 2.V – Six first virial coefficients of the 3D hard sphere system as defined in Eq. (2.47) and reported in [15]. N_a is the number of Avogadro, and $\mathcal{V}$ is the particle volume.

equations of state and the compressibility equation.

Hard sphere systems A Gibbs-Markov point process that models particle hard-core repulsion can be defined by the crude hard sphere pair potential:

$$V_2(\vec{h}) = \begin{cases} +\infty & \text{if } |\vec{h}| < 2a \\ 0 & \text{otherwise.} \end{cases} \tag{2.46}$$

This system has been thoroughly studied as it represents the simplest model of inter-particular repulsion. Several approaches have been proposed to derive its equation of state, and allow to extract the hard sphere packing factor as exposed below.

Virial expansion The virial expansion of an equation of state is the serial expansion of pV/Nk_BT as a function of the molar density $N/N_a\mathcal{V}$ (where N_a is the Avogadro number), or equivalently in $H = N\mathcal{V}/V$. The expansion coefficients $(B, C, D, \dots)$ for the hard sphere system are exactly known, up to the sixth order [15] and are given in table (2.V).

$$\frac{pV}{Nk_BT} = 1 + \frac{B}{N_a\mathcal{V}}H + \frac{C}{N_a^2\mathcal{V}^2}H^2 + \frac{D}{N_a^3\mathcal{V}^3}H^3 + \dots \tag{2.47}$$

Applying the compressibility equation to the virial expansion, this gives the first coefficients of the Taylor expansion of the packing factor $W(H)$:

$$W = \left(1+2\frac{B}{N_a\mathcal{V}}H+3\frac{C}{\mathcal{V}^2N_a^2}H^2+4\frac{D}{\mathcal{V}^3N_a^3}H^3+\ldots\right)^{-1} \quad (2.48)$$

$$= 1-8H+49H^2+\ldots \quad (2.49)$$

One finds that the packing factor decreases when H increases: this is the explanation of the modal form of the curve $H \rightarrow HW$. However, truncated virial expansions as equation (2.49) rapidly fail in describing the hematocrit dependence of the packing factor when H exceeds a few percents. Alternative ways to derive the equation of state and to obtain a more accurate expression for the packing factor have been found to overcome this problem.

Padé approximants obtained by closure relations Padé (rational) approximants of the equation of state $pV/Nk_BT = f(H)$ can be found using classical closure relations between $V_2(\vec{h})$ and $g(\vec{h})$. The Perkus-Yevick (PY) closure relation[5] [156] yields two different equations of state for hard spheres, using either the pressure route (p_{PYP}) or the compressibility route (p_{PYC}) [15]:

$$\frac{p_{PYP}V}{Nk_BT} = \frac{1+H+H^2-3H^3}{(1-H)^3}, \quad (2.50)$$

$$\frac{p_{PYC}V}{Nk_BT} = \frac{1+H+H^2}{(1-H)^3}. \quad (2.51)$$

They are non consistent at a high hematocrit (when H^3 is non negligible), and both fail to describe high density pressure (they do not diverge at the maximal random packing fraction $H_{max} = 0.634$). They are however more reliable than a truncated

[5]Valid at low density of particles, the PY approximate closure relation is: $c(\vec{h}) = g(\vec{h})(1 - \exp(V_2(\vec{h})/k_BT))$, where $c(\vec{h})$ is the direct correlation function defined by the exact Ornstein-Zernicke equation: $g(\vec{h}) - 1 = c(\vec{h}) + m\left(g(\vec{h}) - 1\right) * c(\vec{h})$.

virial expansion as given by Eq. (2.49). The most often used expression of the Perkus-Yevick packing factor is deduced from the compressibility equation:

$$W_{PYC} = \frac{(1-H)^4}{(1+2H)^2}. \tag{2.52}$$

Empirical Carnahan-Starling (CS) equation of state [42], derived from an appropriate combination of the two previous PY Padé approximants, was experimentally proven to better fit the equation of state for hard spheres:

$$\frac{p_{CS}V}{Nk_BT} = \frac{1+H+H^2-H^3}{(1-H)^3}. \tag{2.53}$$

In particular, derived values of the first virial coefficients $(B, C, D, \dots)$ of the hard sphere equation of state are closer to the known exact figures. One could expect that the resulting expression for the packing factor should be more accurate at the third order in H. Using the CS equation, the corrected formula for the packing factor is:

$$W_{CS} = \frac{(1-H)^4}{(1+2H)^2 - 4H^3 - 3H^4} = W_{PYC}\left(1 + 4H^3 - H^4 + \dots\right). \tag{2.54}$$

It must however be noted that the CS packing factor differs by less than 0.005 from W_{PYC} as shown in Fig. (2.7). Both rational expressions of the packing factor are however only approximants of the exact hard sphere packing factor.

Lower dimensions: hard segments or hard disks A number of theoretical studies have been interested in modeling one- or two-dimensional systems of hard particles, for their simplicity of treatment and for the light they shed on three-dimensional configurations. Hard segments in 1D correspond to infinite thick slabs in 3D, whereas hard disks in 2D correspond to hard infinite cylinders. The One-dimensional case can be solved exactly by direct calculus of the partition function [205] and readily gives the exact hard slab packing factor $W^{1D} = (1-H)^2$.

Equivalent numerical results were obtained in pioneering 1D simulations of blood scattering by Routh et al. [91, 170, 171] whose boundary artefacts were definitely resolved in [133]. They gave results comparable to the 1D packing factor, that yields the modal hematocrit dependence of the 1D backscattering (reflection) coefficient.
No exact determination of the packing factor for 2D hard disks exists [15]. The scale particle theory [99] (SPT) gives an approximate 2D equation of state and hard disk packing factor:

$$W_{SPT}^{2D} = \frac{(1-H)^3}{1+H}. \tag{2.55}$$

By taking the more accurate Henderson (He) equation of state [15], a slightly modified expression of the 2D packing factor can also be found:

$$W_{He}^{2D} = \frac{(1-H)^3}{1+H+0.375H^2-0.125H^3} \tag{2.56}$$

$$= W_{SPT}^{2D}\left(1-0.375H^2+\ldots\right). \tag{2.57}$$

By examining the expressions of the exact Tonks'packing factor W^{1D}, and approximate W_{SPT}^{2D}, W_{PYC} in dimensions $d = 1, 2$ and 3, Bascom and Cobbold [17] have remarked that they have a common form as a function of d:

$$W_{Ba} = \frac{(1-H)^{d+1}}{(1+(d-1)H)^{d-1}}. \tag{2.58}$$

They propose to generalize this empirical formula to real values of d (instead of only integer values), and interpret d as a particle fractal symmetry dimension. Recalling that the cases $d = 2$ and $d = 3$ were already approximations of the real packing factor, one can however question the validity of this empirical formula. Moreover, it seems that d can only be a fitting parameter as the physical determinants of the interactions

(temperature, amplitude of the potentials...) cannot easily be related to its value.

Mixtures of convex non-spherical particles To take into consideration the real shape of non-spherical particles on the packing factor, a generalization of the scale particle theory in 3D [15] conveys the packing factor of an isotropic distribution of hard convex particles. After averaging over all directions, one obtains a mean packing factor as a function of the hematocrit and of the Minkowski functionals of the constitutive convex particles. The following formula, firstly mentioned by [132, 213] in the context of scattering, generalizes the PY packing factor of hard spheres to hard convex particles:

$$W_\xi = \frac{(1-H)^4}{(1+(2+\xi)H)^2}, \tag{2.59}$$

where the non-sphericity index $\xi = \frac{\bar{R}\mathcal{S}}{\mathcal{V}} - 3$ vanishes when the convex particle is spherical. In this expression, $\bar{R}$ is the mean radius of curvature, $\mathcal{S}$ is the surface and $\mathcal{V}$ is the volume of the particle. This formula is consistent with the PY packing factor when the particle is spherical. Considering a red blood cell as a cylinder of height $h_0 = 2.2$ μm and radius $R = 3.9$ μm gives $\xi = 2.4$. One observes a diminution of the packing factor, that can reach 0.14 in comparison for $\xi = 0$.

Twersky proposed another generalization of this formula [27, 214] to include the effect of polydispersity in the size of the scatterers. Supposing that the size R of the particles is a random variable obeying the Schulz statistical distribution (a two parameter pdf that includes the Poisson distribution) and introducing the parameter d_S as the square of the variation coefficient $d_S = (E[R^2] - E[R]^2)/E[R]^2$, he derived the packing factor as a function of (H, ξ, d_S):

$$W = \frac{(1-H)^4}{(1+(2+\xi)H)^2}\left((1-H)^2 + (1-H)H\frac{(3+\xi)d_S}{1+5d_S} + H^2\frac{(3+\xi)^2 d_S}{1+4d_S}\right). \tag{2.60}$$

It must be emphasized that this polydisperse packing factor does not take into account the effect of polydispersity on the backscattering cross-section. The parameter d_S should therefore be small, in particular because the cross-section is very sensitive to size changes as it scales at the square volume of the scatterers. This drawback leads us to investigate other physical approaches in the modeling of the packing factor, to directly take into account the attraction between the particles, rather than the indirect effect of aggregation on the polydispersity of the formed aggregates.

Packing factor and attractive interactions

In whole blood under stasis, RBCs form clusters because of short range attractive forces that will be further detailed in section (2.8). The description of the pair potential $V_2(\vec{h})$ must be improved to portray this clustering tendency. Attraction can be modeled by a negative potential well that arises at contact between the supposed spherical particles (of radius a). For isotropic interactions, the energy profile of attracting hard spheres is:

$$V_2(\vec{h}) = \begin{cases} +\infty & \text{if } |\vec{h}| < 2a \\ -\bar{\epsilon}\phi_0\left(\frac{|\vec{h}|-2a}{2a}\right) & \text{otherwise,} \end{cases} \tag{2.61}$$

where $\bar{\epsilon}$ scales as the depth of the attraction well and is representative of the adhesion strength, and $\phi_0(u)$ is the normalized shape of the potential well, chosen such that $\int_0^{+\infty}(1+u)^2\phi_0(u)\,du = 1$. Three typical energy profiles are given in table 2.VI and Fig. (2.6).

The packing factor (and more generally the equation of state) of such systems has been investigated as they are commonly used as models of colloid suspensions, metal liquids, or weakly attractive molecule gas.

The simple sticky hard sphere model [23] that considers adhesion at close contact between spheres ($\lambda_0 \to 0$), is characterized by the stickyness τ (τ^{-1} increases with

Model type	Range parameter	$\phi_0(u)$
Square well potential [1, 15]	λ_0	$\frac{3}{(1+\lambda_0)^3-1}\mathbb{I}_{[0<u<\lambda_0]}$
Baxter sticky spheres [23, 166]	stickyness τ: $\lambda_0 \rightarrow 0$, $\bar{\epsilon}/k_BT = \frac{(1+\lambda_0)^3-1}{3}\ln\left(\frac{1+\lambda_0}{12\lambda_0\tau}\right)$	ibid.
Yukawa attractive tail [98, 100]	$(2\kappa_D a)^{-1}$	$\frac{(2\kappa_D a)^2 e^{-2\kappa_D a u}}{(1+2\kappa_D a)(1+u)}$

TAB. 2.VI – Different models of attractive well potentials. Each model is characterized by a normalized adhesive energy $\bar{\epsilon}/k_BT$ and by a reduced spatial range (λ_0 for the square well potential, 0 for the Baxter model (contact adhesiveness), and $(2\kappa_B a)^{-1}$ for the Yukawa attractive tail).

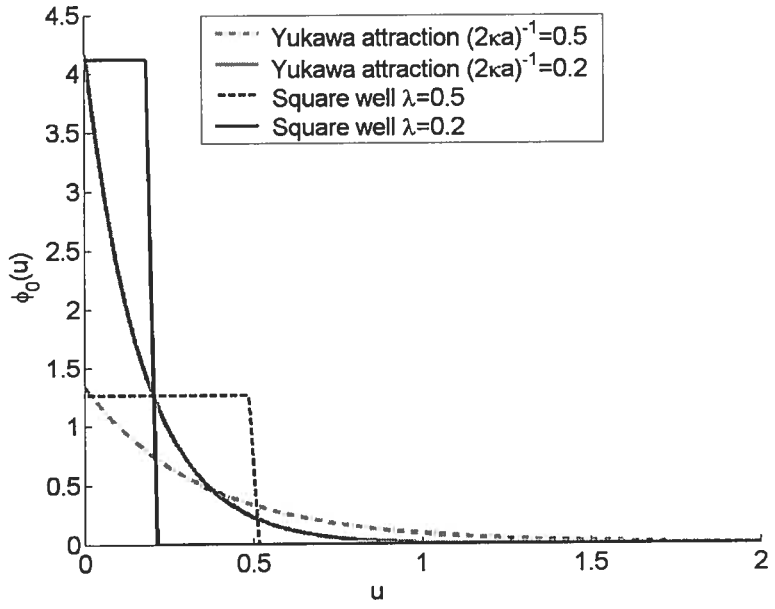

FIG. 2.6 – Normalized shape of the well potential as determined by $\phi_0(u)$.

$\bar{\epsilon}/k_BT$) and has interestingly an analytical packing factor [166] in the Percus-Yevick approximation:

$$W = \frac{(1-H)^4}{\left(1+2H-\Lambda(H,\bar{\epsilon}/k_BT)H(1-H)\right)^2}, \tag{2.62}$$

where $\Lambda(H, \bar{\epsilon}/k_BT)$ is the lower root of the polynomial:

$$\frac{H}{12}\Lambda^2 - \left(\frac{H}{1-H} + \tau\right)\Lambda + \frac{1+H/2}{(1-H)^2} = 0. \tag{2.63}$$

The case $\tau^{-1} = 0$ is consistent with the PY hard sphere packing factor ($\bar{\epsilon} = 0$, $\Lambda = 0$). For an adhesion spatial range that is non negligible, the Baxter sticky sphere model is no longer valid, and the square well model or the Yukawa attractive potential can be representative of attractive particle interactions. Different closure relations have been used to find the dependence $W(H, \bar{\epsilon}/k_BT, \lambda_0)$, where $\lambda_0 \sim 1/2\kappa_D a$ is a non-vanishing spatial range parameter. The analytical solution of the PY packing factor of the square well fluid can be found in [1] whereas [98, 100] give the exact results of the mean spherical approximation (a closure relation[6]) for the Yukawa attractive model.

More simply, for any shape of attraction well $\phi_0(u)$, the Van der Waals equation of state describes the thermodynamics of a low density, weakly attractive fluid ($H \ll 1$, $\bar{\epsilon}/k_BT \ll 1$):

$$(p + N^2 a^{VdW}/V^2)(V - Nb^{VdW}) = Nk_BT, \tag{2.64}$$

where a^{VdW} and b^{VdW} are corrections to the perfect gas ($a^{VdW} = 0$, $b^{VdW} = 0$) equation of state, that are related to the pair-potential:

$$a^{VdW} = -1/2 \int_{|\vec{h}|>2a} V_2(\vec{h})\, d^3h = 12\mathcal{V}\bar{\epsilon}, \tag{2.65}$$

$$b^{VdW} = 4\mathcal{V}. \tag{2.66}$$

Applying the compressibility equation yields a first order approximation to the pa-

[6]The mean spherical approximation assumes $g(\vec{h}) = 0$ for $|\vec{h}| < 2a$ and $c(\vec{h}) = -V_2(\vec{h})/k_BT$ for $|\vec{h}| > 2a$.

cking factor, that fails to predict high order virial coefficients, but is valid for any shape $\phi_0(u)$ of energy profile:

$$W = \left(\frac{1}{(1-4H)^2} - 24H\frac{\bar{\epsilon}}{k_BT}\right)^{-1} \quad (2.67)$$

$$= 1 + (-8 + 24\bar{\epsilon}/k_BT)H + (16 - 192\bar{\epsilon}/k_BT)H^2 + \ldots \quad (2.68)$$

This expression shows that the packing factor at low hematocrit increases with $\bar{\epsilon}/k_BT$, the hard-sphere system corresponding to the case $\bar{\epsilon} = 0$.

Results obtained by the thermodynamic approach

Hematocrit dependence (no aggregation) The PY hard sphere packing factor performs well to describe backscattering by flowing (human, porcine) RBCs in saline suspensions or for bovine whole blood, at various hematocrits and low frequencies, as shown in [142, 188, 232] and in Fig. (2.7). The experimental peak positions of the hematocrit dependence of the backscattering coefficient are consistent (or slightly higher) with the theoretical PY peak (at $H = 0.13$) of the curve $H \rightarrow HW_{PYC}$ obtained using Eq. (2.52). The predicted amplitude of the backscattering coefficient is somewhat underestimated. This can be attributed to various factors: the effect of turbulence scattering [188], the non-sphericity of the particles associated to a certain particle orientation in flow ($d \sim 2.5 < 3$ when fitting Eq. 2.58 with data on porcine RBC suspensions in [142]), the deformability of the non-convex RBCs ($\xi \sim -1.5 < 0$ when fitting Eq. (2.59) originally defined for convex shapes characterized by $\xi > 0$), or a residual aggregative behavior of the suspension (when fitting Eq. (2.62), $\tau \sim 0.7$). It can be observed that the hematocrit dependence of the packing factor does not uniquely define the underlying pair potential characterizing the point process Ω. The fitting of the experimental curves $H \rightarrow HW$ can give values to parameters of a

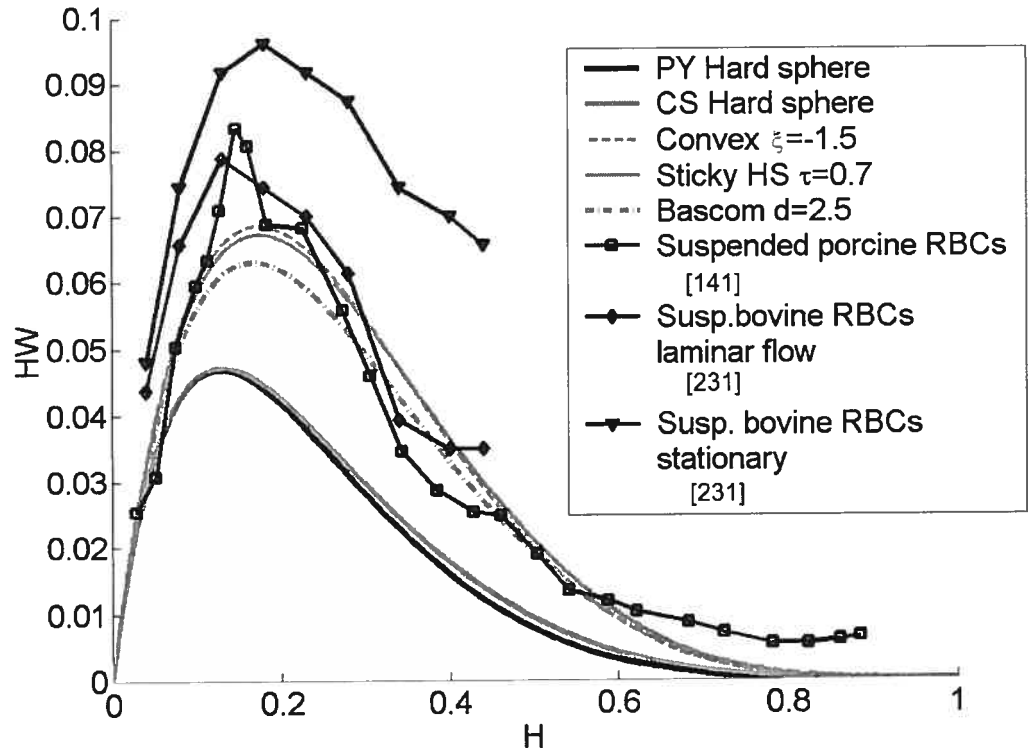

FIG. 2.7 – hematocrit dependence of HW ($\chi(\vec{k}) = WH\frac{\sigma_b(\vec{k})}{\nu}$ in the packing factor approximation). The notations can be found in paragraph (2.7.2).

pre-specified random model Ω, but they will not necessarily have the same physical meaning as defined a priori. Further investigations are therefore needed to specify the validity of the models, and the notion of structure factor could help to better identify the particle physical interactions.

Aggregation dependence The physical description of the adhesive interactions presented in paragraph (2.7.2) enables us to predict the effect of the aggregation level on the packing factor, independently of the hematocrit or the shape of the formed aggregates.

The effect of the stickyness on the Baxter packing factor is shown in figures (2.8) and (2.9). An increase of the adhesion strength (τ^{-1}, the case $\tau^{-1} = 0$ being the hard

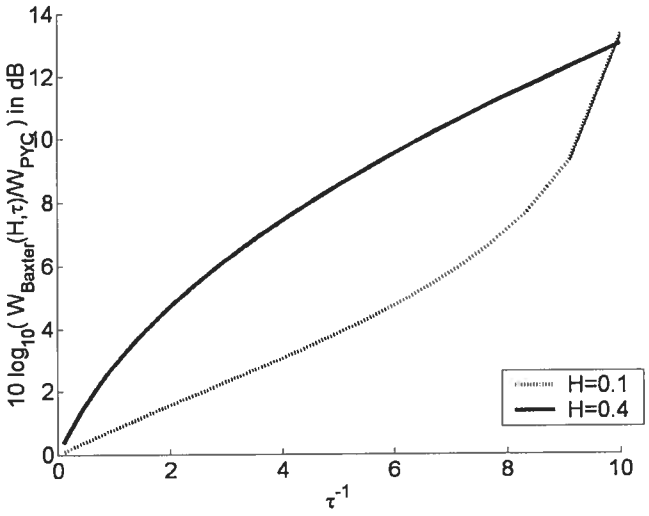

FIG. 2.8 – Increase (in dB, computed by Eq. (2.62)) of the packing factor W with respect to the hard sphere PY approximation as a function of the stickyness factor τ in the Baxter sticky sphere model.

sphere model) shifts the peak hematocrit toward a greater value and increases the packing factor. This effect of the aggregation level is comparable to measurements reported in several studies [126, 190, 225] where the aggregation magnitude varied by changing the radial position (and therefore the shear rate) of the backcatter (or Doppler power) measurement in a Poiseuille flow. In [32], the backscattering coefficient at 6 MHz of RBCs suspended in saline and varying concentrations of dextran 70 peaked at $\sim 0.3 > 0.13$, the peak being higher when the dextran concentration increased from 20 to 40 g.L^{-1}. Experimental measurements in Poiseuille flow of the relation $H \rightarrow \chi(\vec{k})$ are however not always consistent with this point of view [138], the effect of the shear rate heterogeneity being important.

2.7.3 Point process statistics and packing factor

The assumption that the random point process Ω obeys the equilibrium Boltzmann law (subsection 2.7.2) gives several methods inherited from statistical physics for

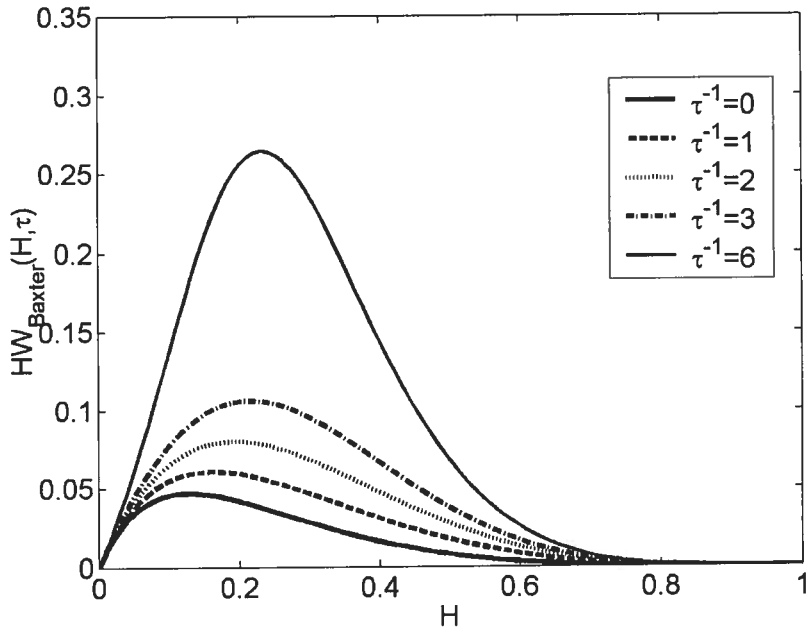

FIG. 2.9 – Influence of the stickyness factor τ on the hematocrit (H) dependence of the sticky sphere packing factor $W_{\text{Baxter}}(H, \tau)$.

predicting the evolution of the packing factor as a function of the particle interactions. Another approach that was called "particle approach" must also be presented. It consists of relating the packing factor W to the descriptive statistical moments of the point process Ω without making the physical assumption of a Gibbs-Markov distribution. In this subsection, the packing factor is firstly related to the statistics of the number of points falling into a given "counting box" , and the results obtained by the particle approach are reviewed.

Packing factor and variance of the number density

When RBCs form clusters, the statistical properties of Ω drastically change: while the hematocrit H remains constant, fluctuations in the microscopic density tend to increase, as group behavior is observed. Variance in the local density could then be proposed as a main determinant of the value of the packing factor. The packing factor thus provides a quantification of the clustering behavior and orderliness of a random point process. In the case of clustering $W > 1$, if $W = 1$ the point process does not form spatial structures, whereas $W < 1$ shows that a certain degree of repulsion and orderliness exists — hardcore interaction e.g. as shown in subsection (2.7.2).

Let $\mathcal{A}$ be a compact set of volume $\mathcal{V}(\mathcal{A})$, which will be used as a "counting box" . One already defined $N_{\mathcal{A}} = \int_{\mathcal{A}} N_{\Omega}(\vec{r})\, d^3r$ as the random number of points from Ω falling into $\mathcal{A}$. The number $N_{\mathcal{A}}$ has a discrete distribution, and one wants to relate the packing factor to descriptive statistics of $N_{\mathcal{A}}$ (as originally proposed by [212] or [139]).

Its mean is $E[N_{\mathcal{A}}] = m\mathcal{V}(\mathcal{A})$ by definition of the number density m. The variance $\mathrm{Var}[N_{\mathcal{A}}]$ can also be expressed (after some algebra) as a function of the pair-correlation function $g(\vec{h})$, of the shape of the counting box $\mathcal{A}$ and of the packing factor W:

$$\frac{\mathrm{Var}[N_{\mathcal{A}}]}{E[N_{\mathcal{A}}]} = W + m \int_{|\vec{h}|<l_{cor}} \left(\frac{\mathcal{V}(\mathcal{A} \cap \mathcal{A}_{-\vec{h}})}{\mathcal{V}(\mathcal{A})} - 1 \right) \left(g(\vec{h}) - 1 \right) d^3h. \tag{2.69}$$

The complete derivation of this formula can be found in (2.12.3). If the typical dimension of $\mathcal{A}$ (e.g. $\mathrm{diam}(\mathcal{A}) = \max\{|x-y| \ / x, y \in \mathcal{A}\}$) is far greater than the correlation length, then $|h| < l_{cor} \Rightarrow \mathcal{V}(\mathcal{A} \cap \mathcal{A}_{-\vec{h}}) \approx \mathcal{V}(\mathcal{A})$. In this case,

$$\lim_{l_{cor}/\mathrm{diam}(\mathcal{A})\to 0} \left(\frac{\mathrm{Var}[N_{\mathcal{A}}]}{E[N_{\mathcal{A}}]} \right) = W. \tag{2.70}$$

Statistical estimation of the packing factor

The formula (2.70) enables us to derive (biased) statistical estimators of the packing factor W if only one realization Ω is available, e.g. when performing computer simulations of the point process, or when observing pictures of a random point collection, by counting the number of points that fall into independent replicas of the box A.

This approach for determining the packing factor has been described by many authors [8, 123, 140, 141] under the name of particle or voxel approach because it fundamentaly relies on the statistics of the discrete number of scatterers falling into quadrats or big voxels.

Suppose that the total scattering volume V can be divided in M voxels $\{A_1, \ldots, A_M\}$, that contain $\{N_1, \ldots, N_M\}$ particles. If $\{N_1, \ldots, N_M\}$ can be considered as independent samples of the random variable $N_{\mathcal{A}}$, then

$$\hat{W} = \frac{MN}{(M-1)} \sum_{i=1}^{M} \left(\frac{N_i}{N} - \frac{1}{M} \right)^2, \tag{2.71}$$

is an estimator of the packing factor (where $N = \sum_i^M N_i$ is the total number of particles).

Its accuracy can be examined in the special case where Ω is a homogeneous Poisson point process. In this case and considering a great number N of particles, $M\hat{W}$ follows a χ^2 distribution with p degrees of freedom. It is already known that $W = 1$ when Ω is Poisson distributed. The estimator $\hat{W}$ is therefore unbiased as $E[\hat{W}] = 1$. However, as the variance $\mathrm{Var}(\hat{W}) \sim 2/M$ slowly decreases with the number of boxes, a precision

of 0.1 for the 95% confidence interval of W around 1 requires $M \sim 200$ voxels.
The choice of M is quite a delicate bias-variance tradeoff, especially if Ω forms structured patterns. If the voxels A_i appear too small (i.e the assumption $l_{cor} \ll \text{diam}(\mathcal{A}) \sim \text{diam}(V)M^{-1/3}$ is not met), then the quantities $\text{Var}[N_A]/E[N_A]$, or $E[\hat{W}]$, are not directly related to the packing factor W, nor to the structure factor $S(\vec{q})$. On the other hand, if the number M of voxels is too small, the variance of $\hat{W}$ could be too high to adequatly measure W.

Simulation results of the particle approach

Most of the studies using the particle approach were dedicated to the understanding of the hematocrit dependence of the packing factor of hard sphere systems, and roughly confirmed the adequacy of the Percus-Yevick approximation [81, 140]. Lim and Cobbold [124] also used this particle method to assess the packing factor of clustering random processes. Although the study related the size of the counting box $\mathcal{A}$ to a 5 MHz wavelength, it must be emphasized that the packing factor W should not be related to any wavelength. The packing factor only represents a pure geometric and statistical index, characterizing particle positioning, that can be estimated using big voxels, independently on any acoustical notion.
To extend the good results obtained by the particle approach in non aggregating conditions, Lim and Cobbold [124] have simulated several random organizations of non-overlapping RBCs in square (parallelepipedic) windows of dimension $300 \times 300(\times 30)$ μm, divided in 100 pixels (voxels) respectively in 2D and 3D. Isotropic monodisperse and polydisperse clusters of sticking non-overlapping disks (spheres) were sequentially dispersed in the sampling window, their number being associated to the target hematocrit. The effect of the compacity (linear vs. clump morphology) of monodisperse clusters was also investigated. The packing factor is shown to be more sensitive to the statistics of the number of cells per cluster (maximum or va-

riance of the random number N_c of RBCs per cluster) than to cluster morphology. Moreover, the peak position of the curve $H \rightarrow HW$ is marginally affected by these statistics. This minor dependence of the packing factor on the geometry of the aggregates was also demonstrated in other geometric models. In the analytical scheme of the Neyman-Scott point process [182], that was suggested as a clustering model for low density aggregating media [175], $W = E[N_c^2]/E[N_c]$. The Neyman-Scott packing factor is therefore independent on the morphology of the clusters.

2.7.4 Experimental failure of the packing factor approximation in conventional US imaging

Frequency dependence and packing factor approximation

The packing factor approximation assumes that $2kl_{cor} \ll 1$ to state that the structure factor reduces to the packing factor. Observing that the Rayleigh conditions are also respected in this approximation ($ka < 2kl_{cor} \ll 1$), the backscattering coefficient can be written:

$$\chi(\vec{k}) = mW\sigma_b(\vec{k}) = \frac{1}{4\pi^2} HW\mathcal{V}k^4\langle\gamma_z\rangle^2 \propto k^4. \tag{2.72}$$

As the correlation length l_{cor} increases when RBCs aggregate, the frequency limit for which the packing factor approximation holds decreases. In parallel with the technological increase of the US frequencies improving imaging scanner resolution, the deviation to the packing factor approximation was observed by a number of groups studying flow-related variations of blood echogenicity. It manifests by a spectral slope β (the exponent of the power-law fitting $\chi(k) = \alpha_0 k^\beta$ on a given frequency range) that is smaller than 4, or by variations of the backscattering coefficient with the insonification angle (angle between the flow streamlines and the incident wavevector). These phenomena are clearly not compatible with eq. (2.72).

Yuan and Shang [232, 233] observed the decrease of β (4 to 3) in a Poiseuille flow of porcine blood, in the frequency range $3.5 - 12.5$ MHz while the mean shear rate was decreased from 22 to 2 s^{-1}. Van der Heiden et al. [216] measured $\beta = 1.3$ in the range $22 - 37$ MHz for a shear rate under 1 s^{-1}, investigating *in vivo* high frequency blood properties using intravascular probes. In a stationnary Couette shear flow of human blood, Foster et al. [84] also reported significant decrease of β down to 0.4 for a very low shear rate of 0.16 s^{-1} and frequencies $35 - 70$ MHz. Angular dependence (40°-80°) of the Doppler power backscattered by porcine whole blood, flowing in a vertical cylindrical flow, was described by Allard et al. [5]. Variations of the order of 5 dB for $H = 40\%$ were measured for mean shear rates ranging from 8.5 s^{-1} to 51 s^{-1} at 10 MHz.

These studies show that RBC aggregates in whole blood do not often satisfy the packing factor approximation, even at low acoustic frequencies. The frequency dependence of the structure factor should therefore be reconsidered in the physiological context of RBC aggregation in low shear flow. This requires a better understanding of the aggregation mechanisms to understand both the spatial pattern induced by clustering and the frequency dependence of the structure factor. Using the whole dependence $\vec{q} \rightarrow S(\vec{q})$ rather than a single value $W = S(0)$ would moreover help to better characterize the interactions between scatterers, as it was observed that the packing factor W or even the hematocrit dependence $H \rightarrow HW$ do not uniquely define the statistical parameters of the random process Ω.

2.8 Physics of red blood cell aggregation

2.8.1 Need to consider the interparticle forces

To model the influence of aggregative conditions on the blood structure factor, a realistic description of the intercellular correlations needs to be found. In a dense medium

as whole blood ($H \approx 40\%$), RBC clusters are not independently positioned, and are even difficult to delineate as the mean nearest-neighbor distance represents a small fraction of the RBC diameter. In addition to pure entropic effect of the steric forces (previously described as hardcore systems), the balance of attractive and repulsive forces between RBCs and of flow-mediated hydrodynamic forces is responsible for the intricate morphology of the RBC network. RBC reversible clustering is mediated by plasmatic proteins, but the underlying basic adhesion mechanisms are still partially understood. Disaggregating hemodynamic stresses are flow-related, and increase with the shear rate. In this section, one portrays these different antagonist forces acting on erythrocytes.

2.8.2 Repulsive forces

Hardcore repulsion

RBCs contain a nearly incompressible hemoglobin Newtonian solution, and therefore cannot overlap. The first contribution to the intercellular repulsion therefore consists of the aforementioned steric forces: they prevent RBC surfaces and inner contents to tangle and lead to cellular collision when flowing. As a first approximation, and considering that erythrocytes are spherical and rigid, the steric interaction (of hardcore particles hc) is:

$$V_{hc}(\vec{h}) = \begin{cases} +\infty & \text{if } |h| < 2a \\ 0 & \text{otherwise.} \end{cases} \tag{2.73}$$

Electrical double layer

Other short range repulsive forces complete the volumic exclusion effect. The RBC glycocalyx, covered by sialic acid, has a negative surface charge density. A degree of repulsion exists between RBCs due to the resulting electrostatic interaction. Because

of the presence of numerous ions in the plasmatic solution, a thin electrical double layer forms at the erythrocyte surface. The electric potential at the surface is governed by the Poisson-Boltzmann equation [122]. The decay of the surfacic electrical potential has a characteristic length of the order of the Debye screening length (according to [145], $\kappa_D^{-1} \sim 0.8$ nm in normal plasmatic conditions). When double layers of two RBCs overlap, an electrical repulsive interaction (the Yukawa repulsive tail) arises because of the ionic redistribution in plasma, that is associated to a positive potential energy:

$$V_e(\vec{h}) = \mathbb{I}_{[2a<h]} \frac{16\pi^2 \sigma_0^2 a^2 \kappa_D^{-2}}{\epsilon_P h} \exp\left(\kappa_D(2a-h)\right). \tag{2.74}$$

In this first order expression (as $1/2\kappa_D a \ll 1$), the electric variables are σ_0, the negative surfacic charge of the RBC, and $\epsilon_P \sim 78\epsilon_0$, the plasma permittivity (where ϵ_0 is the electric constant). An approximate value of the Debye length is given by $1/\kappa_D^2 a^2 = k_B T/(4\pi n_c a^2 Z_c^2 e_+^2/\epsilon_P)$, where $n_c Z_c^2 e_+^2$ is the ionic force of the solvent, n_c and Z_c are the number density and the valence of the plasma counterions, e_+ being the elementary charge. The ionic Brownian motion and concentrations are the determinants of the range of the electrostatic force: the Debye length κ_D^{-1} decreases with the ionic force, and increases with the random motion of the plasmatic ions governed by the temperature.

2.8.3 Adhesive forces

Van der Waals interactions

The Deryaguin-Landau-Verwer-Overbeek (DLVO) description of interparticular colloid interactions is the classical approach [70, 220] that relates colloid stability (non-flocculation) to the balance between attractive Van der Waals forces and repulsive double layer interactions. However, in the context of biological media such as blood,

the low value of the Hamaker constant[7] $\mathcal{A}_h \sim 5 \times 10^{-22}$ J (whereas in classical aqueous solutions $\mathcal{A}_h \sim 1 \times 10^{-20}$ J) allows us to neglect Van der Waals attraction, as proposed in [199].

Depletion forces

There is still a debate about the nature of the non Van der Waals interactions that induce reversible RBC weak adhesion. An established fact is that aggregation forces are dependent on the plasmatic concentration of high molecular weight proteins such as fibrinogen, C-reactive or other inflammation-related proteins [26, 128, 227, 228]. The size of the polymeric chains seems to play a major role, as RBC aggregation can also be artificially caused in saline suspension by the addition of long molecules of dextran [32] or polyethylene glycol [146]. Two sorts of cell-protein interactions were adversely postulated to create cell-cell adhesion, namely the depletion forces [22] and the bridging forces [52, 107].

Depletion is one of the classical mechanisms of aggregation-floculation processes introduced in colloidal fluid theory. It lays on the fact that long polymer chains are non homogeneously dispersed in the volume: they are depleted in the neighborhood of the colloidal particles. Because of steric (or other repulsive) colloid-polymer forces, the long molecules cannot freely fill intercellular gaps that are smaller than their radius of gyration. This results in polymer concentration gradients that create an intercellular osmotic depression and induce an attractive force between RBCs.

Several theoretical treatments of the depletion potential have been proposed, depending on the type of polymer and on the complexity of the polymer-polymer and colloid-polymer interactions. The simple Asakura-Oosawa (AO) [11, 122] model only considers non-specific steric interactions between spherical colloids and polymer chains with a radius of gyration $R_g = 2ra$. Interchain interactions are neglected be-

[7] Between two close colloidal spheres, the Van der Waals energy potential is roughly $V_{vdw}(\vec{h}) = \mathcal{A}_h \frac{2a}{24(2a-h)}$.

cause of the weak polymer concentration. Depletion potential energy between two colloidal particles can be analytically evaluated by computing the Gibbs free energy of the system composed of two spheres and by the surrounding polymers:

$$V_{AO}(h) = -\mathbb{I}_{[2a<h<2(1+r)a]}\Pi\mathcal{V}(1+r)^3\left(1-\frac{3}{2}\frac{h}{2(1+r)a}+\frac{1}{2}\left(\frac{h}{2(1+r)a}\right)^3\right) \quad (2.75)$$

The osmotic pressure Π, and the intensity of the depletion force, depends on the number density n_P of the polymeric chains. A first order virial expansion yields:

$$\Pi = n_P k_B T, \quad (2.76)$$

showing that the polymer concentration is a major determinant of the depletion-mediated adhesion.

Bridging interaction

The second proposed aggregation mechanism is the bridging theory. This approach assumes that RBC adhesion is induced by the adsorption of polymeric chains (ligands) on specific or non-specific receptors at their surface, creating bonds that resist more or less to the hydrodynamic stress. Kinetic rather than thermodynamic approaches have been used to describe the formation and disruption of receptor-ligand complexes in shear flow. Consider two close RBCs flowing in plasma, their binding (or not) can be described by the random number $N_b(t)$ of linking bonds. The dynamics of $N_b(t)$ is related to the number density of ligand/receptors, to the (shear dependent) stress exerted on the bonds, to their length, to the specific mechanical modulus (elasticity...) of the bond, and to the temperature.

A stochastic description of the process is briefly summarized here as it is detailed elsewhere in review articles [237, 238]. The formation of a single complex (C) from

a given surfacic receptor (R) and ligand (L) can be described by the forward and reverse kinetic rates k_f and k_r:

$$R + L \underset{k_r}{\overset{k_f}{\rightleftharpoons}} C \tag{2.77}$$

The formation time required for a free given receptor (R) to create a complex with a ligand is often modeled by an exponential random variable with mean k_f^{-1}. The survival time of a complex (C) before disrupting in (R)+(L) is also modeled by a random exponential variable with mean k_r^{-1}. The formation time depends on the collision frequency (proportional to the shear rate $\dot{\gamma}$ by a Smoluchovski-like expression [223], to the hematocrit, to RBC dimensions, and to the ligand concentration $[L]$) and on the efficiency of the collision (related to the contact time $\propto \dot{\gamma}^{-1}$). An external shear force $f_e \propto \eta_{\text{plasma}} a^2 \dot{\gamma}$, shared between $N_b(t)$ bounds, increases the reverse rate (classical expressions for k_f vs. f_e/N_b are the Bell model [25] or the Dembo model [67]). The differential system satisfied by the probability density function $p_n(t) = P[N_b(t) = n]$ for two cells can be solved when k_f and k_r are known. A pair or a group of linked RBCs ($N_b(t) \geq 1$) will then have different mechanical behaviors than if they were independent ($N_b(t) = 0$).

2.8.4 Hydrodynamic forces

Red cell motion in plasma is governed by short range cell-cell interactions and by hydrodynamic shear stress exerted by flowing plasma on its surface. Hydrodynamic interactions on one cell can be perturbed by the presence of neighboring cells and are more or less pronounced depending on the neighbor distance and on their physical adhesion.

Hydrodynamic force on an isolated erythrocyte in shear flow

Goldsmith and Marlow [88] showed that the nature of the motion of an isolated RBC in a stationary shear flow (described by the linear velocity field $\vec{V}(\vec{r}) = \dot{\gamma} z \vec{e}_y$) depends on the value of shear intensity. The Reynolds particle number $\mathcal{R}_p = \rho_{RBC} \dot{\gamma} a^2 / \eta_{\text{plasma}}$ is often very low. The Péclet number $\mathcal{P}_e = \frac{\eta_{\text{plasma}} \dot{\gamma} a^3}{k_B T}$ (ratio of viscous to Brownian forces) has values that are more usable and physically more pertinent.

When $\eta_{\text{plasma}} \dot{\gamma} \ll 0.1$ Pa ($\mathcal{R}_p \sim 6 \times 10^{-4}$, $\mathcal{P}_e \sim 510$), a single RBC behaves as a rigid oblate spheroid. Its translational motion follows the flow velocity and its rotation is governed by the Jeffery equation [108]: the RBC axis rotates with a maximal angular velocity when aligned with the flow velocity and a minimal velocity when perpendicular (Fig. 2.10). The spin velocity has not been documented. The period T_j of the axis motion on its orbit decreases with the shear rate as $\dot{\gamma} T_j = 2\pi(r_e + r_e^{-1})$, where $r_e \approx 0.38$ is an equivalent hydraulic axis ratio close to the geometric ratio h_0/R of the RBC.

When the shear stress $\eta_{\text{plasma}} \dot{\gamma} \sim 0.1 - 0.4$ Pa ($6 \times 10^{-4} \leq \mathcal{R}_p \leq 24 \times 10^{-4}$, $510 \leq \mathcal{P}_e \leq 2040$), the RBC tends to occupy more time aligned with the flow field than predicted by the Jeffery model. It behaves in a manner analog to a fluid drop. The kinetic energy of the RBC that induced rigid rotation at a low shear rate is in competition with the strain elastic energy stored in the membrane, the tank-treading motion of the membrane and by the inner viscous dissipation hemoglobin solution inside the erythrocyte. At higher shear rates, the RBC ceases to rotate and travels in flow with a constant orientation, the motion being governed by the interplay between viscous friction and red cell deformability properties.

Coupling hydrodynamic force of two red blood cells in shear flow

Consider a pair of rigid buyoant spheres in a shear flow, with translational velocities $\vec{v}_1$ and $\vec{v}_2$, rotation vectors $\vec{\omega}_1$ and $\vec{\omega}_2$, located in $\vec{x}_1 = z\vec{e}_z$ and $\vec{x}_2 = \vec{x}_1 + \vec{h}$. The presence of

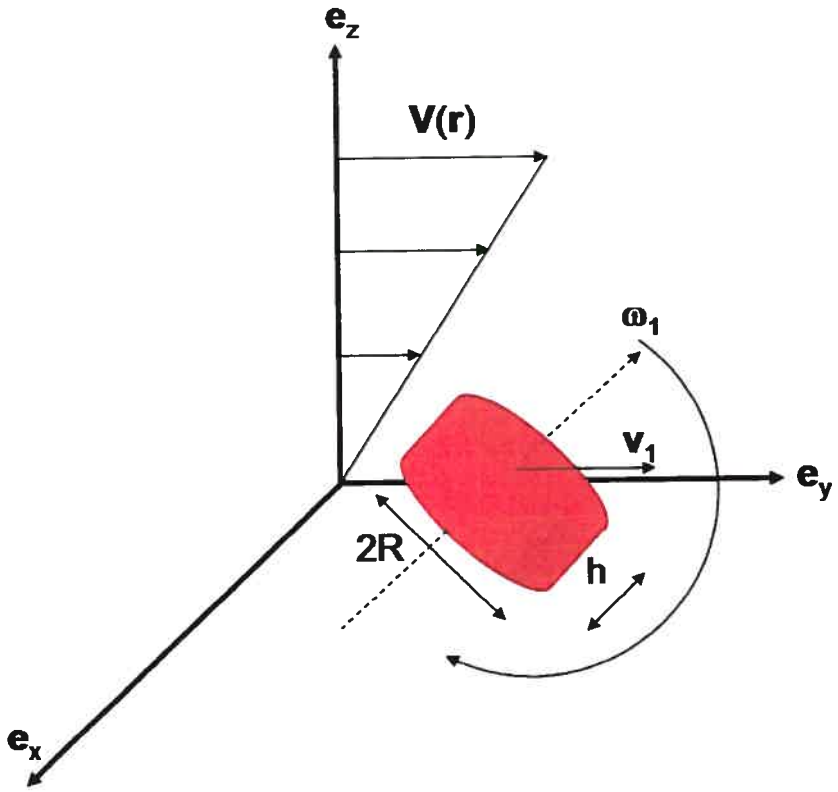

FIG. 2.10 – Rotation of a single RBC in a shear flow.

a second particle modifies the fluid velocity field around particle (1) and consequently the hydrodynamic torque and force experienced by the first sphere. The hydrodynamic force $\vec{F}_h$ exerted on (1) can be expressed as a function of a dimensionless vector interaction coefficient $\vec{C}_h$ defined as:

$$\vec{F}_h = \eta_{\text{plasma}}\dot{\gamma}a^2\vec{C}_h(\mathcal{R}_p, \vec{h}/a, \frac{\vec{v}_1 - \vec{V}(\vec{x}_1)}{a\dot{\gamma}}, \vec{\omega}_1/\dot{\gamma} - \vec{e}_x, \frac{\vec{v}_2 - \vec{V}(\vec{x}_2)}{a\dot{\gamma}}, \vec{\omega}_2/\dot{\gamma} - \vec{e}_x). \quad (2.78)$$

As the Reynolds number $\mathcal{R}_p$ is very small, the Navier-Stokes equation that governs the plasma velocity field transforms to its Stokes form. This implies linearity between

forces, torques and velocities. This linearity and some symmetry concepts ($\vec{\omega}_1 = \vec{\omega}_2$ and $\vec{v}_1 - \vec{V}(\vec{x}_1) = -(\vec{v}_2 - \vec{V}(\vec{x}_2))$ permits to write the relation (the so-called grand resistance tensor) between the interaction coefficient and the velocity-rotation vectors [10, 20]:

$$\vec{C}_h = -(a^*\vec{e}_x \otimes \vec{e}_x + a^*\vec{e}_y \otimes \vec{e}_y + b^*\vec{e}_z \otimes \vec{e}_z)\frac{\vec{v}_1 - \vec{V}(\vec{x}_1)}{2a\dot{\gamma}} - c^*\vec{e}_z \times (\vec{\omega}_1/\dot{\gamma} - \vec{e}_x), \quad (2.79)$$

where a^*, b^* and c^* are non-dimensional tabulated functions[8] of $h/2a$ as given in [10, 20]. The same linear analysis can be used to derive the particle torques as a function of the velocity-rotation vector. It can be noticed that when the two spheres are far apart ($h/2a \gg 1$), the grand resistance tensor reduces to the Stokes' law that governs drag and lift forces of an isolated rigid sphere in a stationary shear flow.

When studying the relative trajectories of two hard spheres in shear flow (in the referential of sphere (1)), two types of orbits can be distinguished depending on the initial conditions. Closed orbits are bounded trajectories: the interparticle distance never diverges and particles are "captured" in a narrow domain that they cannot leave. Open orbits refer to orbits for which the spheres interact only during a limited time and are carried away by the flow, which can however be sufficient for deviating the natural relative trajectory of the two spheres.

For two RBCs now, several differences naturally exist in comparison to the model of two hard spheres. Firstly, cell-cell short range colloid interactions (electrostatic, depletion/bridging or Van der Waals forces) add up to the hydrodynamic drag and lift forces, and critically modify the particle relative trajectories [74]. The collision (i.e. the approach of two RBCs that leads to a capture) is always due to long range ($\sim a$) shear forces, but the spatial extent of the capture basin and the collision efficiency are modulated by the intensity of the colloidal forces in comparison with

[8] $a^* \to 6\pi, b^* \to 6\pi$ and $c^* \to 0$ when $h/2a \to +\infty$

the typical hydrodynamic force $\sim \eta_{\text{plasma}}\dot{\gamma}a^2$. Secondly, the proper deformability of the RBCs, associated with the non-spherical shape could dramatically modify this classical colloid approach.

Hydrodynamics in concentrated media

We are now interested in assessing the hydrodynamic forces that a given RBC undergoes in whole dense blood when the bulk volume is submitted to a stationary shear flow. As the presence of one particle in a viscous flow causes hemodynamic perturbations that slowly decrease as $1/r$, a low density approximation that consists in summing pair hydrodynamic forces, as exposed in last paragraph, fails in the case of whole blood.

This observation shows that the rigorous treatment of the hydrodynamic forces and torques of N particles dispersed in a volume V requires a complex description of the velocity field of the viscous fluid flowing around the particles. Computer simulation seems to be the appropriate tool to predict the intricate behavior of suspensions under shear.

Three different approaches could be adopted to derive interparticular interactions and hence the microstructure (for more details, cf. section 2.9) :

- Molecular dynamics

  For each particle in the volume of interest, the direct colloidal forces are computed and the hydrodynamic force is estimated using either simplified expressions or by computing the resultant of the shear forces.

- Stokesian dynamics

  To avoid the cumbersome computation of the flow field around each particle, one can benefit from the aforementioned Stokes approximation. As the typical particle Reynolds number $\mathcal{R}_p$ and the inverse Péclet number $\mathcal{P}_e^{-1} = k_B T/\eta_{\text{plasma}}\dot{\gamma}a^3$ are small, the inertial and Brownian forces can be neglected. Linearity between velo-

city vectors and hydrodynamic forces can then be written. This leads to effective computational methods for determining the grand resistance tensor and the cell-cell interactions for N particles. This method generalizes the case of the sphere doublet in shear flow.

- Monte Carlo simulations

  Instead of using a dynamic approach to assess the statistical properties of the random point process Ω, Monte Carlo simulation techniques consist of using sampling random methods to generate many realizations $(\Omega_1, \ldots, \Omega_M)$. These samples are further used to build statistical estimators of the desired statistics as the structure factor $S(\vec{q})$ or the pair-correlation function $g(\vec{h})$. These techniques are classically used for particle systems under equilibrium (that satisfy Bolzmann pdf), but can also be generalized to non-equilibrium conditions (as fluids submitted to a shear rate).

2.8.5 Effect of membrane elasticity and discoidal shape

The elastic properties of the RBC membrane (strong area expansion modulus $K_m \sim 0.3-0.5$ Pa.m and low area shear modulus $\mu_m \sim 4-10\times10^{-6}$ Pa.m $\ll K_m$ for normal RBCs according to [118]) and the viscosity η_h of the hemoglobin RBC solution can have an influence on the adhesive strength, and on blood macroscopic biomechanical properties, especially when the hematocrit or when the Péclet number have big values. This is reflected in the high shear rate blood viscosity that reaches a limit $\eta_\infty/\eta_{\text{plasma}} \sim f(H, \eta_h/\eta_{\text{plasma}}, \mu_m a^2/k_B T)$ when $\mathcal{P}_e \to \infty$. The limit $\eta_\infty/\eta_{\text{plasma}}$ is often used as a hemorheologic index of RBC deformability [51].

Thermodynamic and mechanical arguments show that the adhesion efficiency increases with the membrane deformability. Chien and Skalak [53, 195] and more recently Derganc et al. [68] modeled the adhesion process by a surfacic sticking energy $\gamma \sim 10^{-7}$ J.m^{-2} (in normal conditions [194]). This corresponds to an assumption

that is more valid when considering the bridging adsorption theory. This energy was postulated to be controlled by the bridging macromolecule concentrations and by specific affinities between the RBC surface and the ligand. Considering that the discoidal RBC can deform, the free energy of a pair of RBCs includes the sum of the elastic strain energy and of the negative adhesion energy. When the mechanic moduli are small enough, the RBCs can rotate and deform to increase the contact surface area and to find the optimal equilibrium shapes minimizing Gibbs total free energy.

The same kind of thermodynamic argument holds in the depletion-driven adhesion scheme. The free energy of a system of two deformable RBCs surrounded by long polymers that sterically interact with RBCs includes the sum of the elastic strain energy and of the free Gibbs energy of the polymer-colloids system that scales as $n_P k_B T \mathcal{V}_{\text{exclusion}}$, where $\mathcal{V}_{\text{exclusion}}$ is the macromolecule depleted zone. To reach an equilibrium conformation that balances the elastic strain energy and the protein depleted volume, the RBC membrane will tend to deform.

In summary, the RBC membrane, which essentially has a shear deformability, has a role on the biomechanical fluid property of blood at the macroscopic scale, but also at the microscopic scale as it can increase the efficient adhesion strength (Fig. 2.11).

2.8.6 Comparison of the interactions and summary

A summary of the governing forces is given in table (2.8.6). One deduces from the relative amplitude of the interactions that the main non-dimensional parameters that govern RBC microstructure in shear flow are the hematocrit, the reduced macromolecule concentration $n_p a^3$ and radius of gyration r, the balance of surfacic and plasmatic charge $\sigma_0^2 a / n_c Z_c^2 e_+^2$, the reduced Debye length $(2\kappa_D a)^{-1}$, the Péclet number $\mathcal{P}_e = \frac{\eta_{\text{plasma}} \dot{\gamma} a^3}{k_B T}$ and the membrane deformability $k_B T / \mu_m a^2$.

Interaction	Typical energy	Typical range
Thermal motion[a]	$k_BT = 4.3 \times 10^{-21}$ J	-
Typical fibrinogen depletion[b]	$n_P a^3 k_B T \sim 200\ k_B T$	$ra \sim 22$ nm
Typical bridging contact energy[c]	$\gamma a^2 \sim 250\ k_B T$	-
Electrostatic double layer[d]	$\sigma_0^2 a \kappa_D^{-2}/\epsilon_P \sim 7 \times 10^5\ k_B T$	$\kappa_D^{-1} \sim 0.8$ nm
Hydrodynamic[e]	$\eta_{\text{plasma}} \dot{\gamma} a^3 \sim 200\ k_B T$	$a \sim 2.8\ \mu$m
Membrane area expansion[f]	$K_m a^2 \sim 10^9\ k_B T$	-
Shear membrane deformation[g]	$\mu_m a^2 \sim 1000\ k_B T$	-
Intracellular tank treading viscous dissipation[h]	$\eta_{RBC} \dot{\gamma} a^3 \sim 1000\ k_B T$	-
Van der Waals	$\mathcal{A}_h \sim 2\ k_B T$	$a \sim 2.8\ \mu$m

TAB. 2.VII – Comparison of the amplitude of the interactions acting on red blood cells in shear flow

[a] at a physiological temperature $T = 310$K.

[b] calculated for fibrinogen, with normal concentration 200 mg/dL, molecular weight 340 kDa and radius of gyration $2ra \sim 45$ nm, as given by [37].

[c] as given by [194].

[d] the acid sialic charge density $\sigma_0 = 0.036$ C.m^{-2} and typical Debye length $\kappa_D^{-1} = 0.76$ nm are taken from [145].

[e] for a shear rate $\dot{\gamma} = 10$ s^{-1}.

[f] for a unit strain.

[g] for a unit strain.

[h] for a shear rate $\dot{\gamma} = 10$ s^{-1}.

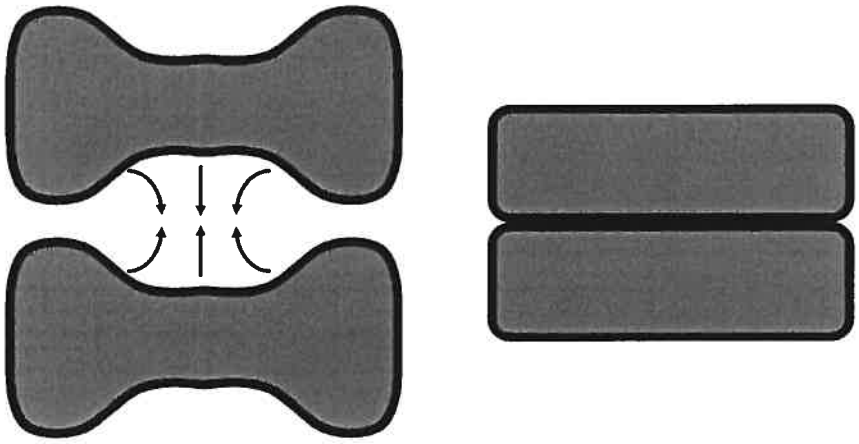

FIG. 2.11 – Deformation of the membrane (keeping the surface constant) to balance elastic and adhesive energies.

2.9 US backscattering by blood: effect of red blood cell aggregation on the structure factor

The notion of packing factor was introduced in section (2.7). This non-dimensional parameter describes low frequency backscattering by blood: the backscattering coefficient at low frequency is directly proportional to W. When W deviates from one, this proves that scattering particles locations are correlated because of repulsion or clustering phenomena. The low frequency approximation is however limited:

- From the US technical point of view, the packing factor approximation is no longer valid when increasing the US frequency or when aggregates are too large compared to the wavelength,

- from the tissue characterization point of view, the packing factor does not uniquely define the underlying microstructure. It represents a single quantity $S(0)$ whereas the whole frequency dependence $S(\vec{q})$ defines the particle interactions more accurately .

Having classified the different interactions responsible for the RBC microstructure in section (2.8), we review in this section the literature concerning the effect of these forces on the structure factor values in the $\vec{k}$-space.

2.9.1 Hard sphere structure factor as a reference

Percus-Yevick approximation

The hard sphere system is naturally taken as a reference. We previously investigated the zero frequency limit of its structure factor, but the non-Rayleigh scattering properties of the hard sphere systems have been less commonly addressed. The Perkus-Yevick closure relation [23] can be solved analytically to derive good approximations of the hard sphere structure factor $S_{PY}(q)$:

$$\frac{1/S_{PY}(q) - W_{PYC}^{-1}}{1 - W_{PYC}^{-1}} = 1 + a_0(H)\psi_0(2qa) + a_1(H)\psi_1(2qa) + a_2(H)\psi_2(2qa), \quad (2.80)$$

where:

$$\psi_0(u) = 3\frac{\sin u - u\cos u}{u^3}, \quad (2.81)$$

$$\psi_1(u) = 4\frac{-2 + 2u\sin u + \cos u(2 - u^2)}{u^4}, \quad (2.82)$$

$$\psi_2(u) = 6\frac{24 + 4\sin u(-6u + u^3) - \cos u(24 - 12u^2 + u^4)}{u^6}, \quad (2.83)$$

and:

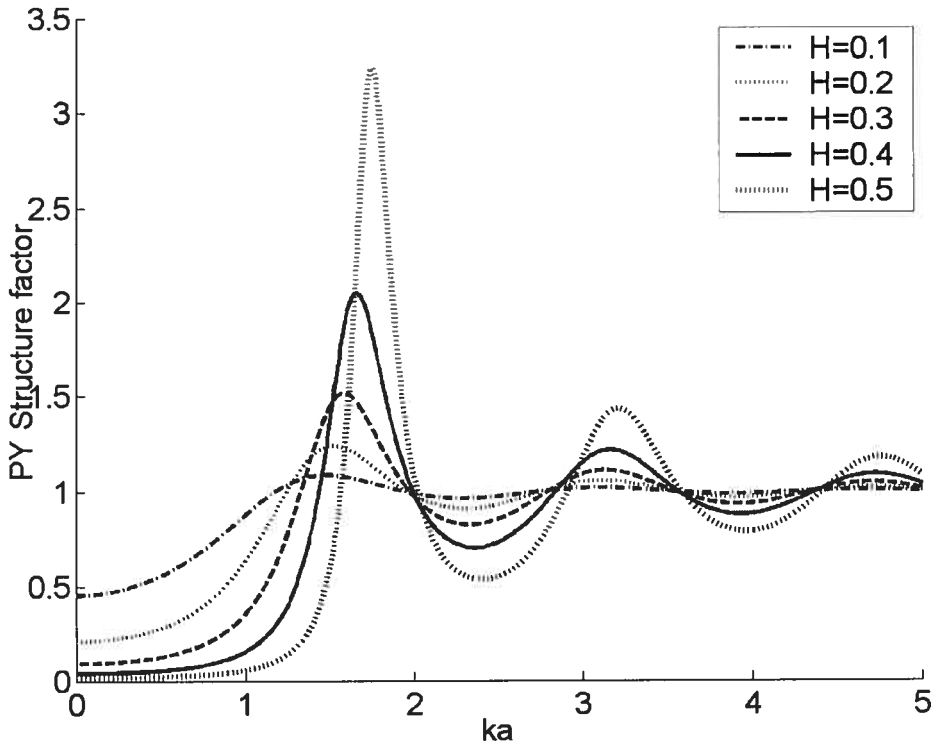

FIG. 2.12 – hematocrit and frequency dependence ($q = 2k$) of the structure factor $S(\vec{q})$ of hard spheres of radius a, obtained by the Percus-Yevick (PY) approximation.

$$W_{PYC}(H) = \frac{(1-H)^4}{(1+2H)^2} \tag{2.84}$$

$$a_0(H) = -\frac{(1+2H)^2}{(1-H/4)(1+H^2/2)} \tag{2.85}$$

$$a_1(H) = 9H/2\frac{(1+H/2)^2}{(1-H/4)(1+H^2/2)} \tag{2.86}$$

$$a_2(H) = -H/4\frac{(1+2H)^2}{(1-H/4)(1+H^2/2)} \tag{2.87}$$

The properties $S_{PY}(0) = W_{PYC} < 1$ and $S_{PY}(q) = 1$ for $qa \gg 1$ are well respected. Some structure factor profiles are shown in figure (2.12).

Other theoretical and experimental findings on hard sphere systems and on the structure factor

The quadratic increase of the structure factor for $ka \lesssim 1$, as observed in figure (2.12), can imply a frequency dependence β of the backscattering coefficient that is greater than 4. This behavior had already been predicted [48, 144] in the so-called dense media scattering model but has never been associated with the Perkus-Yevick structure factor. Experimental confirmations of this elevated frequency dependence in non-aggregating media are scarce: Campbell and Waag [40] have measured $\beta > 4$ for suspension of sephadex particles and other measurements for RBCs were reported in [190, 224]. The difficulty to assess this increase of $\beta > 4$ certainly comes from the decrease of the particle form factor $F(k)$ that superimposes on the increase of the structure factor when $ka \gtrsim 0.25$. One-dimensional models of hard slabs also exhibits this quadratic increase as reported in [81, 170].

2.9.2 Molecular dynamics inspired simulations

Molecular dynamics method

The particle dynamics approach integrates the differential system of the N time-varying positions $(\vec{x}_1(t), \ldots, \vec{x}_N(t))$ inside the box V (boundary artifacts are often treated by assuming periodicity), taking into consideration the conservative forces $\vec{\nabla} V_2(\vec{h})$ and the non-conservative hydrodynamic friction forces $\vec{F}_i$ to portray the spatial pattern $\Omega(t)$:

$$\forall i = 1 \ldots N \quad \rho_{RBC} \mathcal{V} \frac{d^2 \vec{x}_i}{dt^2} = -\sum_{j \neq i} \vec{\nabla} V_p(\vec{x}_i - \vec{x}_j) + \vec{F}_i. \tag{2.88}$$

After a transient period, a time-averaged structure factor is computed on the N particle positions:

$$S(\vec{q}) \approx \frac{1}{N} \left\langle \left| \sum_{i=1}^{N} e^{-i\vec{q}.\vec{x}_i(t)^2} \right|^2 \right\rangle_{t\in[t_0,t_0+\Delta t]} . \tag{2.89}$$

It must be remarked that the total energy

$$U(t) = \sum_{i<j} V_p(\vec{x}_i(t) - \vec{x}_j(t)) + \frac{1}{2}\rho_0(1+\gamma_\rho)\mathcal{V}\sum_{i=1}^{N}\left(\frac{d\vec{x}_i}{dt}\right)^2$$

is decreasing during the motion because of viscous dissipation. When the expressions of the $\vec{F}_i$ are known, several different numerical methods exist to find close solutions to the previous differential system. They will not be detailed in the present paper. In our specific problem of particles flowing in a viscous fluid, the major issue is to evaluate the hydrodynamic forces $\vec{F}_i$ for each particle. Three approaches can be found in the literature: some were devoted to RBCs in flow and used either a simplified approach to derive $\vec{F}_i$ for macrocirculation, or on the contrary sophisticated numerical methods were invented to accurately compute the velocity plasmatic field and the fluid-cell interaction in microcirculation (discrete particle dynamics). The Stokesian dynamics approach could also be a new avenue for the study of RBC motion, since it allows us to efficiently compute the forces $\vec{F}_i$ as a fonction of the velocities $d\vec{x}_i/dt$ using linear approximants. These methods are described in the next paragraphs.

Particle dynamics results: simplified models of hydrodynamic interactions

Two-dimensional motion of disc erythrocytes and the related ultrasound backscatter under the influence of colloid and hydrodynamic forces were numerically modeled in shear flow [82, 83]. A simplified approach was adopted: the velocity of each particle was considered to be the fluid velocity perturbated by a velocity that arose from empirical colloidal forces.

The power of the backscattered signal (from a finite beam and a pulsed field) was found to be angle-dependent and its variation with the central frequency f_0 was

predicted as a function of the shear rate. Maximal backscattering occurred at an angle that did not necessarily correspond to a perpendicular insonification (i.e. at 90° with the velocity. The variance of the clusters orientation, the finite aperture effect and the pulsed nature of the incident wave can explain this angular variation. Moreover, anisotropy was shown to be less pronounced for $k_0a = 0.44$ than for $k_0a = 0.11$, where k_0 is the central wavenumber of the pulsed wave. As $S(\vec{q})$ becomes angle independent when $k_0a \to 0$ and when $k_0a \to \infty$, the anisotropy of the structure factor must indeed be maximal at intermediate k_0a. Increasing the adhesion parameters and decreasing the flow shear rate resulted in an enhanced backscattered power. Moreover, the mean frequency dependence β in the range $40 - 60$ MHz (computed with the central frequency) was shown to decrease from 3.6 ± 0.7 to 0.6 ± 1.1 when decreasing $\dot{\gamma}$ from 2 to 0.05 s^{-1}. This is in accordance with experimental results previously reviewed in (2.7.4).

Particle dynamics results: the discrete particle paradigm

A recent approach in modeling flow of complex fluids is the discrete particle paradigm [31, 73]. Materials are no longer considered as continuums, but are modeled by the association of discrete interacting nanoparticles: some are fluid dissipative particles (plasma and hemoglobin solution), some are solid elastic particles (RBC membrane and vessel wall). The flow of elastic discoidal RBCs in microvessels of diverse geometries and compliances can be investigated with these numerical intensive computational methods. In return, the tuning of the interparticular forces can be somewhat difficult. RBC clustering induced by geometric obstacles, viscoelastic collisions or pathological RBC morphology were investigated by these means in narrow and tortuous microvessels (with diameters close to $2a$).

However these algorithms have not been used to determine bulk material properties (whole blood viscosity, structure factor, pair correlation function,...) as a function

of physical meaningful dimensions like the Péclet number, the reduced shear membrane elasticity or the hematocrit. It seems that this approach is more efficient for investigating RBC microrheology in capillaries, that is greatly constrained by the wall proximity and elasticity. It is also a powerful tool that can model the discoidal shape of the RBC and its deformation in flow. But the generalization of this method to larger vessels for the macroscopical study of blood could lead to tremendous computational difficulties. Moreover, the effect of non-hydrodynamic interparticle forces (depletion or surface adhesion) has not been included in the aforementioned studies.

2.9.3 Particle dynamics results: Stokesian dynamics

The low value of the particle Reynolds number enables us to simplify the Navier-stokes equations that govern plasmatic flow around RBCs. Velocity and flow stress fields are linearly related by a Green function. This greatly simplifies the hydrodynamic forces computation by replacing the solving of Navier-Stokes equations by the determination of a single function.

Hard spheres in flow

Material properties of different models of colloidal fluids in shear flow have been investigated by the so-called Stokesian dynamics method invented by Brady and Bossis [34]. Monodisperse hard spheres flowing in a stationary shear flow in concentrated suspensions have properties that dramatically change as a function of $\mathcal{P}_e$. Phung et al. [160] reported Stokesian dynamics results of viscosity and pair correlation functions for a $H = 0.45$ suspension. In a Brownian dominated flow ($6\pi\mathcal{P}_e \leq 1$), the suspension shear thins as the viscosity decreases since $\eta/\eta_{\text{plasma}} \propto \mathcal{P}_e^{-1}$. For larger values of $\mathcal{P}_e$, hydrodynamic effects govern the structure and the rheology. Anisotropy increases with $\mathcal{P}_e$, because of the velocity gradients and vorticity induced by the shearing. The contact between spheres is more likely in the compressional quadrant: the

pair correlation function at contact $g(2a\vec{e}_r)$ is maximal when the $\vec{e}_r$ lies in the Oyz plane, with an angle of $3\pi/4 \pm \pi$ with $\vec{e}_y$. In the extensional quadrant (the angle between $\vec{e}_r \in Oyz$ and $\vec{e}_y$ is $\pi/4 \pm \pi$), $g(2a\vec{e}_r) \to 0$ when $\mathcal{P}_e$ increases. Spheres therefore form non compact clusters (strings arranged hexagonally), when $6\pi\mathcal{P}_e \sim 1 - 100$, that become so large that they melt when $6\pi\mathcal{P}_e \gtrsim 200$; this induces shear thickening. This phenomenon of shear thickening at high $\mathcal{P}_e$ is scarcely observed for suspensions of RBCs, which tends to prove that RBC deformability plays an important role on blood viscosity and microstructure.

Non agregating elastic RBCs in flow

Breyiannis and Pozrikidis [35] added the effect of capsule elasticity and biconcave shape in a 2D study on the pair correlation function. Considering that the cell cytoplasm has the same viscosity as the plasma and that the membrane mechanically deforms as a capsule with an interfacial elasticity modulus E_m (this physically differs from the shear membrane modulus μ_m), they showed that the contact is also higher in compressional than in extensional positions when $\eta_{\text{plasma}} a\dot{\gamma}/E_m$ increases. Shear thinning or shear thickening of the suspension has unfortunately not been studied in this work.

Colloidal forces

Introduction of interparticle interactions of colloidal nature in dynamics simulations modifies the microstructure and the shear dependence of rheological functions as few Stokesian dynamics studies have recently shown. Silbert et al. [192, 193] showed that the shear thinning ($6\pi\mathcal{P}_e \sim 0-100$) is more pronounced when increasing the depletion energy $\bar{\epsilon}/k_BT$. The viscosity is increased by the adhesive forces. The shear dependence of the structure factors were simulated in [192] for depletion parameters $n_P a^3 \sim 9$ and $r \sim 0.1$. It showed that a peak at $qa \lesssim 0.5$ appears at a low Péclet number and that its

amplitude decreases with $\mathcal{P}_e$. When $6\pi\mathcal{P}_e$ reaches ~ 100, distinctive crystallographic-like sharp peaks appears in the k-space, which reflects the (hexagonal) organization of the clusters in shear. The evolution of the packing factor with the shear rate was not quantified in this study.

Effect of shear flow on the structure factor in brief

More simulation studies are still required to include the effect of the Péclet number on the structure factor. The innovative particle dynamics methods that can even model elastic colloids are however promising.

2.9.4 Monte Carlo simulations

Monte Carlo methods

Classical Monte Carlo (MC) simulations can generate configuration samples that obey Boltzmann distribution at a constant thermodynamic temperature. They concern a set of particles at equilibrium, submitted to conservative interactions. The general principle of MC algorithms is to sample a random process with a probability density function p_Ω that is known up to an unknown constant (often impossible to compute), namely the partition function Z_Ω:

$$p_\Omega(\omega) = \frac{1}{Z_\Omega} \exp(-U_\Omega(\omega)/k_B T). \tag{2.90}$$

This is the case of Gibbs-Markov point processes and therefore MC methods are adequate for simulating particles at equilibrium. After the generation of the samples $\Omega_1, \ldots, \Omega_{M_i}$ drawn after numerous MC iterations, the (mean) structure factor can be estimated by empirical averaging:

$$S(\vec{q}) \approx \frac{1}{M_i} \sum_{i=1}^{M_i} S(\vec{q}; \Omega_i). \tag{2.91}$$

The most popular MC algorithm is the Metropolis sampler. This sequential algorithm consists at each step of randomly choosing a particle, and of proposing a new random position for this particle. If this displacement creates an energy variation of ΔU, then the displacement is accepted with probability $\min\{1, e^{-\Delta U/k_B T}\}$ or is discarded. The resulting Markov chain of configurations converges in probability toward a sample of p_Ω.

Effects of the hydrodynamic interactions forces $\vec{F}_i$ cannot be taken into account in this simulation scheme as they are non conservative. Consequently, classical MC techniques cannot be used to rigourously simulate configurations under shear. The Monte Carlo simulation scheme has however been generalized to non-equilibrium conditions, as in [79]. Each step of the Markov chain represents a time increment, and a new acceptance ratio is defined to simulate the system dynamics. These methods have never been implemented for modeling RBC motion in flow.

Results obtained by Monte Carlo simulations

MC equilibrium 2D simulations were performed to investigate the effects of the adhesion energy and of the anisotropic formation of RBC clusters on the structure factor [176, 177]. They do not directly take into consideration the effect of flow.

In [176], a square well potential models steric and isotropic attractive interactions. The pair potential is assumed to be infinite when particles are in contact and negative $-\epsilon$ at a distance $[2a, 2a(1+\lambda_0)]$. Shear hydrodynamic forces are not taken into consideration but the interaction range $\lambda_0 = 0.4$ was deliberatly assumed greater than for the attractive forces that are only mediated by plasmatic proteins (typically in this case $\lambda_0 \sim 0.01$). By using the given simulation results for $H = 0.4$, the low frequency behavior can be approximated at the second order by:

$$S(q) = W + S_2 q^2 + \dots \tag{2.92}$$

where the packing factor W is shown to increase with ϵ/k_BT:

$$W \sim W_\infty + (W_0 - W_\infty)e^{-\epsilon/\beta_1 k_B T}. \tag{2.93}$$

In Eq. (2.93), $W_0 = W_{SPT}^{2D} = 0.15$ is the packing factor of the disagregated suspension, $W_\infty = 0.9$ is the maximal packing factor for very aggregated media and $\beta_1 = 1.5$ is a fitting parameter.

The second order coefficient S_2 decreases with the adhesive energy:

$$S_2 = \gamma_\infty a^2 + (\gamma_0 - \gamma_\infty)a^2 e^{-\epsilon/\beta_2 k_B T}, \tag{2.94}$$

where $\gamma_0 = 0.05$, $\gamma_\infty = -1.1$ and $\beta_2 = 2$ are fitting parameters. The quadratic approximation of the structure factor in Eq. (2.92) holds for $ka \lesssim 0.35$.

In [177], an angle-dependent interaction potential was chosen to model preferential orientation of rouleaux along the velocity direction (Ox) in 2D. It is however not totally realistic because shear interactions are not conservative forces. The pair potential was defined as

$$V_p(\vec{h}) = \begin{cases} +\infty & \text{if } |h| < 2a \\ -\epsilon\phi_1\left(\frac{1}{2}\left|R_0^{-1}\vec{h}\right|\right) & \text{otherwise} \end{cases} \tag{2.95}$$

where $\pi\phi_1(u)$ is the intersection area of two unit disks with centers separated by a distance $2u$, $R_0 = (1+\lambda_0)a\left((1+\nu)\vec{e}_x \otimes \vec{e}_x + (1+\nu)^{-1}\vec{e}_y \otimes \vec{e}_y\right)$ is an elliptic tensor that controls the elliptic interaction range, λ_0 quantifies the spatial range, ν the anisotropy and ϵ the adhesive energy.

The results obtained can be described by the second order expansion:

$$S(\vec{q}) = W + \vec{q}.\Sigma_2\vec{q} + \dots \tag{2.96}$$

where $\Sigma_2 = s_{xx}\vec{e}_x \otimes \vec{e}_x + s_{yy}\vec{e}_y \otimes \vec{e}_y$ is a zero-frequency Hessian tensor that conditions the low frequency scattering behavior. For $\lambda_0 = 0.4$, the packing factor scales as (Fig. 2.13):

$$W = W_\infty + (W_0 - W_\infty)e^{-\epsilon/\beta_3 k_B T}, \tag{2.97}$$

where $W_0 = W_{SPT}^{2D}$, $W_\infty = (4.6 - 2.6\nu)W_0$ and $\beta_3 = 19 - 10\nu$. The packing factor still increases with the adhesion energy but the plateau value decreases with the anisotropy of the medium.

In isotropic conditions ($\nu = 0$), $s_{xx} \approx s_{yy}$ and decreases with $\epsilon/k_B T$. In anisotropic conditions ($\nu > 0$), while s_{xx} still decreases with $\epsilon/k_B T$, $s_{yy} > s_{xx}$ tends to increase. This shows that the smallest (negative) components of Σ_2 are the principal directions of the aggregates and that the (positive) components of gyration tensor Σ_2 reflect repulsive interactions. In US terms, for frequencies $ka \lesssim 0.35$, the backscatter is greater when the wavevector is perpendicular to the cluster axis and this "acoustic" anisotropy is increased for strong adhesion ϵ and "structure" anisotropy ν (Figs. 2.14, 2.15).

2.9.5 Geometric models

A number of simple geometric models have been proposed to describe the spatial pattern created by clustered RBCs (at a particular time, as a snapshot) and to derive their structure factor. They can be described as geometrical because they simply detail the morphological properties of the medium, without taking into consideration the physical phenomena that govern particle positioning in space.

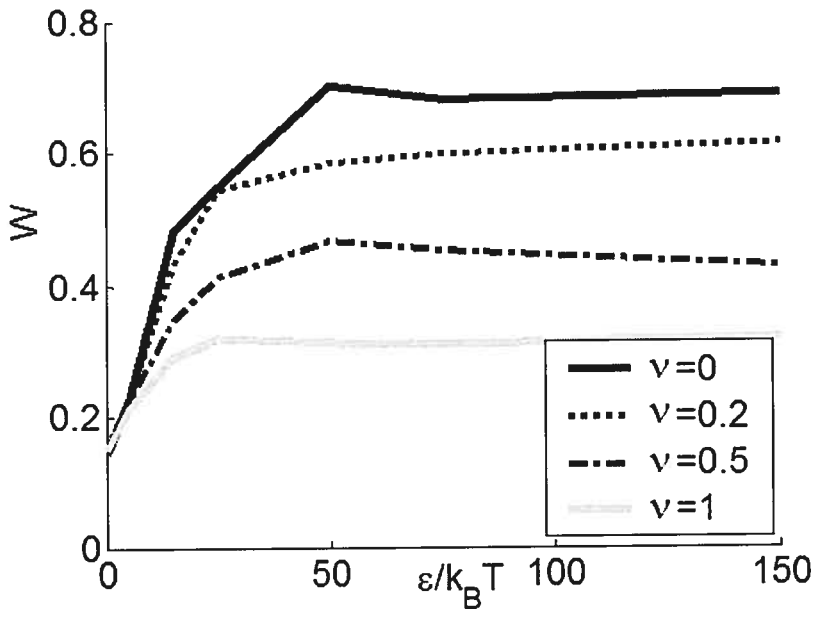

FIG. 2.13 – Packing factor as a function of the adhesion energy ϵ and of the anisotropy index ν in the Gibbs-Markov model described in [177]. The hematocrit is $H = 0.4$.

Neyman-Scott structure factor

The Neyman-Scott point process [175] models clouds of uncorrelated clusters. Assuming gaussian distributed groups, the aggregates can be characterized by an inertia tensor (or spatial covariance matrix) Σ_{NS} and by their random number of particles N_c. These assumptions allow to analytically derive the structure factor, the packing factor and the gyration tensor Σ_2 of the point process:

$$S(\vec{q}) = 1 + (W - 1) \exp\left(-\vec{q}.\Sigma_{NS}\vec{q}\right) = W + \vec{q}.\Sigma_2\vec{q} + \dots \tag{2.98}$$

where $W = E[N_c^2]/E[N_c]$ and $\Sigma_2 = (1 - W)\,\Sigma_{NS}$.

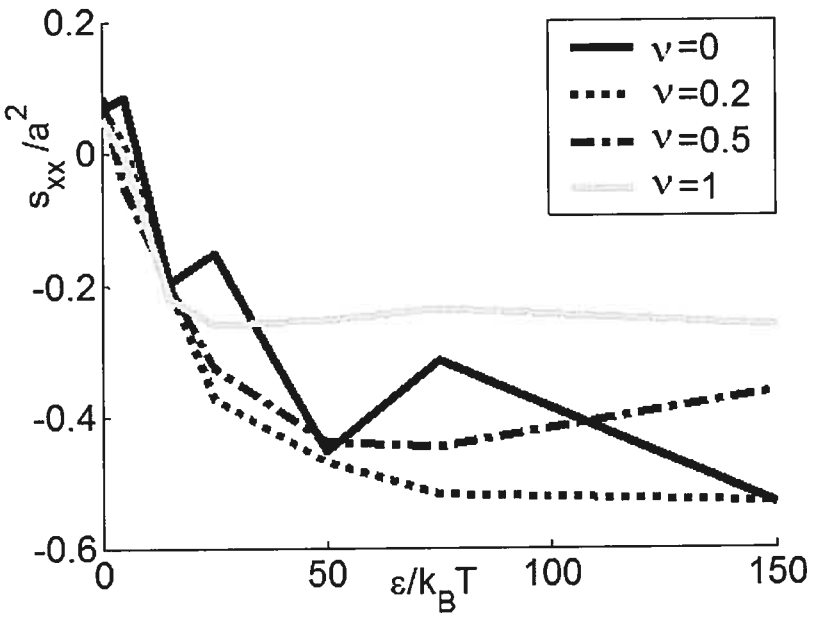

FIG. 2.14 – component s_{xx} of the gyration tensor Σ_2 as a function of the adhesion energy ϵ and of the anisotropy index ν in the Gibbs-Markov model described in [177]. The hematocrit is $H = 0.4$.

Structure factor of identical clusters

Now, media composed of uncorrelated identical deterministic clusters of n_c RBCs as subunits $(\vec{r}_1, \ldots, \vec{r}_{n_c})$ (simple approach closed to the methods used in [175, 204]), can be described by an equivalent structure factor:

$$S(\vec{q}) = \frac{1}{n_c} \left| \sum_{j=1}^{n_c} e^{-\imath \vec{q}.\vec{r}_j} \right|^2 = W + \vec{q}.\Sigma_2 \vec{q} + \ldots \tag{2.99}$$

The low frequency characteristics of the structure factor (packing factor and gyration tensor) can be expressed as a function of the geometry of the clusters:

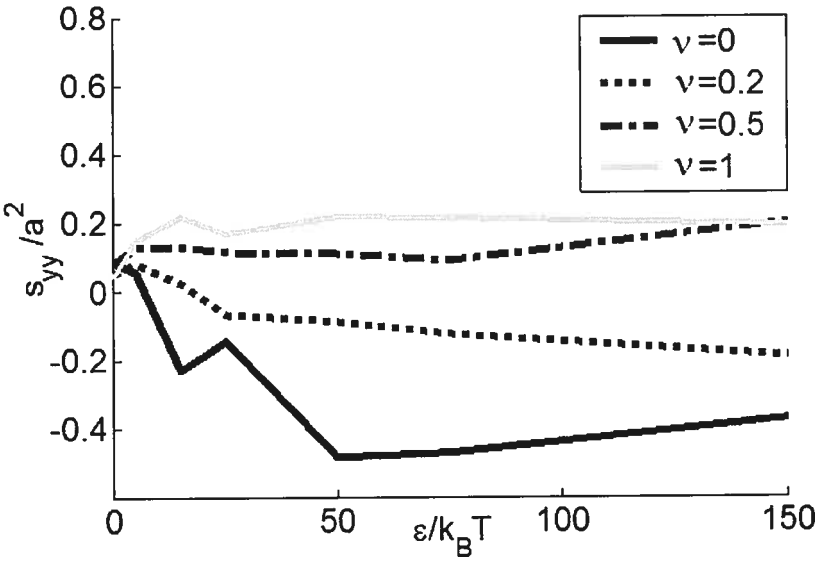

FIG. 2.15 – component s_{yy} of the gyration tensor Σ_2 as a function of the adhesion energy ϵ and of the anisotropy index ν in the Gibbs-Markov model described in [177]. The hematocrit is $H = 0.4$.

$$W = n_c, \tag{2.100}$$

$$\Sigma_2 = -\frac{1}{n_c}\sum_{j=1}^{n_c} \vec{r}_j \otimes \vec{r}_j. \tag{2.101}$$

Geometric interpretation of the packing factor and of Σ_2

These geometric models show that the packing factor can be considered as an efficient number of scatterers per cluster and that the so-called gyration tensor Σ_2 as defined by the second order Taylor expansion:

$$S(\vec{q}) = W + \vec{q}.\Sigma_2\vec{q} + \ldots \tag{2.102}$$

is related to the size of the aggregates. The eigenvectors of this symmetric tensor are the principal axes of the clusters, and their eigenvalues s_{ii} decrease with the spatial

extent of the clusters. When they are all negative, the efficient gyration radii of the clusters are $\sqrt{-s_{ii}}$. Positive values of the eigenvalues (as for the PY structure factor) reflect hardcore or repulsive interactions. The frequency-independent characteristics W and Σ_2 (that quantifies the departure from the Rayleigh scattering regime) would be robust indices quantifying the frequency dependence of the structure factor.

2.10 Discussion

2.10.1 New data reduction for blood US characterization

In subsection (2.4.4), we have seen that most of the US tissue characterization studies quantify the frequency dependence of the backscattering coefficient by a two-parameter law fitting :

$$\chi(f) = \alpha_0 f^{\beta}. \tag{2.103}$$

It seems however that these two values are fitting quantities that are not physically pertinent for blood characterization. As the classical medical frequencies scarcely exceed $ka > 0.5$, it seems that a second order expansion of the structure factor (paragraph 2.9.5) is more helpful to characterize the frequency dependence $\vec{q} \rightarrow S(\vec{q})$. Using the low frequency expansions of the RBC acoustical cross-section (paragraph 2.5.3) and of the structure factor, one can write:

$$\chi(\vec{k}) = m\sigma_b(\vec{k})S(-2\vec{k}) = \frac{1}{4\pi^2}\langle\gamma_z\rangle^2 mk^4\mathcal{V}^2(1-4\vec{k}.\Sigma\vec{k}+\ldots)(W+4\vec{k}.\Sigma_2\vec{k}+\ldots) \tag{2.104}$$

This expression gives a pertinent expansion of the frequency dependence of the backscatter with fitting parameters $\{W, \Sigma_2\}$ that reflect microstructural features of the RBC aggregates:

$$\chi(\vec{k}) = \frac{1}{4\pi^2} H\mathcal{V}k^4\langle\gamma_z\rangle^2 \left(W + 4\vec{k}.\left(\Sigma_2 - W\Sigma\right)\vec{k}\right) + \ldots \tag{2.105}$$

This can be written as a 6^{th} order polynomial in ka if $\vec{k} = k\vec{e}_i$, $\sigma_{ii} = \vec{e}_i.\Sigma\vec{e}_i$ and $s_{ii} = \vec{e}_i.\Sigma_2\vec{e}_i$):

$$a\chi(k\vec{e}_i) = W(ka)^4 \times \left(H\langle\gamma_z\rangle^2/3\pi\right) + \left(\frac{s_{ii} - W\sigma_{ii}}{a^2}\right)(ka)^6 \times \left(4H\langle\gamma_z\rangle^2/3\pi\right) + \ldots \tag{2.106}$$

In comparison with the fitting parameters (α_0, β), the quantities (W, Σ_2) do not depend on the frequency range and are only affected by the microstructure. They are consequently more pertinent physically that (α_0, β) and are easy to determine from a collection of data by a simple polynomial fitting.

In small angle neutron, light or X ray scattering, the range of frequency for which the quadratic approximation of $S(\vec{q})$ is valid is named Guinier domain. The Guinier plot [93] often refers to the graph $q_i^2 \rightarrow \ln S(q_i\vec{e}_i)$ which gives a straight line for $q_i^2 \rightarrow 0$. The Zimm plot [239] is also often used to derive the radius of gyration and the second order virial coefficient B of polymers and could also be useful for our concern. Using the scattering vector dependence of the structure factor at different volumic fractions H, a network of curves $q_i^2 \rightarrow 1/S(q_i, H) - 1$ is drawn. For $q_i a \ll 1$ and $H \ll 1$, these curves define a grid, comparable to a Zimm plot ($s_{ii} = \vec{e}_i.\Sigma_2\vec{e}_i$):

$$1/S(q_x\vec{e}_i, H) - 1 = \frac{2B}{N_A\mathcal{V}}H - q_i^2 s_{ii}. \tag{2.107}$$

The lines are not necessarily parallel (because of the variation of Σ_2 with H). The intercepts give the second virial coefficient $B/N_a\mathcal{V} \sim 4 - 12\bar{\epsilon}/k_BT$ and the slopes provide the radius of gyration in the insonifying direction $\vec{e}_i$.

2.10.2 Interest of microstructure modeling for rheological characterization.

Microstructural models of RBC interactions are not only useful to adequatly scale and predict the evolution of blood acoustical properties in response to shear forces or to the concentration of plasma proteins. Their main interest is their ability to predict other macroscopical blood material properties (as the viscosity) that may have a pathophysiological importance. Rheological properties are known to be microstructure-dependent, and shear-thinning blood viscosity should be predictable as a function of H, RBC physical property, cell-cell interaction parameters (as the adhesive strength $\bar{\epsilon}/k_BT$) and flow conditions ($\mathcal{P}_e$). However, the relation between macroscopic rheology and interaction particle parameters still constitutes an open problem in colloid physics. A few scaling laws $\eta = \eta(\dot{\gamma})$ have already been proposed for colloid suspensions under the form:

$$\frac{\eta - \eta_\infty}{\eta_0 - \eta_\infty} = \Psi\left(\mathcal{P}_e, \epsilon_{min}/k_BT, H\right), \tag{2.108}$$

where η_0, η_∞ are respectively the viscosity at zero and infinite shear rates, Ψ is a given function and ϵ_{min} is the depth of the adhesive pair interaction energy. According to Baxter-Drayton and Barry [24] (studying electrorheological fluids), Ψ is an increasing universal function of $\mathcal{P}_e^{-1}\epsilon_{min}/k_BTe^{-\epsilon_{min}/k_BT}$. Berli et al. [28] propose a dependence of Ψ in $\mathcal{P}_e^{-1}\left(1+\epsilon_{min}/k_BT\right)$. Silbert et al. [193] write Ψ under the form $\mathcal{P}_e^{-0.84}\left(\epsilon_{min}/k_BT\right)^{0.84}$. For red blood cells, an appropriate scaling remains to be found. The role of the membrane deformability, of the RBC discoidal shape and of the range of adhesive interaction (size of the polymers) must also be quantified.

The coupling between the shear dependence of blood backscatter, the RBC microstructure and the hemorheological properties have been experimentally studied using empirical data reductions (as mentioned in paragraph 2.4.4). We think that the pro-

posed definition of the acoustical measurable parameters (W, Σ_2) would give more insight to study the blood suspension. The relation $\mathcal{P}_e \rightarrow (W, \sigma_2)$ should e.g. give clues on the values of the interaction energies, that could moreover be used to assess the shear-thinning behavior of a suspension as described by an equation of the type (2.108). This approach partially solves the problem of the frequency dependence of the data reductions proposed by Haider et al. [95] or by Cloutier et al. [59] for rheoacoustical characterization.

To simply illustrate the interest of using the packing factor approximation for rheoacoustics, let us examine the case of the Baxter sticky sphere model at equilibrium $(\mathcal{P}_e \sim 0)$. From the acoustically derived packing factor W and from the hematocrit H, one can derive the "stickyness" τ^{-1} according to the Eqs (2.62) and (2.63):

$$W = \frac{(1-H)^4}{(1+2H-\Lambda H(1-H))^2}, \tag{2.109}$$

where Λ is related to the stickyness:

$$\frac{H}{12}\Lambda^2 - \left(\frac{H}{1-H} + \tau\right)\Lambda + \frac{1+H/2}{(1-H)^2} = 0. \tag{2.110}$$

Now the low shear $(\mathcal{P}_e \sim 0)$ and low hematocrit viscosity η_0 of a suspension of sticky spheres has been derived by Russel [173]:

$$\eta_0/\eta_{\text{plasma}} = 1 + 2.5H + (5.9 + 1.9\tau^{-1})H^2. \tag{2.111}$$

In this simplistic model at equilibrium, the viscosity η_0 of the suspension can therefore be predicted by knowing the plasma viscosity, the blood hematocrit and then by measuring the acoustical packing factor! Two models are needed to achieve this kind of rheoacoustical characterization. The first describes the relation microstructure - $\{W, \Sigma_2\}$ and the second the microstructure - rheology link. For the concrete case of whole dense blood at finite Péclet, appropriate coupling models still need to be found.

2.11 Summary and conclusion

In this review, we expose three material acoustical properties that are commonly measured in ultrasound tissue characterization, namely the speed of sound, the attenuation coefficient and the backscattering coefficient. The measurement of these parameters should bring new acoustical means for mapping *in vivo* changes of tissue microstructure for diagnosis. As an illustrating example, we report how blood backscattering measurements could bring new insights for *in situ* hematologic and hemorheology. The blood backscattering coefficient is related to the RBC physical properties, to the hematocrit H and critically to the shear-varying RBC microstructure. RBC organization has many physical determinants: hydrodynamic forces (Péclet number $\mathcal{P}_e = \eta_{\text{plasma}}\dot{\gamma}a^3/k_BT$), membrane cell shear deformability (k_BTa^2/μ_m) and cell-cell interactions mediated by plasmatic macromolecules (negative well depth $\bar{\epsilon}/k_BT$ and range r) and counterions (electrostatic double layer) that readily influence RBC spatial pattern and orderliness.

Statistical physics of complex fluids and condensed matter provides appropriate tools to link microscopic colloidal parameters to the macroscopic blood structure factor $S(\vec{q})$, a quantity proportional to the backscattering coefficient. At equilibrium ($\mathcal{P}_e = 0$), some analytical and numerical results are reviewed. They are useful to document how blood backscattering coefficient and its frequency dependence vary with cell-cell interactions. More realistically, non equilibrium computer models of particle systems in simple shear flow ($\mathcal{P}_e > 0$) were introduced to study how blood shear thinning behavior and RBC microstructural variations affect $S(\vec{q})$. A new data reduction for low frequency ($f \lesssim 30$ MHz) backscattering properties, namely the packing factor W and the gyration tensor Σ_2 are introduced. The coupling between whole blood rheology and these acoustical indices still needs further investigations.

2.12 Appendices

2.12.1 Form factor of a volume of revolution

This appendix details the computations to obtain the form factor of a scatterer $\mathcal{V}$ that has an impedance relative contrast given by $\gamma_z(\vec{r}) = \gamma_z(r,\theta,z) = \langle\gamma_z\rangle \mathbb{I}_{[|z|<z_0(r)]}$, where $z_0(r)$ is the radial profile of the scatterer shape, (r,θ,z) are the cylindrical coordinates, and $\langle\gamma_z\rangle$ is the homogeneous contrast of the scatterer.

The backscattering cross-section of the scatterer in the Born approximation is given by Eq. (2.16):

$$\sigma_b(\vec{k}) = \frac{1}{4\pi^2} k^4 \left| \int_{\mathcal{V}} \gamma_z(\vec{r}) e^{2\imath \vec{k}.\vec{r}}\, d^3r \right|^2 . \tag{2.112}$$

This integral can be written in a cylindrical system of coordinates:

$$\sigma_b(\vec{k}) = \frac{1}{4\pi^2} k^4 \left| \int \gamma_z(r,\theta,z) e^{2\imath(k_r r\cos\theta + k_z z)} r\, dr d\theta dz \right|^2 . \tag{2.113}$$

The symmetries of the acoustical impedance allow us to simplify the expression (2.113):

$$\sigma_b(\vec{k}) = \frac{1}{4\pi^2} k^4 \langle\gamma_z\rangle^2 \left| \int r \mathbb{I}_{[|z|<z_0(r)]} e^{2\imath(k_r r\cos\theta + k_z z)}\, dr d\theta dz \right|^2 , \tag{2.114}$$

$$= \frac{1}{4\pi^2} k^4 \langle\gamma_z\rangle^2 \left| \int r\, dr \int dz \mathbb{I}_{[|z|<z_0(r)]} e^{2\imath k_z z} \int_{-\pi}^{\pi} d\theta e^{2\imath k_r r\cos\theta} \right|^2 . \tag{2.115}$$

The equality

$$j_0(x) = \frac{1}{2\pi} \int_{-\pi}^{\pi} e^{\imath x\cos\theta}\, d\theta \tag{2.116}$$

is used to compute the integral in θ:

$$\sigma_b(\vec{k}) = k^4 \langle\gamma_z\rangle^2 \left| \int j_0(2k_r r) r\, dr \int \mathbb{I}_{[|z|<z_0(r)]} e^{2\imath k_z z}\, dz \right|^2 . \tag{2.117}$$

As

$$\int \mathbb{I}_{[|z|<x]} e^{2uz}\, dz = 2x\ \mathrm{sinc}\,(2ux)\,, \tag{2.118}$$

Eq. (2.117) simplifies in:

$$\sigma_b(\vec{k}) = 4k^4\langle\gamma_z\rangle^2 \left| \int r j_0(2k_r r) z_0(r)\,\mathrm{sinc}\,(2k_z z_0(r))\ dr \right|^2. \tag{2.119}$$

Since the form factor $F(\vec{k})$ is defined by the formula:

$$\sigma_b(\vec{k}) = \frac{1}{4\pi^2} k^4 \mathcal{V}^2 \langle\gamma_z\rangle^2 F(\vec{k}), \tag{2.120}$$

the comparison of Eqs (2.119) and (2.120) gives:

$$F(\vec{k}) = \frac{16\pi^2}{\mathcal{V}^2} \left| \int r j_0(2k_r r) z_0(r) \mathrm{sinc}\,(2k_z z_0(r))\ dr \right|^2. \tag{2.121}$$

The volume of the scatterer can be written as:

$$\mathcal{V} = \int r \mathbb{I}_{[|z|<z_0(r)]}\, dr d\theta dz, \tag{2.122}$$

$$= 4\pi \int z_0(r) r\, dr. \tag{2.123}$$

This allows us to find the expected formula for the form factor:

$$F(k_r, k_z) = \left| \int r j_0(2k_r r) z_0(r) \mathrm{sinc}\,(2k_z z_0(r))\ dr \Big/ \int r z_0(r)\, dr \right|^2. \tag{2.124}$$

2.12.2 Second order expansion of the form factor

The second order expansion of the form factor of an homogeneous scatterer $\mathcal{V}$ centered in 0 takes the form $F(\vec{k}) = 1 - 4\vec{k}.\Sigma\vec{k}$. This appendix proves that

$$\Sigma = \frac{1}{\mathcal{V}} \int \vec{r} \otimes \vec{r}\, d^3 r. \tag{2.125}$$

Consider the Born approximation of the backscattering cross-section as given by Eq. (2.16):

$$\sigma_b(\vec{k}) = \frac{1}{4\pi^2} k^4 \left| \int_{\mathcal{V}} \gamma_z(\vec{r}) e^{2\imath \vec{k}.\vec{r}} \, d^3r \right|^2 . \tag{2.126}$$

The second order expansion in $\vec{k}$ of Eq.(2.126) is (as $e^x = 1 + x + x^2/2 + \dots$):

$$\sigma_b(\vec{k}) = \frac{1}{4\pi^2} k^4 \left| \int_{\mathcal{V}} \gamma_z(\vec{r}) \left(1 + 2\imath \vec{k}.\vec{r} - 2 \left(\vec{k}.\vec{r} \right)^2 + \dots \right) d^3r \right|^2 . \tag{2.127}$$

By definition of the dyadic product,

$$(\vec{k}.\vec{r})^2 = \vec{k}. \left(\vec{r} \otimes \vec{r} \right) \vec{k}. \tag{2.128}$$

As the scatterer is homogeneous and centered in 0:

$$\begin{aligned} \int_{\mathcal{V}} \gamma_z(\vec{r}) \vec{r} d^3r &= \langle \gamma_z \rangle \int_{\mathcal{V}} \vec{r} d^3r, & (2.129) \\ &= 0 & (2.130) \end{aligned}$$

Combining Eqs. (2.127), (2.128) and (2.130), and using $\gamma_z(\vec{r}) = \langle \gamma_z \rangle \mathbb{I}_{[\vec{r} \in \mathcal{V}]}$, one obtains:

$$\begin{aligned} \sigma_b(\vec{k}) &= \frac{1}{4\pi^2} k^4 \langle \gamma_z \rangle^2 \left| \int_{\mathcal{V}} d^3r - 2\vec{k}. \left(\int_{\mathcal{V}} \vec{r} \otimes \vec{r} \, d^3r \right) \vec{k} + \dots \right|^2 , & (2.131) \\ &= \frac{1}{4\pi^2} k^4 \langle \gamma_z \rangle^2 \mathcal{V}^2 \left(1 - 4\vec{k}. \left(\frac{1}{\mathcal{V}} \int_{\mathcal{V}} \vec{r} \otimes \vec{r} \, d^3r \right) \vec{k} + \dots \right) . & (2.132) \end{aligned}$$

The comparison of Eq. (2.132) to the definition (2.120) of the form factor $F(\vec{k})$ yields the expected result:

$$F(\vec{k}) = 1 - 4\vec{k}. \left(\frac{1}{\mathcal{V}} \int_{\mathcal{V}} \vec{r} \otimes \vec{r} \, d^3r \right) \vec{k} + \dots \tag{2.133}$$

2.12.3 Packing factor and moments of the density

Let $N_{\mathcal{A}}$ be the random number of points from a point process Ω falling into a counting box $\mathcal{A}$. This appendix proves the following relation between the packing factor W of Ω and the moments of $N_{\mathcal{A}}$:

$$\frac{\mathrm{Var}[N_{\mathcal{A}}]}{E[N_{\mathcal{A}}]} = W + m \int_{|\vec{h}|<l_{cor}} \left(\frac{\mathcal{V}(\mathcal{A} \cap \mathcal{A}_{-\vec{h}})}{\mathcal{V}(\mathcal{A})} - 1 \right) \left(g(\vec{h}) - 1 \right) d^3h. \tag{2.134}$$

The microscopic density N_Ω is firstly introduced to compute $N_{\mathcal{A}}$:

$$N_{\mathcal{A}} = \int \mathbb{I}_{[\vec{r} \in \mathcal{A}]} N_\Omega(\vec{r})\, d^3r. \tag{2.135}$$

The second centered moment of $N_{\mathcal{A}}$ can be expressed as a double integral of the microscopic density:

$$E[N_{\mathcal{A}}^2] = \int \int \mathbb{I}_{[\vec{r}_1 \in \mathcal{A}]} \mathbb{I}_{[\vec{r}_2 \in \mathcal{A}]}\, E[N_\Omega(\vec{r}_1) N_\Omega(\vec{r}_2)]\, d^3r_1 d^3r_2. \tag{2.136}$$

The definition of the pair correlation function $g(\vec{h})$ is as follow:

$$E[N_\Omega(\vec{r}_1) N_\Omega(\vec{r}_2)] = m^2 g(\vec{r}_1 - \vec{r}_2) + m\delta(\vec{r}_1 - \vec{r}_2). \tag{2.137}$$

Inserting (2.137) inside (2.136) gives:

$$E[N_{\mathcal{A}}^2] = \int \int \mathbb{I}_{[\vec{r}_1 \in \mathcal{A}]} \mathbb{I}_{[\vec{r}_2 \in \mathcal{A}]} \left(m^2 g(\vec{r}_1 - \vec{r}_2) + m\delta(\vec{r}_1 - \vec{r}_2) \right) d^3r_1 d^3r_2. \tag{2.138}$$

The change of variable $(\vec{r}_1, \vec{r}_2) \rightarrow (\vec{r}_1, \vec{h})$, where $\vec{h} = \vec{r}_2 - \vec{r}_1$, readily gives:

$$E[N_{\mathcal{A}}^2] = \int \int \mathbb{I}_{[\vec{r}_1 \in \mathcal{A}]} \mathbb{I}_{[\vec{r}_1 + \vec{h} \in \mathcal{A}]} \left(m^2 g(\vec{h}) + m\delta(\vec{h}) \right) d^3r_1 d^3h. \tag{2.139}$$

As we can write

$$\mathbb{I}_{[\vec{r}_1 \in \mathcal{A}]} \mathbb{I}_{[\vec{r}_1 + \vec{h} \in \mathcal{A}]} = \mathbb{I}_{[\vec{r}_1 \in \mathcal{A} \cap \mathcal{A}_{-\vec{h}}]}, \tag{2.140}$$

and since the volume of a set is the integral of its indicator function, we can firstly integrate with respect to $\vec{r}_1$:

$$E[N_{\mathcal{A}}^2] = \int \mathcal{V}\left(\mathcal{A} \cap \mathcal{A}_{-\vec{h}}\right) \left(m^2 g(\vec{h}) + m\delta(\vec{h})\right) d^3h, \tag{2.141}$$

$$= m^2 \int \mathcal{V}\left(\mathcal{A} \cap \mathcal{A}_{-\vec{h}}\right) g(\vec{h})\, d^3h + m\mathcal{V}(\mathcal{A}). \tag{2.142}$$

As $E[N_{\mathcal{A}}]^2 = m^2\mathcal{V}(\mathcal{A})^2$ and since $\int \mathcal{V}\left(\mathcal{A} \cap \mathcal{A}_{-\vec{h}}\right) d^3h = \mathcal{V}(\mathcal{A})^2$, the variance can be calculated:

$$\mathrm{Var}[N_{\mathcal{A}}] = m^2 \int \mathcal{V}\left(\mathcal{A} \cap \mathcal{A}_{-\vec{h}}\right) \left(g(\vec{h}) - 1\right) d^3h + m\mathcal{V}(A). \tag{2.143}$$

Recalling that the packing factor W can be defined as:

$$W = 1 + m \int \left(g(\vec{h}) - 1\right) d^3h, \tag{2.144}$$

we obtain the expected relation:

$$\frac{\mathrm{Var}[N_{\mathcal{A}}]}{E[N_{\mathcal{A}}]} = 1 + m \int \frac{\mathcal{V}\left(\mathcal{A} \cap \mathcal{A}_{-\vec{h}}\right)}{\mathcal{V}(A)} \left(g(\vec{h}) - 1\right) d^3h, \tag{2.145}$$

$$= W + m \int \left(\frac{\mathcal{V}\left(\mathcal{A} \cap \mathcal{A}_{-\vec{h}}\right)}{\mathcal{V}(A)} - 1\right) \left(g(\vec{h}) - 1\right) d^3h. \tag{2.146}$$

Chapitre 3

Modélisation de l'agrégation érythrocytaire par une approche de géométrie stochastique

3.1 Avant-propos au chapitre

Ce chapitre reprend l'article « A point process approach to assess the frequency dependence of ultrasound backscattering by aggregating red blood cells » publié dans le *Journal of the Acoustical Society of America* (D. Savéry, G. Cloutier, 110:6, 3252-3262, 2001). Il décrit une approche géométrique pour modéliser le processus aléatoire de points Ω constitué par les centres des globules rouges. Le modèle ponctuel stochastique exposé ici est le modèle de Neyman-Scott qui a été utilisé dans de nombreux domaines (foresterie, météorologie, géostatistique...) pour décrire spatialement des nuages de points formant des agrégats. Son utilité majeure est le fait que le facteur de structure de Ω peut être exprimé analytiquement. Nous démontrons sa pertinence en « inversant » des données acoustiques expérimentales pour retrouver les caractéristiques statistiques des agrégats formés, à condition que l'hématocrite de la suspension soit faible. On notera que quelques symboles mathématiques auront été modifiés par rapport à la version originale de l'article afin d'harmoniser les notations de cette thèse.

3.2 Abstract

To study the shear-thinning rheological behavior of blood, an acoustical measurement of the erythrocyte aggregation level can be obtained by analyzing the frequency dependence of ultrasonic backscattering from blood. However, the relation that exists among the variables describing the aggregation level and the backscattering coefficient needs to be better clarified. To achieve this purpose, a three-dimensional random model, the Neyman-Scott point process, is proposed to simulate red cell clustering in aggregative conditions at a low hematocrit ($H < 5\%$). The frequency dependence of the backscattering coefficient of blood, in non-Rayleigh conditions, is analytically derived from the model, as a function of the size distribution of the aggregates and of their mass fractal dimension. Quantitative predictions of the backscatter increase due to red cell aggregation are given. The parametric model of backscatter enables two descriptive indices of red cell aggregation to be extracted from experimental data, the packing factor W and the size factor Δ. Previously published backscatter measurements from porcine whole blood at 4.5 % hematocrit, in the frequency range of 3.5 MHz - 12.5 MHz, are used to study the shear-rate dependence of these two indices.

3.3 Introduction

Blood is a complex tissue to characterize by ultrasonic means because of its heterogeneous structure. Blood interacts with acoustic waves because of the presence of cells flowing in the plasma (99 % are red cells) that scatter ultrasound non isotropically. The high density of red cells (their volumic fraction reaches about 45 %) and their ability to form reversible aggregates under the cumulative effects of chemical, physical and hydrodynamic interactions create intricate spatial structures that influence the scattering properties of blood.

Clinically, the purpose of blood characterization by ultrasound is to offer the pos-

sibility of investigating *in vitro* and *in vivo* the rheological attributes of blood. The viscoelasticity and the thixotropy of blood strongly depend on the formation and disruption of red blood cell aggregates and any disturbance in these mechanical parameters can alter the micro and macrocirculation by initiating stasis zones, enhancing thrombus formation, and favoring tissue ischemia [131]. It would consequently be relevant to assess *in vivo* the hemorheological disorders of patients and to take them into account in conventional cardiovascular risk profiles [111].

Classical tissue characterization techniques consist of finding the frequency dependence of attenuation and backscatter properties of the material and using them as acoustical indicators of the underlying microstructure. This was proven useful to detect diseased tissues in several clinical applications. Infarcted myocardium [219], atherosclerotic carotid arteries [203] or cirrhotic livers [201] were shown to have scattering properties that differ from their healthy counterparts. Spectral characterization of blood backscattering has already been performed experimentally [84, 232, 216] and has shown sensitivity to the microstructural packing state of the red blood cells. Theoretical efforts have been made to elucidate the relation between the backscattering properties of blood, usually quantified by the value of the backscattering coefficient, and the frequency of the incident wave, the hematocrit, the flow condition (steady state or turbulent), or the red cell aggregation level [17, 81, 140, 204, 213]. Twersky [213] proposed a parameter called packing factor to describe the backscattering coefficient of a distribution of hard particles. The primary assumption of this theory is that the spatial scale of the inhomogeneities in acoustical impedance must be much smaller than the acoustical wavelength.

This approximation succeeds to explain the hematocrit dependence of the backscattering by non-aggregating suspensions of red cells but fails to predict the frequency dependence observed in experimental conditions when red cell aggregation is significant. As the packing factor is independent on the frequency, the backscattering

coefficient is expected to increase linearly with the fourth power of the frequency [144] in the low frequency approximation. However Yuan and Shung [232], Foster et al. [84], and Van der Heiden et al. [216] observed that the frequency dependence of blood is lower when the flow rate is decreased, and thus when the aggregation is enhanced for frequencies as low as 3.5 MHz.

These results suggest that the theoretical understanding of blood scattering at higher frequencies is incomplete. We propose to generalize the packing factor theory for higher frequencies by introducing the frequency-dependent structure factor. It is intended to use it as a spectral signature of the aggregation process that is more relevant for ultrasonic characterization than a single measurement at a low frequency. The purpose of this study was to predict the frequency dependence of the backscattering coefficient from blood characterized by different levels of red blood cell aggregation. It is hypothesized that the spatial pattern formed by the aggregates of red cells governs the backscattering strength of blood. Red cell positioning is modeled as a random spatial point-process and it is considered that red cell aggregation modifies the statistical parameters of this random phenomenon. The Neyman-Scott process (NSP) gives a random framework that is convenient for the analytical derivation of the backscattering coefficient. In this paper, the method used to theoretically predict the backscattering coefficient of a weak scattering suspension is described in section (3.4), then the NSP is introduced in section (3.5) to model red cell aggregation and to derive the analytical expression of the backscattering properties of blood. In section (3.6), results on the predicted effects of red cell aggregation on the backscattering coefficient are given, and the question of inferring descriptive aggregation parameters using experimental backscatter data is discussed.

3.4 Scattering by a suspension of weak scatterers

3.4.1 Decomposition of the backscattering coefficient

The propagation of an acoustic wave into a linear medium depends on the spatial distribution of density $\rho(\vec{x})$ and compressibility $\kappa(\vec{x})$, where $\vec{x}$ represents the spatial position. When these spatial functions are precisely known, the wave equation can be theoretically solved once the source parameters are given, and conveys the relation between the pressure measured at the surface of the receiver and the various acoustic properties of the medium. In a heterogeneous medium like blood, it would be difficult to describe accurately the exact spatial distributions of density and compressibility. This is why the propagation medium is seen, in this article, as a realization of a random process which can be characterized by statistical mean parameters that depict its macroscopical properties. Measurement of the backscattering properties of a sample of this material should provide clues on the value of these mean parameters as shown in this section.

In this paper, we assume that an ideal backscattering experiment (Fig. 3.1) consists of the insonification of a material volume V by a monochromatic pressure plane wave of intensity I_0 and by the measurement of the power dP of the backscattered wave into a small solid angle $d\Omega$. The result is expressed in normalized terms ($\mathrm{m}^{-1}.\mathrm{sr}^{-1}$) by the differential backscattering coefficient. If the incident plane wave has a wave vector $\vec{k}$ ($|\vec{k}| = \frac{2\pi}{\lambda}$, λ being the wavelength), the (differential) backscattering coefficient $\chi(\vec{k})$ is defined by:

$$\chi(\vec{k}) = \frac{dP}{I_0 \, d\Omega \, V}. \tag{3.1}$$

The fluctuations in density and compressibility within blood are supposed small enough to hypothesize that the Born approximation is valid. We also assume that the medium V is composed of $N = mV$ identical spherical particles whose centers are

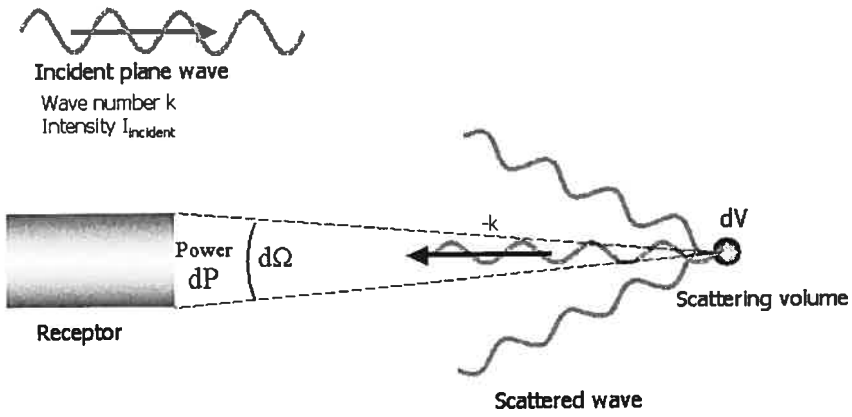

FIG. 3.1 – Scattering experiments and symbols.

positionned in $\Omega = (\vec{x_1}, \ldots, \vec{x}_N\}$, m being the number density of the particles. The N particles are embedded in a homogeneous medium (like the plasma) with a mean characteristic acoustical impedance Z_0.

These hypotheses allow to write the backscattering coefficient in the known factorized form [213]:

$$\chi(\vec{k}) = m\ S(-2\vec{k})\ \sigma_b(\vec{k}). \tag{3.2}$$

In Eq. (3.2) are introduced the structure factor $S(\vec{q}) = \frac{1}{N}|\sum_{i=1}^{N} e^{-\imath\vec{q}.\vec{x}_i}|^2$, function of the scattering vector $\vec{q} = -2\vec{k}$, and the backscattering cross-section of the individual scatterer $\sigma_b(\vec{k})$.

For weak scattering spherical particles of radius a and volume $\mathcal{V} = \frac{4}{3}\pi a^3$, the backscattering cross-section is given by [105]:

$$\sigma_b(\vec{k}) = \frac{1}{4\pi^2} k^4 \mathcal{V}^2 \langle \gamma_z \rangle^2 \Big(3 \frac{\sin(2ka) - 2ka\cos(2ka)}{(2ka)^3} \Big)^2, \tag{3.3}$$

where $\langle \gamma_z \rangle = (Z_p - Z_0)/Z_0$ is the small relative mismatch between Z_p, the particle impedance, and Z_0.

Equation (3.2) exhibits the expected result that the scattering strength of a tissue depends on the intrinsic acoustical properties of the scatterers, described by the backscattering cross-section $\sigma_b(\vec{k})$, and also on the spatial positioning of particles whose second order statistics are described by the structure factor $S(\vec{q})$. The aggregation phenomenon is supposed to only affect the structure factor, as red cell properties and hematocrit remain constant in the sample macroscopical volume.

3.4.2 Pair-correlation function of a point process and structure factor

The structure factor $S(\vec{q})$ can be influenced in a complex way by the hematocrit H, the geometric dimension of the particle and also by the physical factors governing the aggregation process. To theoretically estimate variations of the structure factor, the positioning of the scatterers in the medium is considered as a realization of a random point process, that obeys a random model with average parameters characterizing the aggregation level. Theoretically, a point distribution can be described by its microscopic density $N_\Omega(\vec{x})$:

$$N_\Omega(\vec{x}) = \sum_{i=1}^{N} \delta(\vec{x} - \vec{x_i}), \tag{3.4}$$

where δ is the Dirac δ-function and $\Omega = (\vec{x_i})_{i=1\cdots N}$ are considered as random positions of the scatterers. Writing $\widehat{N}_\Omega(\vec{q}) = \int N_\Omega(\vec{x}) e^{-i\vec{q}.\vec{x}}\, d^3x$ the Fourier transform of the microscopic density, the mean structure factor can be derived from the mean energy spectrum of $N_\Omega(\vec{x})$ by:

$$S(\vec{q}) = \frac{E[|\widehat{N}_\Omega(\vec{q})|^2]}{N}, \tag{3.5}$$

where $E[]$ represents the expected value of a random variable. The pair-correlation function $g(\vec{h}) = \frac{P(\vec{x}\in\Omega \text{ and } \vec{x}+\vec{h}\in\Omega)}{P(\vec{x}\in\Omega)\ P(\vec{x}+\vec{h}\in\Omega)}$, can be related to the structure factor. Writing $E[N_\Omega(\vec{x})N_\Omega(\vec{x}+\vec{h})] = m^2 g(\vec{h}) + m\delta(\vec{h})$, one derives [213] for $\vec{q} \neq \vec{0}$:

$$S(\vec{q}) = 1 + m \int (g(\vec{h}) - 1) e^{-\imath \vec{q}.\vec{h}}\, d^3h. \tag{3.6}$$

This formula shows that variations of the pair-correlation function induced by changes in the spatial organisation of the red cells will directly affect the structure factor and the scattering properties of blood.

3.4.3 Correlation length and corresponding scattering regimes

Depending on the relative values of the correlation length l_{cor}, defined by $|\vec{h}| > l_{cor} \Rightarrow g(\vec{h}) = 1$, and of the wavelength λ, two different aggregation regimes can be distinguished. This correlation length can be roughly seen as the diameter of the clusters present in the medium.

Rayleigh scattering

When $l_{cor} \ll \lambda$, we have the low frequency approximation that leads to the definition of the *packing factor* W, the zero-frequency limit of the structure factor. This happens when scatterers are aggregated in clusters much smaller than the wavelength. In this case,

$$\lim_{q\to 0} S(\vec{q}) = W = 1 + m \int (g(\vec{h}) - 1)\, d^3h, \tag{3.7}$$

and

$$\chi(\vec{k}) = mW\sigma_b(\vec{k}) \approx \frac{1}{4\pi^2} HWk^4\mathcal{V}\langle\gamma_z\rangle^2. \tag{3.8}$$

A medium with uncorrelated particles, corresponding to $l_{cor} \approx 0$ has thus a unit packing factor. A low hematocrit ($H < 5\%$) suspension of non-aggregating red blood cells can be approximated by such a model. The packing factor can be seen as a corrective factor that takes into account the correlations between positions of scatterers. The variations of the packing factor with the hematocrit, polydispersity and shape of hard particles have been theoretically studied by Twersky [27, 213]. For non-aggregating particles, W tends towards 1 when the hematocrit H is low, and vanishes when H is close to 100 %, because, in this case, heterogeneities giving birth to scattering no longer exist in the medium. The peak of low frequency backscattering, that arises when HW is maximal, occurs for $H_{max} \approx 13\%$ for non-aggregating spheres but can vary with the shape of the scatterers or with the polydispersity of the distribution [27].

By definition, W does not depend on the frequency. This low frequency approximation can thus only consider the fourth power frequency dependence (k^4) of the backscattering coefficient in the Rayleigh scattering regime.

Non-Rayleigh scattering and aggregation

At least two situations can provoke the irrelevance of the low frequency approximation: either when the acoustical frequency is increased (to obtain a better spatial resolution) or when the aggregation level is so elevated that the correlation length l_{cor} becomes non negligible compared to the wavelength. One can test the validity of these assumptions by estimating the frequency dependence of the backscattering coefficient, that should be proportional to k^4 under Rayleigh conditions.

Frequency dependences of the backscattering coefficient of whole blood as low as $k^{1.3}$ (in the frequency range of 22-37 MHz [216], at a shear rate under 1 s^{-1}) or $k^{0.4}$ (in the

range 30-70 MHz [84], at a shear rate of 0.16 s^{-1}) have been reported in the literature. This shows that the Rayleigh approximation is inappropriate to study scattering from aggregating red cells as a function of the frequency. A particular random spatial point process, the Neyman-Scott process (NSP), is proposed to predict the effect of aggregation on the backscatter data and to clarify the relation between the frequency and the backscattering coefficient.

3.5 Modeling of red cell aggregation by the Neyman-Scott process

3.5.1 Random point processes

We consider that the set of positions $\Omega = (\vec{x}_1, \ldots, \vec{x}_N)$ of the particle centers is the realization of a random spatial process, N being either constant or a random variable such as $E[N] = mV$. To fully characterize a point process, one can specify [182] the random numbers N_B of points falling into a compact set B included in V. The process of aggregation is supposed locally stationary in the sample volume, which implies that the random variable N_B depends only on the shape of B and not on the position of its center. The pair-correlation function can simply be seen as a second order property, when B is the pair of points $\{\vec{x}, \vec{x} + \vec{h}\}$:

$$g(\vec{h}) = \frac{P(\vec{x} \in \Omega \text{ and } \vec{x} + \vec{h} \in \Omega)}{P(\vec{x} \in \Omega)^2} = \frac{1 - 2P(N_{\{\vec{x}\}} = 0) + P(N_{\{\vec{x}, \vec{x}+\vec{h}\}} = 0)}{\left[1 - P(N_{\{\vec{x}\}} = 0)\right]^2} \tag{3.9}$$

Ω is said to be a Poisson process with number density m when N_B is a Poisson random variable with mean value $m\mathcal{V}(B)$, $\mathcal{V}(B)$ being the volume of B. In this case, Eq. (3.9) with $P[N_B = 0] = e^{-m\mathcal{V}(B)}$ gives $g(\vec{h}) = 1$. No spatial structure exists in the Poisson point process as the correlation length is zero, and this is why a Poisson point process

can be described as a complete random distribution. The evaluation of the structure factor gives, at all frequencies, $S(\vec{q}) = 1$. A stationary Poisson point process thus cannot be an appropriate model to simulate clusters of scatterers as encountered in certain red cell aggregation conditions.

3.5.2 The Neyman-Scott point process

The Neyman-Scott process is a random point process commonly used to model clusters of points. This random model efficiently described different statistical spatial data such as the positioning of trees in the forest [21], the distribution of precious stones in soil [39] or the patterns of rainfall cells [13].

The red cells are supposed to be grouped in clusters having random features obeying to the same probability law. We intend to characterize aggregate morphology by a small number of geometrical quantities taken as aggregation indices. However, the relation between the different physical interactions involved in the aggregation process (hydrodynamics, depletion or bridging effects of the plasmatic macromolecules, electrostatic forces) and the microstructural factors defining the configurations of erythrocyte clusters will not be directly modeled, as we only want to geometrically describe the aggregation level.

The basis of a realization of a NSP lies on a Poisson process Y with a number density m_0. Each point $\vec{Y}_i$ is the center of the i^{th} cluster surrounded by a random number $N_c(i)$ of points, sampled from a random variable N_c. To construct this cluster, $N_c(i)$ independent realizations $\{\vec{X}_{il}\}_{l=1...N_c(i)}$ of a random vector $\vec{X}$ are generated, and the $N_c(i)$ points $\vec{Y}_i + \vec{X}_{il}$ compose the cluster. The microscopic density $N_\Omega(\vec{x})$ can then be written as:

$$N_\Omega(\vec{x}) = \sum_i \sum_{l=1}^{N_c(i)} \delta(\vec{x} - \vec{Y}_i - \vec{X}_{il}). \tag{3.10}$$

The parameters needed to fully describe the NSP are thus :

1. the number density m_0 of the centers of clusters $\{\vec{Y}_i\}$,
2. the discrete probability density function $P(N_c = n)$ of the random number N_c of points per cluster,
3. the spatial probability density function $f_X(\vec{x})$ of the random vector $\vec{X}$ (with mean 0), that characterizes the cluster size.

The characteristic function and the first two moments of the discrete distribution N_B have already been computed [182] as a function of the moments of N_c ($n_c = E[N_c]$ and $\sigma_c^2 = \mathrm{Var[N_c]}$), of $f_X(\vec{x})$ and of the shape of B. The number density m equals $m_0 n_c$ and the pair-correlation function $g(\vec{h})$ can be determined and is given by:

$$g(\vec{h}) = 1 + \frac{1}{m}\left(\frac{\sigma_c^2}{n_c} + n_c - 1\right) \int f_X(\vec{x}) f_X(\vec{x} + \vec{h})\, d^3x. \tag{3.11}$$

According to Eq. (3.6), the structure factor can also be derived by computing the Fourier transform of $g(\vec{h}) - 1$:

$$S(\vec{q}) = 1 + \left(\frac{\sigma_c^2}{n_c} + n_c - 1\right) \left| \int f_X(\vec{x}) e^{-\imath \vec{q}.\vec{x}}\, d^3x \right|^2. \tag{3.12}$$

3.5.3 Aggregation parameters

The random spatial probability density $f_X(\vec{x})$ physically characterizes the spatial dimension of the clusters by determining the dispersion of the red cells around the center of an aggregate. We consider here the simplest random vector distribution to model $f_X(\vec{x})$, i.e. the Gaussian model with zero mean and covariance matrix $E[\vec{X}\vec{X}^T] = \Phi^T \Sigma_{NS} \Phi$. The diagonal matrix Σ_{NS} represents the spatial standard deviations in the principal axes, and the orthogonal matrix Φ is the matrix of the unitary principal axes $\{\vec{e}_1, \vec{e}_2, \vec{e}_3\}$ of the clusters. An anisotropic shape of the clusters would result in different eigenvalues $\{\sigma_1^2 \geq \sigma_2^2 \geq \sigma_3^2\}$ of the covariance matrix $E[\vec{X}\vec{X}^T]$.

On the contrary, if the clusters are isotropic, the covariance matrix takes a simple spherical form: $E[\vec{X}\vec{X}^T] = \sigma^2 I$, where I is the identity matrix.

The structure factor can then be analytically computed by using Eq. (3.12):

$$S(\vec{q}) = 1 + (\frac{\sigma_c^2}{n_c} + n_c - 1)\exp[-(\Phi\vec{q})^T \Sigma_{NS}(\Phi\vec{q})]. \tag{3.13}$$

If the clusters are isotropic, the pair-correlation function and the structure factor have a simpler expression:

$$g(\vec{h}) = 1 + \frac{1}{4\pi^{3/2} m \sigma^3}(\frac{\sigma_c^2}{n_c} + n_c - 1)\exp[-2^{-3/2}|\vec{h}/\sigma|^2], \tag{3.14}$$

and

$$S(\vec{q}) = 1 + (\frac{\sigma_c^2}{n_c} + n_c - 1)\exp[-|\sigma\vec{q}|^2]. \tag{3.15}$$

To link the spatial standard deviation σ, related to the gyration radius of the clusters, to the first two moments $\{n_c, \sigma_c\}$ of N_c, a fractal-like behavior is assumed by writing [74]:

$$\sigma/a = (n_c - 1)^{1/d}. \tag{3.16}$$

The fractal dimension d morphologically characterizes the growth process of the aggregates. Linear aggregates as the rouleaux have a fractal dimension close to 1, whereas compact spherical aggregates have a greater fractal dimension close to 3. As an isotropic model was adopted in the current study, d is related to the packing compactness of the aggregates. The distance between particles of the same cluster tends to decrease when d increases.

Combination of Eq. (3.15) and Eq. (3.16) yields the expression of the Gaussian isotropic structure factor :

n_c	W	Δ	σ/a
1	1	$+\infty$	0
5	6.3	0.35	2
15	19.7	0.19	3.7

TAB. 3.I – Values of the packing factor and of the size factor for the 2D simulations shown on Fig. (3.2),(3.3) and (3.4). The fractal dimension is $d = 2$.

$$S(\vec{q}) = 1 + (W - 1)\ \exp(-\frac{|a\vec{q}|^2}{2\Delta^2}). \tag{3.17}$$

Two non-dimensional aggregation parameters, W, the packing factor, and Δ, a size factor, contribute to $S(\vec{q})$:

1. $W = n_c + \frac{\sigma_c^2}{n_c}$ increases when the number of cells per aggregate grows. W can be seen as an indicator of the size of aggregates in terms of *number* of cells per aggregate. W is the limit of the structure factor when the incident frequency tends towards zero.

2. $\Delta = \frac{1}{\sqrt{2}}(n_c - 1)^{-1/d} = a/(\sqrt{2}\sigma)$ decreases when the spatial dimension of the cluster increases. This index Δ is related to the *spatial* extent of the clusters and controls the rate of decrease of the structure factor between W and 1, when varying the incident frequency.

Figures (3.2), (3.3) and (3.4) illustrate typical spatial patterns generated by the NSP. Three 2D realizations (2D simulations are here shown for convenience but all results presented in the rest of the paper are three-dimensional) are shown in a unit window with $H = 0.4$, $a = 0.01$, $d = 2$, and with N_c, taken as a random integer uniformly distributed between 1 and $2n_c - 1$, with $n_c = 1, 5$ and 15. Table (3.I) gives the packing factors and the size factors corresponding to these configurations.

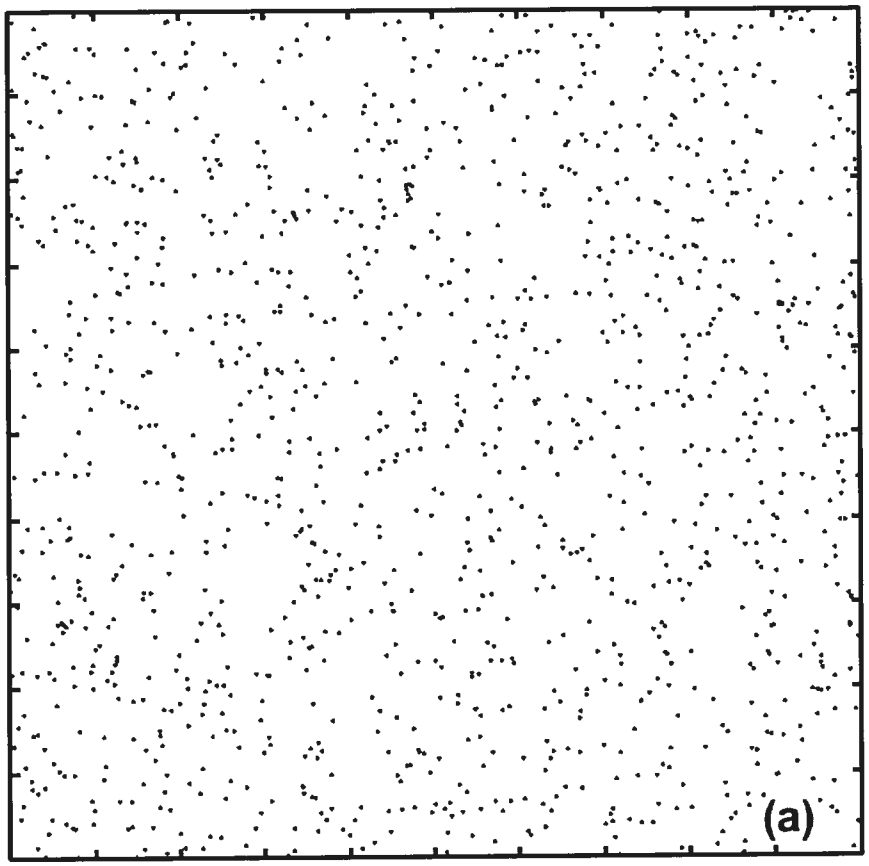

FIG. 3.2 – 2D realizations of a Neyman-Scott model in a unit window. $H = 0.4$, $a = 0.01$, $d = 2$. $N_c = 1$.

3.5.4 Analytical formulation of the backscattering coefficient

By substituting Eqs. (3.17) and (3.3) into Eq. (3.2), and noting that $H = m\mathcal{V}$, one obtains the backscattering coefficient of a medium composed of weak scattering spherical particles with an arrangement described by an isotropic Gaussian Neyman-Scott model:

$$a\chi^{\{W,\Delta\}}(k) = \frac{1}{3\pi}\, H(ka)^4 \langle\gamma_z\rangle^2 \left(3\frac{\sin 2ka - 2ka\cos 2ka}{(2ka)^3}\right)^2 \left(1 + (W-1)\, e^{-\frac{2(ka)^2}{\Delta^2}}\right). \tag{3.18}$$

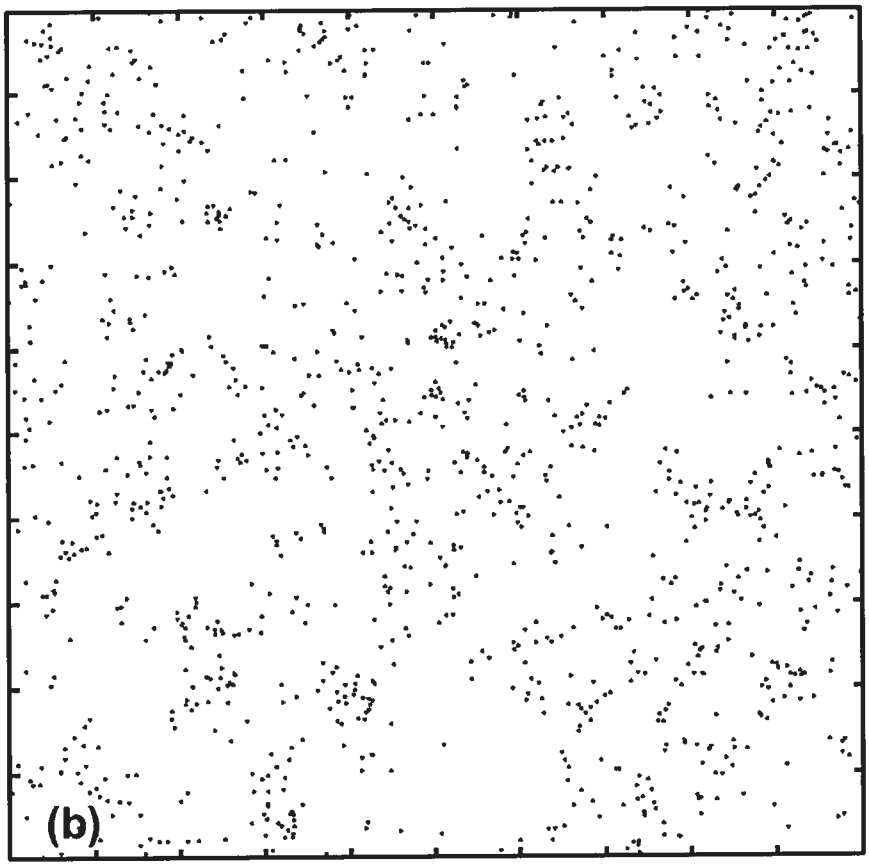

FIG. 3.3 – 2D realizations of a Neyman-Scott model in a unit window. $H = 0.4$, $a = 0.01$, $d = 2$. N_c is uniformly taken between 1 and 9.

3.6 Results and discussion

Because of the variations of the structure factor with the packing factor W and the size factor Δ, the backscattering coefficient of blood varies with the morphology of the red cell aggregates. Depending on the range of frequencies studied, the sensitivity of the backscattering coefficient to changes in aggregation properties can also vary. The proposed model allows to evaluate both the effect of the aggregate size, quantified by the first two moments of the random number of cells per aggregate, n_c and σ_c, and the effect of the geometrical compactness of the aggregates, described by the mass fractal dimension d. In this section, the effect of these factors on the frequency dependence

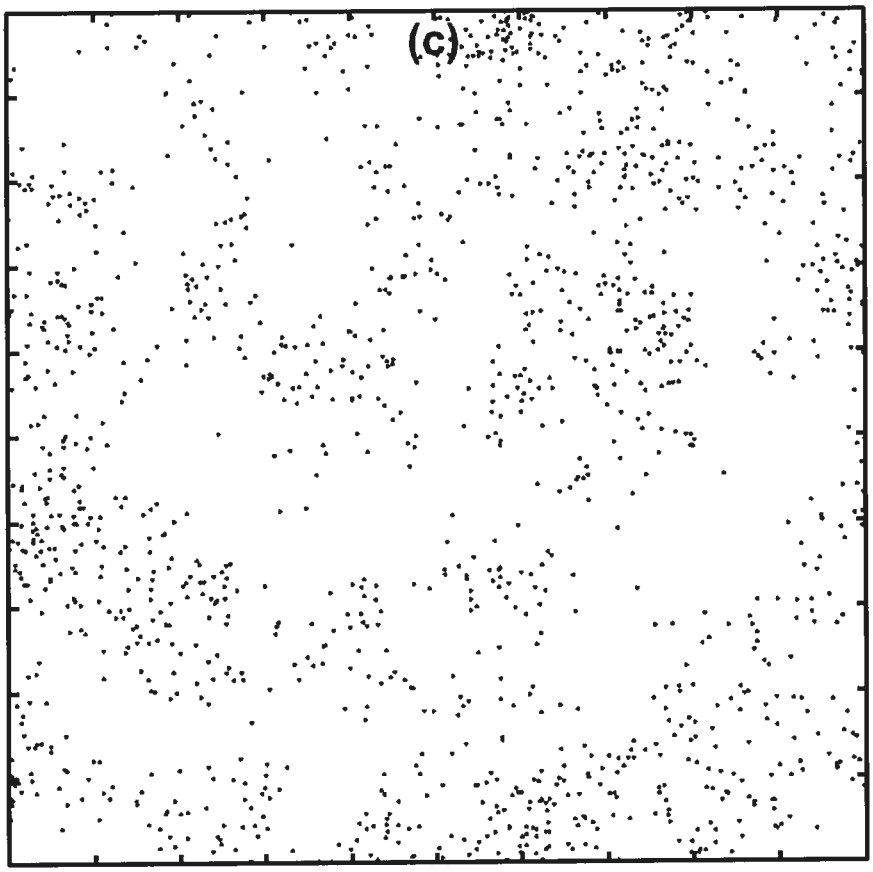

FIG. 3.4 – 2D realizations of a Neyman-Scott model in a unit window. $H = 0.4$, $a = 0.01$, $d = 2$. N_c is uniformly taken between 1 and 29.

of the backscattering coefficient is studied, and an inversion method is proposed to infer aggregation level of porcine red blood cells from experimental backscatter data previously reported in the literature [232].

3.6.1 Relation between the backscattering coefficient and the frequency

Figure (3.7) shows the relation between the backscattering coefficient of diluted porcine blood, computed by the model, and the incident frequency for varying sizes of aggregates ($d = 2$, $\sigma_c/n_c = 10\%$). The chosen hematocrit was $H = 4.5\%$. The radius

a of the red cells was 2.5 μm, and the relative impedance mismatch was chosen at 0.11 by taking published values [233] of the compressibilities and densities of the porcine red cells and of the plasma. The speed of sound c was assumed to be 1540 m.s^{-1}. Several features should be noted, depending on the range of frequencies studied.

- At very low frequencies, the red cells in a single aggregate are concentrated in a domain much smaller than the acoustical wavelength and consequently scatter coherently without phase delay. The aggregates can then be considered as single Rayleigh scatterers with an effective volume $W\mathcal{V}$. Since the central positions of the aggregates are spatially Poisson-distributed in the NSP (at this low hematocrit condition), the backscattered power is simply proportional to $W\mathcal{V}$, and thus is sensitive to variations of the number of cells per aggregate. Furthermore, Rayleigh scattering implies that the backscattering coefficient increases proportionally with k^4, as observed on Fig. (3.7).
- At very high frequencies, red cells are separated by distances corresponding to many wavelengths. Phases between backscattered echoes are then uniformly distributed between 0 and 2π and the structure factor $S(\vec{q})$ becomes 1. The backscattered power is no longer sensitive to the aggregation process but only to the intrinsic properties of the red cells. Figure (3.7) shows that all curves asymptotically approach this aggregation-independent form. When the frequency reaches $1.37 \times \frac{c}{2\pi a} = 134$ MHz (corresponding to the maximal backscattering cross-section of the red cell), the backscattering coefficient has a maximal value and then further decreases because of the progressive cancellation of the echoes scattered by the spherical particles. This results from the fact that the wavelets backscattered by boundaries of the particles interfere when the dimensions of the particle are comparable to the wavelength.
- The intermediate frequency range between the two previous scattering regimes is characterized by a decrease of the spectral slope $\frac{\partial \log \chi(k)}{\partial \log k}$. When the gyration radius of the aggregates is elevated, the size factor Δ decreases. This transition

then appears at lower frequencies and is more pronounced when the packing factor W has a high value. The experimental observation that the frequency dependence decreases in presence of red cell aggregates could be explained by this transitional scattering behavior: non-Rayleigh effects occur more markedly when aggregates are present.

3.6.2 Relation between the backscattering coefficient and the size of aggregates

Figure (3.5) shows the variations of the backscattering coefficient at three fixed frequencies (5 MHz, 15 MHz and 40 MHz) as a function of the mean number of cells per aggregate and fractal dimension d. A constant hematocrit $H = 4.5\%$ and a polydispersity characterized by $\sigma_c/n_c = 10\%$ were used for these computations. Results are presented in terms of the power increase (in dB) due to the aggregation in comparison with the disaggregated state (when $S(\vec{q}) = 1$).

The increase in backscattered power due to aggregation is conditioned both by the fractal dimension of the clusters and by the mean number of particles inside the aggregate.

When $n_c \ll (\lambda/a)^d$, the power increase is simply proportional to n_c : the suspension behaves as a collection of bigger particles with size σ that satisfies the Rayleigh hypothesis $\sigma \ll \lambda$. Combination of a compact growth of aggregates ($d \approx 3$) and of a low frequency insonification results in this type of scattering.

After this linear increase, the raise in power peaks and is controlled by the unphasing. The higher the frequency, the less pronounced is the relative increase of the backscatter due to aggregation.

A spatial growth of the aggregates, without variation of the number of cells per aggregate, would result in phase differences between echoes coming from the cells of the cluster and thus in a decrease of the backscattered power. On the other hand,

an increase of the number of scatterers in the clusters, keeping the aggregate volume constant, increases the scattering strength of each aggregate. These reasons explain why an increase of n_c has two competitive effects: an increase of the power due to the compaction of the aggregate, and a decrease of the power due to the spatial dilation of the aggregates resulting in incoherent echoes.

Generally, for a fixed number of cells per clusters, the power increase is bigger when the clusters are compact, and thus when d is closer to 3. The effect of the fractal dimension is more pronounced when the aggregates are bigger.

As shown by Fig. (3.5), in aggregative conditions, a level of backscattering coefficient ambiguously corresponds to two different values of n_c. Moreover, the fact that two factors, W and Δ, characterize the NSP, shows that at least two measurements must be accomplished to estimate their values. This therefore suggests that a good characterization of the aggregation phenomenon requires measurements on a large band of frequencies rather than at a single frequency. The following subsection gives a method to extract morphological informations on the aggregates by performing measurements over a whole range of frequencies. This can be technically achieved by using either a broad-band transducer that emits short pulses and by making a spectral analysis of the backscattered signal, or by using several transducers with different central frequencies.

3.6.3 Extraction of structural information on the aggregation level from backscattering experiments

On Fig. (3.6), mean results of backscattering experiments obtained by Yuan and Shung [232] are presented for porcine whole blood, circulating in a laminar shear flow, at a low hematocrit $H = 4.5\%$. The *in vitro* model, used by these authors, allowed to control the flow rate inside a cylindrical tube and consequently to modulate the aggregation level of the red cells by changing the mean shear rate. Five different

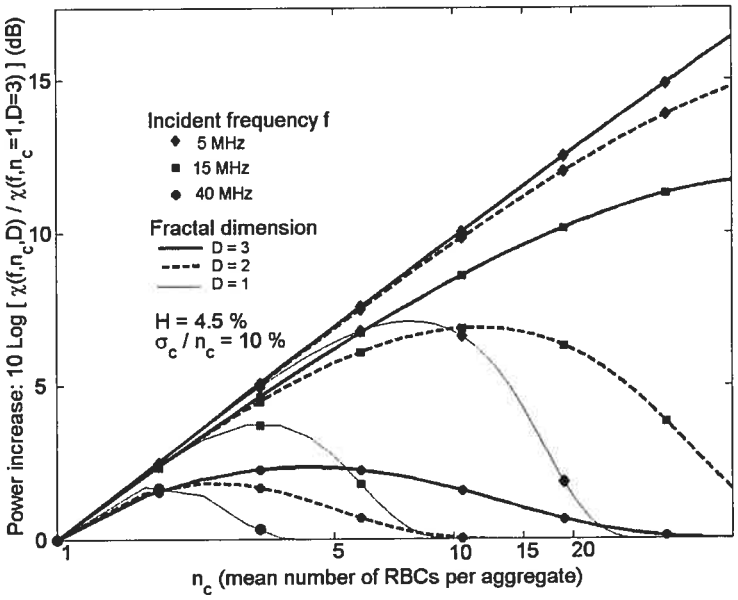

FIG. 3.5 – The backscattered power increase due to the aggregation of red blood cells as predicted by the Neyman-Scott modeling, as a function of the mean number of cells per aggregate n_c, for different frequencies and fractal dimensions of aggregates. The hematocrit is fixed at $H = 4.5$ % and the polydispersity is characterized by $\sigma_c/n_c = 10\%$. The reference power is the disaggregated state, when $n_c = 1$ and $\sigma_c = 0$.

transducers were used to study the frequency dependence of the backscattering coefficient. Mean backscattering coefficients measured for mean shear rates of 2 s^{-1}, 10 s^{-1} and 22 s^{-1} are shown (the plasmatic fibrinogen concentration, a protein that affects the level of aggregation, was kept constant at 210 mg/dL in the three experiments). As expected, at a fixed frequency, the backscattering coefficient decreased when the shear rate increased. The spectral slope is 4 at a shear rate of 22 s^{-1} and decreases with decreasing shear rate (a power law fitting between 3.5 MHz and 12.5 MHz gives a mean spectral slope of 3.7 for 10 s^{-1}, and 3 for 2 s^{-1}).

To assess the aggregation state of the red cells for these flowing conditions, a regression method was used to estimate the parameters W and Δ. The analytical expression of the structure factor obtained by the model was fitted to experimental structure factors

derived from experimental measurements of backscattering coefficients.

Supposing that the experimental backscattering coefficients $\{\chi_i\}_{i=1\cdots M_f}$ were measured at M_f different frequencies $\{f_i\}_{i=1\cdots M_f}$, the corresponding experimental structure factors $\{S_i\}_{i=1\cdots M_f}$ can be computed by using Eq. (3.2). Noting $k_i = \frac{2\pi f_i}{c}$ the sequence of wave numbers, one obtains:

$$S_i = \frac{\mathcal{V}\chi_i}{H\sigma_b(k_i)} \text{ with } \sigma_b(k_i) = \frac{4a^2}{9}(k_i a)^4 \langle\gamma_z\rangle^2 \left|3\frac{\sin 2k_i a - 2k_i a\cos 2k_i a}{(2k_i a)^3}\right|^2. \quad (3.19)$$

If the blood sample is characterized by the structure factor W and the size factor Δ, the theoretical structure factors at the same frequencies should be given by Eq. (3.17):

$$S_i^{theory} = 1 + (W-1)\exp(-\frac{f_i^2}{2f_0^2}\Delta^{-2}), \quad (3.20)$$

with $f_0 = \frac{c}{4\pi a} = 49$ MHz for porcine red blood cells.

A non-linear regression on the parameters $\{W, \Delta\}$ was performed by minimizing the mean quadratic error $J(W,\Delta)$ between the theoretical and the experimental values. It is a two variables optimization problem that consists on minimizing a least-square criterion:

$$J(W,\Delta) = \frac{1}{M_f}\sum_i \left(S_i - S_i^{theory}\right)^2 = \frac{1}{M_f}\sum_i \left(S_i - 1 - (W-1)e^{-\frac{f_i^2}{2f_0^2}\Delta^{-2}}\right)^2 \quad (3.21)$$

The Nelder-Mead simplex algorithm was used to solve this non-linear regression problem. The estimates $\{\widehat{W}, \widehat{\Delta}\}$ and the minimal value $J_{min} = J(\widehat{W}, \widehat{\Delta})$ correspond to the best prediction error $J_{min}^{1/2}$. The resulting curves of the frequency dependence of the backscattering coefficient appear in Fig. (3.6).

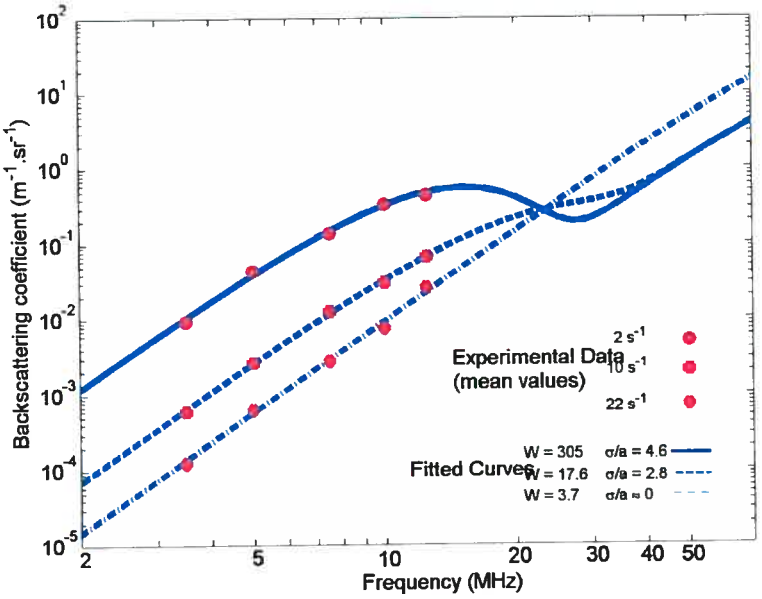

FIG. 3.6 – Experimental backscatter data obtained by Yuan and Shung [232] for porcine whole blood flowing at different shear rates, for a hematocrit $H = 4.5\%$. Fitted curves are also shown with estimated values of W(packing factor) and σ/a (normalized radius of the aggregates).

Table (3.II) gives the numerical values of the aggregation parameters obtained by this fitting procedure. The aggregate spatial extent $\widehat{\sigma}$ and the packing factor $\widehat{W}$ are both decreasing with the shear rate. The hypothesis of the disruption of the clusters with an increase of the shear forces is compatible with this tendency.

To reconstitute the aggregate morphology, the three variables $\{n_c, \sigma_c, d\}$ are required. But the non-linear regression only supplies two factors. In order to estimate the

Shear rate (s^{-1})	$\widehat{W}$	$\widehat{\Delta}$	$\widehat{\sigma}/a$	error $J^{1/2}_{min}$
2	305	0.31	4.6	21
10	17.6	0.51	2.8	0.8
22	3.7	$+\infty$	0	0.5

TAB. 3.II – Estimated values of the aggregation parameters corresponding to experimental data obtained by Yuan and Shung [232].

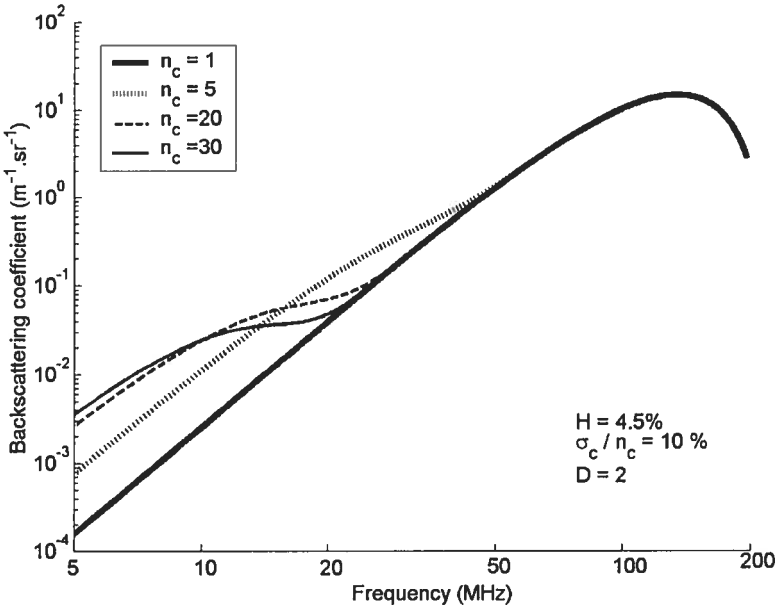

FIG. 3.7 – The backscattering coefficient of porcine blood as a function of the frequency for different aggregation conditions as predicted by the Neyman-Scott modeling.

moments n_c and σ_c of N_c, the fractal dimension d is supposed to be known. The estimated mean number $\widehat{n_c}$ of red cells per aggregate and the polydispersity $\widehat{\sigma_c}$ are computed by using the two relations $\widehat{W} = \widehat{n_c} + \frac{\widehat{\sigma_c^2}}{\widehat{n_c}}$ and $\widehat{\Delta} = \frac{1}{\sqrt{2}}(\widehat{n_c} - 1)^{-1/d}$. Table (3.III) gives the resulting values of $\widehat{n_c}$ and $\widehat{\sigma_c}$ for different fractal dimensions. Some fractal dimensions do not always allow the inversion of the relation, which shows that they may not be physically possible. For a shear rate of 10 s^{-1} *e.g.*, $\widehat{\sigma_c^2}$ is found negative for $d = 3$: the aggregates must have a lower fractal dimension than 3. For a high shear rate, the fractal dimension has a low impact because the size of the aggregates remains small.

Three-dimensional realizations of the NSP are generated to visually show the spatial organization of the red cell aggregates (Figs. 3.8,3.9,3.10). The random number of cells per aggregate (N_c) is supposed to follow a log-normal distribution [115] with the fitted variance and mean. The chosen hematocrit is still 4.5%. For these simulations,

Shear rate (s^{-1})	$\widehat{n_c}$ $d=1$	$\widehat{\sigma_c}$ $d=1$	$\widehat{n_c}$ $d=2$	$\widehat{\sigma_c}$ $d=2$	$\widehat{n_c}$ $d=3$	$\widehat{\sigma_c}$ $d=3$
2	5.6	40.9	22.1	79	98.3	143
10	3.8	7.2	8.8	8.8	23	impossible
22	1	1.6	1	1.6	1	1.6

TAB. 3.III – First moments (mean n_c and standard deviation σ_c) of the size histogram as a function of the mass fractal dimension d for the models fitted to the experimental data of Yuan and Shung [232].

we hypothesized that at a shear rate of 2 s^{-1}, the clusters are more compact and thus have a fractal dimension close to 3, whereas that for a shear rate of 10 s^{-1}, d is smaller (simulation is generated for $d = 2$). When the shear rate is 22 s^{-1}, the fractal dimension does not influence the structure because most of the aggregates are disrupted ($n_c \approx 1$).

3.6.4 Summary of the basic assumptions of the model, its strengths and limitations

In this study, blood is considered as a medium with weakly varying acoustical properties, as the mismatch between the red blood cell impedance and the plasmatic impedance is only 11%. This allows to use the Born approximation to relate the frequency-dependent backscattering coefficient to the characteristics of the spatial distribution of acoustical impedance. It was hypothesized that the red blood cells, that create the fluctuations of impedance, are all similar in shape, and that their relative positioning in the scattering volume results from a stationary random process. The influence of the intrinsic physical properties of the red cells on the backscattering properties of blood is well described by the backscattering cross-section σ_b of a spherical particle in the range of classical imaging frequencies. The influence of the red cell aggregation level is investigated by modeling the spatial density $N_\Omega(\vec{x})$ of the red cell positions by the Neyman-Scott point process. The complexity of modeling

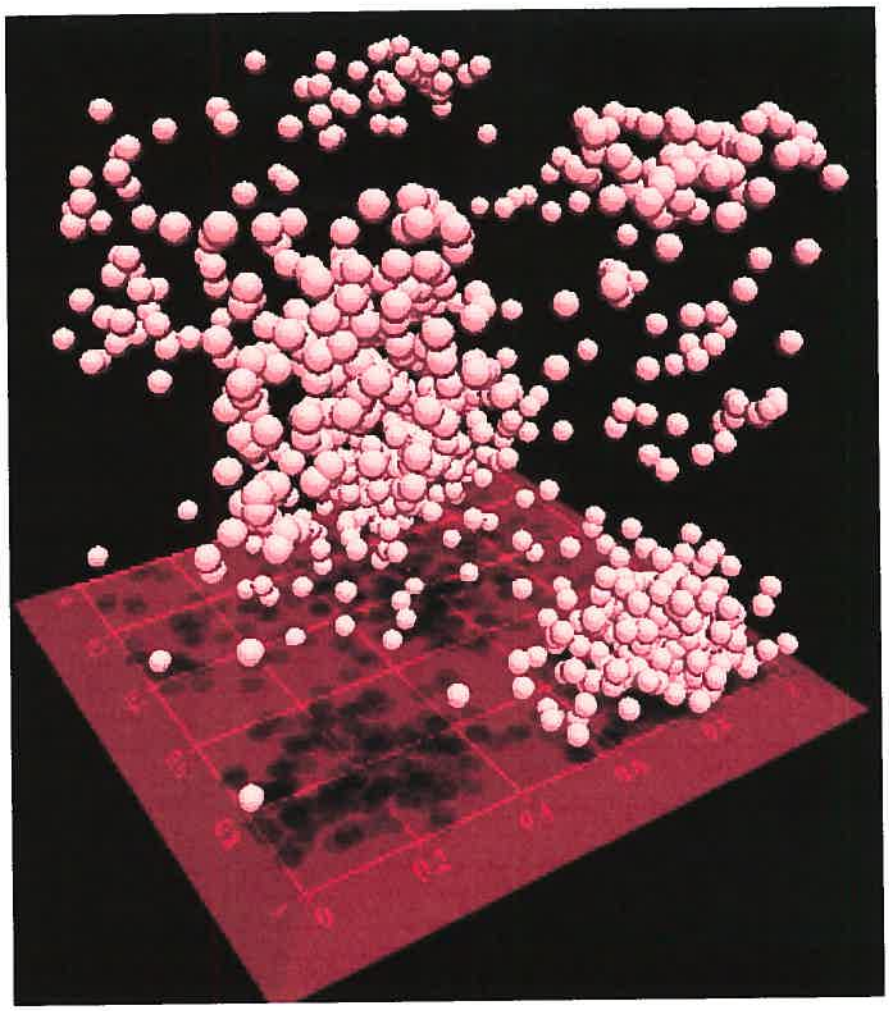

FIG. 3.8 – A realization of the Neyman-Scott process for fitted parameters n_c, σ_c and σ, corresponding to experiments with blood flowing at a 2 s^{-1} and a hematocrit $H = 4.5\%$. The fractal dimension d is 3. The simulation was generated in a cube with dimensions of 150 μm.

$N_\Omega(\vec{x})$ in physiological conditions comes from two reasons. First, the high density of the red cells (about 5×10^6 mm^{-3}), representing a normal hematocrit around 45%, imposes important restrictions on the random positioning of the red cells because of their non-overlapping. Second, the reversible aggregation process favors the creation of groups of red cells with varying morphologies. The NSP provides a statistical description of the aggregates by characterizing their number of cells and their spa-

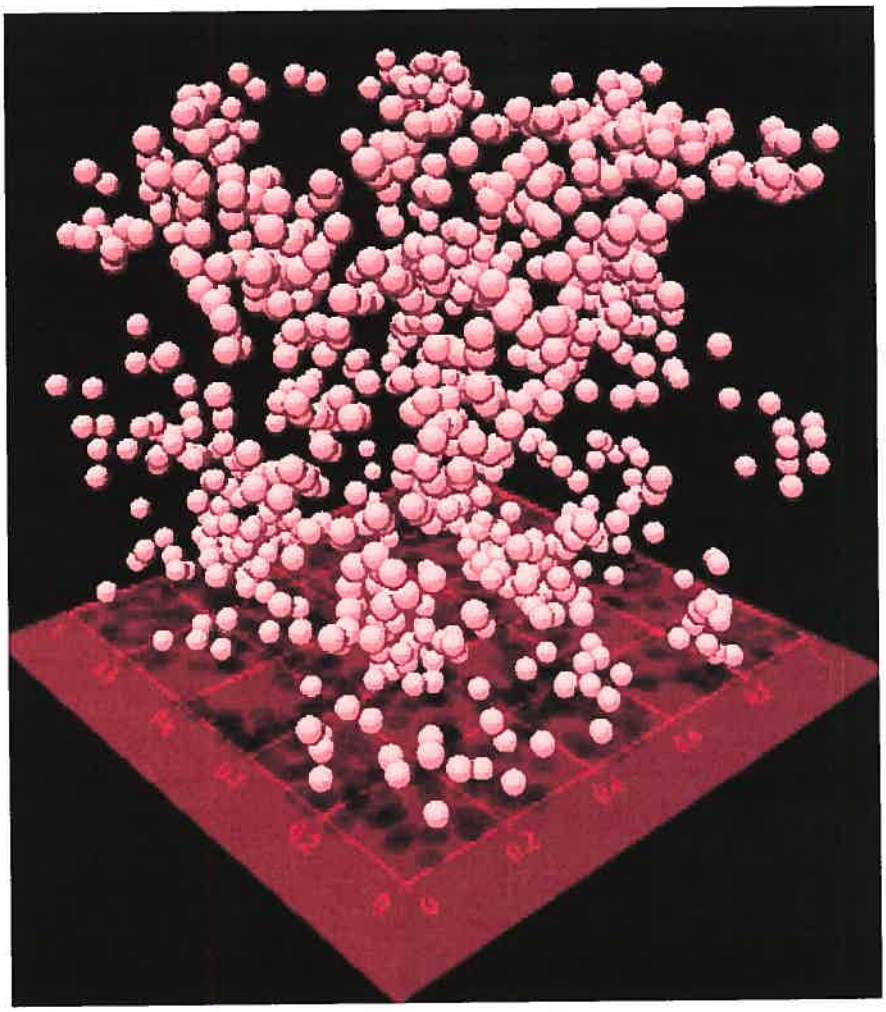

FIG. 3.9 – A realization of the Neyman-Scott process for fitted parameters n_c, σ_c and σ, corresponding to experiments with blood flowing at a shear rate of 10 s^{-1} and a hematocrit $H = 4.5\%$. The fractal dimension d is 2. The simulation was generated in a cube with dimensions of 150 μm.

tial extent. The main advantage of the NSP is the fact that it allows the analytical computation of the Fourier spectrum of $N_\Omega(\vec{x})$, which directly gives the frequency dependent structure factor. It gives a parametric model to the frequency dependence of backscatter experimental data, and provides meaningful morphological features of the aggregates ($\{W, \Delta\}$ or $\{n_c, \sigma_c\}$ when the fractal dimension d is known), that are more physically relevant for blood characterization than the absolute value of the

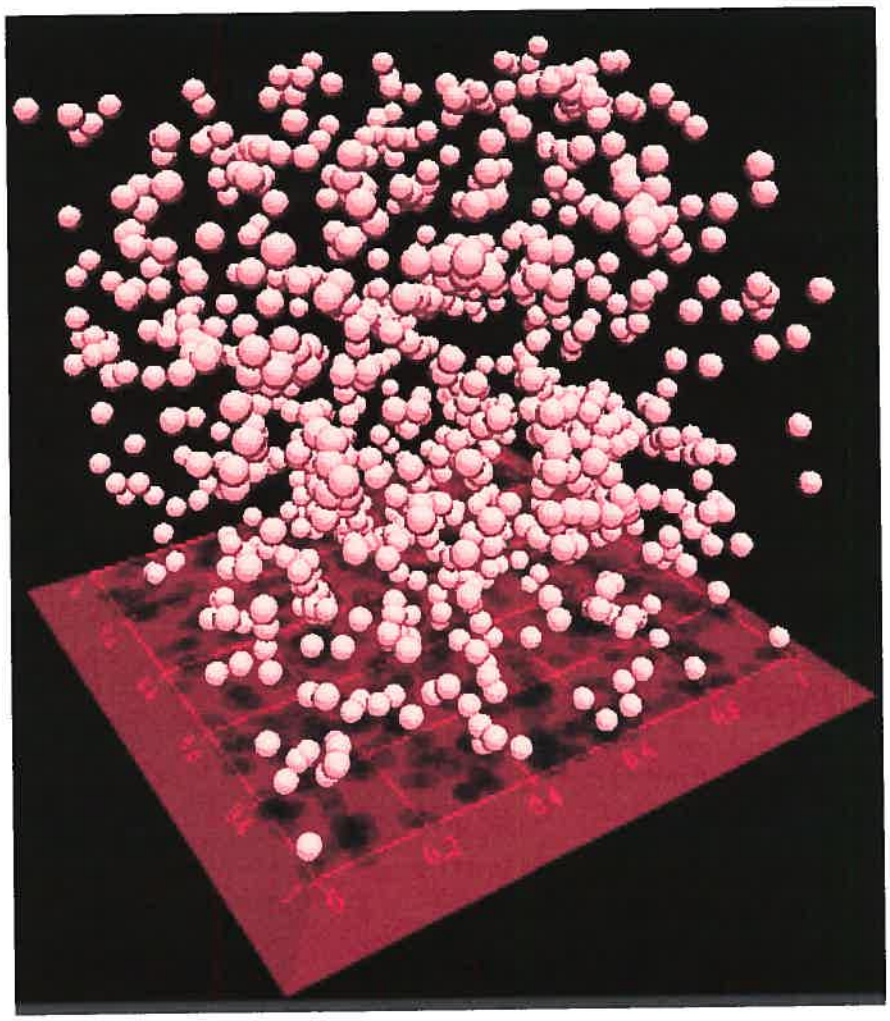

FIG. 3.10 – A realization of the Neyman-Scott process for fitted parameters n_c, σ_c and σ, corresponding to experiments with blood flowing at a shear rate of 22 s^{-1} and a hematocrit $H = 4.5\%$. The fractal dimension d is 1. The simulation was generated in a cube with dimensions of 150 μm.

backscattering coefficient or the spectral slope.

However, the simplicity of the NSP has a drawback: constraints imposed by the high hematocrit behavior are not taken into consideration. Equation (3.18) shows that the backscattering coefficient evolves linearly with the hematocrit when the medium is described by the NSP. But it is known, when the hematocrit is greater than a few percents, that the ultrasonic backscatter of blood tends to decrease. For non-aggregating

red blood cells ($n_c = 1$ and $\sigma_c = 0$), the value of the packing factor predicted by the NSP is 1, whereas in this case W was shown [212, 81] to be hematocrit-dependent (for spherical hard scatterers, the three-dimensional Percus-Yevick approximation yields $W \approx \frac{(1-H)^4}{(1+2H)^2}$). This non-linear relation between the hematocrit and the backscattering coefficient cannot be predicted by the NSP. Moreover, the NSP generates clusters of points that allows cells overlapping. When the medium is dense, this results in unrealistic realizations. Experimentally, the linear relationship between the backscattering coefficient and the hematocrit was shown valid [142] up to $H \approx 5\%$. One can therefore consider that the NSP is appropriate to model red cell aggregative configurations for a hematocrit under 5 %.

Despite these limitations, these results could be clinically valuable in hematological laboratories to study the erythrocyte aggregability for blood sample adjusted to a fixed low low hematocrit. In vitro scattering measurements with diluted red cell suspensions can provide flow dependence of $\{W, \Delta\}$, and would characterize the intrinsic properties of red cells to aggregate. It may be of interest to note that optical microscopic observations [49] of red cell aggregates, already used in research laboratories, are also performed at these low hematocrits for adequate morphological measurements.

One fundamental interest of the Neyman-Scott model was to distinguish intrinsic effects of the aggregation level on the backscattering from the effect of hematocrit. Non-Rayleigh effects associated with the growth of the gyration radius of the aggregates were related to the frequency dependence of the backscattering coefficient. However, to apply inference techniques to blood characterization with more physiological hematocrits (around 45 %) to predict physical parameters describing the aggregation process, spatial stochastic processes that can both describe dense and aggregative media will have to be studied for modeling red cell positionning. Unfortunately, more complex estimation techniques are required to characterize them because spectral properties of such random processes may not be analytically calculated.

3.7 Conclusion

Ultrasound backscattering properties of blood are dependent on the packing state of the red cells. It would be of interest to use this dependence to quantitatively measure the erythrocyte aggregation level by acoustical means. To reach this goal, a clear understanding of the relation existing between the variables describing the aggregation state and the backscatter data must be found. Most of the previous theoretical studies intended to clarify the hematocrit-dependence of the backscattering, or concerned low frequency backscattering by non-Rayleigh red cell aggregates. However, the influence of the aggregation level on the frequency dependence of the backscattering was not directly addressed whereas experimental results showed that at a low shear rate, aggregates of red cells cannot be considered as Rayleigh scatterers even at low frequencies.

To extend scattering theory to aggregating red cell suspensions, the spatial pattern due to the clustering was modeled by a random process. Considering that the erythrocyte positioning is the realization of a Neyman-Scott process, and using the Born approximation, the structure factor of a low hematocrit ($H < 5$ %) but aggregative suspension of red blood cells was predicted analytically, as a function of the size distribution of the aggregates and of their mass fractal dimension. This probabilistic framework conveyed a parametric model to extract the average size of the clusters of red cells and its polydispersity from backscatter data, assuming that the mass fractal dimension is known. Experimental measurements on a 4.5 % hematocrit porcine blood obtained by Yuan and Shung [232] were used to test the efficiency of the model. The disaggregation of the groups of red cells and the decrease of the polydispersity, both associated with an increase of the shear rate, could be determined by a regression technique.

The NSP represents a first step to the random modeling of the microstructural organisation of red blood cells, that helps to understand the frequency dependence of

the backscattering properties of blood due to aggregation. It must be emphasized that $S(\vec{q})$, the structure factor, is a crucial quantity to determine for blood characterization. It reflects the organization of the red cell network, equivalently to the pair correlation function. The zero-frequency limit of the structure factor, the packing factor W, is useful to describe low-frequency scattering (Rayleigh scattering). However, low frequency measurements only give limited structural informations, as Bascom and Cobbold pointed out [17], because the packing factor W does not uniquely define the pair correlation function as the structure factor does. A spatial random model, as the NSP, allows to characterize the spectral variations of the structure factor of a low hematocrit suspension by a small number of variables. This kind of parametric approach appears particularly useful when considering the experimental difficulties in reliably measuring backscattering coefficients of materials [134]. Substantial a priori knowledge of the frequency dependence is expected to compensate for the uncertainties of the measurements. The NSP highlighted two factors as the structure factor W and the size factor Δ, themselves related to meaningful geometrical properties of the red cell aggregates. For high hematocrits and aggregative suspensions, an appropriate model still remains to be found, to discriminate such significant factors and to use them as clinical indices of red cell aggregation.

3.8 Acknowledgement

This work was supported by the following grants:

- Studentship from the "Groupe de recherche en modélisation biomédicale" of the Institute of Biomedical Engineering of the École Polytechnique and Université de Montréal.
- Scholarship from the "Fonds de la recherche en santé du Québec".
- Grants from the Medical Research Council of Canada (# MOP-36467) – now the

Canadian Institutes of Health Research – and the Heart and Stroke Foundation of Québec.

We wish to thank Mrs Isabelle Fontaine for many helpful discussions and for reviewing the manuscript.

Chapitre 4

Modélisation de l'agrégation érythrocytaire par une approche de physique statistique

4.1 Avant-propos au chapitre

Ce chapitre est le manuscrit d'un article intitulé « Influence of red blood cell clustering and microstructure anisotropy on ultrasound blood backscatter. A Monte Carlo Study » par D. Savéry et G. Cloutier. Il représente une continuité logique au chapitre précédent. Nous avons précédemment fait le constat que l'hématocrite jouait un rôle crucial sur l'organisation spatiale des globules rouges. Présents au nombre de cinq millions par millimètre cube, les globules rouges sont soumis à d'importants effets stériques d'exclusion, que l'approche de Neyman-Scott ne pouvait pas prendre en compte. Afin de modéliser une suspension agrégeante d'hématies à un niveau d'hématocrite physiologique, nous avons retenu une approche plus « physique » en modélisant cette fois Ω par un processus ponctuel de Gibbs-Markov. Ce type de distribution aléatoire satisfait l'équation de Boltzmann établie pour un système de particules en équilibre thermodynamique. Les interactions interparticulaires sont modélisées par un potentiel d'énergie de paire, décrivant le non-chevauchement des hématies et leur adhésion à courte portée. Les simulations permettant d'estimer le facteur de structure de Ω ont été effectuées en deux dimensions. L'hématocrite considéré

dans l'étude a la valeur physiologique de 40%. L'effet de l'anisotropie de l'interaction cellule-cellule sur l'anisotropie de la rétrodiffusion ultrasonore est aussi investigué. Les résultats sont exprimés par le coefficient (isotrope) de rétrodiffusion à 5 MHz et les pentes spectrales (dans la bande de fréquences $0-40$ MHz) à 0° et 90° par rapport au grand axe des agrégats.

4.2 Abstract

When flowing at a low shear rate or in stasis, blood appears hyperechogenic on B-mode or power Doppler echographic images. Formation of red blood cell (RBC) aggregates accompanying the blood viscosity enhancement is the underlying mechanism explaining this backscatter increase. To quantitatively investigate the sensitivity of the blood backscattering coefficient to subresolution erythrocyte clustering, Monte Carlo simulations of the RBC spatial pattern were numerically performed. A 2D Markov random point process parameterized by an adhesive energy ϵ and an anisotropy index ν was used to model RBC positions in plasma for a volumic fraction $H = 40\%$. The frequency dependent backscattering coefficient of blood $\chi(f)$ was computed by assuming Born weak scattering conditions. The backscattering coefficient χ^0 at 5 MHz and the spectral slopes n_x, n_y (defined by $\chi(f) \propto f^n$ in the frequency range $0 < f < 40$ MHz) respectively parallel with and perpendicular to the cluster axis, were used to characterize blood sample microstructure. Under isotropic conditions ($\nu = 0$), χ^0 is shown to increase up to 7 dB when ϵ while $n_x = n_y$ decreases from 4.2 to 3.4. Under anisotropic conditions, χ^0 is angle invariant but $n_x < n_y$, the difference being more pronounced when increasing ϵ or ν. The accuracy of the ultrasonic determination of the RBC aggregation state based on the measurement of the scattering features (χ^0, n_x, n_y) was investigated using a pattern recognition approach. An accuracy of 89 % was obtained for distinguishing a disaggregated blood, while classification success

rates for isotropic/anisotropic clustered media were 51 and 45 %. Misclassification results are interpreted in terms of the intrinsic variance of the tissue properties and of limitations of the simulations. This study permits to relate macroscopic ultrasonic characteristics of blood, measurable non invasively, to relevant erythrocyte adhesion energetic features.

4.3 Introduction

Ultrasonic tissue characterization (UTC) techniques aim at diagnosing the pathophysiological state of an imaged tissue by detecting abnormalities in its acoustical properties (as backscatter, attenuation or speed of sound) using echographic means [190]. While textured B-scan images are commonly used to provide anatomical and morphological informations about the investigated organs, UTC echographic approaches can extract complementary diagnosis information by mapping the scattering and absorption properties of tissues, that B-scans cannot quantitatively provide. Biophysical and biochemical activities of the organs were shown to affect the acoustic features measurable by UTC. Cell apoptosis [183], myocardial ischemia [125], or osteoporotic loss of bone [153] are examples of pathological events that could potentially be investigated by these means.

In this paper, the sensitivity of blood scattering properties to the erythrocyte aggregation state is investigated. It represents a typical application of UTC for measuring biophysical phenomena (as cell adhesion) occuring at the micrometric scale, largely under the resolution of any commercial ultrasound (US) imaging system. In presence of plasmatic fibrinogen and at a low shear rate, flowing RBCs physiologically tend to gather and to form aggregates or *rouleaux* [50, 77]. As erythrocytes occupy a high volumic fraction (hematocrit) of about 40%, RBC clustering dramatically affects blood viscosity [38], blood echogenicity [191] and many other macroscopical physical pro-

perties (e.g. optical [75] or dielectric [47]). An abnormal level of RBC aggregation has pathophysiological consequences: increase of blood viscosity perturbates microcirculatory hemodynamics [109], influences the peripheral resistance [127], and is clinically correlated to risks of cardiovascular disease [130]. UTC would therefore be a convenient imaging modality to measure RBC aggregation *in vivo*, and indirectly blood rheology impairments, by detecting blood US backscatter abnormality. This would help to elucidate how hemorheology is involved in the etiology of cardiovascular diseases.

The frequency dependence of the backscattering coefficient $\chi = \chi(f)$ is commonly used as the characteristic US signature of a tissue [190]. In the range of acoustical frequencies covered by medical US transducers (typically 1-40 MHz), a power law $\chi/\chi_0 = (f/f_0)^n$ is often accurate enough to quantify this dependence, where f_0 is a reference frequency (in this paper, $f_0 = 5$ MHz), and $\{\chi_0, n\}$ are intrinsic tissue acoustic properties. Many experiments have shown that blood exposed to a high shear rate can reasonably be treated as a Rayleigh scattering tissue (extrapolating [84] to low frequencies, $\chi_0 = 1.3 \times 10^{-3}$ $\mathrm{m}^{-1}.\mathrm{Sr}^{-1}$, $n = 3.5$, for a shear rate $\dot{\gamma} = 32$ s^{-1}), whereas non-Rayleigh effects arise at a low shear rate ($\chi_0 = 2.8$ $\mathrm{m}^{-1}.\mathrm{Sr}^{-1}$, $n = 0.4$, for $\dot{\gamma} = 0.16$ s^{-1} in [84]). However, the sensitivity of the parameters $\{\chi_0, n\}$ to the erythrocyte aggregation level remains poorly documented. Moreover, an angular variation of these quantities is expected, based on the experimental work by Allard et al. [5].

This paper consequently investigates the sensitivity of $\{\chi_0, n\}$ to RBC aggregation and medium anisotropy using computer simulations. A quantitative description of the microscopic clustering of RBCs is firstly defined using a stochastic approach. The erythrocyte packing state is described by two statistical features and Monte Carlo simulations were used to predict the evolution of $\{\chi_0, n\}$ as a function of the aggregation state and of the insonification angle. The possibility to infer the packing

state of the RBCs using measured backscatter properties is then adressed.

4.4 Methods

An acoustical wave propagating in a linear fluid is scattered when encountering density and compressibility embedded inhomogeneities [144]. In this acoustical context, blood can roughly be seen as a biphasic fluid composed at $H = 40\%$ of RBCs immersed in the Newtonian plasma [57, 174]. Thus, blood backscatter depends on RBC intrinsic acoustical properties and on the geometry of the dense network that erythrocytes collectively form when flowing as aggregates. RBC adhesive and steric forces affect the conformation of this viscoelastic phase (while double layer electrostatic force is neglected because of its nanometric range). The microstructural pattern of the erythrocyte phase is modeled by a random Markov point process described in section (4.4.1), and the weak scatterer approximation is adopted to simulate blood backscattering properties (section 4.4.2). The ability to discriminate aggregating and non aggregating media by only measuring their backscatter UTC features is adressed in section (4.4.5) by using a pattern recognition scheme.

4.4.1 Microstructure model

Random configuration

Two-dimensional models were used in this study because of the computational burden of three-dimensional simulations. A collection of $N = mV$ undistinguishable red blood cells (m is the surface RBC density) was randomly spread on a square periodic surface V. The positions of the RBC centers, noted $\omega = (\vec{x}_1, \ldots, \vec{x}_N)$, jointly define a given configuration. Because of multiple intercellular interactions and hydrodynamic forces acting on cells, all configurations ω are not equally probable. A convenient class of random point process is the Gibbs-Markov stochastic model [217]. A Markov point

process Ω is defined by assigning an energy $U_\Omega(\omega) = U_\Omega(\vec{x}_1, \ldots, \vec{x}_N)$ to each configuration ω of the phase space V^N. This configuration energy is supposed independent of the rotations of the erythrocytes, and two-body interactions are only considered. By writing $V_2(\vec{h})$ the pair potential that represents the interaction energy of two RBCs separated by the intercellular lag $\vec{h}$, one defines $U_\Omega(\omega)$ by the summation:

$$U_\Omega(\omega) = \sum_{i<j} V_2(\vec{x}_i - \vec{x}_j).$$

At a fixed temperature T, the Gibbs-Markov process Ω has, by definition, a probability density function that obeys Boltzmann statistics:

$$p_\Omega(\omega) = \frac{1}{Z_\Omega} e^{-U_\Omega(\omega)/k_B T},$$

where Z_Ω is the normalizing partition function, and k_B is the Boltzmann constant. The choice of $V_2(\vec{h})$ completely defines Ω and therefore all statistical properties of the spatial pattern. In this study, RBC positions are modeled by a Markov point process, which enables to simulate the mean US backscattering coefficient χ as described below.

Choice of pair potential

An analytical expression for $V_2(\vec{h})$ was chosen to simulate non-overlapping of RBCs (hardcore potential) and the alignment of rouleaux along the flow streamlines. A velocity profile satisfying a steady-state simple shear flow along the Ox direction was considered. A computationaly convenient expression of $V_2(\vec{h})$ is empirically defined as follows. Let consider that each RBC center is surrounded by two concentric layers (fig. 4.1) : a forbidden circular zone covering the range of the steric forces, and a surrounding elliptic attractive area. The major axis a is aligned with Ox and the minor axis is noted b. The pair potential was defined as the sum of two energies: a repulsive

positive part that arises when forbidden zones overlap, and an adhesive negative part proportional to the intersection area of the attractive zones. Quantitatively, one writes:

$$V_2(\vec{h}) = V_{rep}\mathbb{I}_{[|\vec{h}|<2R]} - \epsilon\phi\left(\frac{1}{2}\sqrt{\left(\frac{h_x}{a}\right)^2 + \left(\frac{h_y}{b}\right)^2}\right),$$

where $\phi(u)$ is the function of the real variable u[1] defined by:

$$\phi(u) = \frac{2}{\pi}\mathbb{I}_{[|u|<1]}\left(\arccos u - u\sqrt{1-u^2}\right).$$

In the above equations, $\mathbb{I}_{[.]}$ is the indicator function, $V_{rep} \gg \epsilon$ is a constant set to a very large value, ϵ controls the adhesion strength and R represents the RBC radius. Fig. (4.2) shows the energy profile of the chosen pair potential $V_2(\vec{h})$. Two non-dimensional geometric parameters (λ_0, ν) are defined as follows:

$$\begin{aligned} \pi ab &= \pi(1+\lambda_0)^2R^2, \\ a &= (1+\nu)b. \end{aligned}$$

They represent respectively the reduced area of the attractive zone and the excess of the major on the minor axis, the eccentricity of the ellipse being given by $\sqrt{\nu(2+\nu)}/(1+\nu)$.

4.4.2 Scattering model

The ability of a material to generate acoustical echoes (fig. 4.3) can be quantified by the frequency-dependent backscattering coefficient χ [190]. For an heterogenous material composed of weak scattering particles, the expression of the backcattering

[1]The intersection of two identitical ellipses with parallel axes (a, b) and centers separated by the lag $\vec{h} = (h_x, h_y)$ has the area $\pi ab\ \phi\left(\sqrt{h_x^2/a^2 + h_y^2/b^2}/2\right)$.

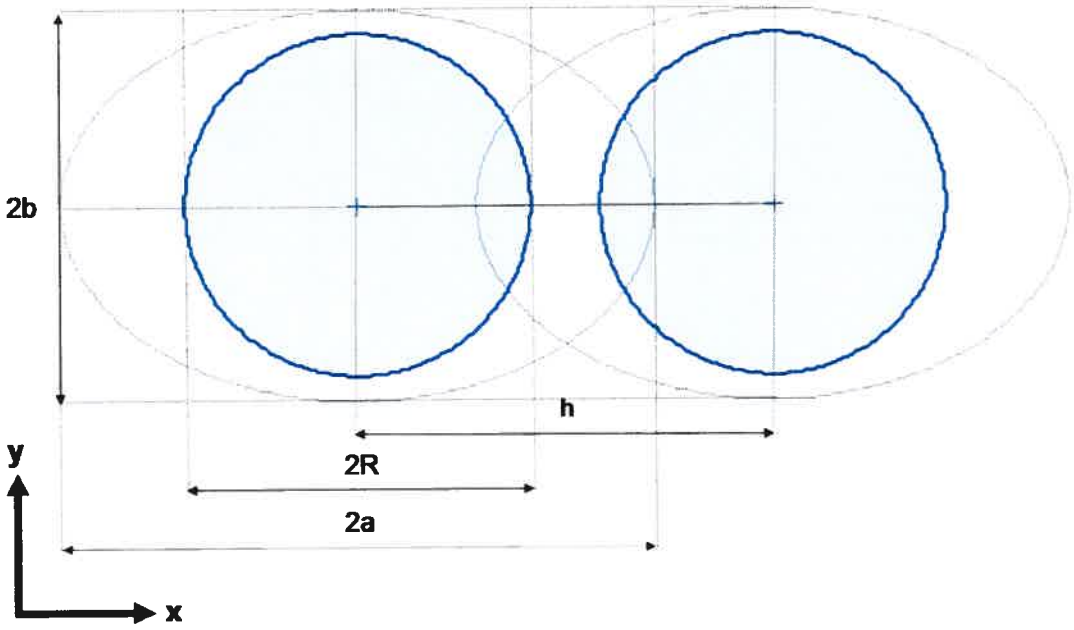

FIG. 4.1 – Geometrical parameters of the interaction ellipse and of the exclusion volume used in the model of pair potential.

coefficient can be factored [175, 212] under the form:

$$\chi(\vec{k}) = mS(-2\vec{k})\sigma_b(\vec{k}), \tag{4.1}$$

where $\vec{k}$ is the incident wave vector ($k = 2\pi f/c$, where f is the interrogating acoustical frequency and $c \sim 1540$ m.s^{-1} is the sound speed), and $\sigma_b(\vec{k})$ is the backscattering cross-section of a single scatterer. The function $S(\vec{q})$ is the mean structure factor [81] of the random configuration Ω of N points, defined for a given scattering vector $\vec{q}$ (noting $\imath = \sqrt{-1}$) by:

$$S(\vec{q}) = E\left[\frac{1}{N}\left|\sum_{\vec{x}\in\Omega} e^{-\imath\vec{q}.\vec{x}}\right|^2\right]. \tag{4.2}$$

The structure factor quantifies the specific effect of the random organization of the scatterers on the backscattering coefficient. For uncorrelated scatterers (i.e. when Ω

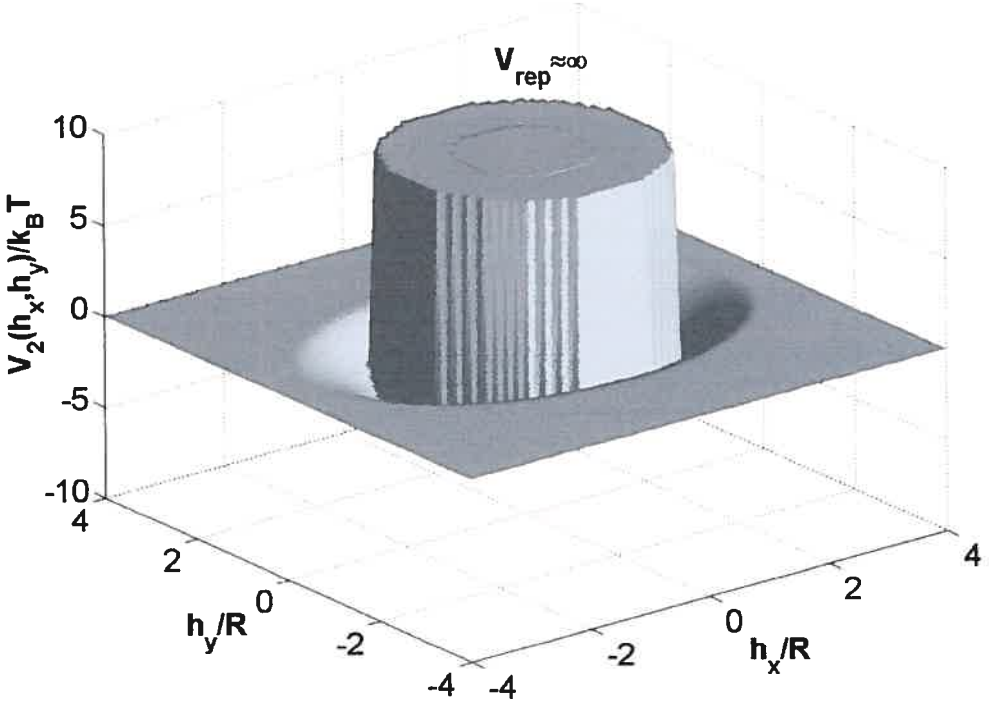

FIG. 4.2 – Energy profile of the pair potential $V_2(\vec{h})$.

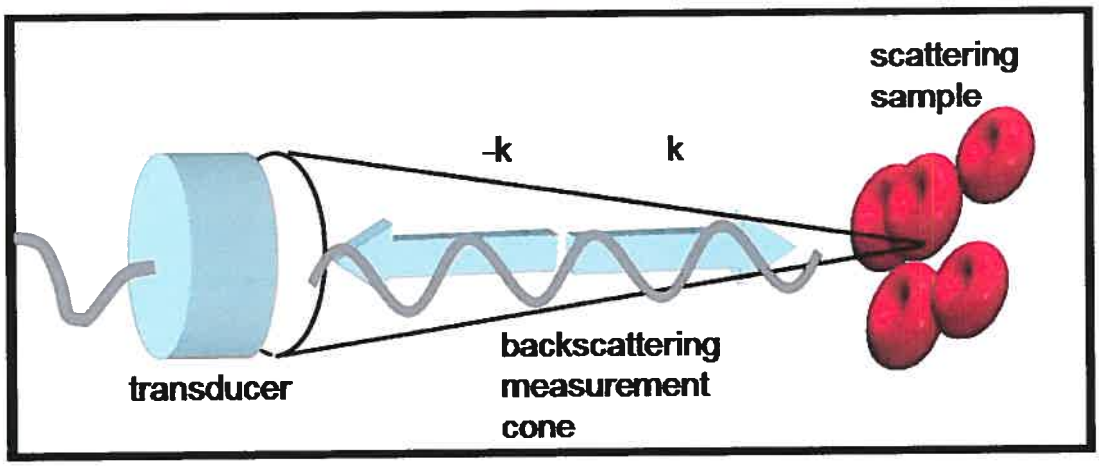

FIG. 4.3 – Schematical description of the scattering experiment.

is a spatial homogeneous Poisson point process, the reference distribution), $S(\vec{q}) \equiv 1$. The backscattering cross-section $\sigma_b(\vec{k})$ is the area of the perfect plane reflector that backscatters the same power than a single red blood cell. RBCs were modeled as aligned weak scattering cylinders of radius R and volume $\mathcal{V}$, that have a small acoustical impedance contrast $\langle \gamma_z \rangle = 0.11$. This assumption allows us to apply the Born approximation [144], and to analytically derive the cross-section perpendicularly to their axis [63]:

$$\sigma_b(\vec{k}) = \frac{1}{4\pi^2} k^4 \mathcal{V}^2 \langle \gamma_z \rangle^2 \left(\frac{j_1(2kR)}{kR} \right)^2, \tag{4.3}$$

where j_1 is the Bessel first order function.

4.4.3 Monte Carlo simulation technique

Simulations of the random point process Ω were generated to estimate the mean structure factor $S(\vec{q})$ and to assess the variance of the sample structure factor. A Monte Carlo Markov chain of configurations was generated to simulate realizations of Ω. The classical Metropolis sampler [137] was the adopted simulation algorithm. It consists of a random walk $(\omega_0, \ldots, \omega_n, \ldots)$ in the phase space V^N that starts from any configuration ω_0 and asymptotically reaches a random sample of Ω. The following iterative procedure was used for a step (n) to $(n+1)$, considering that the current configuration is $\omega^{(n)} = (\vec{x}_1^{(n)}, \ldots, \vec{x}_N^{(n)})$:

- pick at random the particle labelled I uniformly in $\{1, \ldots, N\}$ located in $\vec{x}_I^{(n)}$,
- a new position $\vec{x}_{new}$ is chosen at random, uniformly in V,
- compute the energy change ΔU of the total energy U_Ω, due to a displacement of the particle I from $\vec{x}_I^{(n)}$ to $\vec{x}_{new}$, assuming that V has periodic boundaries,
- define the Metropolis ratio $q = \exp(-\Delta U / k_B T)$,
- generate a uniform random quantity $p \in [0, 1]$,

R	3.5 μm
λ_0	0.4
N	815
L	280 μm
M_i	32600
c	1540 m.s^{-1}
V_{rep}	$10^6\ k_BT$

TAB. 4.I – Monte Carlo simulation parameters.

– if $p \leq q$ then $\vec{x}_I^{(n+1)} = \vec{x}_{new}$ else $\vec{x}_I^{(n+1)} = \vec{x}_I^{(n)}$,

– other positions remain unchanged and $\omega_{n+1} = (\vec{x}_1^{(n)}, \ldots, \vec{x}_I^{(n+1)}, \ldots, \vec{x}_N^{(n)})$.

Values of the different simulation parameters used in the study are given in table (4.I). A Markov chain of $M_i = 40N$ Metropolis steps is generated to obtain a sample ω of the random point process. For each simulation, a map N_{ij} of the particle density is processed by dividing the square simulation plane $V = L^2$ in N_p^2 pixels and by computing the number of particles N_{ij} falling into each pixel (i, j). This matrix is used for the computation of the structure factor using the following method. The array N_{ij} is simply the sampling of the microscopic density $N_\Omega(\vec{r})$, which is defined by:

$$N_\Omega(\vec{r}) = \sum_{\vec{x} \in \Omega} \delta(\vec{x} - \vec{r}),$$

where δ is the Dirac function and $\vec{r}$ is the current point inside V. As the structure factor is related to the microscopic density by a Fourier transform,

$$S(\vec{q}) = \frac{1}{N} \left| \int_V N_\Omega(\vec{r}) e^{-\imath \vec{q}.\vec{r}} d^2r \right|^2,$$

one can compute $S(\vec{q})$ by performing a 2D Fast Fourier Transform of the density matrix N_{ij}. This gives the structure factor values $S(-2\vec{k})$ on a centered grid of wavevectors, regularly spaced by $\Delta k = \pi/L$ and maximal wavenumber $\pi N_p/2L$. The sample backscattering coefficient is finally assessed on each pixel of the wavevector

grid using the structure factor values and the equations (4.1) and (4.3). After averaging several independent sample backscattering coefficients, the mean backscattering coefficient can also be estimated as a function of the model parameters $\epsilon, \nu, \lambda_0, m, \ldots$

4.4.4 Data reduction and tissue acoustic properties

Having estimated the function $\chi(f_x, f_y)$, the amount of backscatter data characterizing each sample was reduced by computing four UTC parameters $(\chi_x^0, \chi_y^0, n_x, n_y)$ summarizing the frequency and angular dependence of χ on the frequency range $0 - 40$ MHz. They were obtained by performing two power-law regressions along the two orthogonal principal directions (Ox) and (Oy):

$$\begin{aligned} \chi(f_x, 0) &= \chi_x^0 (f_x/f_0)^{n_x}, \\ \chi(0, f_y) &= \chi_y^0 (f_y/f_0)^{n_y}. \end{aligned}$$

A reference backscattering level at $f_0 = 5$ MHz, χ_{ref}, was defined by the formula $\chi_{ref} = mW_0\sigma_b^0 = 2.84 \times 10^{-4}$ m^{-1}.Sr^{-1}, where $W_0 = (1-H)^3/(1+H)$ is the Percus-Yevick (PY) packing factor [212] for 2D hard disks and volumic fraction $H = 0.4$, and σ_b^0 is the RBC cross-section at 5 MHz, computed using eq. (4.3). The quantity W_0 is expected to accurately describe the low frequency structure factor of a non-aggregating suspension of RBCs. As Shung et al. [188] experimentally demonstrated that the PY approximation was valid to describe scattering by non-aggregating RBCs, one could postulate that the PY approach should also be accurate in 2D. A backscatter feature vector $\vec{V} = [V_1, V_2, V_3, V_4]^T$ is defined hereafter to characterize the scattering properties of a given sample in a 4D-feature space:

$$
\begin{aligned}
V_1 &= 10\log_{10}(\chi_x^0/\chi_{ref}), \\
V_2 &= 10\log_{10}(\chi_y^0/\chi_{ref}), \\
V_3 &= n_x, \\
V_4 &= n_y.
\end{aligned}
$$

The two components V_1, V_2 represent the backscatter enhancement at 5 MHz (in dB) due to clustering, in comparison with the theoretical disaggregated medium, and V_3, V_4 represent the spectral slopes of the backscatter frequency dependence on the range $0 - 40$ MHz.

4.4.5 Descriptive power of the tissue acoustic properties

To assess to which extent the acoustical features $\vec{V}$ can be used to infer the microstructure of a sample as defined by (ϵ, ν), a statistical pattern recognition scheme is adopted. Three types (C_1, C_2, C_3) of aggregating conditions were defined by partitioning the plane $(\epsilon/k_BT, \nu) \in [0; 150] \times [0, 1]$ as follows:

- $C_1 : (\epsilon/k_BT, \nu) \in [0; 5] \times [0, 1]$,

- $C_2 : (\epsilon/k_BT, \nu) \in]5; 150] \times \{0\}$,

- $C_3 : (\epsilon/k_BT, \nu) \in]5; 150] \times]0, 1]$.

The class C_1 is the non-aggregating class, C_2 represents the isotropic aggregation conditions, and anisotropic clustering conditions are assembled in class C_3. A training set of 2800 samples was generated to assess the statistical characteristics of the three

classes:

- the means $\vec{m}_i = E[\vec{V}|\vec{V} \in C_i]$, $i = 1, 2, 3$,

- and the variance-covariance matrices $\Gamma_i = E[\vec{V}\vec{V}^T|\vec{V} \in C_i] - \vec{m}_i\vec{m}_i^T$.

Assuming that $\vec{V}$ follows a normal distribution in each class, one can build a simple maximum-likelihood classifier [207] that takes the form:

$$\hat{C}(\vec{V}) = \text{argmin}_i\Big((\vec{V} - \vec{m}_i)^T\Gamma_i^{-1}(\vec{V} - \vec{m}_i) + \ln|\det(\Gamma_i)|\Big).$$

A test set of 3×1000 samples chosen in the three classes, with $(\epsilon/k_BT, \nu)$ uniformly drawn in each defined partition was generated to assess the classifier quality. The classification quality was quantified by a 3×3 matrix (e_{ij}) computed on the test set:

$$e_{ij} = P\left(\hat{C}(\vec{V}) = i|\vec{V} \in C_j\right).$$

Diagonal terms indicate the chances of recognition success whereas non-diagonal ratios indicate misclassifications rates.

4.5 Results

4.5.1 Spatial pattern of aggregated cells

The growth, orientation and organization of RBC clusters in response to different aggregation conditions can be visualized in figure (4.4). One realization of the point process is represented for selected values of (ϵ, ν). The steric repulsion has a clear impact on the particle spatial organization. Increasing ϵ results in cluster growth, whereas ν modulates structure anisotropy, not independently of the cluster size. When ν deviates from zero, RBCs form aligned layers of linear clusters, whereas when $\nu = 0$,

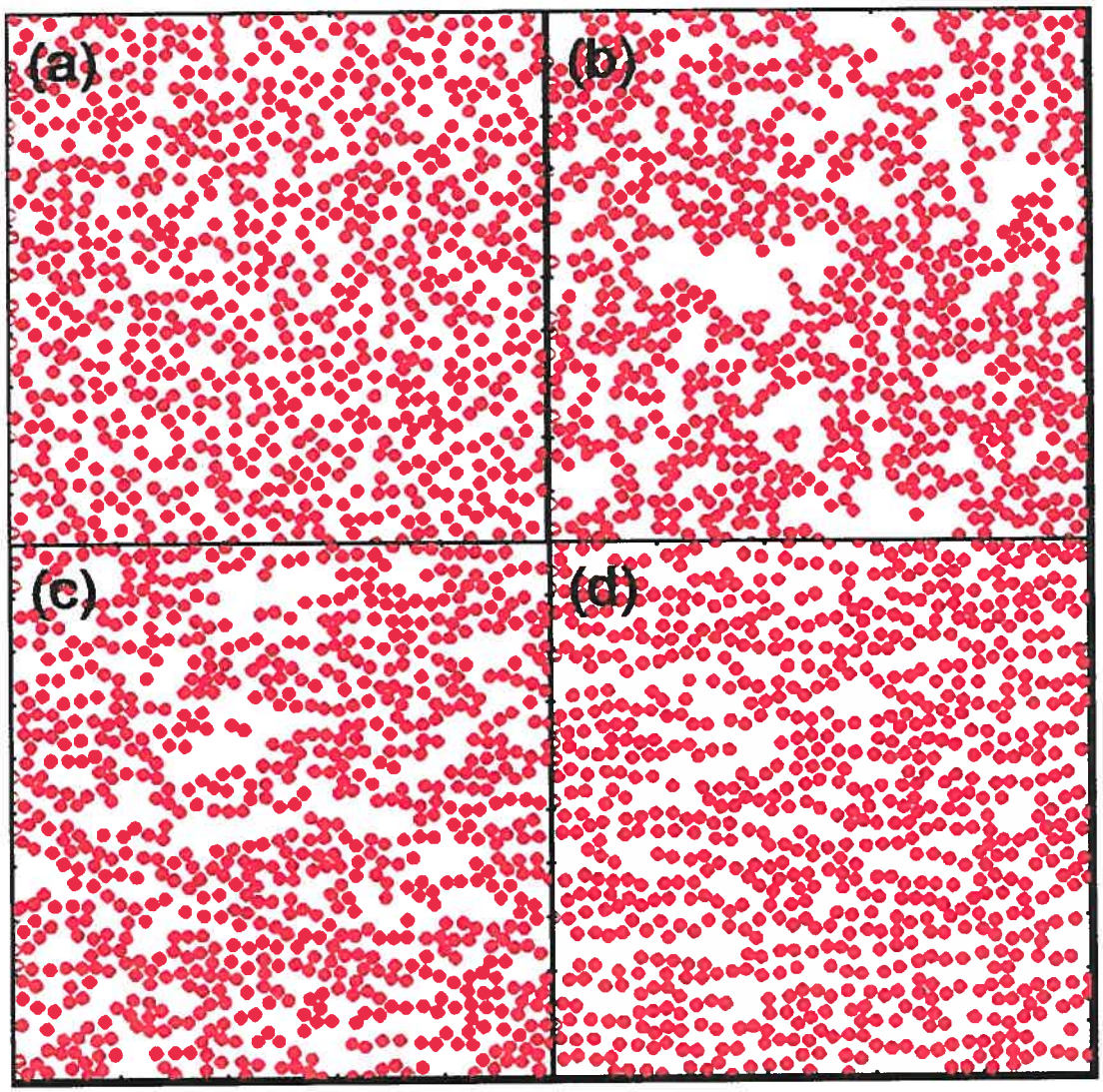

FIG. 4.4 – Realizations of the random point process Ω for different statistical parameters. From upper left to bottom right: (a): $\epsilon = 0, \nu = 0$, (b): $\epsilon = 150 k_B T, \nu = 0$, (c): $\epsilon = 50 k_B T, \nu = 0.5$, (d): $\epsilon = 150 k_B T, \nu = 1$.

no particular growth direction is favored, which creates compact erythrocyte clumps.

4.5.2 Backscatter and frequency dependence

Variations of the mean backscattering coefficient in the frequency range 0-130 MHz are given in figure (4.5). The backscattering coefficient increases with the frequency,

Point process statistical parameters		Scattering properties (mean ± SEM, $n = 100$, $*: P < 0.01$, $**: P < 0.001$ paired t-test)			
ν	ϵ/k_BT	χ_x^0/χ_{ref}	χ_y^0/χ_{ref}	n_x	n_y
0	0	0.84 ± 0.06	0.79 ± 0.06	4.21 ± 0.04	4.18 ± 0.04
0	25	3.64 ± 0.23	3.87 ± 0.24	3.53 ± 0.04	3.51 ± 0.04
0	150	4.92 ± 0.33	5.08 ± 0.32	3.39 ± 0.04	3.38 ± 0.04
1	25	1.87 ± 0.14	1.91 ± 0.11	3.63 ± 0.04 **	4.16 ± 0.04 **
1	150	1.93 ± 0.15	1.84 ± 0.12	3.54 ± 0.04 **	4.21 ± 0.05 **

TAB. 4.II – Backscattering properties as a function of (ϵ, α).

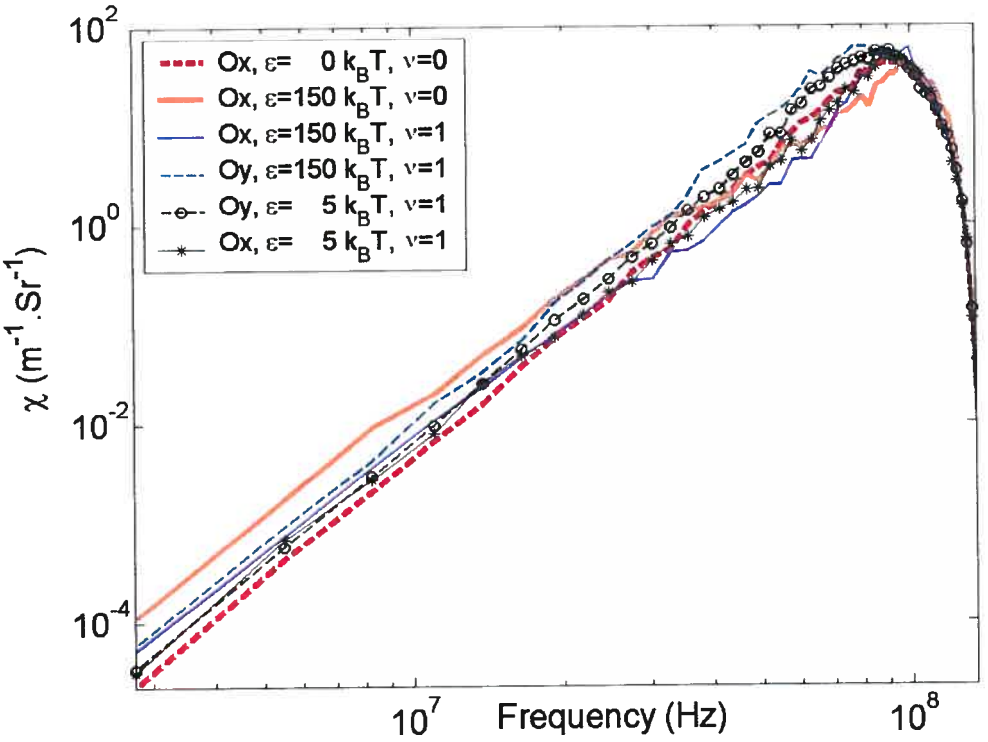

FIG. 4.5 – Frequency dependence of the backscattering coefficient for different aggregation conditions (ϵ: aggregation energy, ν anisotropy index) and insonification angles (Ox: velocity axis, Oy: perpendicular axis).

but at a rate that is specific to the RBC microstructure variables (ϵ, ν) and to the insonifying angle.

Isotropic conditions

Under isotropic conditions ($\nu = 0$) and when ϵ increases, the backscatter at a fixed frequency increases and the curve $f \rightarrow \chi(f)$ bends. The angle of insonification does not influence the backscattering coefficient (data are not shown on fig. (4.5) for sake of clarity). The backscatter at 5 MHz increases with the adhesion energy, reaching a plateau value $\sim 5\chi_{ref}$. The curve bending can be quantified by the variations of (n_x, n_y). The spectral slopes appear in fig. 4.7 as a function of the adhesion energy. For $\nu = 0$, their values do not significantly differ. Their value decrease from 4.2 (disaggregated medium) to 3.4 ($\epsilon = 150 k_B T$).

Anisotropic conditions

Anisotropic behavior arises when $\nu > 0$. It is revealed by an angular dependence of the blood scattering properties and also by changes in the low frequency echogenicity. For $\epsilon > 0$, the spectral slope along Oy is greater than along Ox (paired t-tests, $n = 100$, $P < 0.001$, for $\nu > 0.2$ and $\epsilon > 0$) as shown on fig. (4.7). The difference is more pronounced when either ν or ϵ increase. The slope n_x decreases rapidly with the adhesion energy (similarly to the isotropic conditions), while n_y decay rate decreases with ν. For $\nu = 1$, $n_y \sim 4.2$ and slightly depends on ϵ. The angle-independent backscatter at 5 MHz is modulated by the anisotropy as shown on fig. (4.6). The plateau value ($\lim_{\epsilon \rightarrow \infty} \chi_x^0 / \chi_{ref}$) decreases with ν, falling from 5 to 1.9.

4.5.3 Classification of tissue

Class properties

Tables (4.III) and (4.IV) give the statistical characteristics (means and covariance properties) of the three classes. As the low frequency characteristics χ_x^0 and χ_y^0 do not statistically differ, according to last subsection, only the three components $\vec{V} =$

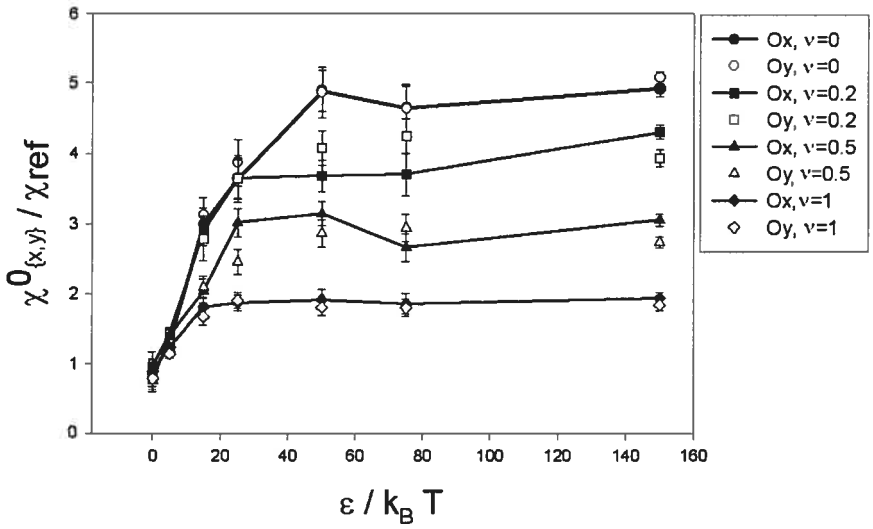

FIG. 4.6 – Normalized backscattering coefficient at 5 MHz, in perpendicular (Oy) and in parallel (Ox) with the growth axis as a function of the aggregation potential ϵ and of the anisotropy index ν.

Class	$E[V_2]$	$E[V_3]$	$E[E_4]$
C_1	-0.9	4.1	4.2
C_2	5.0	3.5	3.6
C_3	2.4	3.5	4.1

TAB. 4.III – Mean scattering properties inside the three classes. V_2 is the backscatter enhancement in dB (0 = non aggregating hard sphere system), V_3 is the spectral slope along the flow axis (Ox), and V_4 is the spectral slope along (Oy).

$[V_2, V_3, V_4]^T$ were used for classifying tissues. Class centroids are positionned as follows in the feature space. The disaggregated class C_1 has a small backscatter at 5 MHz (-0.9 dB) and high equal spectral slopes ($E[V_3], E[V_4] \sim 4.2$). The tissues from the isotropic aggregation class C_2 have a high 5 MHz mean echogenicity (+5 dB) and smaller equal spectral slopes ($E[V_3], E[V_4] \sim 3.5$). Anisotropic aggregation class has an intermediate backscattering behavior (+2.4 dB) but distinct spectral slopes ($E[V_4] > E[V_3]$).

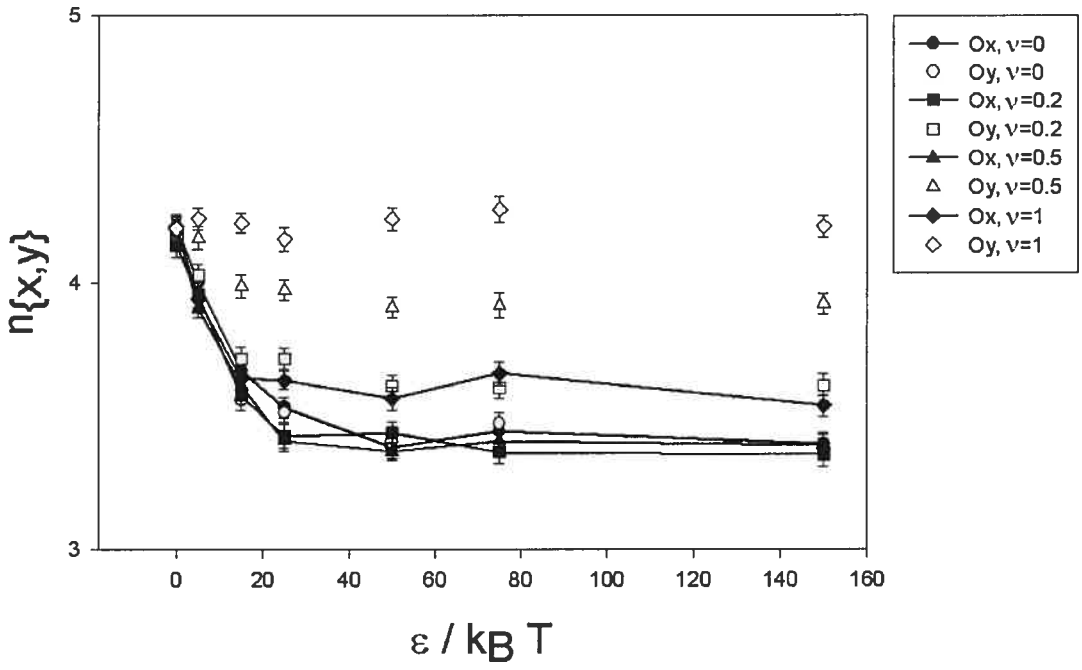

FIG. 4.7 – Spectral slopes in the frequency range $0 - 40$ MHz, in perpendicular (Oy) and in parallel (Ox) with the growth axis as a function of the aggregation potential ϵ and of the anisotropy index ν.

Classification efficiency

The classification accuracy is given by:

$$(e_{ij}) = \begin{pmatrix} 0.89 & 0.17 & 0.22 \\ 0.07 & 0.51 & 0.33 \\ 0.04 & 0.32 & 0.45 \end{pmatrix}.$$

In the case that only low frequency measurements are available, the spectral slopes are not measured and a blood sample is described by a single parameter V_2. To assess the resulting loss of information, one trains the classifier with the scalar V_2. A reduced recognition capacity is observed:

Class	σ_2	σ_3	σ_4	ρ_{23}	ρ_{24}	ρ_{34}
C_1	3.1	0.4	0.4	−0.09	−0.80	0.02
C_2	3.2	0.4	0.4	−0.10	−0.80	0.06
C_3	3.3	0.4	0.4	−0.05	−0.83	−0.05

TAB. 4.IV – Variance-correlation properties inside the three classes. The standard deviation of V_i is noted σ_i, and the correlation between V_i and V_j is ρ_{ij}.

$$(e'_{ij}) = \begin{pmatrix} 0.83 & 0.18 & 0.35 \\ 0.01 & 0.50 & 0.27 \\ 0.16 & 0.32 & 0.38 \end{pmatrix}.$$

4.6 Discussion

The feasibility of the ultrasonic measurement of RBC aggregation relies on significative variations of acoustic scattering properties of blood with microstructural changes. Monte Carlo numerical simulations allow one to estimate these variations for known aggregation variables. *In vitro* or *in vivo* experiments cannot provide such controled aggregation conditions, as many hemodynamic (flow rate, shear rate, vessel geometry and rheology, pulsatility flow parameters, turbulence or sedimentation) and biophysical/biochemical phenomena (plasmatic protein interactions, coagulation) have adverse effects on blood microrheology. The biophysical modeling of cell aggregation is however simplified in this study, as it is assumed that the main determinant of the scattering behavior of blood is the spatial reorganization of RBCs in plasma. The microstructure was therefore modeled by static statistical distributions (Boltzmann thermodynamic equilibrium), taking indirectly into consideration shear non-equilibrium effects by modulating directly the medium anisotropy and the interparticle adhesive strength.

4.6.1 Backscatter at 5 MHz

The backscattering coefficient at 5 MHz was angle independent, as its values perpendicular to and parallel with the cluster axis were not significantly different. Variations of χ^0 as a function of (ϵ, ν) therefore characterize low frequency sensitivity to the overall size of the clusters, independently of their orientation. However, the plateau value $\lim_{\epsilon\to\infty} \chi^0$ decreases with the anisotropy index ν because the morphological characteristics (as mean interparticle spacing, number of cells per aggregate, aggregate gyration radius) of clusters vary with the interaction ellipse elongation, while the surface $\pi(1+\lambda_0)^2R^2$ is maintained constant. The strongest variations of the backscatter as a function of ϵ were observed at low frequency. These results therefore show that the presence of aggregation should more easily be detected at low frequency than at high frequency. Foster et al. [84] also noticed this decrease of sensitivity when increasing the frequency (in their study, backscatter enhancement due to a shear diminution 32 $s^{-1} \rightarrow 0.16$ s^{-1} was +14.3 dB at 35 MHz and reduced to +2.9 dB at 70 MHz). This phenomenon is in fact equivalent to the decrease of the spectral slope with ϵ. However, the insensitivity of χ^0 to the insonification angle proves that high frequency tissue features carry complementary informations on medium microstructure that low frequency scattering properties cannot measure, as described below.

4.6.2 Spectral slopes

Isotropic conditions

The spectral slopes $\{n_x, n_y\}$ are high frequency informations that are expected to complete the partial microstructural description provided by χ^0. When no aggregation occurs, $n_x = n_y$ and their common value (4.21 ± 0.04) is greater than 4, the theoretical slope expected in the Rayleigh scattering regime [144]. The steric repulsions that induce negative correlations on particle positions can explain this increased value.

Similar results for dense media were already predicted in analytical theoretical studies [48, 144] and were observed in experimental investigations [40, 224].

The increase of ϵ, keeping $\nu = 0$, resulted in a decrease of spectral slope from 4.21 to 3.4 (fig. 4.7). This can be compared to various in vitro measurements: Van der Heiden et al. [216] measured slope decrease from 3.1 to 1 (along Oy, frequencies $20 - 40$ MHz) for shear rate decreasing from 1000 s^{-1} to 0.02 s^{-1}, whereas Foster et al. [84] demonstrated that the spectral slope between 30 and 70 MHz could fall from 3.5 to 0.4 when the shear rate fell from 32 s^{-1} to 0.16 s^{-1}. The range of variations given by our results is however smaller than these experimental values. These discrepancies are probably due to the bidimensionality of the simulations. Three-dimensional spatial patterns can generally adopt much more variable configurations than in 2D, which possibly affects the range of the acoustical properties.

Anisotropic conditions

The anisotropy of the medium is revealed by differences existing between n_x and n_y that arise when $\nu > 0$. The parallel slope n_x decreases faster than n_y when anisotropic clusters grow along Ox. Anisotropic backscattering behavior has already been reported in a variety of tissues: myocardial fibers [96], skeletal muscle [206], kidney [106], vessel wall [147], blood [5]..., and these studies generally showed that the backscattered power is maximal when the ultrasound beam perpendicularly intersects the biggest structures. The experimental study on porcine blood flowing in a stationary Poiseuille flow by Allard et al. [5] showed that the maximum Doppler power at 10 MHz is observed for an insonification angle between 45 and 60 degrees. Discrepancies between our results and those experimental findings can be explained by the nature of the velocity field. Non homogeneity of the shear rate in Poiseuille flow can induce major reorganization of RBCs inside the lumen, which leads to complex pattern of rouleaux orientation. In the simulation study by Fontaine et al. [82] that uses a 2D

particle dynamics approach to document the effect of shear rate on the backscattered power, the angular dependence was also different from ours. The finite beam and non-zero bandwidth of the transmitted acoustic pulse, as considered in [82], likely contribute to this difference of scattering behavior.

4.6.3 Tissue classification

The quality of the tissue classifier depends on the distance between class centroids in the feature space and on the overlap of the marginal distributions. The training set showed that classes had distinct means (multivariate Hotelling t_2-test, $n = 1000$, $p < 0.001$) allowing a classification. Detection of non aggregated RBCs is satisfactory (error: 11%). For aggregated media, the classifier reasonably succeeded in finding that RBCs effectively aggregate (error 17% and 22% to detect that RBCs aggregate respectively for C_2 and C_3) but the distinction between isotropy/anisotropy could be erratic (absolute success: 51% and 45%).

When using only low frequency backscatter information, the distinction between aggregated and non-aggregated media is still acceptable for C_1 (83% of success) and C_2 (82%) but is less accurate for C_3 (65%). The distinction between isotropic and anisotropic aggregating samples is degraded (success of 50% and 38% for C_2 and C_3) but is surprisingly comparable to the results obtained using also the spectral slopes. The interest of using high frequency US would essentially be the ability to discriminate small isotropic RBC clusters and big linear aggregates.

We expect yet that UTC classification with real ultrasonic data could be more accurate. Obtained values of the spectral slope are indeed somewhat higher in our simulations than in flow experiments in aggregating conditions (minimal 2D simulated slope: 3.4 whereas spectral slopes as low as 0.5 in [84] were e.g. measured). Furthermore, predicted backscatter increase due to aggregation is also less important than experimental values. We explain this reduced range of variations by the bidi-

mensionality of the simulations. Spatial 2D arrangements of the red cells inside V cannot vary a lot because of the high volumic fraction of the cells submitted to steric interactions. Small interparticle gaps strongly constrain relative positions of RBCs. In 3D real conformations, relative motion is less restricted, and one could postulate that class features should be more distinct.

Intraclass variance is essentially due to the variability of χ^0 in each class C_i. Observed misclassifications can also be explained by the elevated value of this variance. It can be shown that the variance of the sample backscattering coefficient is inversely proportional to the scattering volume V. In our case, for computational reasons, $L = V^{1/2} = 280$ μm is smaller than typical dimension of a real scattering volume, which explains why the variance of the simulated sample backscatter can be unrealistically high compared to 3D insonifications. A practical interpretation of this result is that a reduction of the variance by averaging several independent measurements of tissue backscatter is essential.

4.7 Conclusion

A new stochastic approach for modeling the 2D spatial pattern formed by RBCs flowing in blood was proposed in this study. It enabled us to evaluate the influence of erythrocyte aggregation (characterized by an adhesive intercellular energy ϵ) and rouleaux orientation (anisotropic index ν) on the macroscopical US backscattering properties of blood. The frequency and angular dependencies of blood backscatter was characterized by three acoustic indices : the (isotropic) backscatter χ^0 at 5 MHz, and two spectral slopes (n_x, n_y) in parallel and perpendicular to the growth direction of RBC clusters. The backscatter χ^0 increased with ϵ, n_x decreased with ϵ, while n_y remained nearly constant. This entails that blood backscatter for frequencies ranging between $\sim$ 10 and 40 MHz is more pronounced perpendicularly than in parallel with

the aggregate principal axis.

The efficiency of a UTC measurement of RBC aggregation has been assessed using the simulated results for training a statistical tissue classifier. The backscatter enhancement (compared to non-aggregated media) at low frequency, rather than at higher frequency, was shown to be an efficient acoustical indice to detect RBC clustering. From our results, high frequency scattering properties convey more microstructural information (anisotropy, extent of the aggregates), but variability of the sample feature is elevated. The interest of averaging backcatter measurement is here demonstrated. Three-dimensional simulations in the same controled aggregating conditions could be useful to precise the feasibility of a quantitative determination of RBC biophysical interactions by a UTC procedure.

4.8 Acknowledgments

This work was supported by an operating grant from the Institutes of Health Research of Canada (# MOP-36467) and by a research scholarship from the Fonds de la Recherche en Santé du Québec.

Chapitre 5

Discussion - Conclusion

5.1 Résumé et originalité du travail

L'hémorhéologie est une discipline encore récente, à la croisée des sciences des matériaux et des sciences biomédicales. Son intérêt diagnostique est lié au fait que les maladies génétiques touchant la fonction érythrocytaire, mais aussi les pathologies vasculaires (athérosclérose, thrombose...) sont associées à des lois de comportement hémorhéologiques anormales (viscosité, viscoélasticité ou thixotropie altérées). Interagissant avec les processus d'inflammation et d'hémostase, la compliance vasculaire, la fonction endothéliale, et plus généralement avec l'hémodynamique, les déterminants de la rhéologie sanguine participent au développement athéromateux. Pour comprendre pathophysiologiquement l'implication de l'hémorhéologie dans l'étiologie des maladies cardiovasculaires, un outil d'imagerie *in vivo* de ces déterminants est désormais nécessaire.

S'insérant parmi les méthodes ultrasonores de caractérisation des tissus, la mesure du coefficient de rétrodiffusion sanguin $\chi(\vec{k})$ serait appropriée à cette fin. Quelques étapes de calibration de normalisation de la puissance du signal radio-fréquence permettraient son implantation sur un échographe clinique. Afin de poser les bases méthodologiques d'une telle méthode, cette thèse s'est attachée à décrire quantitativement l'évolution de $\chi(\vec{k})$ avec le niveau d'agrégation érythrocytaire responsable

du caractère rhéofluidifiant du sang. Nous avons systématiquement séparé l'effet des propriétés acoustiques élémentaires du globule rouge (section de rétrodiffusion du globule rouge σ_b) et l'effet de l'organisation spatiale des hématies (facteur de structure S) dans l'expression du coefficient de rétrodiffusion :

$$\chi(\vec{k}) = mS(-2\vec{k})\sigma_b(\vec{k}),$$

la densité en nombre des globules rouges étant notée m.

La détermination de $\sigma_b(\vec{k})$ est un problème acoustique, que nous avons résolu sous l'hypothèse de Born (de faible diffusion). Nous avons prouvé semi-analytiquement qu'assimiler acoustiquement un globule rouge à un cylindre plat constituait une bonne approximation, quels que soient les angles d'incidence et la fréquence $\lesssim 200$ MHz.

La détermination du facteur de structure $S(\vec{q})$, propre au processus aléatoire de points constitué par les centres des globules rouges, représente plutôt un problème de physique statistique, qui permet le passage du microscopique au macroscopique.

Dans sa forme basse fréquence $S(0) = W$ et à l'équilibre, le facteur de structure (appelé alors facteur de *packing*) est relié à la compressibilité isotherme d'un système thermostaté de particules. Nous avons montré que la physique statistique des fluides fournissait des méthodes adéquates pour modéliser le facteur de *packing* de globules rouges non agrégés et agrégés — en fonction de l'hématocrite, et par exemple du facteur de collage de Baxter du chapitre (2), des statistiques du nombre de globules rouges par amas dans le chapitre (3), ou bien de l'énergie d'adhésion et de l'anisotropie dans le chapitre (4).

À fréquences modérées, nous proposons d'approximer la dépendance en fréquence $S(\vec{q})$ par une loi polynômiale ($S(\vec{q}) = W + \vec{q}.\Sigma_2\vec{q}$) plutôt que par une loi en puissance, comme pratiqué jusqu'à présent en caractérisation ultrasonore des tissus. Le tenseur symétrique Σ_2 indique les directions principales de la microtructure. Ses valeurs propres négatives donnent le rayon de gyration des amas de diffuseurs, tandis

que ses valeurs propres positives reflètent la répulsion interparticulaire. Dans le cas des systèmes de sphères dures, modélisant correctement une suspension saline non agrégeante de globules rouges, nous avons donné l'approximation de Perkus-Yevick du facteur de structure, généralisant ainsi à plus hautes fréquences le facteur de *packing* de Perkus-Yevick, déjà formulé depuis longtemps. Le modèle de Neyman-Scott a permis également de trouver une expression analytique simple du facteur de structure pour des suspensions diluées agrégeantes. Le modèle de Gibbs-Markov du chapitre (4) a permis quand à lui de constater l'effet de l'adhésion et de l'anisotropie sur le facteur de structure.

5.2 Applications à l'imagerie échographique

L'insonification d'un tissu par une sonde d'un appareil clinique diffère bien entendu du cas idéal de l'incidence d'une onde plane monochromatique, correspondant strictement à la définition du coefficient de rétrodiffusion. De plus, l'électronique de réception et d'amplification modifie substantiellement le signal échographique radio-fréquence reçu par les élements de transducteur. Le caractère pulsé et focalisé de l'insonification échographique classique a néanmoins l'immense avantage de permettre la cartographie des propriétés acoustiques tissulaires. C'est pourquoi le travail de normalisation de la puissance radio-fréquence, nécessaire à l'imagerie du coefficient de rétrodiffusion, serait une avancée remarquable pour la caractérisation quantitative des tissus.
Dans cette thèse, une modélisation quadratique de $k \longrightarrow \chi(k\vec{e}_x)$ est proposée sous la forme (pour ka modéré, $\sigma_{xx} = \vec{e}_x.\Sigma\vec{e}_x$ et $s_{xx} = \vec{e}_x.\Sigma_2\vec{e}_x$) :

$$a\chi(k\vec{e}_x) = W(ka)^4 \times \left(H\langle\gamma_z\rangle^2/3\pi\right) + \left(\frac{s_{xx} - W\sigma_{xx}}{a^2}\right)(ka)^6 \times \left(4H\langle\gamma_z\rangle^2/3\pi\right).$$

Dans cette expression, la microstructure des globules rouges n'influe que sur les valeurs

de W et $\frac{s_{xx}-W\sigma_{xx}}{a^2}$. Ayant déterminé les paramètres a, H et $\langle\gamma_z\rangle$ (ou au besoin pris des valeurs moyennes pour du sang humain), on voit que l'on pourra déterminer expérimentalement W et $\left(\frac{s_{xx}-W\sigma_{xx}}{a^2}\right)$ en effectuant une régression polynômiale du type :

$$a\chi(k\vec{e_x}) = A_4(ka)^4 + A_6(ka)^6,$$

à condition que la bande passante du transducteur couvre une gamme de fréquences assez étendue pour effectuer une régression admissible. On remarquera que le terme A_4 est indépendant de l'angle d'insonification, tandis que A_6 varie suivant les composantes du tenseur $\Sigma_2 - W\Sigma$.

Procéder à l'imagerie des paramètres W et s_{xx} permettrait une caractérisation tissulaire physique innovante pour la problématique de mesure hémorhéologique *in vivo*. On pourrait ainsi envisager de compléter le B-scan classique par une image couleur W- ou s-scan en mode duplex. Puisque W ou Σ_2 dépendent de l'hémodynamique locale (taux de cisaillement), la détection d'une agrégabilité érythrocytaire anormale demanderait d'estimer les vitesses sanguines par vélocimétrie Doppler par exemple.

5.3 Applications à la physiopathologie

Nous savons que des anomalies hémorhéologiques représentent des facteurs de risques cardiovasculaires. Pour améliorer le diagnostic cardiovasculaire, ou plus généralement pour améliorer notre compréhension du développement de la maladie, la mesure ultrasonore de l'échogénicité sanguine se présente comme la seule méthodologie non-invasive pouvant révéler le comportement hémorhéologique *in vivo*.

Cliniquement, plusieurs études « empiriques » sur l'implication pathophysiologique de l'hyperéchogénicité sanguine sont apparues lorsque l'instrumentation échocardiographique (citons en particulier les sondes transœsophagiennes, à fréquences et « péné-

trabilité » accrues) a permis de visualiser l'échogénicité sanguine en mode B. Ces manifestations d'hyperéchogénicité ont été baptisés échocontrastes spontanés (*Spontaneous Echo Contrast*, SEC) par les cliniciens. Ces SEC peuvent être détectés dans l'aorte descendante, dans le ventricule gauche par échographie transœsophagienne, ou dans les membres inférieurs.

Leur présence a été corrélée à un certain nombre d'évenements pathologiques :

- La formation de thrombi dans l'oreillette gauche (de causes multiples : arryhthmies [18], fibrillation auriculaire [221], sténose mitrale [89, 158], transplantation cardiaque [69] ...) est une cause commune d'embolie cérébrale. Liée à des facteurs de coagulation, la présence de thrombus sanguin dans le cœur s'accompagne de celle des SEC. La quantification des SEC auriculaires pour choisir la médication anticoagulante adaptée a déjà été proposée dans [30].
- Les SEC aortiques, mesurés par échographie transœsophagienne, sont corrélés avec une fraction d'éjection ventriculaire basse, l'âge du patient, l'athérosclérose aortique et la dilation luminale aortique d'après [159, 230]. Leur observation démontre un risque élevé d'accident cardiovasculaire (mort de cause cardiovasculaire $\times 2$ sur 60 mois pour une population de patients ayant subit une échographie transœsophagienne).
- Dans les membres inférieurs, Cloutier et coll. [57] ont montré que l'échogénicité Doppler était accrue chez les sujets hyperlipidémiques.

Nous voyons ainsi que la détection d'hyperéchogénicité sanguine s'avère utile comme marqueur d'athérothrombogénicité. Sa quantification par la mesure absolue du coefficient de rétrodiffusion devrait donner plus d'assise à cet indice échographique.

L'utilisation des ultrasons pour la compréhension physiopathologique des liens hémorhéologie - inflammation - hémostase - athérogénèse doit être généralisée et encouragée. Elle est encore balbutiante: les protocoles de mesure (sites...) restent à définir. Il faut de plus noter que la mesure d'agrégabilité devra s'effectuer en connaissance de

l'hémodynamique (taux de cisaillement) et de l'hématocrite.

5.4 Applications en caractérisation de matériaux

Pour révéler la structure des polymères, la diffusion des rayons X, de la lumière ou des neutrons est une méthode de choix. Elle permet par exemple de déterminer leur rayon de gyration, le second coefficient du viriel (caractérisant les interactions intermoléculaires), ou d'autres paramètres structuraux plus fins. Cette voie de caractérisation des macromolécules est possible car l'échelle moléculaire typique est de l'ordre de la longueur d'onde du rayon incident.

En diffusion des ultrasons, dans la gamme de fréquences utilisées par les échographes cliniques, la longueur d'onde s'étale entre l'échelle millimétrique et micrométrique. Or les structures inter-cellulaires ou cellulaires ont des dimensions de cet ordre : on comprend alors pourquoi la diffusion des ultrasons par les tissus relève d'une physique somme toute comparable à celle de la diffraction de rayonnements nanométriques par les polymères et les fluides.

Les colloïdes tiennent une place accrue dans l'industrie, la santé, l'environnement... La caractérisation par rétrodiffusion ultrasonore de ces suspensions (stabilité, floculation) aux constituants micrométriques serait novatrice : son avantage tiendrait dans la « légèreté » de son instrumentation, et dans la possibilité de faire du contrôle temps réel *in situ*, même pour des concentrations élevées. Il semble que les modèles de rétrodiffusion développés ici pour le sang seraient aisément transposables à d'autres types de suspensions colloïdales (faiblement diffusantes).

5.5 Conclusion

Une tendance qui se répand en imagerie médicale est la quantification des mesures pour l'amélioration du diagnostic clinique. Elle se justifie par le fait que les images

numériques fournissent non seulement des indices morphologiques sur l'anatomie des organes observés, mais également des informations de nature plus fonctionnelle sur les propriétés physico-chimiques des tissus interrogés par rayon X, excités par un champ magnétique ou soumis à une vibration acoustique.

Dans ce contexte, le coefficient de rétrodiffusion ultrasonore sanguin χ porte de l'information microstructurale sur l'organisation spatiale des hématies en suspension, que l'on veut révéler par « spectroscopie » de rétrodiffusion. Cette thèse a permis de modéliser la dépendance fréquentielle $\chi(f)$ en fonction de paramètres pertinents à l'hémorhéologie : l'hématocrite, la polydispersité et le rayon de gyration des agrégats de globules rouges pour des suspensions diluées, l'énergie d'adhésion et l'anisotropie structurelle pour des suspensions denses bidimensionnelles.

Une nouvelle réduction de données de rétrodiffusion est proposée afin de construire de nouveaux types d'images paramétriques. La cartographie du facteur de *packing* W et des composantes du tenseur de gyration Σ_2, couplée avec l'étude hémodynamique fournie par vélocimétrie Doppler, devrait être une technique prometteuse pour remonter aux indices physiques d'agrégabilité telle que l'énergie d'adhésion intercellulaire. Un tel type d'imagerie devrait fournir des outils plus pertinents pour le diagnostic et la compréhension des maladies cardiovasculaires.

Références

[1] Acedo L. Santos A. A square-well model for the structural and thermodynamic properties of simple colloidal systems. Journal of Chemical Physics. 115(6):2805-2817, 2001.

[2] Agre P. Casella JF. Zinkham WH. McMillan C. Bennett V. Partial deficiency of erythrocyte spectrin in hereditary spherocytosis. Nature. 314(6009):380-383, 1985.

[3] Ahuja AS. Acoustical properties of blood: a look at the basic assumptions. Medical Physics. 1(6):311-316, 1974.

[4] Ahuja AS. Hendee WR. Effects of red cell shape and orientation on propagation of sound in blood. Medical Physics. 4(6):516-520, 1977.

[5] Allard L. Cloutier G. Durand LG. effect of the insonification angle on the doppler backscattered power under red blood cell aggregation conditions. IEEE Transactions on Ultrasonics Ferroelectrics & Frequency Control. 43(2):211-219, 1996.

[6] Allard L. Cloutier G. Power Doppler ultrasound scan imaging of the level of red blood cell aggregation: An in vitro study. Journal of Vascular Surgery. 30(1):157-168, 1999.

[7] Anderson ME. McKeag MS. Trahey GE. The impact of sound speed errors on medical ultrasound imaging. Journal of the Acoustical Society of America. 107(6):3540-8, 2000.

[8] Angelsen BA. A theoretical study of the scattering of ultrasound from blood. IEEE Transactions on Biomedical Engineering. 27(2):61-7, 1980.

[9] Apfel RE. Prediction of tissue composition from ultrasonic measurements and mixture rules. Journal of the Acoustical Society of America. 79(1):148-52, 1986.

[10] Arp PA. Mason SG. The kinetics of flowing dispersions. VIII. Doublets of rigid spheres (Theoretical). Journal of Colloid and Interface science. 61(1):21-42, 1977.

[11] Asakura S. Oosawa F. On interaction between two bodies immersed in a solution of macromolecules. J. Chem. Phys. 22:1255-1256, 1954.

[12] Atkinson P. Berry MV. Random noise in ultrasonic echoes diffracted by blood. J. Phys A. 7(11):1293-1302, 1974.

[13] Bacchi B. Ranzi R. Borga M. Statistical characterization of spatial patterns of rainfall cells in extratropical cyclones. Journal of Geophysical Research-Atmospheres. 101:26277-26286, 1996.

[14] Bakke T. Gytre T. Haagensen A. Giezendanner L. Ultrasonic measurement of sound velocity in whole blood. Scand. J. Clin. Lab. Invest. 35:473-478, 1975.

[15] Barker JA. Henderson D. What is "liquid" ? Understanding the states of matter. Reviews of Modern Physics. 48(4):587-670 1976.

[16] Barnes C. Evans JA. Lewis TJ. Low-frequency ultrasound absorption in aqueous solutions of hemoglobin, myoglobin, and bovine serum albumin: the role of structure and pH. Journal of the Acoustical Society of America. 83(6):2393-404, 1988.

[17] Bascom PA. Cobbold RS. On a fractal packing approach for understanding ultrasonic backscattering from blood. Journal of the Acoustical Society of America. 98(6):3040-3049, 1995.

[18] Bashir M. Asher CR. Schaffer K. Murray RD. Apperson-Hansen C. Jasper SE. Thomas JD. Klein AL. Left atrial appendage spontaneous echo contrast in pa-

tients with atrial arrhythmias using integrated backscatter and transesophageal echocardiography. American Journal of Cardiology. 88(8):923-927, 2001.

[19] Baskurt OK. Tugral E. Neu B. Meiselman HJ. Particle electrophoresis as a tool to understand the aggregation behavior of red blood cells. Electrophoresis. 23(13):2103-2109, 2002.

[20] Batchelor GK. Green JT. The hydrodynamic interaction of two small freely-moving spheres in a linear shear flow. J. Fluid Mech. 56(2):375-400, 1972.

[21] Batista JLF. Maguire DA. Modeling the spatial structure of tropical forests. Forest Ecology & Management. 110:293-314, 1998.

[22] Baumler H. Donath E. Krabi A. Knippel W. Budde A. Kiesewetter H. Electrophoresis of human red blood cells and platelets. Evidence for depletion of dextran. Biorheology. 33(4-5):333-351, 1996.

[23] Baxter RJ, Ornstein-Zernike relation for a disordered fluid, Aust. J. Phys. 21:563-569, 1968.

[24] Baxter-Drayton Y. Brady JF. Brownian electrorheological fluid as a model for flocculated dispersions. J. Rheol. 40:1027-1056, 1996.

[25] Bell GI. Models for the specific adhesion of cells to cells. Science. 200:618-627, 1978.

[26] Ben Ami R. Barshtein G. Zeltser D. Goldberg Y. Shapira I. Roth A. Keren G. Miller H. Prochorov V. Eldor A. Berliner S. Yedgar S. Parameters of red blood cell aggregation as correlates of the inflammatory state. American Journal of Physiology - Heart & Circulatory Physiology. 280(5):1982-1988, 2001.

[27] Berger NE. Lucas RJ. Twersky V. Polydisperse scattering theory and comparisons with data for red blood cells. Journal of the Acoustical Society of America. 89(3):1394-1401, 1991.

[28] Berli CLA. Quemada D. Parker A. Modelling the viscosity of depletion floculated emulsions. Colloids and Surfaces A. 203:11-20, 2002.

[29] Bessis M. Mohandas N. Mesure continue de la déformabilité cellulaire par une méthode diffractométrique. Comptes Rendus Hebdomadaires des Séances de l'Académie des Sciences - D: Sciences Naturelles. 278(25):3263-3265, 1974.

[30] Black IW. Spontaneous echo contrast: where there's smoke there's fire. Echocardiography. 17(4):373-382, 2000.

[31] Boryczko K. Dzwinel W. Yuen DA. Dynamical clustering of red blood cells in capillary vessels. Journal of Molecular Modeling. 9(1):16-33, 2003.

[32] Boynard M. Lelievre JC. Size determination of red blood cell aggregates induced by dextran using ultrasound backscattering phenomenon. Biorheology. 27(1):39-46, 1990.

[33] Bradley EL. Sacerio J. The velocity of ultrasound in human blood under varying physiologic parameters. J. Surg. Res. 12:200-207, 1972.

[34] Brady JF. Bossis G. Stokesian dynamics. Annual review of Fluid Mechanics. 20:111-157, 1988.

[35] Breyiannis G. Pozrikidis C. Simple shear flow of suspensions of elastic capsules. Theoretical and Computational Fluid Dynamics. 13:327-347, 1990.

[36] Briehl RW. Solid-like behaviour of unsheared sickle haemoglobin gels and the effects of shear. Nature. 288(5791):622-624, 1980.

[37] Brown JH. Volkmann N. Jun G. Henschen-Edman AH. Cohen C. The crystal structure of modified bovine fibrinogen. Proceedings of the National Academy of Sciences of the United States of America. 97(1):85-90, 2000.

[38] Bucherer C. Lacombe C. Lelièvre JC. Viscosité du sang humain. Dans MY. Jaffrin. F. Goubel. Biomécanique des Fluides et des Tissus Biologiques, Masson, Paris, 1998.

[39] Caers J. A general family of counting distributions suitable for modeling cluster phenomena. Mathematical Geology. 28:601-624, 1996.

[40] Campbell JA. Waag RC. Ultrasonic scattering properties of three random media with implications for tissue characterization. Journal of the Acoustical Society of America. 75(6):1879-1886, 1984.

[41] Cao PJ. Paeng DG. Shung KK. The "black hole" phenomenon in ultrasonic backscattering measurement under pulsatile flow with porcine whole blood in a rigid tube. Biorheology. 38(1):15-26, 2001.

[42] Carnahan NF. Starling KE. Equation of state for non-attracting rigid spheres. J. Chem. Phys. 51:635-636, 1969.

[43] Carstensen EL. Li K. Schwann HP. Determination of the acoustic properties of blood and its components. Journal of the acoustical society of America. 25:286-289, 1953.

[44] Carstensen EL. Schwann HP. Absorption of sound arising from the presence of intact cells in blood. Journal of the acoustical society of America. 31:185-189, 1959.

[45] Carstensen EL. Schwann HP. Acoustic properties of hemoglobin solutions. Journal of the acoustical society of America. 31:305-311, 1958.

[46] Charara J. Bucherer C. Lacombe C. Lelièvre JC. Role of fibrinogen in the rheological behavior of normal RBC suspensions. A viscometric study. Euromech 186, Nancy, 1984.

[47] Chelidze T. Dielectric spectroscopy of blood. Journal of Non-Crystalline Solids. 305(1-3):285-294, 2002.

[48] Chen JF. Zagzebski JA. Frequency dependence of backscatter coefficient versus scatterer volume fraction. IEEE Transactions on Ultrasonics Ferroelectrics & Frequency Control. 43(3):345-353, 1996.

[49] Chen S. Gavish B. Zhang S. Mahler Y. Yedgar S. Monitoring of erythrocyte aggregate morphology under flow by computerized image analysis. Biorheology. 32:487-496, 1995.

[50] Chien S. Shear dependence of effective cell volume as a determinant of blood viscosity. Science. 168(934):977-979, 1970.

[51] Chien S. Usami S. Dellenback RJ. Bryant CA. Comparative hemorheology–hematological implications of species differences in blood viscosity. Biorheology. 8(1):35-57, 1971.

[52] Chien S. Jan KM. Red cell aggregation by macromolecules: roles of surface adsorption and electrostatic repulsion. Journal of Supramolecular Structure. 1(4):385-409, 1973.

[53] Chien S. Sung LA. Simchon S. Lee MM. Jan KM. Skalak R. Energy balance in red cell interactions. Annals of the New York Academy of Sciences. 416:190-206, 1983.

[54] Chien S. Red cell deformability and its relevance to blood flow. Annual Review of Physiology. 49:177-192, 1987.

[55] Cloutier G. Shung KK. Cyclic variation of the power of ultrasonic Doppler signals backscattered by polystyrene microspheres and porcine erythrocyte suspensions. IEEE Transactions on Biomedical Engineering. 40(9):953-962, 1993.

[56] Cloutier G. Shung KK. Study of red cell aggregation in pulsatile flow from ultrasonic Doppler power measurements. Biorheology. 30(5-6):443-461, 1993.

[57] Cloutier G. Qin Z. Ultrasound backscattering from non-aggregating and aggregating erythrocytes–a review. Biorheology. 34(6):443-470, 1997.

[58] Cloutier G. Weng X. Roederer GO. Allard L. Tardif F. Beaulieu R. Differences in the erythrocyte aggregation level between veins and arteries of normolipidemic

and hyperlipidemic individuals. Ultrasound in Medicine & Biology. 23(9):1383-93, 1997.

[59] Cloutier G. Qin Z. Shear rate dependence of ultrasound backscattering from blood samples characterized by different levels of erythrocyte aggregation. Annals of Biomedical Engineering. 28(4):399-407, 2000.

[60] Colton D. Coyle J. Monk P. Recent developments in inverse acoustic scattering theory. SIAM Review. 42(3):369-414, 2000.

[61] Cooke JP. Flow, NO, and atherogenesis. Proceedings of the National Academy of Sciences of the United States of America. 100(3):768-770, 2003.

[62] Copley AL. Agrégation et désagrégation érythrocytaire. Dans Stoltz JF. Hémorhéologie et agrégation érythrocytaire. Compte-rendu du premier symposium international. Genève. EMI inter. Paris. 1986.

[63] Coussios CC. The significance of shape and orientation in single-particle weak-scatterer models. Journal of the acoustical society of America, 112(3):906-915, 2002.

[64] Dai HP. Feng R. Ultrasonic attenuation in red blood cell suspensions. Ultrasonics. 26(3):168-170, 1988.

[65] Danesh J. Collins R. Appleby P. Peto R. Association of fibrinogen, C-reactive protein, albumin, or leukocyte count with coronary heart disease: meta-analyses of prospective studies. JAMA. 279(18):1477-1482, 1998.

[66] de Kroon MG. Slager CJ. Gussenhoven WJ. Serruys PW. Roelandt JR. Bom N. Cyclic changes of blood echogenicity in high-frequency ultrasound. Ultrasound in Medicine & Biology. 17(7):723-728, 1991.

[67] Dembo M. Torney DC. Saxman K. Hammer DA., The reaction limited kinetics of membrane-to-surface adhesion and detachment. Proceedings of the royal society of London B. 234:55-83. 1988.

[68] Derganc J. Bozic B. Svetina S. Zeks B. Equilibrium Shapes of Erythrocytes in Rouleau Formation, Biophys. J. 84:1486-1492, 2003.

[69] Derumeaux G. Habib G. Schleifer DM. Ambrosi P. Bessou JP. Metras D. Cribier A. Luccioni R. Soyer R. Letac B. Standard orthotopic heart transplantation versus total orthotopic heart transplantation. A transesophageal echocardiography study of the incidence of left atrial thrombosis. Circulation. 92(9):196-201, 1995.

[70] Deryaguin BV. Landau L. Theory of the stability of strongly charged lyophobic sols and the adhesion of strongly charged particles in solutions of electrolytes. Acta Phys. Chem USSR. 14:633-662, 1941.

[71] Discher DE. Mohandas N. Evans EA. Molecular maps of red cell deformation: hidden elasticity and in situ connectivity. Science. 266(5187):1032-1035, 1994.

[72] Dufaux J. Snabre P. Guiffant G. Le voyage des globules rouges. Pour la Science. 297:2-7, 2002.

[73] Dzwinel W. Boryczko K. Yuen DA. A discrete-particle model of blood dynamics in capillary vessels. Journal of colloid and interface science. 258(1):163-173, 2003.

[74] Elimelech M. Gregory J. Jia X. Williams RA. Particle deposition and aggregation: measurement, modeling, and simulation. Butterworth-Heinemann. Oxford. 1995.

[75] Enejder AMK. Swartling J. Aruna P. Andersson-Engels S. Influence of cell shape and aggregate formation on the optical properties of flowing whole blood. Applied Optics. 42(7):1384-1394, 2003.

[76] Evans E. Fung YC. Improved measurements of the erythrocyte geometry. Microvascular Research. 4(4):335-447, 1972.

[77] Fåhraeus R. The suspension stability of blood. Physiol. Rev. 9:241-274, 1929.

[78] Fåhraeus R. Lindqvist T. The viscosity of the blood in narrow capillary tubes. Am. J. Physiol. 96:6562-6568, 1931

[79] Farhat H. Eu BC. Monte Carlo method and the nonequilibrium structure and non-Newtonian viscosity of a sheared simple liquid. Journal of Chemical Physics. 110(1):97-108, 1999.

[80] Fischer EI. Armentano RL. Pessana FM. Graf S. Romero L. Christen AI. Simon A. Levenson J. Endothelium-dependent arterial wall tone elasticity modulated by blood viscosity. American Journal of Physiology - Heart & Circulatory Physiology. 282(2):389-394, 2002.

[81] Fontaine I. Bertrand M. Cloutier G. A system-based approach to modeling the ultrasound signal backscattered by red blood cells. Biophysical Journal. 77(5):2387-2399, 1999.

[82] Fontaine I. Savéry D. Cloutier G. Simulation of ultrasound backscattering by red cell aggregates: effect of shear rate and anisotropy. Biophys. J. 82:1696-1710, 2002.

[83] Fontaine I. Cloutier G. Modeling the frequency dependence (5-120 MHz) of ultrasound backscattering by red cell aggregates in shear flow at a normal hematocrit. J Acoust Soc Am 113(5):2893-2900 2003.

[84] Foster FS. Obara H. Bloomfield T. Ryan LK. Lockwood GR. Ultrasound backscatter from blood in the 30 to 70 MHz frequency range. Proceedings of the IEEE Ultrasonics Symposium, 1994. IEEE(3):1599-1602, 1994.

[85] Frangos SG. Gahtan V. Sumpio B. Localization of atherosclerosis: role of hemodynamics. Archives of Surgery. 134(10):1142-1149, 1999.

[86] Fung YC. Biomechanics, mechanical properties of living tissues, 2nd edition. Springer. 1993.

[87] Giannattasio C. Piperno A. Failla M. Vergani A. Mancia G. Effects of hematocrit changes on flow-mediated and metabolic vasodilation in humans. Hypertension. 40(1):74-77, 2002.

[88] Goldsmith HL. Marlow J. Flow behaviour of erythrocytes. I. Rotation and deformation in dilute suspensions. Proc R. Soc. London. B. 182:351-384, 1972.

[89] Gonzalez-Torrecilla E. Garcia-Fernandez MA. Perez-David E. Bermejo J. Moreno M. Delcan JL. Predictors of left atrial spontaneous echo contrast and thrombi in patients with mitral stenosis and atrial fibrillation. American Journal of Cardiology. 86(5):529-534, 2000.

[90] Goss SA. Johnston RL. Dunn F. Compilation of empirical ultrasonic properties of mammalian tissues. II. Journal of the Acoustical Society of America. 68(1):93-108, 1980.

[91] Gough W. Routh HF. Williams RP. Weak reflection of a wave by a one-dimensional array of randomly spaced elements, with reference to the scattering of ultrasound by blood. Phys Med Biol 33(7):793-804, 1988.

[92] Greenleaf J.F. Tissue Characterization with ultrasound. CRC Press. 1986.

[93] Guinier A. Fournet J. Small angle scattering of X-rays. Wiley Interscience. New York. 1955.

[94] Guyton AC. Hall JE. Textbook of medical physiology. WB Saunders company. 1996.

[95] Haider L. Snabre P. Boynard M. Rheo-acoustical study of the shear disruption of reversible aggregates. Ultrasound scattering from concentrated suspensions of red cell aggregates. Journal of the Acoustical Society of America. 107(3):1715-1726, 2000.

[96] Hall CS. Scott MJ. Lanza GM. Miller JG. Wickline SA. The extracellular matrix is an important source of ultrasound backscatter from myocardium. Journal of the Acoustical Society of America. 107(1):612-1619, 2000.

[97] Hansen JP. McDonald IR. Theory of Simple Liquids. Academic Press. New York. 1986.

[98] Hayter JP. Penfold J. An analytic structure factor for macroion solutions. Mol. Phys., 42:109-118, 1981.

[99] Helfand E. Frisch HL. Lebowitz JL. Theory of two-and one-Dimensional Rigid Sphere Fluids. J. Chem. Phys. 34:1037, 1961.

[100] Herrera JN. Cummings PT. Ruiz-Estrada H. Static structure factor for simple liquid metals. Mol. Phys. 96(5):835-847, 1999.

[101] Henon S. Lenormand G. Richert A. Gallet F. A new determination of the shear modulus of the human erythrocyte membrane using optical tweezers. Biophysical Journal. 76(2):1145-1151, 1999.

[102] Hoffmeister BK. Whitten SA. Kaste SC. Rho JY. Effect of collagen and mineral content on the high-frequency ultrasonic properties of human cancellous bone. Osteoporosis International. 13(1):26-32, 2002.

[103] Hunt JW. Worthington AE. Xuan A. Kolios MC. Czarnota GJ. Sherar MD. A model based upon pseudo regular spacing of cells combined with the randomisation of the nuclei can explain the significant changes in high-frequency ultrasound signals during apoptosis. Ultrasound in Medicine & Biology. 28(2):217-226, 2002.

[104] Hushcha T. Peytcheva A. Kaatze U. Broadband acoustic spectra of aqueous solutions of human serum albumin. Journal of Physics-Condensed Matter. 14(41):9461-9464, 2002.

[105] Insana MF. and Brown DG. Acoustic scattering theory applied to soft biological tissues. Dans Shung KK. Thieme GA. Ultrasonic scattering in biological tissues. CRC Press. Boca Raton. 1993.

[106] Insana MF. Modeling acoustic backscatter from kidney microstructure using an anisotropic correlation function. Journal of the Acoustical Society of America. 97(1):649-655, 1995.

[107] Izumida Y. Seiyama A. Maeda N. Erythrocyte aggregation: bridging by macromolecules and electrostatic repulsion by sialic acid. Biochimica et Biophysica Acta. 1067(2):221-226, 1991.

[108] Jeffery GB. On the motion of ellipsoidal particles immersed in a viscous fluid. Proc. R. Soc. Lond. A. 102:161-179, 1922.

[109] Johnson PC. Bishop JJ. Popel S. Intaglietta M. Effects of red cell aggregation on the venous microcirculation. Biorheology. 36(5-6):457-460, 1999.

[110] Kaatze U. Hushcha TO. Eggers F. Ultrasonic broadband spectrometry of liquids: A research tool in pure and applied chemistry and chemical physics. Journal of Solution Chemistry. 29(4):299-368, 2000.

[111] Koenig W. Ernst E. The possible role of hemorheology in atherothrombogenesis. Atherosclerosis. 94:93-107, 1992.

[112] Koenig W. Sund M. Filipiak B. Doring A. Lowel H. Ernst E. Plasma viscosity and the risk of coronary heart disease: results from the MONICA-Augsburg Cohort Study, 1984 to 1992. Arteriosclerosis, Thrombosis & Vascular Biology. 18(5):768-772, 1998.

[113] Koenig W. Sund M. Lowel H. Doring A. Ernst E. Association between plasma viscosity and all-cause mortality: results from the MONICA-Augsburg Cohort Study 1984-92. British Journal of Haematology. 109(2):453-458, 2000.

[114] Kuo IY. Shung KK. High frequency ultrasonic backscatter from erythrocyte suspension. IEEE Transactions on Biomedical Engineering. 41(1):29-34, 1994.

[115] Lee KW. Change of particle size distribution during Brownian coagulation. J. Colloid Interface Sci. 92:315-325, 1983.

[116] Lee AJ. Mowbray PI. Lowe GD. Rumley A. Fowkes FG. Allan PL. Blood viscosity and elevated carotid intima-media thickness in men and women: the Edinburgh Artery Study. Circulation. 97(15):1467-1473, 1998.

[117] Lelièvre JC. Bucherer C. Microrhéologie des cellules circulantes. Dans Jaffrin MY. Goubel F. Biomécanique des fluides et tissus, Masson, Paris, 1998.

[118] Lenormand G. Henon S. Richert A. Simeon J. Gallet F. Direct measurement of the area expansion and shear moduli of the human red blood cell membrane skeleton. Biophysical Journal. 81(1):43-56, 2001.

[119] Libby P. Inflammation in atherosclerosis. Nature. 420(6917):868-874, 2002.

[120] Libby P. Ridker PM. Maseri A. Inflammation and atherosclerosis. Circulation. 105(9):1135-1143, 2002.

[121] Libby P. Les maladies cardiovasculaires. Pour la Science. 296:60-67, 2002.

[122] Likos CN. Effective interactions in soft condensed matter physics. Physics reports. 348:267-439, 2001.

[123] Lim B. Bascom PAJ. Cobbold RSC. Particle and voxel approaches for simulating ultrasound backscattering from tissue. Ultrasound in Medicine & Biology. 22(9):1237-1247, 1996.

[124] Lim B. Cobbold RS. On the relation between aggregation, packing and the backscattered ultrasound signal for whole blood. Ultrasound in Medicine & Biology. 25(9):1395-1405, 1999.

[125] Lin LC. Yen RF. Hwang JJ. Chiang FT. Tseng CD. Huang PJ. Ultrasonic tissue characterization evaluates myocardial viability and ischemia in patients with coronary artery disease. Ultrasound in Medicine & Biology. 26(5):759-769, 2000.

[126] Lin YH, Shung KK, Ultrasonic backscattering from porcine whole blood of varying hematocrit and shear rate under pulsatile flow. Ultrasound in Medicine & Biology. 25(7):1151-1158, 1999.

[127] Linde T. Sandhagen B. Hagg A. Morlin C. Wikstrom B. Danielson BG. Blood viscosity and peripheral vascualr resistance in patients with untreated essential hypertension. Journal of Hypertension. 11(7):731-736, 1993.

[128] Lominadze D. Dean WL. Involvement of fibrinogen specific binding in erythrocyte aggregation. FEBS Letters. 517(1-3):41-44, 2002.

[129] Lowe GD. Fowkes FG. Dawes J. Donnan PT. Lennie SE. Housley E. Blood viscosity, fibrinogen, and activation of coagulation and leukocytes in peripheral arterial disease and the normal population in the Edinburgh Artery Study. Circulation. 87(6):1915-1920, 1993.

[130] Lowe GD. Lee AJ. Rumley A. Price JF. Fowkes FG. Blood viscosity and risk of cardiovascular events: the Edinburgh Artery Study. British Journal of Haematology. 96(1):168-173, 1997.

[131] Lowe GDO. Agents lowering blood viscosity, including defibrinogenating agents. Dans Verstraete M. Fuster V. Topol EJ. Cardiovascular Thrombosis: Thrombocardiology and Thromboneurology, Second Edition. Lippincott-Raven Publishers. Philadelphia, 1998.

[132] Lucas RJ. Twersky V. Inversion of ultrasonic scattering data for red blood cell suspensions under different flow conditions. Journal of the Acoustical Society of America. 82(3):794-799, 1987.

[133] Lui EYL. Tavakkoli J. Cobbold RSC. Influence of boundary conditions on a one-dimensional ultrasound backscattering model of blood. Ultrasound in Medicine & Biology. 27(4):571-578, 2001.

[134] Madsen EL. Dong F. Frank GR. Garra BS. Wear KA. Wilson T. Zagzebski JA. Miller HL. Shung KK. Wang SH. Feleppa EJ. Liu T. O'Brien WD. Topp KA. Sanghvi NT. Zaitsev AV. Hall TJ. Fowlkes JB. Kripfgans OD. Miller JG. Interlaboratory comparison of ultrasonic backscatter, attenuation, and speed measurements. Journal of Ultrasound in Medicine. 18(9):615-631, 1999.

[135] Malek AM. Alper SL. Izumo S. Hemodynamic shear stress and its role in atherosclerosis. JAMA. 282(21):2035-2042, 1999.

[136] Maruvada S. Shung KK. Wang SH. High-frequency backscatter and attenuation measurements of porcine erythrocyte suspensions between 30-90 MHz. Ultrasound in Medicine & Biology. 28(8):1081-1088, 2002.

[137] Metropolis N. Rosenbluth, A. Rosenbluth R. Teller A. Teller E. Equation of state calculations by fast computing machines. J. Chem. Phys. 21:1087-1092, 1953.

[138] Missaridis TX. Shung KK. The effect of hemodynamics, vessel wall compliance and hematocrit on ultrasonic Doppler power: an in vitro study. Ultrasound in Medicine & Biology. 25(4):549-59, 1999.

[139] Mo LY. Cobbold RS. A stochastic model of the backscattered Doppler ultrasound from blood. IEEE Transactions on Biomedical Engineering. 33(1):20-27, 1986.

[140] Mo LYL. Cobbold RSC. A unified approach to modeling the backscattered Doppler ultrasound from blood. IEEE transactions on iomedical engineering. 39(5):450-461, 1992.

[141] Mo LYL. Cobbold RSC. Theoretical models of ultrasonic scattering in blood. Dans Shung KK. Thieme GA. Ultrasonic scattering in biological tissues. CRC Press. Boca Raton. 1993.

[142] Mo LYL. Kuo IY. Shung KK. Ceresne L. Cobbold RSC. Ultrasound scattering from blood with hematocrits up to 100 percent. IEEE Transactions on Biomedical Engineering. 41(1):91-95, 1994.

[143] Mohandas N. Evans E. Mechanical properties of the red cell membrane in relation to molecular structure and genetic defects. Annual Review of Biophysics & Biomolecular Structure. 23:787-818, 1994.

[144] Morse PM. Ingard KU. Theoretical Acoustics. Princeton University Press. 1968.

[145] Neu B. Meiselman HJ. Depletion-mediated red blood cell aggregation in polymer solutions. Biophysical Journal. 83(5):2482-2490, 2002.

[146] Neu B. Armstrong JK. Fisher TC. Meiselman HJ. Aggregation of human RBC in binary dextran-PEG polymer mixtures. Biorheology. 38(1):53-68, 2001.

[147] Nguyen CT. Hall CS. Wickline SA. Characterization of aortic microstructure with ultrasound: Implications for mechanisms of aortic function and dissection. IEEE Transactions on Ultrasonics Ferroelectrics & Frequency Control. 49(11):1561-1571, 2002.

[148] Njeh CF. Fuerst T. Diessel E. Genant HK. Is quantitative ultrasound dependent on bone structure? A reflection. Osteoporosis International. 12(1):1-15, 2001.

[149] O'Brien WD. Sagar KB. Warltier DC. Rhyne TL. Acoustic propagation properties of normal, stunned and infarcted myocardium – morphological and biochemical determinants. Circulation. 91(1):154-160, 1995.

[150] Oelze ML. Zachary JF. O'Brien WD. Characterization of tissue microstructure using ultrasonic backscatter: theory and technique for optimization using a Gaussian form factor. Journal of the Acoustical Society of America. 112(3):1202-11, 2002.

[151] Otto C. Geiss HC. Laubach E. Schwandt P. Effects of direct adsorption of lipoproteins apheresis on lipoproteins, low-density lipoprotein subtypes, and hemorheology in hypercholesterolemic patients with coronary artery disease. Therapeutic Apheresis. 6(2):130-135, 2002.

[152] Pace NG. Cowley AC. Campbell AM. Short pulse acoustic excitation of microbubbles. Journal of the Acoustical Society of America. 102(3):1474-1479, 1997.

[153] Padilla F. Peyrin F. Laugier P. Prediction of backscatter coefficient in trabecular bones using a numerical model of three-dimensional microstructure. Journal of the acoustical society of America. 113(2):1122-1129, 2003.

[154] Paeng DG. Cao PJ. Shung KK. Doppler power variation from porcine blood under steady and pulsatile flow. Ultrasound in Medicine & Biology. 27(9):1245-1254, 2001.

[155] Pearson MJ. Lipowsky HH. Influence of erythrocyte aggregation on leukocyte margination in postcapillary venules of rat mesentery. American Journal of Physiology – Heart & Circulatory Physiology. 279(4):1460-1471, 2000.

[156] Perkus JK. Yevick GJ. Analysis of classical statistical mechanics by means of collective coordinates. Physical Review. 110(1):1-13, 1958.

[157] Petsev DN. Interaction and adhesion of vesicles: Coupling between attractive interactions and bilayer membrane flexibility. Langmuir. 15(4):1096-1100, 1999.

[158] Peverill RE. Harper RW. Gelman J. Gan TE. Harris G. Smolich JJ. Determinants of increased regional left atrial coagulation activity in patients with mitral stenosis. Circulation. 94(3):331-339, 1996.

[159] Pitsavos C. Aggeli C. Lambrou S. Frogoudaki A. Brili S. Barbetseas J. Panagiotakos D. Stefanadis C. Toutouzas P. Prognosis of spontaneous echocardiographic contrast in the thoracic aorta. American Journal of Cardiology. 91(7):822-826, 2003.

[160] Phung TN. Brady JF. Bossis G. Stokesian dynamics simulation of Brownian suspensions. Journal of Fluid Mechanics. 313:181-207, 1996.

[161] Poiseuille JLM. Recherches expérimentales sur le mouvement des liquides dans les tubes de très petits diamètres. Comptes rendus de l'académie des sciences. 11:961-967, 1940.

[162] Pribush A. Meiselman HJ. Meyerstein D. Meyerstein N. Dielectric approach to the investigation of erythrocyte aggregation: I. Experimental basis of the method. Biorheology. 36(5-6):411-423, 1999.

[163] Pries AR. Secomb TW. Gaehtgens P. The endothelial surface layer. Pflugers Archiv – European Journal of Physiology. 440(5):653-666, 2000.

[164] Qin Z. Durand LG. Cloutier G. Kinetics of the "black hole" phenomenon in ultrasound backscattering measurements with red blood cell aggregation. Ultrasound in Medicine & Biology. 24(2):245-256, 1998.

[165] Qin Z. Durand LG. Allard L. Cloutier G. Effects of a sudden flow reduction on red blood cell rouleau formation and orientation using RF backscattered power. Ultrasound in Medicine & Biology. 24(4):503-511, 1998.

[166] Regnaut C. Ravey JC. Application of the adhesive sphere model to the structure of colloidal suspensions. J. Chem. Phys. 91(2):1211-1221, 1989.

[167] Rosenson RS. Lowe GD. Effects of lipids and lipoproteins on thrombosis and rheology. Atherosclerosis. 140(2):271-280, 1998.

[168] Ross R. Atherosclerosis – an inflammatory disease. New England Journal of Medicine. 340(2):115-126, 1999.

[169] Rouffiac V. Peronneau P. Hadengue A. Barbet A. Delouche P. Dantan P. Lassau N. Levenson J. A new ultrasound principle for characterizing erythrocyte aggregation: in vitro reproducibility and validation. Investigative Radiology. 37(8):413-420, 2002.

[170] Routh HF. Gough W. Williams RP. One-dimensional computer simulation of a wave incident on randomly distributed inhomogeneities with reference to the scattering of ultrasound by blood. Med. Biol. Eng. Comput. 25:667-671, 1987.

[171] Routh HF. Williams RP. Gough W. Weak reflection of ultrasound by elements arranged in the steps of a one-dimensional random walk, with reference to backscatter by blood. Med. Biol. Eng. Comput. 27:198-203, 1989.

[172] Rotstein R. Landau T. Twig A. Rubinstein A. Koffler M. Justo D. Constantiner D. Zeltser D. Shapira I. Mardi T. Goldin Y. Berliner S. The erythrocyte adhesiveness/aggregation test (EAAT). A new biomarker to reveal the presence of low grade subclinical smoldering inflammation in individuals with atherosclerotic risk factors. Atherosclerosis. 165(2):343-51, 2002.

[173] Russel WB. The Huggins coefficient as a means for characterizing suspended particles. J. Chem. Soc. Faraday Trans. 80:31-41, 1984.

[174] Savéry D. Cloutier G. Modeling of the acoustic signal backscattered by a biphasic suspension: application to the characterization of red blood cell aggregation. Dans Acoustical Imaging symposium. Bristol. Plenum Press. New York. 2000.

[175] Savéry D. Cloutier G. A point process approach to assess the frequency dependence of ultrasound backscattering by aggregating red blood cells. Journal of the Acoustical Society of America. 110(6):3252-3262, 2001.

[176] Savéry D. Cloutier G. Monte Carlo simulations of ultrasound backscattering by aggregating red blood cells. Proceedings of the IEEE Ultrasonics symposium, 2001. IEEE(2):1229-1232, 2001.

[177] Savéry D. Cloutier G., Anisotropy of ultrasonic backscatter by blood in shear flow: Monte Carlo simulations. Proceedings of the IEEE Ultrasonics symposium, 2002. IEEE(2):1503-1506, 2002.

[178] Scandinavian Simvistatin Survival Study Group. Randomised trial of cholesterol lowering in 4444 patients with coronary heart disease: the Simvistatin Survival Study. Lancet. 344:1383-1389, 1994.

[179] Schmid-Schonbein H. von Gosen J. Heinich L. Klose HJ. Volger E. A counter-rotating "rheoscope chamber" for the study of the microrheology of blood cell aggregation by microscopic observation and microphotometry. Microvascular Research. 6(3):366-376, 1973.

[180] Schmid-Schonbein H. Heidtmann H. Nonspecific rheological abnormalities in sickle cell disease. Blood Cells. 8(1):89-101, 1982.

[181] Schneditz D. Heimel H. Stabinger H. Sound speed, density and total protein concentration in blood. J. Clin. Chem. Clin. Biochem. 27:803-806, 1989.

[182] Serra J. Image Analysis and Mathematical Morphology – Vol. 1. Ac. Press. London. 1982.

[183] Sherar MD. Noss MB. Foster FS. Ultrasound backscatter microscopy images the internal structure of living tumour spheroids. Nature. 330(6147):493-495, 1987.

[184] Shehada RE. Cobbold RS. Mo LY. Aggregation effects in whole blood: influence of time and shear rate measured using ultrasound. Biorheology. 31(1):115-135, 1994.

[185] Shung KK. Sigelmann RA. Reid JM. Scattering of ultrasound by blood. IEEE Transactions on Biomedical Engineering. 23(6):460-467, 1976.

[186] Shung KK. Sigelmann RA. Reid JM. Angular dependence of scattering of ultrasound from blood. IEEE Transactions on Biomedical Engineering. 24(4):325-331, 1977.

[187] Shung KK. Reid JM. Ultrasonic instrumentation for hematology. Ultrasonic Imaging. 1(3):280-294, 1979.

[188] Shung KK. Yuan YW. Fei DY. Tarbell JM. Effect of flow disturbance on ultrasonic backscatter from blood. Journal of the Acoustical Society of America. 75(4):1265-1272, 1984.

[189] Shung KK. Cloutier G. Lim GC. The effects of hematocrit, shear rate, and turbulence on ultrasonic Doppler spectrum from blood. IEEE Transactions Biomedical Engineering. 39(5):462-469, 1992.

[190] Shung KK. and Thieme GA. Ultrasonic scattering in biological tissues. CRC Press. Boca Raton. 1993.

[191] Sigel B. Machi J. Beitler JC. Justin JR. Coelho JC. Variable ultrasound echogenicity in flowing blood. Science. 218(4579):1321-1323, 1982.

[192] Silbert LE. Melrose JR. Ball RC. A structural analysis of concentrated, aggregated colloids under flow. Molecular Physics. 96:1667-1675, 1999.

[193] Silbert LE. Melrose JR. Ball RC. The rheology and microstructure of concentrated, aggregated colloids. J. Rheol. 43(3):673-698, 1999.

[194] Skalak R. Zarda PR. Jan KM. Chien S. Mechanics of Rouleau formation. Biophys. J. 35:771-781, 1981.

[195] Skalak R. Chien S. Theoretical models of rouleau formation and disaggregation. Annals of the New York Academy of Sciences. 416:138-48, 1983.

[196] Sloop GD. A unifying theory of atherogenesis. Medical Hypotheses. 47(4):321-325, 1996.

[197] Sloop GD. Garber DW. The effects of low-density lipoprotein and high-density lipoprotein on blood viscosity correlate with their association with risk of atherosclerosis in humans. Clinical Science. 92(5):473-479, 1997.

[198] Sloop GD. A critical analysis of the role of cholesterol in atherogenesis. Atherosclerosis. 142(2):265-268, 1999.

[199] Snabre P. Mills P. Rôle des interactions électrostatiques dans le phénomène d'agrégation érythrocytaire. Dans Stolz JF. Hémorhéologie et agrégation érythrocytaire. Proceedings. Geneva. EM Inter. 1986.

[200] Steinberg D. Atherogenesis in perspective: hypercholesterolemia and inflammation as partners in crime. Nature Medicine. 8(11):1211-1217, 2002.

[201] Stetson P. Sommer G. Ultrasonic characterization of tissues via backscatter frequency dependence. Ultrasound Med. Biol. 23:989-996, 1997.

[202] Stuart J. Johnson CS. Rheology of the sickle cell disorders. Baillieres Clinical Haematology. 1(3):747-75, 1987.

[203] Takiuchi S. Rakugi H. Honda K. Masuyame T. Hirata N. Ito H. Sugimoto K. Tanagitani Y. Moriguchi K. Okamura A. Higaki J. Ogihara T. Quantitative ultrasonic tissue characterization can identify high-risk atherosclerotic alteration in human carotid arteries. Circulation 102:766-770, 2000.

[204] Teh BG. Cloutier G. Modeling and analysis of ultrasound backsacttering by spherical aggregates and rouleaux of red blood cells, IEEE Transactions on ultrasonics ferroelectrics and frequency control, 47(4):1025-1035, 2000.

[205] Tonks L. The Complete Equation of State of One, Two and Three-Dimensional Gases of Hard Elastic Sphere. Phys Rev 50:955-963, 1936.

[206] Topp KA. O'Brien WD. Anisotropy of ultrasonic propagation and scattering properties in fresh rat skeletal muscle in vitro. Journal of the Acoustical Society of America. 107(2):1027-1033, 2000.

[207] Tou JT. Gonzalez RC. Pattern Recognition Principles. Addison Wesley Company. Reading. 1974.

[208] Toubal M. Asmani M. Radziszewski E. Nongaillard B. Acoustic measurement of compressibility and thermal expansion coefficient of erythrocytes. Physics in Medicine & Biology. 44(5):1277-1287, 1999.

[209] Toss H. Lindahl B. Siegbahn A. Wallentin L. Prognostic influence of increased fibrinogen and C-reactive protein levels in unstable coronary artery disease. FRISC Study Group. Circulation. 96(12):4204-4210, 1997.

[210] Tsang WCO. The size and shape of human red blood cells. MS Thesis. University of California. San Diego. 1975.

[211] Twersky V. Transparency of pair-correlated, random distributions of small scatterers, with applications to the cornea. Journal of the Optical Society of America. 65(5):524-530, 1975.

[212] Twersky V. Acoustic bulk parameters in distributions of pair-correlated scatterers. J. Acoust Soc Am. 84:409-415, 1978.

[213] Twersky V. Low-frequency scattering by correlated distributions of randomly oriented particles. J. Acoust Soc Am. 81(5):1609-1618, 1987.

[214] Twersky V. Low-frequency scattering by mixtures of correlated non-spherical particles. J. Acoust Soc Am. 84(1):409-415, 1988.

[215] Vander AJ. Sherman JH. Luciano DS. Physiologie Humaine 2^{nde} édition. McGraw Hill. Montréal. 1977.

[216] Van der Heiden MS. de Kroon MG. Bom N. Borst C. Ultrasound backscatter at 30 MHz from human blood: influence of rouleau size affected by blood modification and shear rate. Ultrasound in Medicine & Biology. 21(6):817-826, 1995.

[217] Van Lieshout MNM. Markov Point Processes and their Applications. Imperial College Press. 2001.

[218] Van Leeuwenhoek A. Concerning the circulation and stagnation of the blood in tadpoles. Philosophical Transactions London. 22:447, 1702.

[219] Vered Z. Mohr G. Barzilai G. Gessler CJ. Wickline SA. Wear KA. Shoup TA. Weiss AN. Sobel BE. Miller JG. Ultrasound integrated backscatter tissue characterization of remote myocardial infarction in human subjects. Journal of the American College of Cardiology 13:84-91, 1989.

[220] Verwey EJW. Overbeek JTG. Theory of the stability of lyophibic colloids. Elsevier. Amsterdam. 1948.

[221] Vincelj J. Sokol I. Jaksic O. Prevalence and clinical significance of left atrial spontaneous echo contrast detected by transesophageal echocardiography. Echocardiography. 19(4):319-324, 2002.

[222] Vitale DF. Bonow RO. Gerundo G. Pelaggi N. Lauria G. Leosco D. Coltorti F. Bordini C. Rengo C. Rengo F. Alterations in ultrasonic backscatter during exercise-induced myocardial ischemia in humans. Circulation. 92(6):1452-1457, 1995.

[223] von Smoluchovski M. Versuch einer Mathematischen Theorie der Koagulationkinetic kolloider Lösungen. Z. Phys Chem. 92:129-188, 1917.

[224] Wang SH. Shung KK. An approach for measuring ultrasonic backscattering from biological tissues with focused transducers. IEEE Transactions on biomedical engineering. 44(7):549-554, 1997.

[225] Wang SH. Shung KK. In vivo measurements of ultrasonic backscattering in blood. IEEE Transactions on Ultrasonics Ferroelectrics & Frequency Control. 48(2):425-431, 2001.

[226] Waugh RE. Agre P. Reductions of erythrocyte membrane viscoelastic coefficients reflect spectrin deficiencies in hereditary spherocytosis. Journal of Clinical Investigation. 81(1):133-141, 1988.

[227] Weng X. Cloutier G. Beaulieu R. Roederer GO. Influence of acute-phase proteins on erythrocyte aggregation. American Journal of Physiology. 271(6):2346-2352, 1996.

[228] Weng X. Roederer GO. Beaulieu R. Cloutier G. Contribution of acute-phase proteins and cardiovascular risk factors to erythrocyte aggregation in normoli-

pidemic and hyperlipidemic individuals. Thrombosis & Haemostasis. 80(6):903-908, 1998.

[229] Wu SJ. Shung KK. An in vitro study of the effects of Doppler angle, fibrinogen, and hematocrit on ultrasonic Doppler power. IEEE Transactions on Ultrasonics Ferroelectrics & Frequency Control. 46 (1):197-204, 1999.

[230] Yamamura O. Miyoshi Y. Hiraki S. Ono H. Ootaki H. Fujiyama J. Kuriyama M. Spontaneous echo contrast in descending aorta correlates with low blood-flow velocity in carotid arteries and hemostatic abnormalities. Angiology. 52(11):749-758, 2001.

[231] Yarnell JW. Baker IA. Sweetnam PM. Bainton D. O'Brien JR. Whitehead PJ. Elwood PC. Fibrinogen, viscosity, and white blood cell count are major risk factors for ischemic heart disease. The Caerphilly and Speedwell collaborative heart disease studies. Circulation. 83(3):836-844, 1991.

[232] Yuan YW. Shung KK. Ultrasonic backscatter from flowing whole blood. I: Dependence on shear rate and hematocrit. Journal of the Acoustical Society of America. 84(1):52-58, 1988.

[233] Yuan YW. Shung KK. Ultrasonic backscatter from flowing whole blood. II: Dependence on frequency and fibrinogen concentration. Journal of the Acoustical Society of America. 84(4):1195-1200, 1988.

[234] Yuan YW. Ultrasonic scattering from blood. PhD. thesis. Pennsylvania State University. University Park. 1988.

[235] Yuan YW. Shung KK. Echoicity of whole blood. Journal of Ultrasound in Medicine. 8(8):425-34, 1989.

[236] Zhao H. Wang X. Stoltz JF. Comparison of three optical methods to study erythrocyte aggregation. Clinical Hemorheology & Microcirculation. 21(3-4):297-302, 1999.

[237] Zhu C. Bao G. Wang N. Cell mechanics: mechanical response, cell adhesion, and molecular deformation. Annual Review of Biomedical Engineering. 2:189-226, 2000.

[238] Zhu C. Kinetics and mechanics of cell adhesion. Journal of Biomechanics. 33(1):23-33, 2000 Jan.

[239] Zimm BH. Apparatus and methods for measurement and interpretation of the angular variation of light Scattering; preliminary results on polystyrene Solutions. J.Chem.Phys. 16(12):1099-1116, 1948.

[240] Zlonis M. The mystique of the erythrocyte sedimentation rate. A reappraisal of one of the oldest laboratory tests still in use. Clinics in Laboratory Medicine. 13(4):787-800, 1993.

Annexe A

Articles de conférence

Dans cette appendice, on trouvera deux articles des conférences *IEEE Ultrasonics Symposium* de 2001 et 2002 référencés dans la bibliographie en [176] et [177].

MONTE CARLO SIMULATION OF ULTRASOUND BACKSCATTERING BY AGGREGATING RED BLOOD CELLS

David Savéry*, Guy Cloutier
Laboratory of Biorheology and Medical Ultrasonics, University of Montreal Hospital,
2099 Alexandre de Sève (Y-1619), Montreal, QC, Canada, H2L 2W5

Abstract – When blood flows at a low shear rate, red cells aggregate and form clusters that affect vascular resistance to flow and blood echogenicity. This study intends to clarify the relation between the red cell aggregation level and the ultrasonic backscatter increase. Red cell positioning in plasma is modeled by a 2D Markov point process at a 40% hematocrit. A square well potential is adopted to take into account the erythrocyte adhesive interaction energy. Monte Carlo simulations of the point process and computations of the mean structure factor enables to assess the frequency dependence of the blood backscatter for different aggregation potentials. The ultrasonic sensitivity to the erythrocyte clustering phenomenon is demonstrated and could be used as a non invasive measurement method of blood microstructure and rheology.

I. INTRODUCTION

Main scatterers of the ultrasound wave in blood are red cells. As the red cell density is high, the intricate spatial pattern created by the packed network of erythrocytes has a strong influence on the backscattering properties of blood. In particular, the erythrocyte aggregation phenomenon was shown to affect blood echogenicity, in relation with the protein plasmatic concentrations or with the hydrodynamic shear forces acting on red cell aggregates.

Viscous properties of blood, as its shear-thinning rheological behavior, are related to the size of the red cell clusters. Therefore, rheological characteristics of blood should be measurable by ultrasonic means if the aggregation-dependence of blood backscattering was known.

Ultrasonic techniques of tissue characterization consist mainly in measuring attenuation and backscattering acoustical properties of the tissues to distinguish their healthy or pathological state. The present study intends to predict how the erythrocyte aggregation level affects the frequency dependence of the blood backscattering.

Theoretical and experimental studies agreed when quantitative prediction of the backscattering coefficient of non-aggregating suspension of red cells in laminar flow, in Rayleigh conditions, was made as a function of the hematocrit [1]. But the effect of aggregation on the scattering properties of blood still remains unclear.

Therefore, the purpose of this paper is to extend predictions of the backscattering coefficient of blood to aggregating conditions. A two-dimensional Monte Carlo approach is adopted to simulate erythrocyte positioning in blood. This allows to estimate the mean backscattering coefficient of a 2D suspension of aggregating red cells as a function of the frequency and of an energetic aggregation index, namely the effective aggregation potential.

II. METHODS

Expression of the backscattering coefficient

The backscattering coefficient $\chi(\mathbf{k})$ of a suspension of weak scattering identical particles is given by [2]:

$$\chi(\mathbf{k})=m\,\sigma_b(-2\mathbf{k})\,S(-2\mathbf{k}), \qquad (1)$$

where $\mathbf{k}$ is the wave vector of the incident plane wave ($|\mathbf{k}|=2\pi f/c$, f being the acoustical frequency of the wave and $c\approx1540$ m/s is the speed of sound), m is the number density of the scatterers, $\sigma_b(-2\mathbf{k})$ is the backscattering cross-section of the individual scatterer, and $S(-2\mathbf{k})$ is the structure factor of the medium.

Red cell acoustic properties

The number density m is directly related to the hematocrit H in whole blood, as $H=mV_s$, V_s being the volume of the red cells. The backscattering cross-section reflects the scattering strength of a single red

Savéry D. Cloutier G. Monte Carlo simulations of ultrasound backscattering by aggregating red blood cells. Proceedings of the IEEE Ultrasonics symposium, 2001. IEEE(2):1229-1232, 2001.

cell. Red cells are considered as cylinders with diameter $2a$=7 μm and volume V_s=87 μm^3. Their axis are supposed to be aligned, perpendicularly to the wave vector. This assumption about the invariance of the red cell orientations allowed simplification of the simulations in two dimensions. In this case, the backscattering cross-section is given by:

$$\sigma_b(-2k) = \frac{k^4}{4\pi^2} V_s^2 \overline{C}^2 \left(\frac{J_1(2ka)}{ka} \right)^2, \qquad (2)$$

where J_1 is the Bessel function of first order and $\overline{C} \approx 0.11$ is the mean relative mismatch between red cell and plasmatic acoustical impedances.

Notion of structure factor

The microscopic organization of the scatterers directly influences the structure factor of the material. When the scattering particles are independently positioned in space (Poisson point process), $S(-2\mathbf{k})=1$, whereas when scatterers form organized patterns, $S(-2\mathbf{k})$ reflects the global effect of phase differences between wavelets backscattered by red cells.

Suppose that M red cells occupy a volume V, and have random positions given by $\{\mathbf{x}_i\}_{i=1...M}$. Then $S(-2\mathbf{k})$ is given by the ensemble average :

$$S(-2\mathbf{k}) = E[\, |\, \Sigma_i \exp(-2j\mathbf{k}.\mathbf{x}_i)\, |^2\,]/M. \qquad (3)$$

An appropriate model of random point process must be chosen to simulate red cell positioning in the sample volume. An energy $U(\mathbf{x}_1,\ldots,\mathbf{x}_M)$ is assigned to each configuration of the red cells.

The Boltzmann law then yields the probability density function of the M dependent positions $\{\mathbf{x}_i\}$ as a function of their total energy:

$$P(\mathbf{x}_1,\ldots\mathbf{x}_M) = 1/Z \exp(-U(\mathbf{x}_1,\ldots,\mathbf{x}_M)/k_B T), \qquad (4)$$

where Z is the partition function, the normalizing constant so that the sum of all probabilities is unity, T is the absolute temperature and k_B is the Boltzmann constant.

We consider that red cells are attractive hard cylinders by assuming that every pair of red cells has a potential V_p and that the configuration energy is the sum of all pair potentials $U(\mathbf{x}_1,\ldots,\mathbf{x}_M) = \Sigma_{i<l} V_p(\mathbf{x}_i,\mathbf{x}_l)$. The square well potential model is chosen to define V_p.

For two red cells centered in $\mathbf{x}_i$ and $\mathbf{x}_j$:

$$\begin{aligned} V_p(\mathbf{x}_i,\mathbf{x}_j) &= V_{rep} && \text{when } d(\mathbf{x}_i,\mathbf{x}_j) < 2a \\ &= -V_{agg} && \text{when } 2a < d(\mathbf{x}_i,\mathbf{x}_j) < 2a + h_{agg} \\ &= 0 && \text{when } 2a + h_{agg} < d(\mathbf{x}_i,\mathbf{x}_j). \end{aligned}$$

V_{rep} is a repulsion potential that forbids red cells to overlap and V_{agg} is an adhesive energy that models intercellular attractive forces at distances smaller than h_{agg}.

Simulation method

To assess the ensemble average $S(-2\mathbf{k})$, L random samples of configurations with probabilities obeying to the Boltzmann law are generated using a Monte Carlo Metropolis method. Their mean structure factor is used as an estimate of $S(-2\mathbf{k})$. The Metropolis algorithm consists in an iterative method that converges from any initial configuration to obtain a sample that has an appearance probability given by Eq. (4). The detail of the algorithm that generates a sequence of M red cell centers $\{\mathbf{x}_1(N),\ldots,\mathbf{x}_M(N)\}_{N=0...N_\infty}$ is as follows:

Initialization

For $i=1...M$, $\mathbf{x}_i(0)$ is chosen randomly with a uniform probability in V.

Step (N) to (N+1)

- Choose randomly a particle I among the M scatterers.
- Propose a new position ξ in V instead of $\mathbf{x}_I(N)$.
- Compute the difference ΔU of energy due to the displacement of I from $\mathbf{x}_I(N)$ to ξ.
- Accept the transition $\mathbf{x}_I^{(N+1)}=\xi$ with the probability $\min\{1, \exp(-\Delta U)/k_B T\}$ otherwise $\mathbf{x}_I(N+1)=\mathbf{x}_I(N)$.

Iterate until $N=N_\infty$ chosen in advance. Then $\{\mathbf{x}_1(N_\infty),\ldots,\mathbf{x}_M(N_\infty)\}$ is a random configuration with a probability of appearance that approximates the Boltzmann law.

This process is achieved L times to obtain L independent samples. For each sample, its structure factor is computed from the position of the centers. The mean structure factor is then computed by averaging the L structure factors obtained.

III. Results

The backscattering coefficient of the simulated medium is dependent on the following factors:

- the frequency f,

- the hematocrit H,
- the interaction distance h_{agg}, and
- the interaction potentials V_{rep} and V_{agg}.

The positioning of M=815 red cells (H=40%) is simulated in a 2D window with dimensions 280 µm × 280 µm. The convergence is supposed to be reached after N_∞=32600 steps of the Metropolis sampler. A number L=100 of independent realizations are performed to obtain the mean structure factor on a large frequency band. A large repulsion potential $V_{rep}=10^6 k_B T$ is chosen to forbid red cell overlapping. The interaction distance was set to h_{agg} =2.8 µm and the value of the aggregation potential V_{agg} is increased from 0 (no aggregation) to $10k_BT$ (high aggregative behavior).

Effect of the aggregation potential on the aggregate morphology

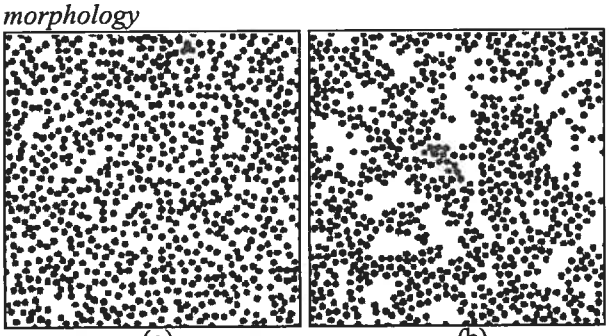

Figure 1: Two simulations of red cell positioning
a: V_{agg}=0 (no aggregation)
b: $V_{agg}=10k_BT$ (aggregated medium)

Figure 1 illustrates the effect of the aggregation potential on the packing conformation of the erythrocytes. For the disaggregated state, the high density combined with the non-overlap constraint influenced the spatial correlation between particles. A level of the aggregation potential $V_{agg}=10k_BT$ increased the likelihood of surface adhesion, and therefore increased the compactness of red cell aggregates and the size of the plasmatic gaps between erythrocytes (while the hematocrit is kept constant).

Effect of the aggregation potential on the frequency dependence

Figure 2 shows the quantitative evolution of the mean backscattering coefficient χ computed using equations (1), (2) and (3), as a function of the frequency and of the aggregation potential.

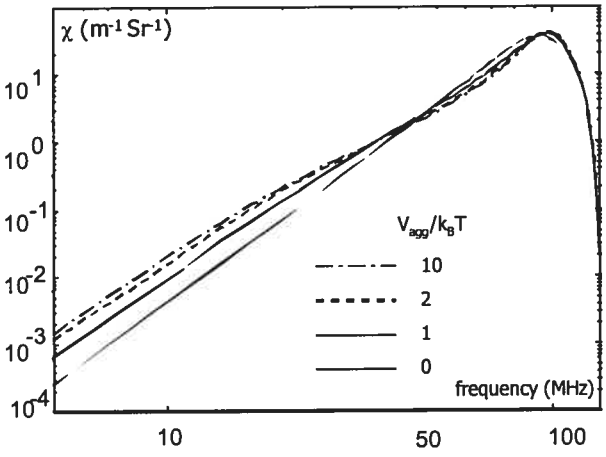

Figure 2: Backscattering coefficient as a function of the frequency and of the aggregation potential

Generally, the backscattering coefficient was observed to increase with the frequency and peaks around 90 MHz. Under 10 MHz, χ linearly increased with f^4, according to the Rayleigh law. At a given frequency under 50 MHz, the backscatter also increased with V_{agg}.

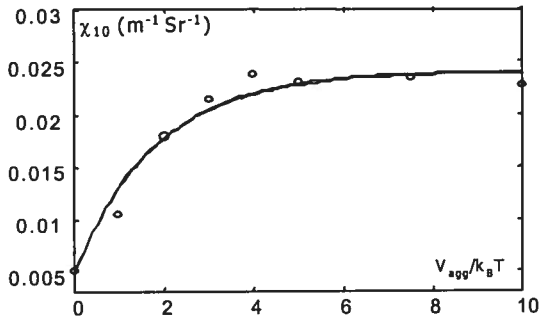

Figure 3: Backscattering coefficient at 10 MHz as a function of the aggregation potential

The variations of the frequency dependence were assessed by computing two quantities characterizing the evolution of χ between 10 MHz and 50 MHz: χ_{10}, the backscattering coefficient at 10 MHz, and $n=\log(\chi_{50}/\chi_{10})/\log(50/10)$, the mean spectral slope, so that :

$$\chi(f)/\chi_{10} \approx (f/10)^n \qquad 10 \text{ MHz} < f < 50 \text{ MHz} \qquad (5)$$

Figure 3 shows the influence of the aggregation potential on χ_{10}. The increase of χ_{10} is fitted to an exponential law that gives:

$$\chi_{10}/\chi^0 = 1 + 3.8\ (1\text{-}\exp(-V_{agg}/1.8k_BT)), \qquad (6)$$

where χ^0 represents the backscattering coefficient at 10 MHz of a non-aggregating suspension for H=40%.

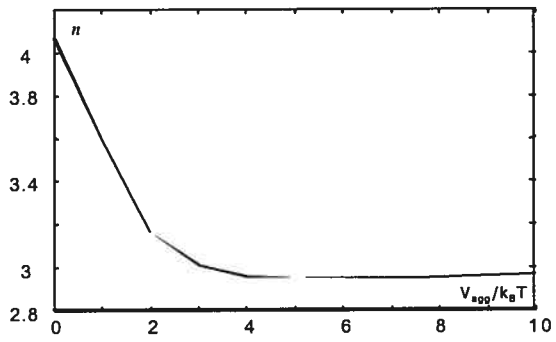

Figure 4: Mean spectral slope between 10 and 50 MHz as a function of the aggregation potential

Figure 4 shows the deviation from the Rayleigh law when the aggregation potential increases, as the spectral slope n decreases from 4 to 3 when increasing the aggregation potential.

IV. Discussion and Conclusion

Monte Carlo simulations were performed to model spatial patterns created by red cells submitted to different aggregating conditions. They enabled to elucidate, in two dimensions, the relation between the red cell aggregation level and the backscattering strength of blood at a physiological hematocrit and for non-Rayleigh frequencies, whereas previous models were restricted to low hematocrits [3] or to low frequencies [4].

Experimental studies [5] revealed two acoustical phenomena when decreasing the shear rate for a given blood sample: the increase of the backscatter at a constant frequency and the decrease of the spectral slope.

The 2D results presented here showed similar trends when increasing the aggregation potential governing the random process of erythrocyte positioning. Associated to the interaction length h_{agg}, the aggregation potential V_{agg} seems to be a valuable and sensitive quantity that efficiently models red cell packing. The effect of the interaction length h_{agg}, related to the size of the plasmatic protein molecules, has not been investigated in this study. V_{agg} and h_{agg} could be used as global physical indices related to the strength of the adhesion, to the intensity of the shear disrupting forces and to the length of the protein bonds linking erythrocytes.

It must be noted that the generalization of this model for a three-dimensional medium would be algorithmically similar. Further 3D studies are expected to provide results that would allow to assess $\{h_{agg}, V_{agg}\}$ by measuring the frequency dependence of the backscattered power.

V. References

[1] L.Y.L. Mo, I.Y. Kuo, K.K. Shung, L. Ceresne and R.S.C. Cobbold, "Ultrasound scattering from blood with hematocrits up to 100 %," IEEE Trans. Biomed. Eng., vol. 41, pp. 91-95, Jan 1994.

[2] V. Twersky, "Low frequency scattering by correlated distributions of randomly oriented particles," J. Acoust. Soc. Am., vol. 81, pp 1609-1614, May 1987.

[3] D. Savéry and G. Cloutier, "A point process approach to assess the frequency dependence of ultrasound backscattering by aggregating red blood cells," J. Acoust. Soc. Am., to be published.

[4] B. Lim and R.S.C. Cobbold, "On the relation between aggregation, packing and the backscattered ultrasound signal for whole blood," Ultrasound in Medicine & Biology, vol. 25, pp 1395-1405, Nov 1999.

[5] Y.W. Yuan and K.K. Shung, "Ultrasonic backscatter from flowing whole blood: II. Dependence on frequency and fibrinogen concentration," J. Acoust. Soc. Am., vol. 84, pp 1195-1200, Dec 1988.

* Guy Cloutier e-mail : [redacted]

ANISOTROPY OF ULTRASONIC BACKSCATTER BY BLOOD IN SHEAR FLOW: MONTE CARLO SIMULATIONS

David Savéry*, Guy Cloutier
Laboratory of Biorheology and Medical Ultrasonics, Research Center, University of Montreal Hospital,
2099 Alexandre de Sève (Y-1619), Montreal, QC, Canada, H2L 2W5

Abstract – The relation between the heterogeneous microstructure of biological tissues and their measurable scattering properties is still poorly understood. In particular, physical explanation of blood hyperechogenicity when submitted to low shear forces appears incomplete. To quantify the contribution of erythrocyte aggregation to this phenomenon, Monte Carlo 2D simulations of red cell spatial pattern are performed. The backscattering coefficient of blood at 5 and 40 MHz is estimated for two orthogonal insonification angles, as a function of effective adhesive energy V_{agg} and anisotropy index α. Isotropic aggregation resulted in an enhanced backscatter at 5 MHz (+7 dB) but had a minor effect at 40 MHz. Addition of spatial anisotropy essentially diminished the backscatter at 5 MHz, independently on the angle, whereas at 40 MHz, the perpendicular backscatter largely exceeded the parallel backscatter (+6 dB). This showed that anisotropy present in the spatial microscopic pattern can be detected in the high frequency scattering regime, while low frequency backscatter is more affected by larger geometrical features as the aggregate size.

I. INTRODUCTION

Blood echogenicity, when measured in B mode, power Doppler imaging or in RF analysis, is known to vary with several experimental factors. Instrumental parameters as the frequency of the transmitted ultrasonic wave or the insonification angle with respect to the flow velocity affect blood echogenicity. Blood backscatter also intrinsically varies as a function of the local hemodynamics. It was shown e.g. that flow stasis enhances blood echogenicity resulting in the appearance of smoke-like spontaneous echocontrasts [1].

This variability of the macroscopic blood scattering properties is mainly due to microstructural changes induced by the formation of red cell aggregates in plasma. Erythrocytes, main scatterers of ultrasound in blood, form a viscoelastic dense gel in plasma that adopts varying configurations in response to shear forces. Moreover, plasmatic proteins, such as fibrinogen, can modulate this clustering behavior by modifying surface intercellular forces. Several clinical studies have shown that an elevated red cell aggregation level is correlated to risks of cardiovascular disease, probably because the presence of aggregates alters the ability of blood to flow through microvasculature. It is therefore intend to define an ultrasonic measurement procedure that detects red cell aggregation abnormalities to understand the impact of hemorheology on the etiology of cardiovascular diseases.

Theoretical studies that aim at quantitatively understanding how the erythrocyte aggregation level affects blood echogenicity are still unsatisfactory. Experimental frequency and angular dependenciese are not in agreement with Rayleigh law and therefore another formulation of the backscattering properties of blood was adopted [2]. In previous studies, the increase of the backscatter as well as the decrease of its frequency dependence observed when erythrocytes form compact clumps could be predicted. But only recently [3] anisotropic shearing effects were taken into consideration. Allard et al. [4] observed such anisotropy when measuring the Doppler power under several insonification angles. In some situations, Red cells tend to adhere in linear "rouleaux" rather than in isotropic clusters. They align preferentially along the streamlines, creating directional spatial patterns. In this paper, it is intended to elucidate both the frequency and angular dependencies of blood backscatter in such shearing conditions. Extending a previous study [2], a Monte Carlo approach is retained to simulate cluster formation of aligned rouleaux. The backscattering coefficient χ is assessed and its sensitivity at 5 and 40 MHz to the aggregation level is quantified.

II. METHODS

Expression of the backscattering coefficient

The intrinsic physical property quantifying the echogenic strength of a suspension of weak scatterers is the backscattering coefficient that can be factorized under the form:

$$\chi(\mathbf{k})=m\,\sigma_b(-2\mathbf{k})\,S(-2\mathbf{k}), \qquad (1)$$

where $\mathbf{k}$ is the wave vector of the incident plane wave ($|\mathbf{k}|=2\pi f/c$, f being the acoustical frequency of the wave and $c\approx1540$ m/s is the speed of sound), m is the number density of the scatterers, $\sigma_b(-2\mathbf{k})$ is the backscattering cross-section of a single particle, and $S(-2\mathbf{k})$ is the structure factor of the medium.

Red cells are hypothesized to be cylindrical, their axis being normal to the 2D simulation plane. The analytical expression of their cross-section was taken as in a previous study [2]:

$$\sigma_b(-2k)=\frac{1}{4\pi^2}k^4\,V_s^2C^2\left(\frac{J_1(2kR)}{kR}\right)^2. \qquad (2)$$

V_s is the volume of the red cells, R is their radius, J_1 is the Bessel function of order *1*, and $C=0.11$ represents the relative contrast of acoustical impedance between the bulk plasma and erythrocytes. The structure factor of a collection of M weak scatterers centered in random positions $\{\mathbf{x}_i\}_{i=1\ldots M}$ represents the ensemble average:

$$S(-2\mathbf{k})=\mathrm{E}[\,|\,\Sigma_i\exp(-2j\mathbf{k}.\mathbf{x}_i)\,|^2\,]/M. \qquad (3)$$

Stochastic model of red cell positioning

These red cell random positions are supposed to follow a probability density function P as given by the Boltzmann law. The appearance probability P of a given configuration derives from a global system energy, defined as the sum of space-invariant pair potentials V_p and is given by (k_B is the Boltzmann constant, Z a constant named partition function, and T is the temperature):

$$P(\mathbf{x}_1,\ldots\mathbf{x}_M)=1/Z\,\exp(-\Sigma_{m<n}V_p(\mathbf{x}_m-\mathbf{x}_n)/k_BT). \qquad (4)$$

Choice of the pair potential

Simplified anisotropic interactions between red cells are modeled considering that they adhere more likely along the x direction (streamlines of a stationary shear flow) rather than along the y direction. Hydrodynamic forces are indirectly taken into consideration by this modeling. An elliptic interaction area with long axis Ox is drawn around each rigid cell. A negative attractive energy between two cells is defined proportional to the intersection area of the interaction ellipses. A very high repulsive positive energy V_{rep} is also added to the global potential when the cells are closer than their diameter $2R$, which prevents cell overlapping. Analytically:

$$V_p(\mathbf{h})=V_{rep}\phi_{rep}\left(\frac{|\mathbf{h}|}{2R}\right)-V_{agg}\phi_{agg}\left(\frac{1}{2}\sqrt{\left(\frac{h_x}{a}\right)^2+\left(\frac{h_y}{b}\right)^2}\right), \qquad (5)$$

Where $\mathbf{h}$ is the vector lag between red cells and the two following numerical functions are introduced:

$$\phi_{rep}(\varepsilon)=1_{|\varepsilon|<1}$$
$$\phi_{agg}(\varepsilon)=\frac{2}{\pi}1_{|\varepsilon|<1}\left(\arccos\varepsilon-\varepsilon\sqrt{1-\varepsilon^2}\right) \qquad (6)$$

The axes of the interaction ellipses are noted {a,b}, R<a<b. Non-dimensional quantities {σ,α} are defined as $ab=\sigma^2R^2$ and 1+α=a/b.

Simulation method

The Metropolis sampler algorithm as described previously [2] was used to generate 100 independent samples of the random point process. The structure factor on a large frequency range was computed by Fast Fourier Transform of the digitized number density of the simulation area. It was averaged over the 100 samples to obtain its mean value, which enabled to assess the backscattering coefficient.

III. RESULTS

The influence of the aggregation potential V_{agg} and of the anisotropy index α on the backscattering coefficient χ at 5 (low frequency) and 40 MHz (high frequency) was specifically studied. Some parameters were kept constant: the dimension σ=1.4 (elliptic area kept constant), and the repulsion potential $V_{rep}=10^6$ k_BT. The simulation area was a 2D window with dimensions 280 μm × 280 μm for M=815 red cells (hematocrit=40%).

Resulting spatial pattern

Figure 1 shows typical configurations when increasing V_{agg} or α. Erythrocytes aggregates form clumps when α=0 or aligned structures when increasing α.

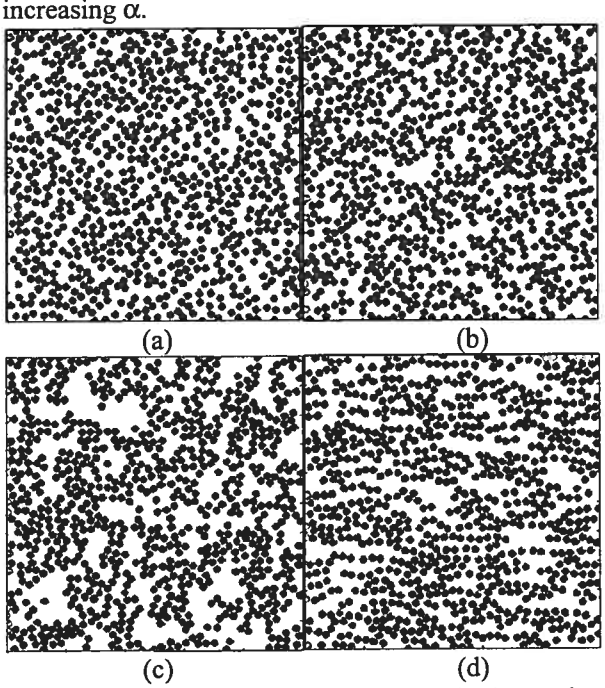

Figure 1: Simulations of red cell positioning under different aggregating conditions

a	V_{agg}=0	α=0
b	V_{agg}=5 k_BT	α=0
c	V_{agg}=200 k_BT	α=0
d	V_{agg}=200 k_BT	α=1

Isotropic clustering and frequency dependence

Figure 2 shows the frequency dependence of the backscattering coefficient in isotropic conditions when varying the aggregation potential. Variations of χ_5 and χ_{40} (in dB, compared to the disaggregated state, exponent 0) with V_{agg} are reasonably well described by the exponential formulas (Figure 3) :

$$10\log_{10}(\chi_5/\chi_5^0) = 7\,(1-\exp(-V_{agg}/19k_BT))\ \text{dB}$$
$$10\log_{10}(\chi_{40}/\chi_{40}^0) = 1.3\,(1-\exp(-V_{agg}/6k_BT))\ \text{dB} \quad (7)$$

Anisotropic clustering and scattering

The preferential growth of clusters along the *Ox* direction leads to angle-dependent physical properties. Figures 4 and 5 depict the differential behavior of χ_5 and χ_{40} in parallel and perpendicularly to the flow, when varying both V_{agg} and α. Increase of α has minimal impacts on χ_5, whatever the orientation. It tends to diminish the effect of clustering by diminishing χ_5, but no marked anisotropic backscattering can be observed at such a low frequency. On the contrary, at 40 MHz, backscatter tends to increase when the incident wave perpendicularly intersects the linear rouleaux, whereas it decreases in parallel with flow. Anisotropic scattering behavior is more pronounced when α increases jointly with V_{agg}.

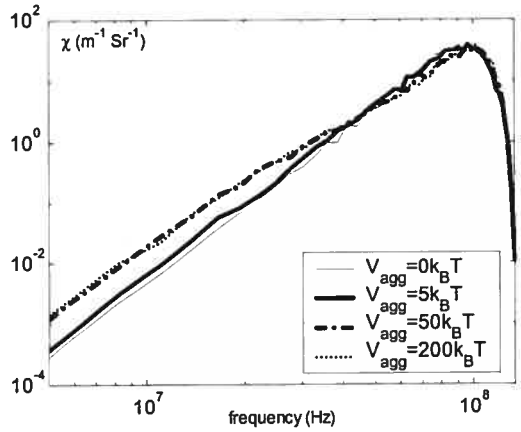

Figure 2: Frequency dependence of the backscatter in isotropic aggregating conditions (α=0)

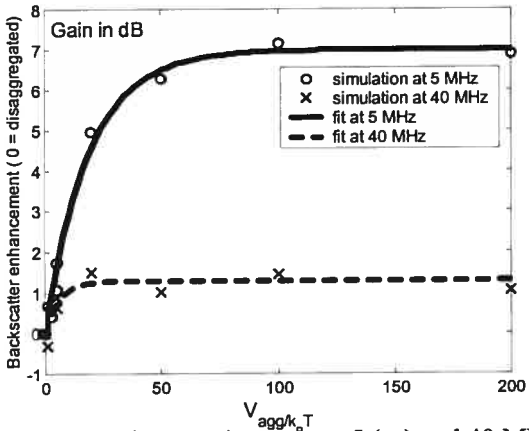

Figure 3: Backscatter increase at 5 (χ_5) and 40 MHz (χ_{40}) due to isotropic aggregation (α=0)

IV. Discussion and Conclusion

Results obtained in isotropic conditions (α=0) essentially give the same trends obtained in previous

Monte Carlo simulations [2]: isotropic aggregation induces a backscatter increase that is less pronounced at high frequencies.

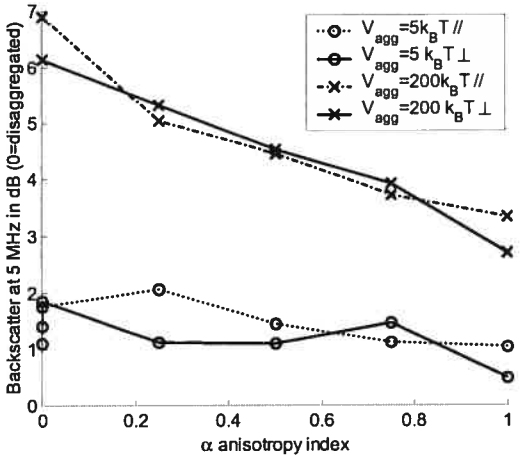

Figure 4: Effect of the anisotropy index and of the aggregation potential on the backscatter at 5 MHz

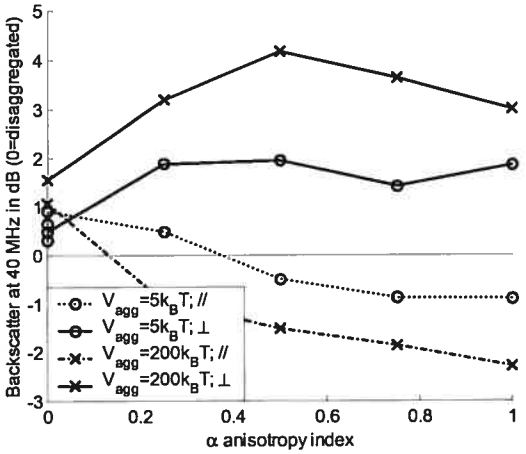

Figure 5: Effect of the anisotropy index and of the aggregation potential on the backscatter at 40 MHz

This study enabled to extend these results by also modeling layered clustering of red cells as obtained when submitting blood to a constant shear rate. At 5 MHz, linear growth of aggregates enhances blood echoicity (up to 7 dB) in no particular direction. However, angular variation of backscatter dramatically changes at 40 MHz. Backscattering is enhanced perpendicularly to the flow and decreases in parallel. This shows that high frequency ultrasound is not only sensitive to the orientation of the scattering particles, as Coussios points out in [5], but can more generally be affected by anisotropy of the global organization formed by scatterers at a higher length scale.

In the experimental study performed by Allard et al. [4], the Doppler power at 10 MHz measured in the center of a Poiseuille flow peaked at an angle of 50° with the flow axis, and varied by 5 dB in the angle range 40°-80° at a shear rate of 17 s^{-1}. The fact that it does not peak at 90° can be attributed to the different spatial distribution of the aggregates between 3D Poiseuille (non homogeneous shear rate) and 2D Couette flow. Furthermore, the proposed modeling does not strictly mimic particle motion in a shear flow, as the task of simulating hydrodynamic interactions between flowing plasma and embedded cells is computationally intensive. It was intended to describe the resulting spatial pattern using a reduced number of descriptive parameters. These parameters $\{V_{agg}, \alpha, \sigma\}$ could be taken as efficient measurable characteristics that have to be related to blood viscosity or to other microrheological variables.

ACKNOWLEDGMENT

This work was supported by grant # MOP-36467 from the Canadian Institute of Health Research.

V. REFERENCES

[1] B. Sigel, J. Machi, J.C. Beitler, J.R. Justin, J.C. Coelho, "Variable ultrasound echogenicity in flowing blood," Science, vol. 218, pp 1321-1323, Dec 1982.

[2] D. Savéry, G. Cloutier, "Monte Carlo simulation of ultrasound backscattering by aggregating red blood cells," in IEEE Ultrasonics Symposium Proceedings, 2001, pp. 1229-1232.

[3] I. Fontaine, D. Savéry and G. Cloutier, "Simulation of ultrasound backscattering by red cell aggregates: effect of shear rate and anisotropy," Biophys. J., vol. 82, pp 1696-1710, Apr 2002.

[4] L. Allard, G. Cloutier and L.G. Durand, "Effect of the insonification angle on the Doppler backscattered power under red blood cell aggregation conditions," IEEE Trans. Ultrason. Ferroelect. Freq. Contr., vol. 43, pp 211-219, Mar 1996.

[5] C.C. Coussios, "The significance of shape and orientation in single-particle weak-scatterer models," J. Acoust. Soc. Am., vol. 112, pp 906-915, Sep 2002.

* Guy Cloutier e-mail : [redacted]

Annexe B

Article de revue scientifique

Dans cette annexe, on trouvera l'article [82] paru dans Biophysical Journal en 2002.

Biophysical Journal Volume 82 April 2002 1696–1710

Simulation of Ultrasound Backscattering by Red Cell Aggregates: Effect of Shear Rate and Anisotropy

Isabelle Fontaine, David Savéry, and Guy Cloutier

Laboratory of Biomedical Engineering, Clinical Research Institute of Montreal, Montreal, Quebec, H2W 1R7, and Laboratory of Biorheology and Medical Ultrasonics, University of Montreal Hospital, Montreal, Quebec H2L 2W5, Canada

ABSTRACT Tissue characterization using ultrasound (US) scattering allows extraction of relevant cellular biophysical information noninvasively. Characterization of the level of red blood cell (RBC) aggregation is one of the proposed application. In the current paper, it is hypothesized that the microstructure of the RBCs is a main determinant of the US backscattered power. A simulation model was developed to study the effect of various RBC configurations on the backscattered power. It is an iterative dynamical model that considers the effect of the adhesive and repulsive forces between RBCs, and the effect of the flow. The method is shown to be efficient to model polydispersity in size, shape, and orientation of the aggregates due to the flow, and to relate these variations to the US backscattering properties. Three levels of aggregability at shear rates varying between 0.05 and 10 s^{-1} were modeled at 40% hematocrit. The simulated backscattered power increased with a decrease in the shear rate or an increase in the RBC aggregability. Angular dependence of the backscattered power was observed. It is the first attempt to model the US power backscattered by RBC aggregates polydisperse in size and shape due to the shearing of the flow.

INTRODUCTION

Ultrasound (US) has become an important imaging modality in the medical field because it is safe, rapid, noninvasive, and relatively inexpensive. The US signal is emitted by a piezoelectric transducer, and, as the mechanical waves propagate through the tissues, a part of the signal is partially scattered back toward the transducer according to the acoustic inhomogeneities encountered. The most well-known application of US backscattering is the formation of B-mode images, obtained by representing the variations in amplitude of the signal backscattered from tissues as gray levels. In recent years, other applications have emerged, such as tissue characterization. Because the properties of the scattered wave vary with size, the acoustic impedance (density and compressibility), and the microstructural organization of the cells, US scattering can be used to detect the presence of tissue abnormalities, such as cancerous cells (Landini and Verrazzani, 1990; Ursea et al., 1998).

For a region of interest in a blood vessel, the main scatterers of the US waves are the red blood cells (RBCs). The backscattered signal is thus associated to the properties of the blood sample, e.g., the hematocrit and the level of aggregation. Red cell aggregation results from complex cellular interactions that depend on the size and concentration of certain proteins in the plasma, the intrinsic deformability of the red cells, their glycocalyx (external layer), and the hematocrit. The aggregative tendency of RBCs changes among individuals and is modulated by the flow conditions, which vary within the arterial/venous tree. Thrombosis (Chabanel et al., 1994), hypertension (Razavian et al., 1992), hyperlipidemia (Razavian et al., 1994), diabetes (Schmid-Schönbein and Volger, 1976), and coronary artery disease (Neumann et al., 1991) are, among others, pathologies often associated with abnormally high levels of RBC aggregation. It would therefore be valuable to detect such abnormalities by US methods, but the relation between the level of aggregation and the US measurements is still unclear.

Experimental measurements have shown that the US backscattered power increases with the level of RBC aggregation (Cloutier and Qin, 1997). It was observed that the US power backscattered by aggregating RBCs, such as human, porcine, or equine RBCs, was shear-rate-dependent (Sigel et al., 1982; Yuan and Shung, 1988; Shehada et al., 1994; Cloutier and Qin, 2000), whereas the US power backscattered by nonaggregating RBCs, such as bovine RBCs or a saline suspension of RBCs, was little affected by the shearing condition (Yuan and Shung, 1988). In the studies performed with aggregating RBCs, power variations of the order of 15 dB were observed as a function of the shear rate at acoustical frequencies below 10 MHz. Moreover, it was observed that the dependence of the backscattered power with the frequency of insonification is modified by the level of aggregation (Foster et al., 1994). There is thus a need to provide a model of US backscattering by aggregating RBCs to interpret these experimental findings and shed some light on the mechanisms of US backscattering by blood.

Many models were proposed to characterize US backscattering, however the majority of them addressed the problem of nonaggregating RBCs (Berger et al., 1991; Mo and Cobbold, 1992; Zhang et al., 1994). Our group recently simulated US backscattering by RBCs by modeling the US system characteristics and the RBCs' shape and positions

Submitted December 28, 2000, and accepted for publication December 31, 2001.

Address reprint requests to Dr. Guy Cloutier, Laboratory of Biorheology and Medical Ultrasonics, Research Center, CHUM Notre-Dame Hospital, Pavilion J.A. de Sève (Y-1619), 2099 Alexandre de Sève, Montreal, QC H2L 2W5, Canada. Tel.: 514-890-8000 (24703); Fax: 514-412-7505; E-mail: [redacted]

0006-3495/02/04/1696/15 $2.00

(Fontaine et al., 1999; Teh and Cloutier, 2000). These models guided us to formulate the following hypothesis: the spatial organization of aggregating RBCs is the main determinant of the US backscattered power. Several authors studied the ultrasonic signal signature as a function of the spatial organization of scatterers (Landini and Verrazzani, 1990; Varghese and Donohue, 1993). Unfortunately, their modeling approaches could hardly be applied to a complex medium such as blood, because they modeled regularly positioned scatterers, isotropic media, or dilute systems of scatterers. To our knowledge, the positions of aggregated RBCs cannot easily be related to a known spatial distribution. Furthermore, the eventual presence of spatial anisotropy in the medium adds more complexity to the modeling.

The purpose of this study is to determine the effect of realistic configurations of RBCs, and to study whether a change in their spatial organization would lead to significant variations of the US backscattered power. To achieve this, an iterative flow-dependent simulation model of aggregating particles was developed. To solely study the effect of the positioning of the particles, the suspension of RBCs was modeled by spheres. A wide variety of configurations of RBCs was obtained by varying both the flow shear rate, and the strength of interactions between the red cells. Modeling the exact mechanisms of RBC aggregation is outside the scope of this paper. To our knowledge, it is the first attempt to model polydispersity in size, shape, and orientation of aggregates due to the shearing of the flow and to relate these variations to US backscattering.

The next section presents a brief overview of the theoretical principles underlying the mechanisms of RBC aggregation and US backscattering by blood. This section is followed by the description of the dynamic model of RBC aggregation, which includes the effect of the flow as well as the repulsive and adhesive forces modeled according to the intrinsic aggregability of RBCs. Then, the model used to estimate the backscattered US signal and the backscattered power is described. The results and discussion are presented next. In conclusion, the proposed dynamic aggregation modeling approach is shown to be an efficient tool to simulate realistic structural arrangements of RBCs under shear flow. The structure factor of the aggregates is proposed to relate the backscattered power to the microstructural properties of RBCs. The simulation results are compared to experimentally measured variations of the US backscattered power with the angle of insonification (Allard et al., 1996).

THEORY

Mechanisms of RBC aggregation

Two mechanisms were proposed to explain the aggregation of RBCs, the bridging model and the depletion model. According to the bridging model, the formation of RBC aggregates results from the adsorption of plasmatic macromolecules at the surface of the RBCs (Chien, 1975; Brooks et al., 1980; Chien, 1981). In contrast, the depletion model suggests that the exclusion of the plasmatic macromolecules near the surface of RBCs induces aggregation (Bäumler et al., 1996; Armstrong et al., 1999). The depletion layer would result in a reduction of the osmotic pressure in the gap between two nearby RBCs, creating an attractive force between them. In addition to the adhesive forces, due to either adsorption or depletion of macromolecules and the Van der Waals forces, which are always present in a colloidal suspension, there are repulsive forces that hinder the formation of RBC aggregates. The main repulsive forces are the steric forces due to the glycocalyx, and the electrostatic repulsive forces due to the presence of negative charges at the surface of RBCs (Bäumler et al., 1989). The flow also plays a significant role in the phenomenon of RBC aggregation. At low shear rates, the flow can promote RBC aggregation, whereas, at higher shear rates it rather has a dispersing effect.

Mechanisms of US backscattering by blood

US backscattering by blood is a complex phenomenon to characterize because of the high density of RBCs in blood. Tissue scattering properties are often described by their backscattering coefficient (BSC) that is, by definition, the average power backscattered per steradian by a unit volume of blood, insonified by a monochromatic plane wave of unit intensity (Shung and Thieme, 1993). For a suspension of weak identical scatterers (weak in the sense that the acoustic impedance of the scatterers is similar to that of the suspending plasmatic medium), it is given by

$$\mathrm{BSC} = \sigma_{bs}(H/V)S, \tag{1}$$

where σ_{bs} is the backscattering cross-section of a single scatterer (i.e., the power backscattered by a single particle), H is the hematocrit, V is the volume of the identical scatterers, and S is the structure factor. Both σ_{bs} and S depend on the incident acoustic wave frequency. Similar forms of the previous equation can be found in the literature (Mo and Cobbold, 1992; Twersky, 1987). For Rayleigh scattering, which implies that the wavelength of the incident wave is much larger than the size of the scatterers, the backscattering cross-section (σ_{bs}) is proportional to the square of the particle volume and to the fourth power of the incident wave frequency (Shung and Thieme, 1993; Fontaine et al., 1999). The structure factor (S) characterizes the spatial organization of the scatterers in the frequency domain. The frequency domain highlights the periodicities in the tissue microstructure, emphasizing the most recurrent interparticle intervals. In crystallography and other fields of research, the structure factor is often computed by x-ray diffraction to

characterize the microstructure of small molecules. For US backscattering, it is equal to (Twersky, 1975)

$$S(\mathbf{k}) = 1 + \rho \int e^{-j2\mathbf{kr}}[g(\mathbf{r}) - 1]\, d\mathbf{r}, \qquad (2)$$

where $\mathbf{k}$ is the wavevector ($\mathbf{k} = 2\pi\, \mathbf{e}_{inc}/\lambda$, where $\mathbf{e}_{inc}$ is the unit vector showing the direction of the incident wave, and λ is the wavelength), ρ is the number density of the particles, and $g(\mathbf{r})$ is the pair-correlation function that represents the normalized probability of finding two particles separated by a distance $\mathbf{r}$. In other words,

$$g(\mathbf{r}) = \frac{\mathrm{P}(\mathbf{x} \text{ and } \mathbf{x} + \mathbf{r} \text{ are particle centers})}{\mathrm{P}(\mathbf{x} \text{ is a particle center})^2}, \qquad (3)$$

where P indicates the probability. As the positions of the particles become uncorrelated, the pair-correlation function tends toward 1. The distance of correlation refers to the largest distance $\mathbf{r}$ such that $g(\mathbf{r}) \neq 1$.

If the positions of the particles are correlated only on short distances in comparison to the wavelength, the BSC (Eq. 1) can be estimated by using the low-frequency limit of the structure factor, called the packing factor (W). From Eq. 2,

$$S(\mathbf{k} \to 0) \approx W = 1 + \rho \int [g(\mathbf{r}) - 1]\, d\mathbf{r}. \qquad (4)$$

The packing factor of totally uncorrelated particles in space is equal to 1, whereas it takes the value of 0 for perfectly ordered particles (crystallographic arrangement). In the case of identical nonaggregating hard spheres, the packing factor is entirely determined by the number density of particles, and it can be estimated by using the Percus–Yevick approximation (Twersky, 1975). The packing factor (W) can be shown to be the ratio of the variance of the number of particles per voxel to the mean number of particles per voxel, when it is large compared to the size of the aggregates. This approximation was used in the modeling of the US backscattered power by nonaggregating RBCs at low frequencies (Lucas and Twersky, 1987; Mo and Cobbold, 1992; Lim et al., 1996; Fontaine et al., 1999). In this particular case, backscattering at low frequencies is independent of the incident wave orientation because the packing factor is not angular dependent.

It is still unclear if the packing factor approximation is fully valid in the presence of RBC aggregates because the distance of correlation between the positions of the particles can increase significantly in this case. Moreover, because an angular dependence of the backscattered power for aggregating RBCs was observed at 10 MHz (Allard et al., 1996), this suggests that the length of correlation of aggregated RBCs may be too important to ensure the validity of the low-frequency approximation (Eq. 4) at this frequency. Thus, the anisotropy of the pair-correlation function $g(\mathbf{r})$ should be taken into consideration for modeling US backscattering by aggregated RBCs.

Alternatively to Eq. 2, the structure factor can also be expressed as a function of the microscopic density N, defined by the center position of each particle $\mathbf{r}_i = (x_i, y_i)$. This function is defined two dimensionally by

$$N(x, y) = \sum_{i=1}^{M} \delta(x - x_i, y - y_i), \qquad (5)$$

and

$$S(\mathbf{k}) = \frac{1}{M}\left|\mathcal{F}(N)\right|^2 = \frac{1}{M}\left|\sum_i e^{-j2\mathbf{k}\cdot\mathbf{r}_i}\right|^2, \qquad (6)$$

where M is the number of scatterers, δ is the Dirac function, and $\mathcal{F}(N)$ is the Fourier transform of the microscopic density function.

The power spectrum of the microscopic density function of a suspension of perfectly random scatterers is constant over the whole range of frequencies (Poisson point process). Because the position that a particle can take is constrained by the presence of its neighbors, the positions of a large number of nonoverlapping (rigid) particles cannot be totally random in a given volume. Thus, the structure factor of such a suspension is characterized, in the spectral domain, by regular oscillations, whose period can be related to the size of the particles. In the case of nonaggregating RBCs at a hematocrit of 40%, the oscillation frequency is >100 MHz (Fontaine et al., 1999). Because RBC aggregation results in an increase of the correlation length, the amplitude of the oscillations of $S(\mathbf{k})$, and its low-frequency limit should be different from the case of no aggregation. In the present study, in addition to the structure factor given by Eq. 6, the pair-correlation function $g(\mathbf{r})$ was also determined to understand the effect of RBC aggregation on the length of correlation. From Eqs. 2 and 6, it can be shown that the pair-correlation function $g(\mathbf{r})$ is obtained from the inverse Fourier transform of the structure factor.

METHODS

Aggregation modeling

An iterative two-dimensional (2D) model was developed to simulate the formation of RBC aggregates in a Couette shear flow. The proposed 2D dynamic model takes into consideration the displacement due to the adhesive and repulsive forces between RBCs and the effect of the flow. The interaction between pairs of particles was modeled according to their intercellular distance. The exact mathematical expressions describing the interactions between RBCs are not known, because the mechanisms of RBC aggregation still remain ambiguous (depletion or adsorption), and because these interactions fluctuate significantly according to the type and concentration of macromolecules in the plasma. Nevertheless, it can be assumed that the adhesion between two red cells will occur only if those particles are close enough. Moreover, the adhesive forces have to be greater than the forces that tend to disaggregate the particles, i.e., the electrostatic and steric forces, and the effect of the flow. Thus, the level of

aggregation results from multiple forces that depend on the positions of the red cells in the medium, with respect to the surrounding particles. In the current model, the motion of the RBCs was defined according to the summation of the displacement resulting from each type of force (attraction, repulsion, and flow shear motion). The model includes the possibility to consider RBC hyperaggregation by modifying the importance of the adhesive forces with respect to the other forces.

The particles were initially positioned randomly without overlap in a 2D space of 300 by 300 μm. The simulated hematocrit was 40% (corresponding to ~1500 particles in the region of interest, ROI), each RBC being modeled by a disk of 5.5 μm in diameter. This diameter was selected to match an average volume of RBCs of 87 μm^3. At each time step, the vector displacements resulting from each force were summed for every RBC. Once the displacements were computed for all particles, they were moved for the next iteration. The process was continued until the size of the aggregates reached a steady state. Simulations of RBC aggregation were performed at shear rates of 0.05, 0.08, 0.1, 0.3, 0.5, 1, 2, 5, 8, and 10 s^{-1}. Three levels of RBC aggregability were modeled.

The accuracy of such an iterative dynamical model is limited by the sampling of the time scale and the finite spatial window. Even if new developments would allow for modeling more accurately the adhesive/repulsive forces (Donath and Voigt, 1986), it would be difficult to implement the aggregation process numerically with such precision. A single simulation already required several days to reach the stable state. As explained below, the choice of the quantitative parameters of the model was mainly performed to obtain different levels of aggregation and to minimize particle superposition. The parameters were also selected to allow the rotation of the aggregates at low shear rates, as opposed to disaggregation at high shear rates. Even with those limitations imposed by the numerical modeling strategy (disks, 2D model, finite spatial window, time sampling), the results are innovative, because they allow the understanding of the effect of specific organizational characteristics of RBCs and RBC aggregates, modulated by the shear rate, on the US backscattered power.

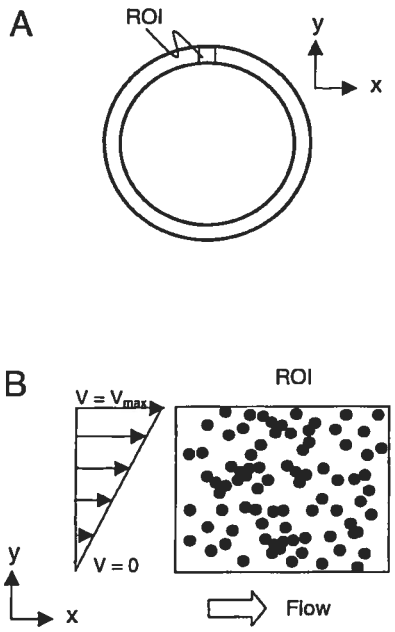

FIGURE 1 (*A*) Top view of the two coaxial cylinders composing the Couette flow system. The ROI is located in the small gap between the two cylinders. The x axis refers to the direction of the flow parallel to the cylinders, and the y axis refers to the radial direction between the cylinders. (*B*) Magnification of the ROI and illustration of the velocity profile, assuming a constant shear rate in the ROI.

Displacement related to the flow

The displacement of one particle due to the flow depends on its position in the ROI because a predetermined velocity profile was imposed. For a Couette flow, which can be obtained in the gap between two coaxial cylinders, the velocity component of a point particle is proportional to the shear rate and its radial coordinate. According to the reference axes schematized in Fig. 1 *a*, the radial position of the particle (axis y) determines its velocity along the x axis. The motion of one RBC along x was described by

$$(v_x)_{flow} = \gamma y \quad \text{and} \quad (\Delta x)_{flow} = (v_x)_{flow}\Delta t, \qquad (7)$$

where $(v_x)_{flow}$ represents the fluid velocity along x, γ is the shear rate, and y is the radial position perpendicular to the cylinders. The variable Δx is the displacement of the RBC within a discrete time increment Δt. The radial velocity $(v_y)_{flow}$ was supposed null (no secondary flow). Figure 1 *b* illustrates the magnified ROI and the velocity profile of the RBCs. When a RBC was moved outside the ROI (x = 300 μm + ξ), the RBC was reentered in the ROI at $x = \xi$. The chosen time increment could not be too small to limit the time required to run the simulations. In contrast, a large time increment did not allow enough precision in the motion of the RBCs. A time increment Δt = 10 ms appeared to be a good compromise.

Displacement related to the adhesive and repulsive forces

The formation of RBC aggregates requires the presence of macromolecules in the plasma. The intercellular distance between aggregated RBCs is a function of the length of the bond (bridging model), or of the thickness of the depletion layer (depletion model). Fibrinogen is the primary macromolecule in normal plasma that causes RBC aggregation. Previous studies (Jan and Chien, 1972; Chien, 1981) estimated the intercellular distance between aggregated RBCs in the presence of fibrinogen to 25 nm by electron microscopy. Although this technique is subjected to artifacts due to the preparation of the cells (RBCs are sedimented, fixed, and dehydrated) and due to the intrinsic limitations of the measurement method, this distance represents enough precision for the current model. Thus, this value was taken as a reference to model the equilibrium distance of a doublet of RBCs.

Displacement related to the repulsive forces

The displacement resulting from the repulsive forces was modeled as illustrated in Fig. 2. It was assumed constant for intercellular distances (d) smaller than 25 nm (center–center distance varying between 0 and 5.525 μm). Because of the finite time resolution, the particles could temporarily be brought closer to each other than the equilibrium distance of 25 nm. When this happened, the repulsive forces, that include the steric and the electrostatic effect, were modeled to put back the RBCs at distances larger than 25 nm. According to Fig. 2, when two RBCs were separated by <25 nm, they were moved by 12.5 nm in the opposite direction (the angle of the doublet in the 2D space was maintained when moving the cells). This displacement corresponds to half the equilibrium intercellular distance (25 nm/2). For intercellular distances >25 nm, the repulsive force was modeled as an exponentially decreasing function. The rate of decrease of the repulsive force was set equal to the Debye–Hückel constant, κ, which is equal to the reciprocal of the double layer thickness $(0.8\ nm)^{-1}$ for normal red cells in a saline solution (0.9% NaCl) (Chien, 1981; Jan and Chien, 1973). The repulsive forces were only considered for intercellular distances <50 nm because of the very fast decay of the exponential function. In

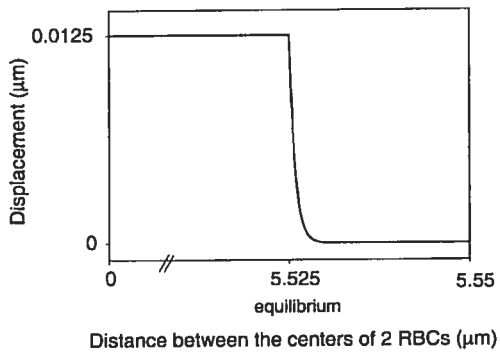

FIGURE 2 Displacement resulting from the repulsive forces expressed as a function of the distance separating two neighboring RBCs (center–center).

summary, the motion due to the repulsive forces resulting from the presence of two RBCs centered at $\mathbf{r}_i$ and $\mathbf{r}_j$ can be written as

$$|\Delta\mathbf{r}|_{repul} = 12.5 \text{ nm}$$

$$\text{if} \quad 0 \leq |\mathbf{r}_i - \mathbf{r}_j| \leq 5.525 \ \mu\text{m} \tag{8a}$$

$$|\Delta\mathbf{r}|_{repul} = 12.5e^{-\kappa(d-0.025)} \text{ nm}$$

$$\text{if} \quad 5.525 \ \mu\text{m} < |\mathbf{r}_i - \mathbf{r}_j| \leq 5.55 \ \mu\text{m} \tag{8b}$$

$$|\Delta\mathbf{r}|_{repul} = 0$$

$$\text{otherwise,} \tag{8c}$$

where $\kappa = 1.25 \times 10^3 \ \mu\text{m}^{-1}$, and the intercellular distance $d = |\mathbf{r}_i - \mathbf{r}_j| - 5.5 \ \mu\text{m}$.

Displacement related to the adhesive forces

According to several authors, the aggregation level of normal RBCs is stable or increases as the shear rate is raised from 0 to ~0.5 s^{-1} (Chien, 1976; Copley et al., 1976). This a priori information was used for the modeling of the displacement attributed to the adhesive forces (adsorption or depletion forces). The effect of the adhesive forces was determined to avoid disaggregation of an existing doublet positioned perpendicular to the Couette flow direction at 0.5 s^{-1}. The adhesive displacement necessary to maintain the doublet aggregated was set to 40.5 nm in the direction of the other RBC, for RBCs separated by less than 50 nm (this distance is arbitrarily selected to twice the postulated equilibrium RBC intercellular distance to consider the discrete nature of the model). The adhesive displacement was set to 40.5 nm for intercellular distances between 0 and 50 nm (center–center distances varying between 5.5 and 5.55 μm), whatever the angle of the doublets. When cellular overlap occurred at a given iteration (center–center distances <5.5 μm), the adhesive forces were supposed to be null. No displacement due to the adhesive forces was considered for intercellular distances larger than 50 nm.

Modeling of hyperaggregation

Hyperaggregation was modeled by modifying the amplitude of the displacement related to the adhesive forces, or its domain of influence. Two levels of hyperaggregation were considered. The intermediate level was obtained by considering the adhesive and repulsive forces for RBCs separated by <75 nm (instead of 50 nm for the case of the lowest aggregability). The same displacement as in the original modeling was then applied for the adhesive forces (40.5 nm). The highest RBC aggregability was obtained by considering the adhesive forces for RBCs separated by <100 nm. The displacement resulting from the application of the adhesive forces was also more important, i.e., 60 nm instead of 40.5 nm for the lowest and the intermediate levels of RBC aggregability.

At each iteration, the displacements resulting from the adhesive and repulsive forces, and from the flow were summed as schematized in Fig. 3. The displacement related to the flow is always parallel to the x axis, and the direction of the displacement related to the adhesive and repulsive forces depends on the position of the neighboring particles. For clarity, the latter was only illustrated for one of the two particles composing the doublet. The net displacement was computed by a vectorial summation, and all the RBCs were moved at the same time. Note that the magnitudes of the displacements in Fig. 3 are not illustrated at the real scale, to facilitate the reading. The combined effect of all forces on a single rouleau of five RBCs can be observed in Fig. 4. At a low shear rate of 0.1 s^{-1}, the rouleau tended to rotate and to be aligned with the flow after several iterations. At 0.5 s^{-1}, the 5-cell aggregate was disrupted to the size of a doublet. The doublet also rotated with the flow. At a high shear, the rouleau was broken into individual cells. This simple behavior, presented here to illustrate the modeling process, becomes more complex when the aggregate is surrounded by numerous cells/aggregates, at a normal hematocrit.

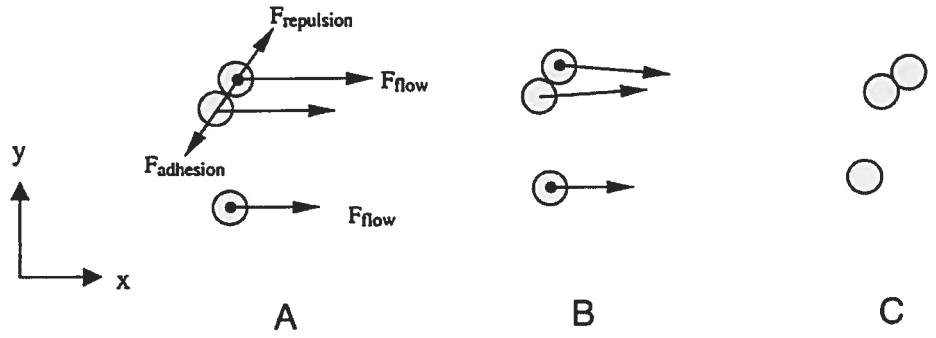

FIGURE 3 An example of the vector displacements considered in the dynamic simulation of RBC aggregation. (*a*) Illustration of the vector displacement resulting from each force. The displacement resulting from the flow is parallel to x, and is proportional to the radial position of the RBC (y). The adhesive force is directed toward the RBC that causes the force, and the repulsive force is oriented in the opposite direction. For clarity, they were illustrated only for one of the two RBCs composing the doublet (they are the exact opposite for the other RBC). (*b*) Resulting vector displacement after summation. (*c*) Configuration of the RBCs after motion from one iteration.

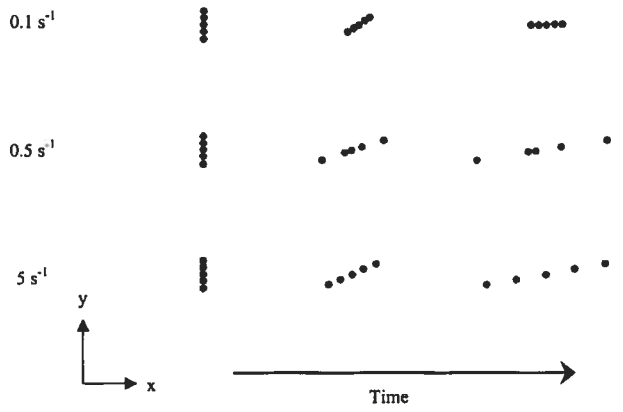

FIGURE 4 Motion of a single rouleau of five RBCs resulting from the combined effect of all simulated forces for different iterations (time increments). The examples correspond to the lowest aggregability simulated at shear rates of 0.1, 0.5, and 5 s^{-1}.

Ultrasound backscattering modeling

The simulation model of the US backscattered radio-frequency (RF) signal is described in details elsewhere (Fontaine et al., 1999). The simulation model assumes a linear mode of propagation of the acoustic waves in a weak scattering medium (Born approximation), and is valid for a small region of interest in the far field of the transducer. The backscattered RF signal can then be modeled as the convolution of the US system characteristic function (T), the function characterizing the acoustical impedance mismatch of the RBC with respect to the surrounding media (C), and the microscopic density function (N). In two dimensions,

$$\mathrm{RF}(x,y) = \frac{\partial^2}{\partial y^2}\mathrm{T}(x,y) \otimes \mathrm{C}(x,y) \otimes \mathrm{N}(x,y), \quad (9)$$

where y is the ultrasonic wave direction of propagation corresponding to the direction perpendicular to the flow motion (Fig. 1).

The transducer transfer function was modeled as a Gaussian envelope modulated by a cosine function,

$$T(x,y) = \exp\left[\frac{-1}{2}\left(\frac{x^2}{\psi_x^2} + \frac{y^2}{\psi_y^2}\right)\right]\cos\left(\frac{4\pi f y}{c}\right). \quad (10)$$

In the above equation, ψ_x and ψ_y are the standard deviations of the 2D Gaussian function representing the beamwidth and the bandwidth of the transmitted waves. The beamwidth defines the lateral resolution of the measuring system, whereas the bandwidth determines the axial resolution (a large bandwidth corresponds to a good axial resolution, and vice-versa). The parameter $2f/c$ in Eq. 10 represents the transducer spatial frequency, where f is the ultrasonic frequency and c is the speed of sound. In the current manuscript, the US system was modeled with $\psi_x = 0.43$ mm, $\psi_y = 0.03$ mm, and $f = 10$ MHz. The selected value of ψ_y corresponds to a bandwidth of ~10 MHz at −3 dB (wideband signal). The speed of US, c, in blood was assumed equal to 1570 m/s. In theory, the BSC given by Eq. 1 corresponds to the insonification of the medium by a monochromatic plane wave (infinitely small bandwidth). In the current simulation, a 10-MHz bandwidth was modeled, which better represents realistic transducer responses for backscattering experiments.

The convolution operation (Eq. 9) implies that all RBCs are identical in shape and impedance. The function C, describing the shape and the mismatch in acoustic impedance of each RBC, was modeled as the projection of a sphere. In 2D,

$$\mathrm{C}(x,y) = 2\sqrt{a^2 - x^2 - y^2} \quad \text{for} \quad x^2 + y^2 \le a^2, \quad (11)$$

where $a = 2.75$ μm represents the radius of the simulated spherical RBC.

The 2D aggregation model described earlier was used to generate the function N. This function characterizes the position of each RBC in the 2D space. It was computed from the x and y coordinates of the center of all RBCs. Each simulation, performed from different random initial spatial conditions, was repeated four times to allow statistical averaging. All simulations were performed with MATLAB 5.3 (The MathWorks Inc., Natick, MA).

Rotation of the transducer

To allow the study of the anisotropy of the backscattered power, US backscattering was modeled at various angles of insonification by doing a rotation of the transducer transfer function. As performed by Teh and Cloutier (2000), the x–y plane in Fig. 1 was mapped onto the p–q plane. The function characterizing the transducer was computed on the rotated axes. The following equations were used to transform the x–y plane onto the p–q plane:

$$\begin{bmatrix} p \\ q \end{bmatrix} = \begin{pmatrix} \sin\theta & \cos\theta \\ -\cos\theta & \sin\theta \end{pmatrix}\begin{bmatrix} x \\ y \end{bmatrix}, \quad (12)$$

where θ represents the angle of rotation of the axes. Thus, 0° corresponds to a direction of insonification parallel to the flow, whereas 90° represents a direction perpendicular to the flow direction.

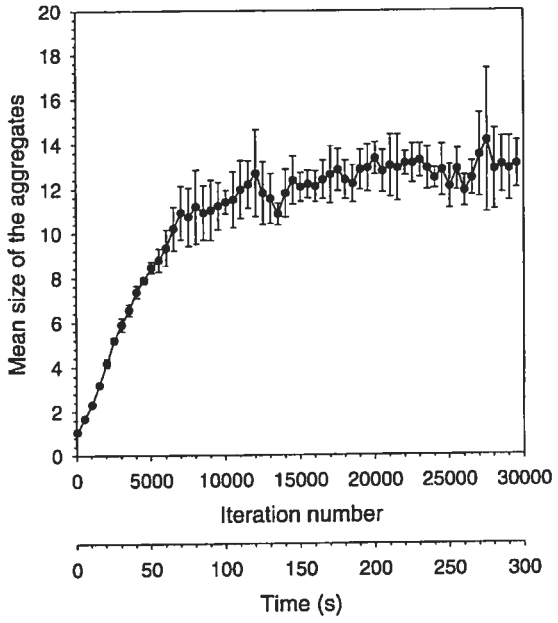

FIGURE 5 Mean size of the aggregates (mean number of RBCs/aggregate) as a function of the number of iterations (time) of the simulation model, at 0.1 s^{-1}, for the lowest RBC aggregability. Results are expressed in terms of mean ± one standard deviation ($n = 4$). A mean aggregate size of 1 corresponds to a single RBC.

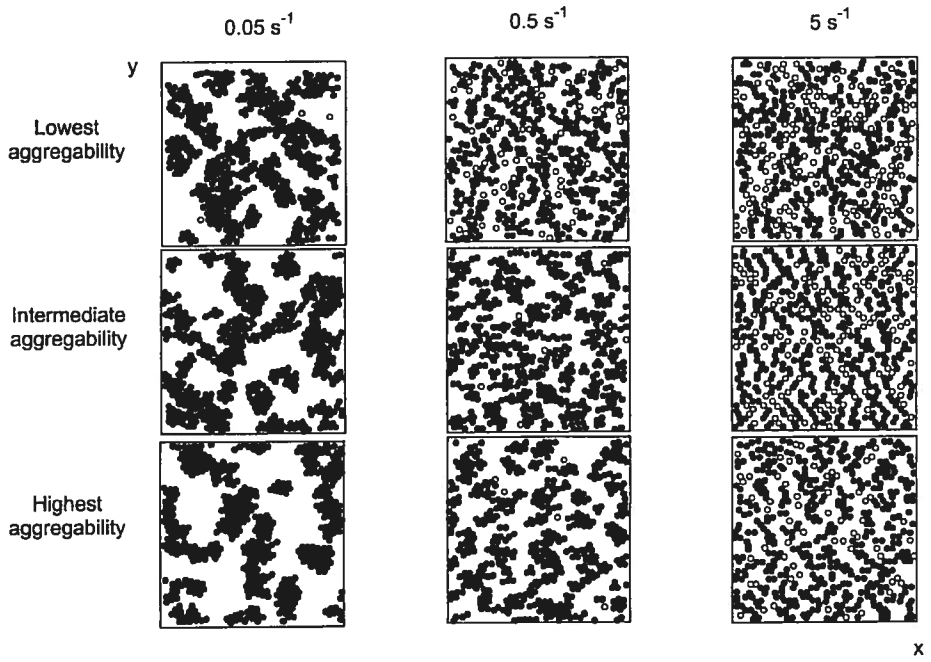

FIGURE 6 Simulation results of RBC aggregation at 40% hematocrit. Filled circles represent aggregated RBCs, and empty circles represent nonaggregated cells. Zoomed areas of 180 by 180 μm are illustrated. The simulated areas are 300 by 300 μm. Each panel was obtained at the steady state of aggregation (plateau of the kinetics of aggregation, see Fig. 5).

Computation of the US backscattered power

The backscattered power was computed on the 2D spectrum of the RF image obtained from Eq. 9. The spectrum of the RF image was computed from the central portion (256 by 256 μm) of the simulated ROI to avoid errors from the edges. The backscattered power (POW) was computed from the spectrum of the transducer transfer function (T) previously derived, the spectrum of the cell function (C) and that of the microscopic density function (N),

$$\mathrm{POW} = \frac{1}{M_s} \sum_{f_x} \sum_{f_y} \left| \mathcal{F}\left(\frac{\partial^2}{\partial y^2} \mathrm{T}\right) \mathcal{F}(\mathrm{C}) \mathcal{F}(\mathrm{N}) \right|^2, \quad (13)$$

where M_s is the number of samples in the frequency domain (f_x, f_y).

RESULTS

Aggregation modeling

Figure 5 shows the evolution of the mean size of the aggregates as a function of the iteration number (time), for a shear rate of 0.1 s^{-1} and the lowest aggregability ($n = 4$). The application of a constant shear rate resulted in an increase of the mean size of the aggregates as a function of time. The number of iterations required to reach the steady state and the maximum size of the aggregates varied with the shear rate and the RBC aggregability.

Figure 6 shows different structures of RBC aggregates obtained with the simulation model for different shear rates and RBC aggregabilities. Filled circles represent aggregated RBCs, and empty circles represent nonaggregated cells. The number of aggregated RBCs and the size of the aggregates increased as the shear rate was decreased or the aggregability was raised. Figure 7 illustrates the mean size of the aggregates obtained at the steady state of aggregation (plateau in Fig. 5) for all simulated conditions. At the lowest shear rate of 0.05 s^{-1}, the mean number of RBCs per aggregate was 24.9 ± 1.8, 39.6 ± 3.6, and 45.8 ± 4.1 for the lowest (●), intermediate (▼), and highest (■) RBC aggregabilities, respectively. At the highest shear rate (10 s^{-1}), the mean size of the aggregates was 2.4 ± 0.1 for the lowest RBC aggregability, 2.6 ± 0.1 for the intermediate level, and 3.6 ± 0.1 for the highest aggregability. Figure 8 illustrates the size distribution of the aggregates at 0.05, 0.08, 0.5, and 5 s^{-1}. The variance in the aggregate size increased as the shear rate was reduced. At low shear rates (0.05 and 0.08 s^{-1}), there were many aggregates of intermediate sizes and some very large aggregates. At 0.05 s^{-1}, there could be one aggregate composed of more than 300 RBCs, which represents ⅓ of all RBCs in the ROI. At higher shear rates (0.5 and 5 s^{-1}), the size distribution of the aggregates was more uniform.

To better understand the spatial organization of the particles, the pair-correlation function $g(\mathbf{r})$ was estimated. Results at 0.05, 0.3, and 1 s^{-1} are presented in Fig. 9 for the lowest and highest RBC aggregabilities. As expected, there was a greater probability that two particles be separated by

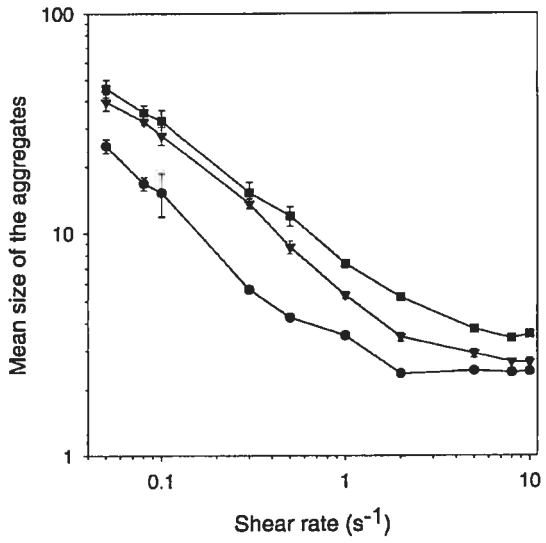

FIGURE 7 Mean size of the aggregates as a function of the shear rate, at the steady state of aggregation. Simulations of the ● lowest, ▼ intermediate, and ■ the highest RBC aggregability are presented. Results are expressed in terms of mean ± one standard deviation (n = 4).

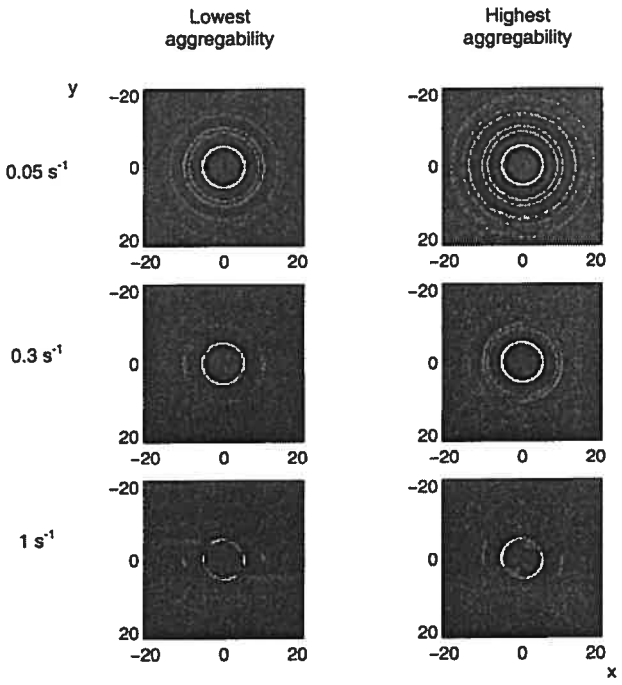

FIGURE 9 Examples of pair-correlation functions $g(\mathbf{r})$ at the lowest and highest RBC aggregabilities for shear rates of 0.05, 0.3, and 1 s^{-1}. Axes are expressed in micrometers.

5.5 μm (interior circles in each panel), which is the diameter of the RBC. An increase in the level of RBC aggregation resulted in a higher probability that two RBCs be separated by multiples of the particle diameter. As the aggregation level was raised, the probability that two particles be separated by 5.5, 9.5, 11, 14.5, 16.5, and 19 μm increased (see the explanation in Discussion). In some simulations, such as 1 s^{-1}, the anisotropy in the spatial organization of nearby RBCs could be observed, meaning that the aggregation of the RBCs was more important along the direction of the flow (x). This can be observed in Fig. 10, which shows cross-sections of the pair-correlation functions along the axes $x = 0$ and $y = 0$ obtained at 0.05 s^{-1} for the highest aggregability, and 1 s^{-1} for the lowest aggregability. The amplitude of the function $g(\mathbf{r})$ is plotted between -20 and 20 μm along x (for $y = 0$), and along y (for $x = 0$). At 0.05 s^{-1} and the highest aggregability, the probability that two particles be separated by a distance $\mathbf{r}$ is approximately the same in both directions below 20 μm. In contrast, at 1 s^{-1} for the lowest aggregability, the probability that two particles be separated by their diameter is ~4 times more important along the direction of the flow (x) than perpendicularly (y).

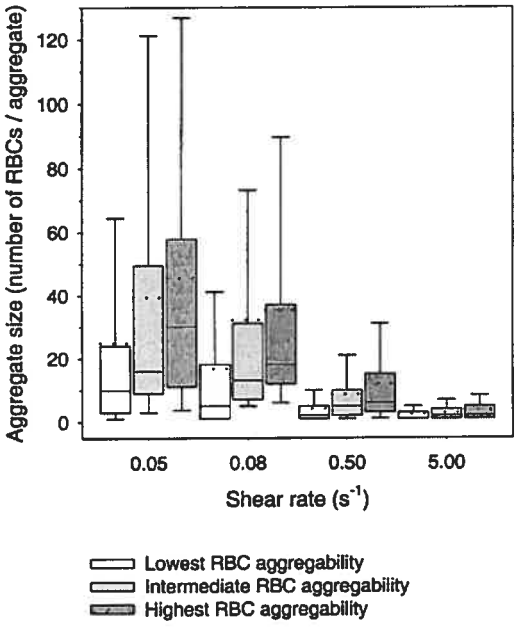

FIGURE 8 Size distribution of the aggregates at 0.05, 0.08, 0.5, and 5 s^{-1}. The boundary of the box closest to zero indicates the 25th percentile, a line within the box marks the median, and the boundary of the box farthest from zero indicates the 75th percentile. Whiskers above and below the box indicate the 90th and 10th percentile, and the dotted line indicates the mean. The □ lowest, □ intermediate, and ■ highest RBC aggregability are presented.

Ultrasound backscattering

The US backscattered power was computed for all simulations for a direction of insonification perpendicular to the

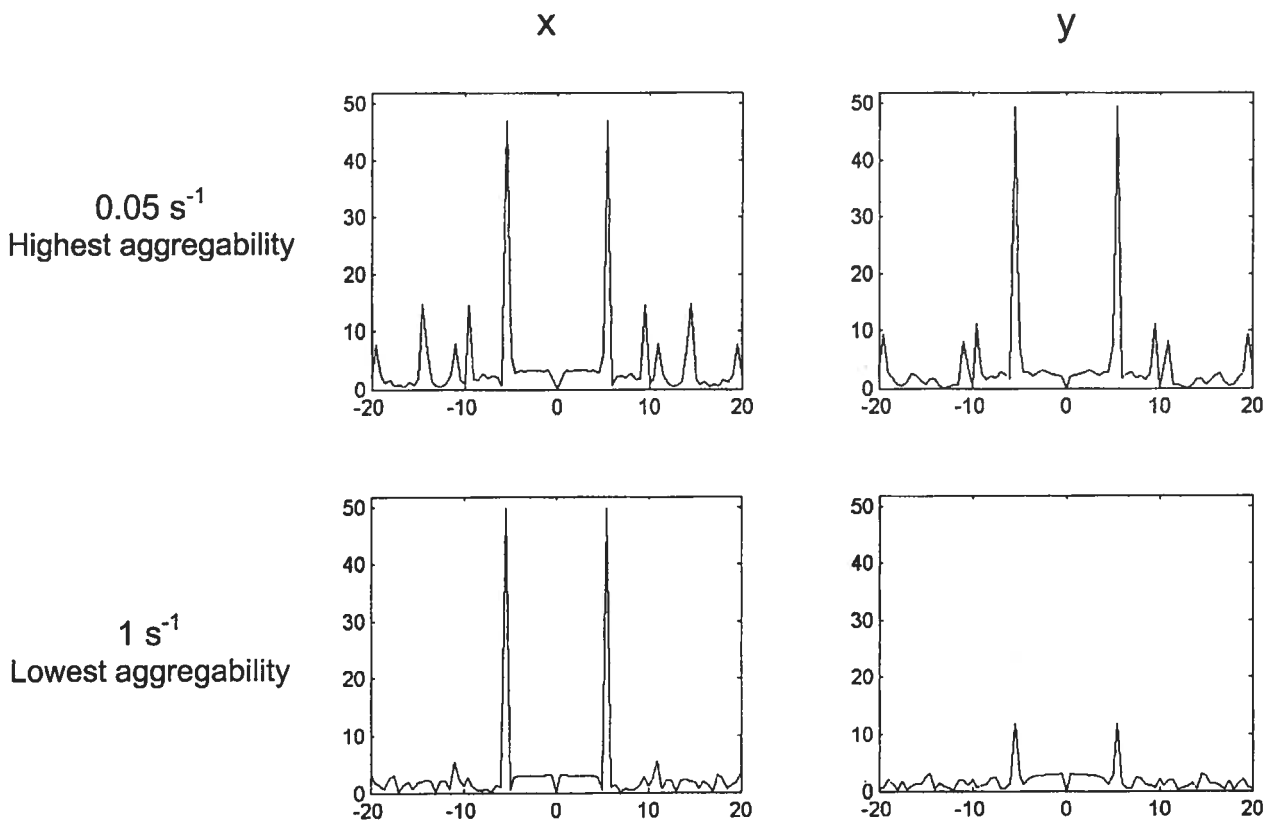

FIGURE 10 Cross-sections of the pair-correlation functions $g(\mathbf{r})$ along x ($y = 0$) and along y ($x = 0$), at 0.05 s^{-1} for the highest RBC aggregability, and at 1 s^{-1} for the lowest RBC aggregability. The amplitude of the pair-correlation functions is displayed between -20 and 20 μm.

flow. As can be seen in Fig. 11, for a given simulation, the backscattered power increases with the iteration number, which is similar to the temporal evolution of the mean size of the aggregates (Fig. 5). As seen in Fig. 12 for any level of aggregation, the backscattered power generally decreased as the shear rate was increased, except at the highest shear rates (>5 s^{-1}), where the behavior of the backscattered power presented more variations. As expected, the backscattered power increased, in most cases, with an enhancement of the RBC aggregability, and it was maximum at 0.05 s^{-1}. For the lowest aggregability, the range of variation of the backscattered power was 7.6 dB between 0.05 and 10 s^{-1}. For the intermediate aggregability, the range was of 8.2 dB, and 11.6 dB for the highest aggregability.

In Fig. 13, the backscattered power was computed as a function of the insonification angle for the three RBC aggregabilities at 0.05 and 5 s^{-1}. For any given aggregability, angular variations of the order of 6 dB were observed at 0.05 s^{-1}. The backscattered power was maximum between approximately $-60°$ (120°) and 60° (240°), and minimum at 90° (270°). Opposing quadrants of the backscattered power appeared to be symmetrics ($\pm 180°$). At 5 s^{-1}, the three curves corresponding to the different aggregabilities were not as distinct from one to another. The angular variations of the backscattered power were of the order of 5 dB for the lowest aggregability, 4 dB for the intermediate aggregability, and 3 dB for the highest aggregability. The positions of the minimum and maximum backscattered power were not as clearly defined at 5 s^{-1} than at 0.05 s^{-1}. These results clearly indicate that the size of the aggregates is not the only determinant of the US backscattered power because, for a given size, the angle of insonification affects the intensity of the backscattered echoes.

DISCUSSION

The simulation model of RBC aggregation mimics various configurations of RBC aggregates and computes the corresponding backscattered power. The model is innovative in that it tracks the positions of RBCs, whose motion is conditioned by the flow, and the adhesive and repulsive forces determined by the surrounding RBCs. According to the balance of forces, the aggregates could rotate with the flow or disaggregate, and thus various sizes and structures of aggregates were obtained. This behavior shown in Fig. 4

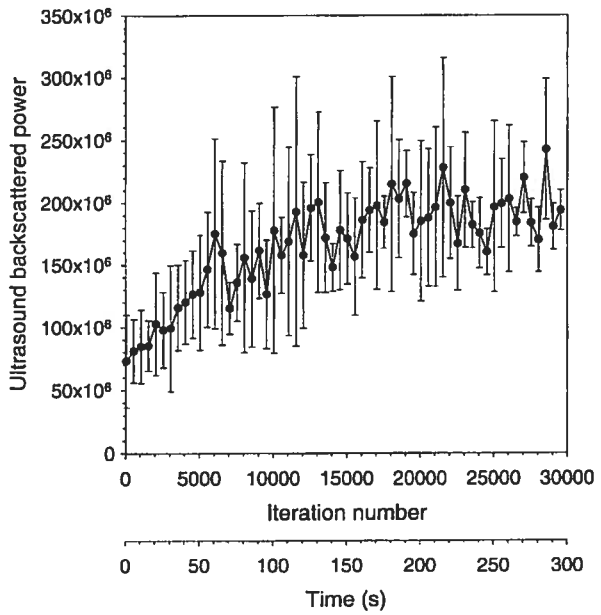

FIGURE 11 Mean backscattered power (relative units) as a function of the number of iterations (time) of the simulation model, at 0.1 s^{-1}, for the lowest RBC aggregability. The direction of insonification was perpendicular to the flow. Results are expressed in terms of mean ± one standard deviation (n = 4).

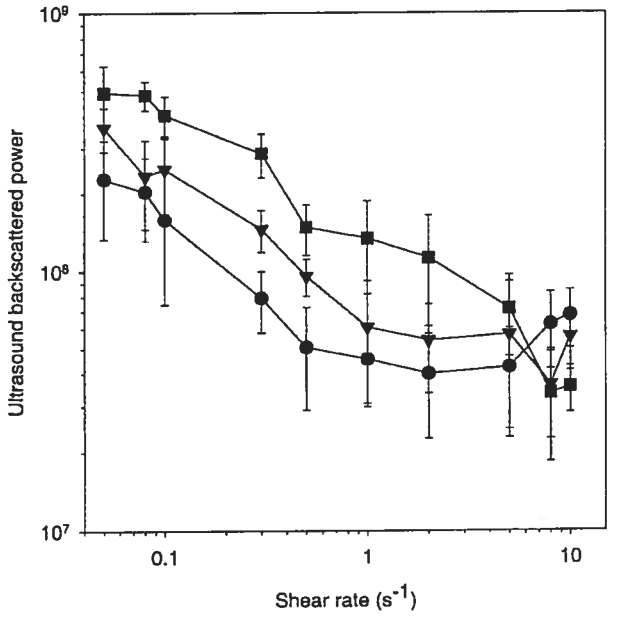

FIGURE 12 Simulated backscattered power (relative units) as a function of the shear rate for the ● lowest, ▼ intermediate, and ■ highest RBC aggregability. The direction of insonification was perpendicular to the flow. Results are expressed in terms of mean ± one standard deviation (n = 4).

was found to be satisfying, because it is similar to previous experimental observations, where the motion of rouleaux of human RBCs was shown under a microscope in a diluted suspension (Goldsmith and Marlow, 1972). In this last study, the RBC aggregates were found to rotate and deform, with a preferred alignment parallel to the flow.

Figure 6 demonstrated for aggregating RBCs that a wide variety of particle arrangements can be obtained at a fixed hematocrit of 40%. This resulted in a wide family of pair-correlation functions with the level of aggregation (Fig. 9), and thus of scattering behavior. The pair-correlation function illustrates the tendency of the RBCs to be aggregated and their preferred orientation. It allowed analysis of the regularity in the spatial arrangement of the RBCs, which cannot be easily observed from the realizations. From Figs. 9 and 10, it can be observed that, at 0.05 s^{-1}, the most probable interparticle distances were 5.5 μm (RBC diameter), 9.5, 11, and 14.5 μm. The reason for the presence of several peaks around 11 μm is illustrated in Fig. 14. For rouleau-shaped aggregates (Fig. 14, *left*), the intercellular distances are multiples of the RBC diameter, thus 5.5 and 11 μm. However, RBC aggregates can take different shapes, as illustrated in Fig. 14, *right*. In this case, the distance separating the centers of the farthest RBCs (c and d) is less than twice their diameter (9.5 μm). Other aggregate structures can be shown to result in intercellular distances of 14.5 μm.

Limitations of the packing factor, introduction of the structure factor

The properties of the structure factor are directly related to the spatial organization of the RBCs through the Fourier transformation of the function N. For nonaggregating cells, the spatial organization of the RBCs is mainly dependent on the hematocrit. Because the RBCs are much smaller than the wavelength (f = 10 MHz ↔ λ = 157 μm, with c = 1570 m/s), the backscattered power can be reasonably predicted in this case by considering only the low frequency limit of the structure factor. The structural arrangement of identical hard spheres is isotropic and the packing factor can be computed by the variance in the cell concentration of the scatterers within relatively large voxels (Mo and Cobbold, 1992). In the current modeling, aggregation of RBCs in a Couette flow resulted in an anisotropic spatial organization, which was shown to influence the backscattered signal at 10 MHz (Fig. 13). Thus, a scalar aggregation index such as the packing factor cannot fully predict the variations of the backscattered power, even at a relatively low frequency such as 10 MHz. Because RBC aggregation increases the correlation distance between the particle positions, the range of validity (in terms of frequency) of the packing factor approximation is reduced. Furthermore, there is a growing interest to characterize blood scattering at higher frequencies for high-resolution imaging. To describe the effect of red cell aggregation, it is thus preferable to refer to

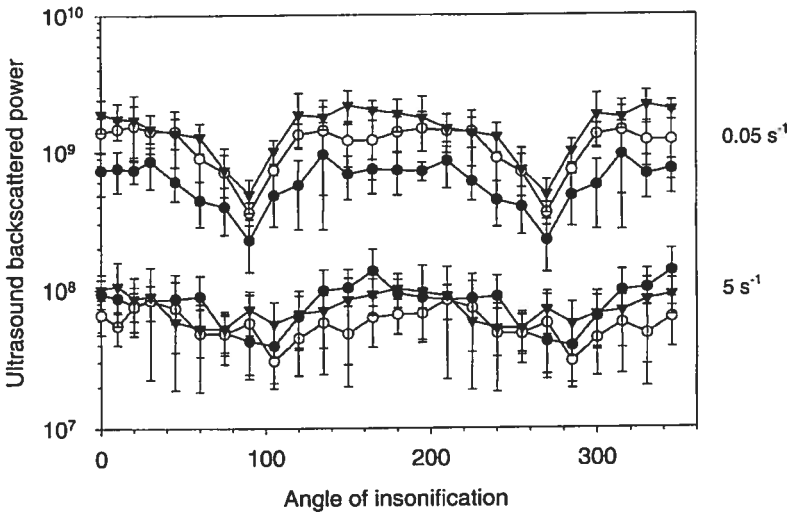

FIGURE 13 Simulated backscattered power (relative units) as a function of the angle of insonification at 0.05 and 5 s^{-1} for the three levels of RBC aggregability (● lowest; ○ intermediate, and ▼ highest aggregability). The angle of 0° corresponds to the alignment with the flow (x axis) going toward the US transducer, whereas 90° corresponds to measurements perpendicular to the flow (y axis).

the structure factor, which describes the frequency and the orientational dependence of the backscattered power.

A 2D representation of the structure factor is presented in Fig 15. Figure 15 *a* gives the structure factor of a nonaggregated suspension of RBCs, and Fig. 15 *b* was computed from the flow-dependent simulation model of RBC aggregation at the same hematocrit (lowest aggregability, 0.05 s^{-1}). It was shown previously (Fontaine et al., 1999) that, even in the case of nonaggregating RBCs, the correlation in the positions of the particles resulting from their size produces oscillations in the structure factor. The same behavior is observed here in Fig. 15 *a*. The structure factors obtained from aggregating RBCs in shear flow (Fig. 15 *b*) present similar oscillations, but also anisotropic characteristics. Moreover, it can be observed that the anisotropic characteristics of the simulated structure factor vary with the range of frequencies considered. The effect of RBC aggregation on the structure factor can be more easily observed from the examples of the one-dimensional representation of $S(\mathbf{k})$. Figure 16 illustrates cross-sections (magnitude as a function of the frequency) of the structure factor at an angle parallel to the flow ($Y = 0°$). The structure factor of nonaggregated RBCs at 40% hematocrit is represented in Fig. 16 *a*. The effect of an increase in the level of RBC aggregation can be observed in Fig. 16, *b* and *c*. Increasing the aggregation (at the same hematocrit) resulted in an increase in the magnitude of the function at low frequencies (<30 MHz), and in an increase of the magnitude of the oscillations (at multiples of ~150 MHz).

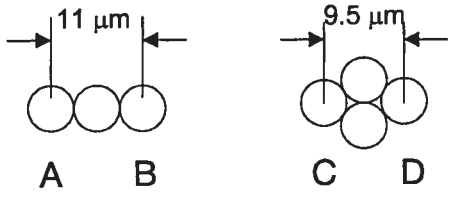

FIGURE 14 Illustration of two possible configurations of RBC aggregates. On the left, RBCs *a* and *b* are separated by twice the particle diameter, i.e., 11 μm, whereas on the right, RBCs *c* and *d* are separated by 9.5 μm.

Variations of the backscattered power with the shear rate and anisotropy

Experimentally, measured variations in the ultrasonic backscattered power could be as high as 15 dB as a function of the shear rate (Yuan and Shung, 1988; Cloutier and Qin, 2000), whereas the maximum simulated variation for the highest aggregability was 11.6 dB in the current study (Fig. 12). The use of a 2D model may be the explanation for the smaller variations, because the 3D structure of the aggregates could not be considered. It is also possible that we underestimated the aggregability of porcine, equine, or human RBCs that were used in the different experimental studies reported in the literature.

Previous experimental results at 10 MHz suggested that the backscattered power could be isotropic for nonaggregated RBCs, or in the presence of large clusters, and angular-dependent for intermediate levels of aggregation (Allard et al., 1996). This was concluded from acquisitions performed in a tube between 40° and 80° using porcine whole blood (0° corresponded to the flow going toward the transducer). For the anisotropic cases, the maximum backscattered power was measured between 45° and 60°. Our simulation results did show anisotropy of the backscattered power for aggregating particles in a shear flow. The location of the maximum could not always be easily located (see Fig. 13), but, in most cases, it was found between −60° and 60° (120° and 240°). Although it is difficult to compare tube flow with Couette flow, our

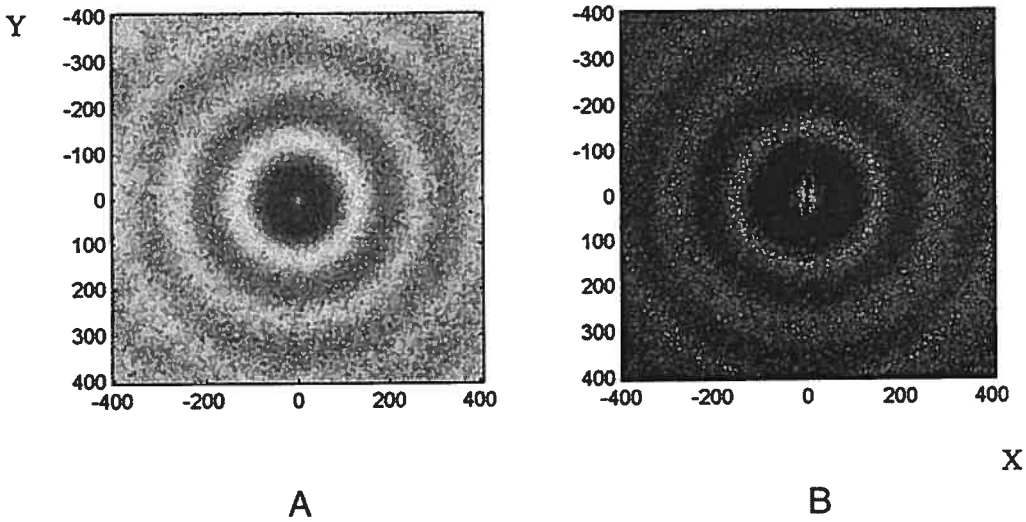

FIGURE 15 Illustrations of the structure factor $S(\mathbf{k})$ of (*A*) a nonaggregated suspension (hematocrit = 40%), and (*B*) a suspension of aggregated RBCs at 0.05 s^{-1} (hematocrit = 40%, lowest aggregability). Axes are expressed in MHz.

current simulations suggest that maximum backscattering obtained in the presence of aggregated RBCs would most likely occur for a slight angulation of the transducer with respect to the flow direction. This is in agreement with the experimental observations (Allard et al., 1996).

Previous simulation results, obtained by modeling a low hematocrit of long rouleaux, suggested that the maximum backscattered power should be found perpendicular to the long axis of rouleaux (Teh and Cloutier, 2000). These results were in good agreement with experimental results obtained by using a suspension of carbon fibers (Allard et al., 1996). In this case, all scatterers were of the same size and probably oriented, on average, in the same direction. In the study of Allard et al. (1996), the maximum backscattered power was assumed to correspond to an orientation of the transducer perpendicular to the maximum section of the fiber scatterers. The spatial organization of physiological-aggregated RBCs and the corresponding acoustic response are much more complex. As the hematocrit increases, the interactions between the echoes scattered from the different aggregates are multiplied. Thus, the backscattered power cannot be predicted based on the individual backscattering cross-section of the aggregates taken separately. It is more convenient to describe the results in terms of the direction that maximizes the level of aggregation of the red cells. In the presence of a high hematocrit of aggregates, the direction of maximum backscattering is not necessarily perpendicular to the flow.

The pair-correlation functions (Figs. 9 and 10) suggest that the anisotropy in the structural arrangement of the aggregates is more important at intermediate shear rate (1 s^{-1}) than at very low shear rate (0.05 s^{-1}). However, the angular variations of the backscattered power at 10 MHz do not seem to be directly related to this observation (Fig. 13). The difficulty in explaining the behavior of the backscattered power with the angle of insonification is related to the fact that the anisotropic characteristics of the backscattered signal are frequency dependent. When a tissue is insonified with a transducer at a given central frequency and bandwidth, it is equivalent to filtering the tissue scattering properties around this frequency. It can be observed by looking at all structure factors (Fig. 15 shows some examples) that the anisotropic properties of the tissue are not constant over the whole of frequencies. We thus think that the anisotropic characteristics at a low frequency (10 MHz), observed in the current simulations, would most probably be due to anisotropy in the positioning of the particles at large distances (~30–50 μm). This is not very easy to observe from the pair-correlation function that enhances the structural properties at smaller distances (~0–15 μm).

Considering the variations of the structure factor, a slight modification of the transducer central frequency or bandwidth is likely to modify the properties of the backscattered signal. Experimental results (Foster et al., 1994; Van Der Heiden et al., 1995) and preliminary simulation results (Fontaine and Cloutier, 2000) suggested that the increase in the backscattered power with the level of aggregation is frequency dependent. Additional efforts are thus necessary to elucidate the mechanisms of US backscattering as a function of frequency and aggregation level.

Limitations of the model

One obvious limitation of the model is the 2D ROI. A 3D modeling would allow more complex arrangements, which

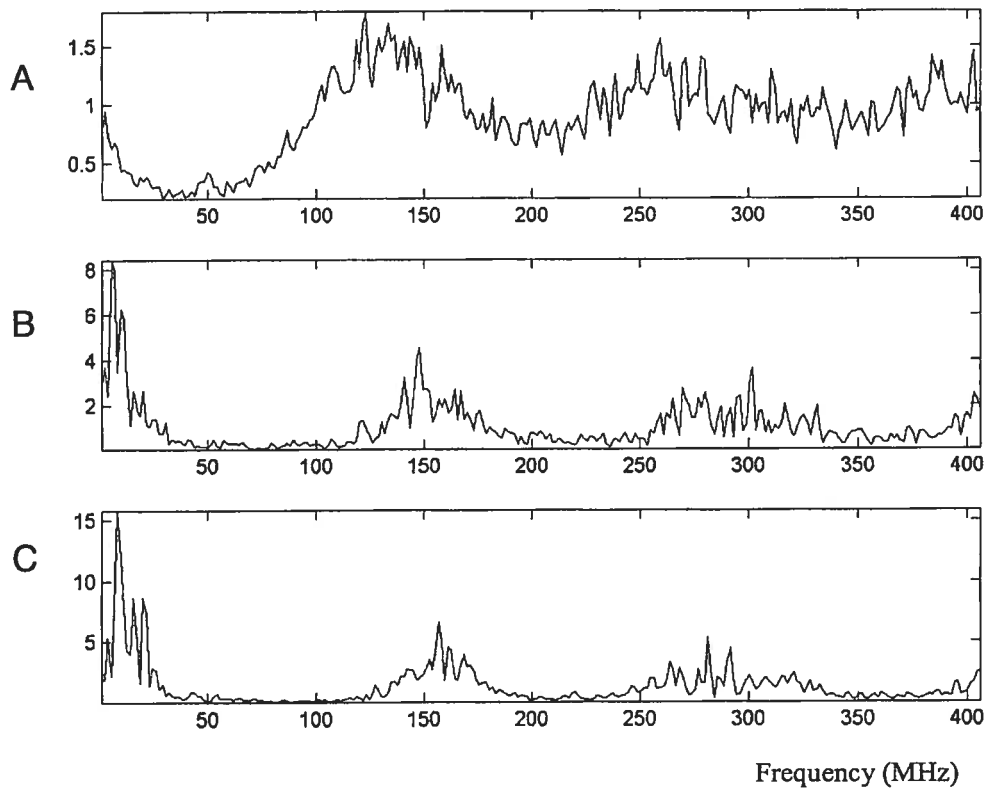

FIGURE 16 Cross-sections of the structure factors showing the amplitude as a function of the frequency (MHz) along $Y = 0$ MHz for (*A*) a nonaggregated suspension, (*B*) an intermediate level of aggregation (0.05 s^{-1}), and (*C*) a suspension with the highest level of aggregation (0.05 s^{-1}). All simulations were performed at 40% hematocrit.

would better mimic the physiological conditions. The 2D modeling may result in an underestimation of the size of the aggregates, and a lower backscattered power. The isotropic shape of the scatterers (RBCs were not modeled as biconcave particles) most likely diminishes the probability to form aggregates shaped as rouleaux because the adhesive force between the RBCs cannot be modulated according to their orientation. In the current model, the formation of rouleaux was indirectly enhanced by the flow, which favors a direction of aggregation parallel to it. This modeling aspect could be improved in future versions by considering the orientation of the cells. Also, at the highest shear rates, the displacement of the particles resulting from the application of the flow during one time interval became quite important. This displacement in a single iteration might be too large in comparison to the small-scale phenomenon of RBC aggregation, and particle superposition could more likely occur. This may be the explanation for the lack of consistency of the backscattered power, seen in Fig. 12, at the highest simulated shear rates (>5 s^{-1}). Although the variance in the mean size of the aggregates was small (Fig. 7), variability in the level of particle superposition modified the spatial arrangement of RBCs, and consequently the backscattered power.

One can argue that the dynamic model of aggregation is a simplistic approximation of the real biophysical interactions involved among RBCs, and that the choice of the displacements attributed to the different forces was somewhat subjective. The quantitative values of the adhesive and repulsive forces are not known from the literature, and they may be influenced by a number of factors such as the type and concentration of macromolecular proteins, the membrane properties of RBCs, the temperature, the pH, and they can vary significantly among individuals. The present model modulated the degree of aggregation by varying the capture radius for the interaction and displacements attributed to the adhesive forces. Although of hypothetical value, this modeling approach may reflect the variation of aggregation due to the type, size, and configuration of the plasmatic macromolecules involved (fibrinogen, immunoglobulins, haptoglobin, ceruloplasmin, C-reactive protein, α_2-macroglobulin, and possibly others) (Weng et al., 1996). Although this model may be criticized, it was shown to be powerful to study the effect of various geometrical configurations of aggregated RBCs on the US scattered signal. It is believed that the hypotheses of the model are acceptable to pursue this goal. The results shown in the previous section demonstrate that the proposed simulation model is

an efficient method to model various configurations of RBC aggregates and to study their effect on the US backscattered signal. Furthermore, as mentioned before, the kinetics of aggregation (Figs. 5 and 11) are in good agreement with experimental observations.

CONCLUSION

US backscattering by blood is a complex phenomenon, affected by the level of RBC aggregation, the hematocrit, the US beam characteristics, and the angle of insonification. The simulation model presented in the current study is an efficient tool to predict the ultrasonic response to various RBC spatial organizations. The motion of interacting particles in shear flow was modeled, and it was shown to be similar to that of aggregating RBCs. The results demonstrated that variations in the ultrasonic backscattered power can be explained by considering the properties of the microstructure of the RBCs. We showed that the polydispersity in the size of the aggregates, the correlation in the positions of the RBCs, the shape, and orientation of the scatterers must be considered to establish a suitable index of aggregation measurable by US. Although limited to two dimensions, this model can contribute to the better understanding of the effect of the size and shape of RBC aggregates on the backscattering properties. Additional experimental results would be required to validate the simulations as a function of the angle of insonification. It would also be interesting to study the backscattering properties at various frequencies, hematocrits, and under different flow conditions.

This work was supported by operating grants from the Institutes of Health Research of Canada (MOP-36467) and the Heart and Stroke Foundation of Quebec, and by a research scholarship from the Fonds de la Recherche en Santé du Québec. The authors would like to acknowledge Dr. Hans Bäumler for helpful discussions and Dr. Michel Bertrand for his contribution to the first version of the ultrasound backscattering model (nonaggregating red blood cells).

REFERENCES

Allard, L., G. Cloutier, and L. G. Durand. 1996. Effect of the insonification angle on the Doppler backscattered power under red blood cell aggregation conditions. *IEEE Trans. Ultrason. Ferroelect. Freq. Contr.* 43: 211–219.

Armstrong, J. K., H. J. Meiselman, and T. C. Fisher. 1999. Evidence against macromolecular "bridging" as the mechanism of red blood cell aggregation induced by nonionic polymers. *Biorheology.* 36:433–437.

Bäumler, H., E. Donath, A. Krabi, W. Knippel, A. Budde, and H. Kiesewetter. 1996. Electrophoresis of human red blood cells and platelets. Evidence for depletion of dextran. *Biorheology.* 35:333–351.

Bäumler, H., E. Donath, L. Pratsch, and D. Lerche. 1989. Aggregation and disaggregation of human red blood cells in neutral polymer electrolyte solutions. *In* Hémorhéologie et Agrégation érythrocytaire. Théorie et Application cliniques. J. F. Stoltz, M. Donner, and A. L. Copley, editors. Éditions Médicales Internationales, Paris. 24–37.

Berger, N. E., R. J. Lucas, and V. Twersky. 1991. Polydisperse scattering theory and comparisons with data for red blood cells. *J. Acoust. Soc. Am.* 89:1394–1401.

Brooks, D. E., G. Russell, G. Janzen, and J. Janzen. 1980. Mechanisms of erythrocyte aggregation. *In* Erythrocyte Mechanics and Blood Flow. G. R. Cokelet, H. J. Meiselman, and D. E. Brooks, editors. Liss, A. R., Inc., New York. 119–140.

Chabanel, A., M. H. Horellou, J. Conard, and M. M. Samama. 1994. Red blood cell aggregability in patients with a history of leg vein thrombosis: influence of post-thrombotic treatment. *Br. J. Haematol.* 88:174–179.

Chien, S. 1975. Biophysical behavior of red cells in suspensions. *In* The Red Blood Cell. D. M. Surgenor, editor. Academic Press, New York, San Francisco, London. 1031–1133.

Chien, S. 1976. Electrochemical interactions between erythrocyte surfaces. *Thromb. Res.* 8:189–202.

Chien, S. 1981. Electrochemical interactions and energy balance in red blood cell aggregation. *In* Topics in Bioelectochemistry and Bioenergetics. John Wiley & Sons, Chichester, New York, Brisbane, Toronto. 73–112.

Cloutier, G., and Z. Qin. 1997. Ultrasound backscattering from nonaggregating and aggregating erythrocytes—a review. *Biorheology.* 34: 443–470.

Cloutier, G., and Z. Qin. 2000. Shear rate dependence of ultrasound backscattering from blood samples characterized by different levels of erythrocyte aggregation. *Ann. Biomed. Eng.* 28:399–407.

Copley, A. L., R. G. King, and C. R. Huang. 1976. Erythrocyte sedimentation of human blood at varying shear rates. *In* Microcirculation. J. Grayson and W. Zingg, editors. Plenum Press, New York. 133–134.

Donath, E., and A. Voigt. 1986. Electrophoretic mobility of human erythrocytes. On the applicability of the charged layer model. *Biophys. J.* 49:493–499.

Fontaine, I., M. Bertrand, and G. Cloutier. 1999. A system-based approach to modeling the ultrasound signal backscattered by red blood cells. *Biophys. J.* 77:2387–2399.

Fontaine, I., and G. Cloutier. 2000. Frequency dependence of simulated ultrasound signals backscattered by aggregating red blood cells. *In* Acoustical Imaging. M. Halliwell and P. N. T. Wells, editors. Kluwer Academic/Plenum Publishers, New York, Boston, Dordrecht, London, Moscow. 297–302.

Foster, F. S., H. Obara, T. Bloomfield, L. K. Ryan, and G. R. Lockwood. 1994. Ultrasound backscatter from blood in the 30 to 70 MHz frequency range. *IEEE Ultrason. Symp. Proc.* 1599–1602.

Goldsmith, H. L. and J. Marlow. 1972. Flow behaviour of erythrocytes. I. Rotation and deformation in dilute suspensions. *Proc. Royal Soc.* 182: 351–384.

Jan, K. M., and S. Chien. 1972. Role of the electrostatic repulsive force in red cell interactions. 7th European Conference Microcirculation. 11: 281–288.

Jan, K. M., and S. Chien. 1973. Role of surface electric charge in red blood cell interactions. *J. Gen. Physiol.* 61:638–654.

Landini, L., and L. Verrazzani. 1990. Spectral characterization of tissues microstructure by ultrasounds: a stochastic approach. *IEEE Trans. Ultrason. Ferroelect. Freq. Contr.* 37:448–456.

Lim, B., P. A. J. Bascom, and R. S. C. Cobbold. 1996. Particle and voxel approaches for simulating ultrasound backscattering from tissue. *Ultrasound Med. Biol.* 22:1237–1247.

Lucas, R. J., and V. Twersky. 1987. Inversion of ultrasonic scattering data for red blood cell suspensions under different flow conditions. *J. Acoust. Soc. Am.* 82:794–799.

Mo, L. Y. L., and R. S. C. Cobbold. 1992. A unified approach to modeling the backscattered Doppler ultrasound from blood. *IEEE Trans. Biomed. Eng.* 39:450–461.

Neumann, F. J., H. A. Katus, E. Hoberg, P. Roebruck, M. Braun, H. M. Haupt, H. Tillmanns, and W. Kübler. 1991. Increased plasma viscosity and erythrocyte aggregation: indicators of an unfavourable clinical outcome in patients with unstable angina pectoris. *Br. Heart J.* 66:425–430.

Razavian, S. M., V. Atger, P. H. Giral, M. Cambillau, M. Del-Pino, A. C. Simon, N. Moatti, and J. Levenson. 1994. Influence of HDL subfractions

on erythrocyte aggregation in hypercholesterolemic men. *Arterioscler. Thromb.* 14:361–366.

Razavian, S. M., M. Del Pino, A. Simon, and J. Levenson. 1992. Increase in erythrocyte disaggregation shear stress in hypertension. *Hypertension.* 20:247–252.

Schmid-Schönbein, H., and E. Volger. 1976. Red-cell aggregation and red-cell deformability in diabetes. *Diabetes.* 25:897–902.

Shehada, R. E. N., R. S. C. Cobbold, and L. Y. L. Mo. 1994. Aggregation effects in whole blood: influence of time and shear rate measured using ultrasound. *Biorheology.* 31:115–135.

Shung, K. K., and G. A. Thieme. 1993. Ultrasonic Scattering in Biological Tissues. CRC Press, Boca Raton, Ann Arbor, London, Tokyo.

Sigel, B., J. Machi, J. C. Beitler, J. R. Justin, and J. C. U. Coelho. 1982. Variable ultrasound echogenicity in flowing blood. *Science.* 218: 1321–1323.

Teh, B. G., and G. Cloutier. 2000. The modeling and analysis of ultrasound backscattering by red blood cell aggregates with a system-based approach. *IEEE Trans. Ultrason. Ferroelect. Freq. Contr.* 47:1025–1035.

Twersky, V. 1975. Transparency of pair-correlated, random distributions of small scatterers, with application to the cornea. *J. Opt. Soc. Am.* 65:524–530.

Twersky, V. 1987. Low-frequency scattering by correlated distributions of randomly oriented particles. *J. Acoust. Soc. Am.* 81:1609–1618.

Ursea, R., J. Coleman, R. H. Silverman, F. L. Lizzi, S. M. Daly, and W. Harrison. 1998. Correlation of high-frequency ultrasound backscatter with tumor microstructure in iris melanoma. *Ophthalmology.* 105: 906–912.

Van Der Heiden, M. S., M. G. M. De Kroon, N. Bom, and C. Borst. 1995. Ultrasound backscatter at 30 MHz from human blood: influence of rouleau size affected by blood modification and shear rate. *Ultrasound Med. Biol.* 21:817–826.

Varghese, T., and K. D. Donohue. 1993. Characterization of tissue microstructure scatterer distribution with spectral correlation. *Ultrasonic Imaging.* 15:238–254.

Weng, X., G. Cloutier, R. Beaulieu, G. O. Roederer. 1996. Influence of acute-phase proteins on erythrocyte aggregation. *Am. J. Physiol. Heart Circ. Physiol.* 40:H2346–H2352.

Yuan, Y. W., and K. K. Shung. 1988. Ultrasonic backscatter from flowing whole blood. I: Dependence on shear rate and hematocrit. *J. Acoust. Soc. Am.* 84:52–58.

Zhang, J., J. L. Rose, and K. K. Shung. 1994. A computer model for simulating ultrasonic scattering in biological tissues with high scatterer concentration. *Ultrasound Med. Biol.* 20:903–913.

Annexe C

Permissions des éditeurs

Les autorisations des éditeurs de copier les articles publiés de cette thèse sont fournies dans cette annexe.

Dear David Savéry,

The American Institute of Physics grants you permission to reuse the article referenced below in your PhD thesis:

Savéry D. Cloutier G. A point process approach to assess the frequency dependence of ultrasound backscattering by aggregating red blood cells. Journal of the Acoustical Society of America. 110(6):3252-3262, 2001 Dec.

Regards,

Shannon Quigley

American Institute of Physics

[redacted]

~~~~~~~~~~~

Ann C. Perlman

Office of the Publisher, Journals and Technical Publications

Rights & Permissions

American Institute of Physics

Suite 1NO1

[redacted]

TEL

FAX
~~~~~~~~~~~

Comments/Response to Case ID: 006AE214

ReplyTo: Copyrights@ieee.org

From: Sandra Bjornsen Date: 07/25/2003

Subject: Re: permission to include two conference articles in a PhD thesis

Send To: David Savéry

[redacted]

cc:

SUBJECT: 1."Monte Carlo Simulations of Ultrasound Backscattering by Aggregating Red Blood cells Cells" by D. Savery and G. Cloutier

2. "Anisotropy of Ultrasonic Backscatter by Blood in Shear Flow: Monte Carlo Simulations" by D. Savery and G. Cloutier

Dear Mr. Savery:

This is in response to your letter of 21 July 2003 in which you have requested permission to reprint, in your upcoming thesis/dissertation, the above IEEE copyrighted material. We are happy to grant this permission.

Our only requirement is that the following copyright/credit notice appears prominently on the first page of each reprinted paper, with the appropriate details filled in:

© 2003 IEEE. Reprinted, with permission, from (complete publication information).

Sincerely yours,

Sandra Bjornsen

-=-

IEEE Intellectual Property Rights Office
445 Hoes Lane, Piscataway, NJ 08855
Telephone: (732) 562-3966
E-Mail: copyrights@ieee.org FAX: (732) 981-8062